MODELLING OF HIGH TEMPERATURE SUPERCONDUCTORS FOR AC POWER APPLICATIONS

THÈSE N^{O} 2579 (2002)

PRÉSENTÉE À LA FACULTÉ INFORMATIQUE ET COMMUNICATION

ÉCOLE POLYTECHNIQUE FÉDÉRALE DE LAUSANNE

POUR L'OBTENTION DU GRADE DE DOCTEUR ÈS SCIENCES TECHNIQUES

DANS LE DOMAINE DES SYSTÈMES DE COMMUNICATION

PAR

Svetlomir STAVREV
Ingénieur électricien, diplômé de l'Université Technique de Varna, Bulgarie
et de nationalité bulgare

acceptée sur proposition du jury:

Prof. M. Hasler, directeur de thèse
Dr B. Dutoit, rapporteur
Prof. R. Flükiger, rapporteur
Dr C. Friend, rapporteur
Prof. M. Q. Tran, rapporteur
Prof. H. ten Kate, rapporteur

Lausanne, EPFL
2002

To my family

Acknowledgements

This Ph.D. thesis contains the results of three and a half years of research, which has been performed at the Laboratory of Nonlinear Systems (former Chair of Circuits and Systems) at the Swiss Federal Institute of Technology – Lausanne. Most of the research work has been done within the framework of the European projects SACPA and BIG-POWA, funded by the RTD Directorate of the European Commission and by the Swiss Federal Office of Science and Education.

There are three persons that I am particularly grateful to – Prof. Martin Hasler, my thesis director – for accepting me as a Ph.D. assistant in his laboratory and for the academic freedom, which he granted to me for the selection of the subject and orientation of my thesis; Dr. Bertrand Dutoit, my thesis supervisor – for the continuous advising and support during the years I have worked in his group, and also for providing all measurements that I have used for the modelling and validation of the results of the thesis; Dr. Nadia Nibbio – for her pioneering work in the finite element method modelling of superconductors in our laboratory, which has served as a basis for a large part of my thesis.

I would also like to thank all my former and present colleagues from the Laboratory of Nonlinear Systems at the Swiss Federal Institute of Technology - Lausanne for maintaining a nice, friendly and creative atmosphere in the lab. In particular, Dr. Mårten Sjöström, who had the questionable privilege to share the same office with me for 3 years and who has been cooperative and helpful in many situations, Dr. Thomas Schimming, our system administrator, for his permanent availability and expertise, needed in the difficult moments, which occur from time to time to PC users, Mr. Francesco Grilly for his cooperativeness, and also Mrs. Christiane Good, our kind secretary, who has always taken the professional and personal problems of the assistants in the lab as problems of her own.

Among our different partners from the European projects SACPA and BIG-POWA, with whom I have worked, I would like to thank sincerely Dr. Yifeng Yang from the University of Southampton for the many stimulating discussions we have had and his expertise in superconductivity, which he has generously shared with me, and especially for the courtesy of providing and letting us use the initial algorithm with Brandt's method, which I have used for comparison and validation of my finite element method results; Dr. Emmanuel Vinot and Dr. Pascal Tixador from Institut National Polytechnique de Grenoble for their collaboration, which resulted in several papers, and Dr. Chris Friend from BICC Cables, presently working in Oxford Instruments, former coordinator of the SACPA and BIG-POWA projects, who had written the project proposals and to whom both projects owe in a way their existence.

I gratefully acknowledge the cooperation and pieces of advice, which I have received from Dr. Patrick Lombard from CEDRAT S.A., concerning the development of the user subroutine in Flux2D, the software with which I have achieved all finite element method results, presented in the thesis.

Last but not least, I would like to thank my parents Vancha and Dimitar for their love and continuous support during all the years I have spent abroad, and my lovely wife Mariya for her patience and affection, which she demonstrated in the last and most difficult months of this thesis.

Abstract

This Ph.D. thesis is focused on the development of novel models for calculation of AC losses, current and magnetic field profiles in high-temperature superconductors (HTS). The thesis is concentrated on the modelling of Bi-2223 conductors at 77 K, which for the moment have the most advanced manufacturing technology and will be primarily used in the first large-scale power applications of high-temperature superconductors. The analysis of AC losses in Bi-2223 conductors is the leading thread in the structure of the thesis.

An introduction to high-temperature superconductivity is made with special emphasis on the mechanisms of AC losses in HTS. Presented are some of the most promising power applications of HTS materials together with a discussion on the required improvements in their performance.

A model for dissociating the hysteresis, eddy-current and resistive flux-creep loss contributions, based on relatively broad-range frequency measurements on Bi-2223 tapes has been used for analysis of the frequency behaviour of the transport-current loss in self-field. The hysteresis, eddy-current and flux-creep loss components have been separated due to their different frequency dependence. The study of eddy current loss in the silver sheath and matrix has been complimented by numerical simulations using a simple electromagnetic model of HTS tapes.

Described is an original method for estimating the performance of Bi-2223 tapes in typical power grid perturbations by experiments and analysis of over-critical current excursions of various waveform, frequency and current amplitude up to $20\times I_c$.

For precise calculation of the AC losses and studying the electromagnetic properties of HTS with smooth current-voltage characteristics and complex geometry, the finite element method (FEM) has been used. The implementation of the power-law model of the E-J characteristic of HTS into the FEM software package Flux2D is presented. The Flux2D implementation has been validated by means of comparison with results from theoretical predictions, electrical measurements, and other numerical methods. The significance of the power index n and the lateral distribution of the critical current density J_c in multifilamentary HTS tapes has been evaluated by FEM simulations.

New anisotropic models of $J_c(B)$ and $n(B)$ for textured Bi-2223 materials have been developed. The models are based on experimental data; they are fairly simple and take into account the orientation of the local magnetic field. These models have been used in FEM simulations on monofilamentary and multifilamentary Bi-2223 conductors with different geometry and filament arrangement. In conductors with given $J_c(B)$ dependence, the notion of effective AC critical current has been defined.

The AC losses in Bi-2223 multifilamentary flat tapes and wires of round and square geometry in various operating conditions have been calculated and compared. The AC loss analysis has been supported and complimented by current density and magnetic flux distributions in the different conductors. The influence of the shape factor of the geometry and the filament orientation with respect to the local magnetic field has been thoroughly investigated. The optimal geometry and filament arrangement have been determined for each application.

Version abrégée

L’objectif principal de cette thèse est le développement de nouveaux modèles pour le calcul des pertes AC et des profils de courant et champ magnétique dans les supraconducteurs à haute température (HTS). La thèse est concentrée sur la modélisation des conducteurs Bi-2223 à 77 K qui, pour le moment, ont la technologie de fabrication la plus avancée et seront principalement utilisés dans les premières applications de puissance des supraconducteurs à haute température. La réduction et l'optimisation des pertes AC des conducteurs Bi-2223 est le principal fil conducteur dans la structure de la thèse.

Une introduction à la supraconductivité à haute température est faite avec une attention particulière sur les mécanismes des pertes AC dans les HTS. Certaines des applications de puissance les plus prometteuses des matériaux HTS sont présentées ainsi qu'une discussion sur les améliorations de leurs performances que cela implique.

Un modèle pour dissocier les contributions aux pertes d’origine hystérétique, par courants de Foucault ou résistives liées aux mécanismes de flux-creep a été utilisé. L'analyse du comportement fréquentiel des pertes avec un courant transport en champ propre dans des rubans Bi-2223 est à la base de ce modèle. Les composantes d’origine hystérétique, liées aux courants de Foucault ou aux mécanismes de flux-creep ont été séparées grâce à leur différente dépendance en fréquence. L'étude des pertes par courants de Foucault dans la gaine et la matrice d’argent a été complétée par des simulations numériques utilisant un modèle électromagnétique simple des rubans HTS.

Une méthode originale a été utilisée pour estimer la performance des rubans Bi-2223 lors de perturbations typiques au réseau électrique. L'analyse d’expériences d’excursions au-dessus du courant critique avec diverses formes d’onde, à différentes fréquences et avec des amplitudes jusqu’à $20 \times I_c$ ont permis de faire ces estimations de performance.

L’implémentation du modèle en loi de puissance de la caractéristique E-J de matériaux HTS dans le logiciel de calcul par éléments finis (FEM) Flux2D est présentée. Cette implémentation dans Flux2D a été validée par des comparaisons avec des résultats de prévisions théoriques, des mesures électriques, ainsi que d'autres méthodes numériques. L’importance de l'index de puissance n et de la distribution transversale de la densité de courant critique J_c dans des rubans multifilamentaires de HTS a été évaluée par des simulations FEM.

Des nouveaux modèles anisotropes de $J_c(B)$ et de $n(B)$ pour les matériaux Bi-2223 texturés ont été développés. Ces modèles sont basés sur des données expérimentales; ils sont assez simples et tiennent compte de l'orientation du champ magnétique local. Ils ont été utilisés dans des simulations FEM sur les conducteurs monofilamentaires et multifilamentaires Bi-2223 avec différentes géométries et configurations de filaments. Dans des conducteurs avec une dépendance $J_c(B)$ donnée, la notion de courant critique efficace AC a été définie.

Les pertes AC dans les rubans plats et fils Bi-2223 multifilamentaires avec géométrie ronde et carrée ont été calculées et comparées dans diverses conditions opérationnelles. L'analyse des pertes AC a été vérifiée et complétée par le calcule des distributions de densité de courant et flux magnétiques dans les différents conducteurs. L'influence du facteur de forme de la géométrie et de l'orientation des filaments par rapport au champ magnétique local a été étudiée à fond. Une configuration optimale de la géométrie et des filaments a été déterminée pour chaque application.

Table of Contents

CHAPTER 1. INTRODUCTION 1

1.1 Superconductivity 1

1.2 Applications of superconductors 2

1.3 Motivations and outline of this thesis 3

CHAPTER 2. HIGH-T_C SUPERCONDUCTIVITY 5

2.1 Introduction 6

2.2 Fundamentals of high-T_c superconductivity 6

2.2.1 Basic features of superconductors 6
2.2.2 Type-II superconductors 9
2.2.3 Critical currents in high-T_c superconductors 13
2.2.4 Advanced HTS materials 14

2.3 AC loss mechanisms in high-T_c superconductors 16

2.3.1 AC losses in the superconductor 17
2.3.2 AC losses in the metal matrix 19

2.4 Power applications of high-T_c superconductors 22

2.4.1 Cables 23
2.4.2 Fault Current Limiters 23
2.4.3 Transformers 24
2.4.4 Magnetic energy storage devices 25
2.4.5 Other applications 25

2.5 Major issues for full-scale industrial applications 26

2.5.1 Development of the superconductivity market 27
2.5.2 Necessary improvements in BSCCO conductors 28

2.6 Conclusions 29

CHAPTER 3. MODELLING AND AC LOSSES OF BI-2223 TAPES WITH APPLIED TRANSPORT CURRENT 31

3.1 Introduction 32

3.2 Measurement of transport current losses 32

3.3 Calculation of AC losses of HTS in self-field.. 35
3.3.1 Hysteresis loss in self-field...35
3.3.2 Theoretical and empirical derivations of eddy current loss.......................................37

3.4 Frequency-dependence modelling of transport current AC losses in self-field 39
3.4.1 Frequency behaviour of self-field AC losses in related studies 39
3.4.2 Model for AC loss dissociation in a broad frequency range 41
3.4.3 Hysteresis loss 46
3.4.4 Flux-creep resistive loss near I_c 49

3.5 Eddy current loss in self-field... 50
3.5.1 Measured eddy current loss in Bi-2223 tapes..50
3.5.2 Numerical modelling of eddy current loss 54
3.5.3 Comparison between measured, simulated and empirically derived eddy current loss 60

3.6 Response of Bi-2223 tapes to over-critical current excursions................... 67
3.6.1 Over-I_c voltage-current waveforms 68
3.6.2 Resistive behaviour in the over-I_c regime 70
3.6.3 Models for temperature-rise estimation..71

3.7 Conclusions 75

CHAPTER 4. NUMERICAL MODELLING OF HIGH-T_C SUPERCONDUCTORS WITH B-INDEPENDENT J_C AND N 77

4.1 Introduction.. 78

4.2 Basis for modelling of type-II superconductors... 78
4.2.1 The critical state model...78
4.2.2 The constitutive equations of type-II superconductors...81

4.3 Engineering approaches for modelling of HTS 84

4.4 Numerical methods for 2D modelling of HTS 85
4.4.1 Brandt's method and its numerical implementations 86
4.4.2 The finite element method...87

4.5 FEM modelling of HTS with Flux2D.. 89
4.5.1 Implementation of the E-J power law model in Flux2D 89
4.5.2 Newton-Raphson algorithm for nonlinear problems...90
4.5.3 Effect of the residual resistivity ρ_0 93
4.5.4 Boundary conditions for different applications..95
4.5.5 Mesh optimization and CPU time 96

4.6 AC losses and current distribution in HTS tapes – validation of the Flux2D implementation 99
4.6.1 Comparison with measurements and Norris's losses in self-field........ 100
4.6.2 Comparison with Brandt's model and the CSM in applied field 103
4.6.3 Comparison with other FEM models........ 107

4.7 Influence of the finite *n*-value of Bi-2223 tapes 111
4.7.1 Influence of the *n*-value on the current density distribution........ 112
4.7.2 Influence of the *n*-value on the AC loss 114

4.8 Modelling of Bi-2223 tapes with lateral J_c variation 116
4.8.1 Models of $J_c(x)$ and $n(x)$ dependence 116
4.8.2 Current and power density distributions in multifilamentary tapes with different models of $J_c(x)$ 119
4.8.3 Current flow and AC loss in the individual filaments 120
4.8.4 AC losses in tapes with different models of $J_c(x)$ in self-field and in external magnetic field........ 122

4.9 Summary and conclusions 125

CHAPTER 5. FEM MODELLING OF BI-2223/AG CONDUCTORS WITH $J_C(B)$ AND $N(B)$ 127

5.1 Introduction........ 128

5.2 Defining the J_c values for numerical simulations of HTS........ 128

5.3 Modelling of HTS tapes with $J_c(B)$ and $n(B)$ in perpendicular magnetic fields 129
5.3.1 Models for $J_c(B)$ dependence in perpendicular magnetic field 129
5.3.2 Comparison between modelling with constant J_c and $J_c(B)$ in perpendicular magnetic field........ 132
5.3.3 AC losses in transport current applications in perpendicular magnetic field........ 138

5.4 Modelling of monofilamentary conductors in different applications 139
5.4.1 Isotropic and anisotropic models of $J_c(B)$ and $n(B)$ for mono-filamentary wires and tapes........ 139
5.4.2 Specifications of the simulated monofilamentary conductors........ 144
5.4.3 Revisiting the definition of I_c in conductors with $J_c(B)$........ 145
5.4.4 Monofilamentary conductors with transport current........ 148
5.4.5 Monofilamentary conductors in applied external magnetic field........ 151
5.4.6 Monofilamentary conductors with transport current and applied magnetic field 158

5.5 Modelling of multifilamentary conductors in different applications 165
5.5.1 Specifications of the simulated multifilamentary conductors 165
5.5.2 Modelling of $J_c(B)$ and $n(B)$ in tapes and wires with various filament arrangement 168
5.5.3 Effective I_c in the multifilamentary conductors........ 169
5.5.4 Tapes and wires with transport current........ 171

5.5.5 Tapes and wires in applied external magnetic field of varying orientation..............175
5.5.6 Tapes and wires with transport current and applied magnetic field..........................180

5.6 Summary and conclusions 182

CHAPTER 6. CONCLUSION 185

6.1 General conclusions and achievements of this thesis................................ 185

6.2 Future considerations 187

APPENDIX A. CALCULATION OF HYSTERESIS LOSS IN SELF-FIELD............ 189

APPENDIX B. INTRODUCTION TO THE GALERKIN FINITE ELEMENT METHOD 191

LIST OF SYMBOLS AND ACRONYMS... 195

REFERENCES 197

CURRICULUM VITAE 206

PUBLICATIONS…………………………………………………………………… 207

Chapter 1. Introduction

1.1 Superconductivity

One of the hallmarks of the 20th century physics was the discovery of superconductivity, a phenomenon found out by Kamerlingh Onnes in 1911 at the University of Leiden [Onn11]. It had been known for years that the electric resistance of metals should disappear as the temperature approaches the absolute zero, however the limiting values of the resistance at finite temperatures were not known at that time. In his pioneering experiments with liquid helium Onnes was able to obtain temperatures as low as 1 K, and observed that instead of a smooth decrease of the resistance of mercury (Hg) as the temperature was gradually reduced towards 0 K, it sharply disappeared below a certain temperature (4 K), which is now referred to as the *critical temperature* (T_c). Onnes recognized that below 4 K mercury passes into a new state with electric properties unlike any known before, and this new state was called the *superconducting state*.

Later, many different superconductors have been discovered. Metallic elements and alloys, which exhibit superconducting properties below 30 K have been named low-temperature superconductors (LTS), in contrast to certain oxide compounds with T_c exceeding 30 K, named high-temperature superconductors (HTS). Above their T_c, the superconductors have electric resistance higher than the resistance of good metal conductors, such as copper (Cu), as shown in Fig. 1-1. Most of them are resistive materials at room temperature.

With the years of development of superconductivity, the critical temperature has been increasing and now may exceed 130 K for certain oxide superconductors, see Fig. 1-2. The higher the T_c, the easier is the construction and maintenance of cryogenic systems needed to cool down the superconductors in their applications.

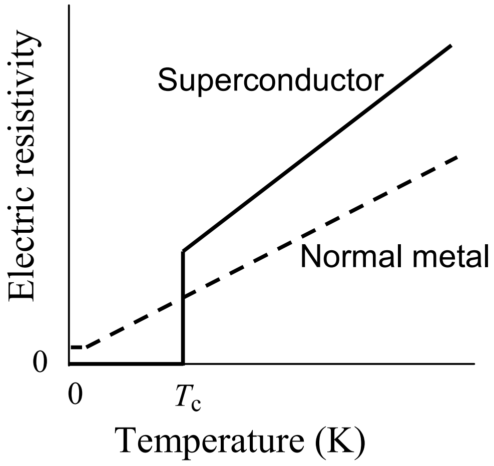

Figure 1-1 Resistivity in normal metals and in superconductors.

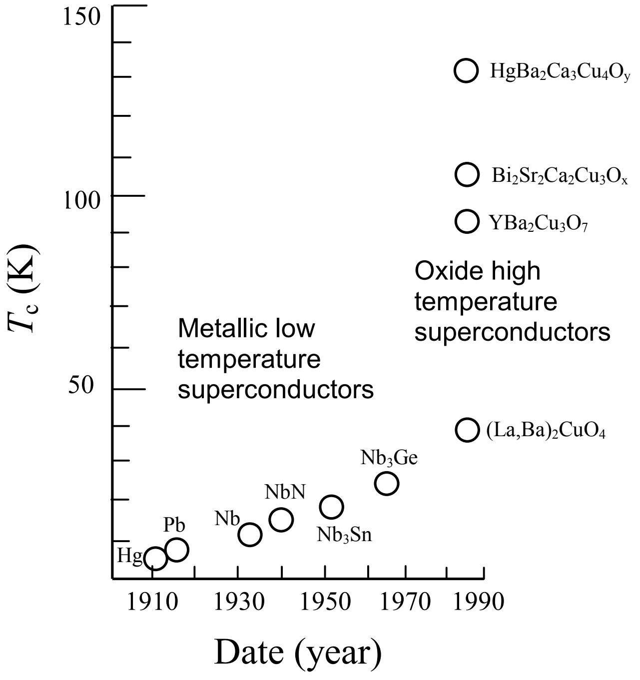

Figure 1-2 Evolution of the critical temperature of superconductors.

1.2 Applications of superconductors

The idea of loss-less transmission of electricity was inspired from the discovery of superconductivity. In addition to zero resistance below the T_c, superconductors are able to carry very large currents through a small cross-section. Their current densities exceed by far (1 to 2 orders of magnitude) the admissible ones of standard metal conductors, such as copper or aluminium. Nowadays, one of the most promising power applications of superconductors is their usage in electric power distribution grids, where the existing Cu overhead lines will be replaced by underground superconducting cables, as it is shown in Fig. 1-3. By using superconductors, the electricity in the near future will be carried in a cheaper, environmental-friendly and more efficient way. Other possible large-scale applications of superconductors in electric power networks include transformers, fault-current limiters, motors and generators, as well as magnetic energy storage devices.

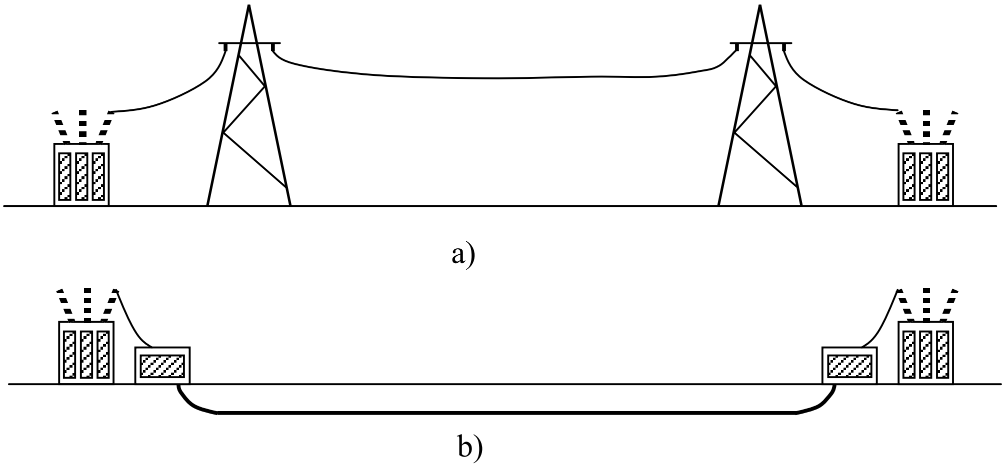

Figure 1-3 Power transmission lines – standard Cu overhead lines (a) and superconducting underground cable (b).

Another remarkable feature of superconductors are their magnetic properties, among which the repulsion of any magnetic field in the superconducting state. This property, known as the Meissner effect, opens the possibility to use superconductors as bearing material in magnetic levitation applications (MAGLEV). An impressive example is the use of superconducting magnets for contactless acceleration in high-speed trains, developed and used in Japan, the USA and Germany. The Japanese Railways MAGLEV trains, shown in Fig. 1-4, may reach 500 kph in straight segments; they have low operation and maintenance cost, less environmental impact and large transport capacity.

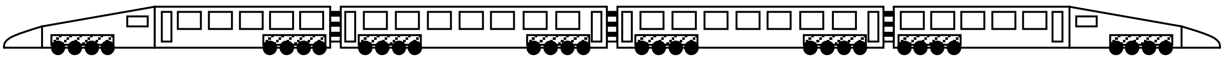

Figure 1-4 Bullet train of the Japan Railway Company using superconducting magnets for contactless acceleration up to 500 kph.

A leading use of superconductors for many years on has been to produce high and stable magnetic fields. Such fields are employed for example with Magnetic Resonance Imaging (MRI) for high-quality medical scanning equipment, as well as in nuclear physics for super-powerful particle accelerators, where they may exceed 15 T.

Superconductors offer also a great diversity of electronics (small-scale) applications. The Josephson tunnelling effect is widely used in superconducting quantum interference devices (SQUID) and in different types of digital circuits and systems. A superconductor reflects perfectly electromagnetic waves. This property is used for microwave resonators and spectral detectors.

Last but not least, worth mentioning are some emerging high technology applications. Certain superconductors are able to switch from the superconducting state to the non-superconducting state in 10^{-12} sec, i.e. about 1000 times faster than silicon, which suggests that computers made from superconducting elements might be 1000 times faster than those with silicon chips. While the full advantages may be difficult to obtain, substantial improvements in the speed of central processor units are expected in the foreseeable future.

1.3 Motivations and outline of this thesis

A great boost in the development of superconductivity was triggered in 1986, when J. George Bednorz and Karl Müller from the IBM research laboratory in Zurich discovered the first oxide compounds with superconducting properties above the theoretical ceiling of 30 K and the era of high-temperature superconductivity began [Bed86].

While the use of LTS materials for the implementation of powerful DC magnets had been a leading application of superconductors for years, the new HTS compounds offered new possibilities for AC power applications at 77 K, the temperature of liquid nitrogen.

Unfortunately, zero resistance is observed in superconductors only when DC current is applied and Joule (heat) dissipation appears in AC operating conditions. Despite the reigning optimism after the discovery of HTS in 1986, their massive industrial applications, initially previewed for the horizon 1995-2000, still have not come into existence. Presently, there are some overwhelming considerations for large-scale industrial applications of HTS materials, among which the aspect of AC losses is of primary importance since their magnitudes are still above the desired application levels. The reduction of every watt of dissipated power will be precious for the utilities and there will be no real industrial applications if the AC losses in the current state-of-the-art high-T_c superconductors do not fall within acceptable limits.

Before the implementation of various HTS devices, such as cables, coils and transformers, the expected levels of AC losses need to be evaluated at the design stage. There are no comprehensive theoretical models for the current and field equations in HTS of complex geometry and cross-sections. In addition, HTS have smooth nonlinear current voltage characteristics and the existing theoretical models, such as the critical state model of Bean, do not fully apply to such materials. Hence comes the need of advanced numerical or other modelling techniques for calculating correctly the current and magnetic field distributions and AC losses in HTS components and prototypes, which is the main motivation for initiating this Ph.D. thesis.

The central frame of the thesis is the modelling of high-T_c superconductors for AC applications in different operating conditions – with applied transport current and/or external magnetic field of varying orientation.

The finite element method has been selected for the electromagnetic analysis and AC loss calculation in HTS, since it is allows modelling of nonlinear materials with field or position dependent properties and complex geometry.

Chapter 2 gives an introduction to high-T_c superconductivity and its applications. Special attention is paid to the explanation of the different loss mechanisms in HTS. An overview is made on the state-of-the-art of the most advanced HTS materials. Outlined are the main power applications of HTS, including a discussion on the major issues and challenges for large-scale applications.

Chapter 3 deals with modelling and AC losses in HTS tapes with applied transport current. Analysed is the frequency behaviour of self-field AC losses, based on measurements on 14 mono and multifilamentary tapes in a broad frequency range. A model for dissociating the different self-field loss contributions is presented. The analysis of eddy current loss is complement by numerical simulations. Described is an original method for estimating the performance of the tapes in over-critical current excursions.

Chapter 4 presents the implementation of the nonlinear power-law model of the E-J characteristics of HTS into the finite element method software package Flux2D. The validation of the Flux2D implementation has been achieved by comparison with electrical measurements in self-field, with theoretical predictions, and with other numerical methods. An evaluation of the significance of the n-value in the power-law E-J characteristics of HTS has been obtained by means of numerical simulations. More advanced models with lateral dependence of the critical current density J_c have been used in order to quantify the effect of the locally varying J_c along the width of multifilamentary tapes in different operating conditions.

Chapter 5 presents new models of anisotropic and isotropic dependence of J_c and the n-value on the magnetic flux density B. These models allow simulations of mono and multifilamentary HTS conductors with various geometries in applied current and/or external field of any orientation. The concept of effective $I_c(B)$ is introduced. Results from numerical simulations of HTS mono and multifilamentary tapes and wires in different applications are described, outlining the main factors for AC loss levels – the geometric shape of the conductors and their filament configuration. The optimal geometry and filament arrangement has been defined for each application.

Finally, Chapter 6 presents the main conclusions and outlines the contributions of this thesis; this chapter also gives some considerations for possible continuation of the modelling approaches developed in the thesis.

Chapter 2. High-T_c Superconductivity

Abstract

An introduction to superconductivity and high-temperature superconductors is made. Presented are the fundamental features of type-II superconductors, including an overview of the most advanced high-temperature superconducting materials. Special emphasis is made on the explanation of the different types of losses in AC operating conditions. Given are some examples of the most promising power applications of high-temperature superconductors. Finally, a discussion is made on the major issues and challenges for large-scale industrial applications.

2.1 Introduction

The purpose of this general chapter is to make an introduction to high-T_c superconductivity and its applications. By outlining the current state of the development of high-T_c superconductors, as well as the loss mechanisms in AC operating conditions, it is intended to serve as a bridge and explanation to the following chapters of this thesis.

Section 2.2 describes the fundamentals of superconductivity, the main features of type-II superconductors, as well as the most advanced HTS materials; Section 2.3 gives a background on the different mechanisms for AC losses in HTS, which represent a major stumbling block for widespread industrial applications; Section 2.4 makes an overview of the most promising HTS power applications, and Section 2.5 contains a discussion on the main challenges and issues in the development and utilization of high-T_c superconductors.

This chapter covers by no way all aspects of the physics of HTS materials, some of which are not yet completely understood. More detailed introduction to superconductivity can be found in [Car83], [Inn78], [She94], [Tin75] and [Wil83], which have served as basic references for this chapter.

2.2 Fundamentals of high-T_c superconductivity

2.2.1 Basic features of superconductors

Type-I superconductors

Certain metals, such as titanium, aluminum, tin, mercury, lead, and others, become superconducting, i.e. their electric resistance completely disappears, when they are cooled below their critical temperature. These metals were the first superconductors to be discovered and have been later named *type-I superconductors*.

It was discovered that superconductivity is destroyed, i.e. the metal becomes normal again, in the presence of certain magnetic field, which is referred to as the critical field H_c. The value of H_c is related thermodynamically to the free-energy difference between the normal and the superconducting state.

The critical temperatures, magnetic fields and magnetic flux densities of several type-I superconductors are given in Table 2-1. H_c in metal superconductors is very low.

TABLE 2-1. T_c, H_c and B_c in type-I superconductors

Metal	*T_c (K)*	*H_c (A/m)*	*B_c (Tesla)*
Titanium (Ti)	0.4	0.42×10^4	0.0056
Aluminum (Al)	1.2	0.79×10^4	0.0105
Tin (Sn)	3.7	2.40×10^4	0.0305
Mercury (Hg) - α	4.2	3.30×10^4	0.0411
Lead (Pb)	7.2	6.40×10^4	0.0803

The superconducting transition temperatures and the critical magnetic fields at 0K.
Sources [Inn78] and [Lar00].

AC resistivity

Zero resistance in a superconducting metal means that there is no voltage drop along the metal when a current is passed through, and by consequence no power is dissipated. This is, however, strictly true only for a DC current of constant value.

The appearance of resistance when AC current is applied can be explained if one makes the assumption that below the T_c the electrons in the metals can be divided into two categories: “superelectrons” which form so-called Cooper pairs and carry electricity without resistance and the rest behaving like “normal” electrons, which scatter and when passing through the metal lattice experience resistance [Inn78].

In the case of constant DC current, there must be no electric field present in the metal; otherwise the superelectrons would accelerate continuously and the current would increase. In this case, there is no electromotive force to drive the normal electrons and all the current is lead through by the superelectrons, so no power dissipation appears at all.

In AC current, an electric field must be present to accelerate the electrons. Because of the inertial mass of the electrons (even if of very small magnitude), the supercurrent lags behind the electric field. Hence the superelectrons present inductive impedance. In addition, due to the presence of electric field, some current will be carried by the normal electrons, so that in overall the AC current will cause some power dissipation in a superconducting metal.

Perfect diamagnetism (Meissner effect)

Superconductors have unique combination of electric and magnetic properties. Although the term ‘superconducting’ implies zero resistance, superconductors do not simply behave as perfect conductors (R = 0). In a perfect conductor the resistance around an imaginary close path is zero, therefore the amount of magnetic flux enclosed within this path cannot change. This must be true for any such imaginary circuit, which may happen only if the flux density at every point in the perfect conductor does not vary with time, i.e.:

$$dB / dt = 0 \tag{2.1}$$

This means that if a perfect conductor at room temperature with no applied magnetic field is cooled to a very low temperature, and then a magnetic field is applied, the magnetic flux will not be allowed to enter the specimen and the interior will remain flux-free, since *dB/dt* must hold.

On the contrary, if a perfect conductor is subjected to an applied field before the cooling, the flux density inside will be the same as that of the external field. This is due to the value of the relative magnetic permeability in most metals, which is very close to unity, except for the ferromagnetic materials. If the metal is then cooled down to a low temperature, this will have no effect on the magnetization, and the flux distribution will remain unchanged. Now, as the applied field is removed, *dB/dt* must hold again, so that currents will be induced in the interior of the perfect conductor, maintaining the flux inside unchanged, see Fig. 2-1a.

In 1933, Meissner and Ochsenfeld measured the flux distribution of metal superconductors, cooled down to their T_c while in a magnetic field [Mei33]. Surprisingly, they found out that a metal in the superconducting state never allows a magnetic flux density to exist in its interior, i.e. it exhibits perfect diamagnetism and the following equality always holds:

$$B = 0 \tag{2.2}$$

This property, which cannot be explained by an equivalence of superconductors with perfect conductors, has been named Meissner effect. The magnetic behaviour of a superconductor in contrast to a perfect conductor is illustrated in Fig. 2-1b.

The expulsion of an applied field is a result of the existence of induced currents in a superconductor, which generate magnetic field, opposite in direction and equal in magnitude to the external field, so that the total field inside the superconductor is zero. The cancellation of flux lines within the superconductor may be viewed as if the external field lines are 'forced' to circumvent the specimen and not allowed to enter inside. The pattern of the external field depends on the shape of the specimen and is characterized by the *demagnetizing factor* η of the geometry. For superconductors of slab geometry in parallel field (thin rectangle with infinite length) the demagnetizing factor is zero. For a cylinder in transversal field, η is 1/2, see Fig. 2-2; for a sphere it is 1/3, and for a strip (thin rectangle in field perpendicular to its long side) the demagnetizing factor is nearly 1 (exactly 1 in case of infinite width of the strip).

The state of perfect diamagnetism is retained only if the temperature is below T_c and the magnetic field below H_c.

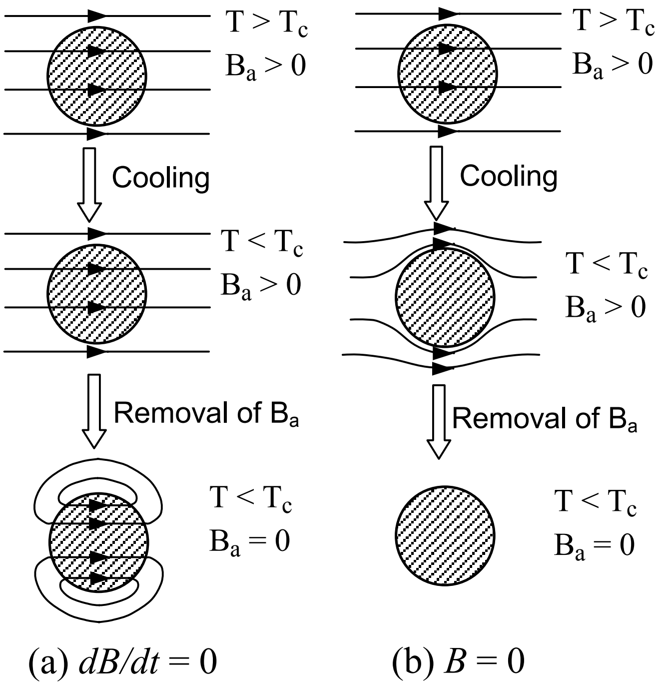

Figure 2-1 (a) in a perfect conductor the flux applied before the cooling is trapped so that *dB/dt* = 0 inside; (b) in a metal superconductor the flux is always expelled so that *B* = 0 inside (Meissner effect).

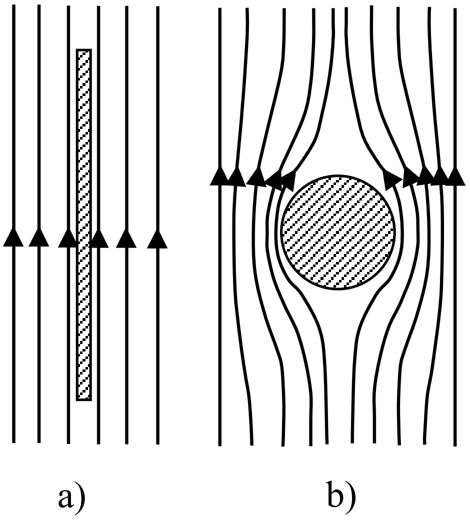

Figure 2-2 Pattern of the exterior field when demagnetizing factor is nearly zero for a slab of finite length (a) and when it is 1/2 for a cylinder in transverse field (b).

2.2.2 Type-II superconductors

A significant contribution to the theory of superconductivity was made by Abrikosov in 1957 when he published a paper describing some new phenomena related to the Ginzburg-Landau theory, quite different from the behaviour of the earlier type-I superconductors [Abr57]. He pointed out the existence of some new materials, which exhibited a continuous increase in flux penetration starting at a first critical field H_{c1} with reaching $\mathbf{B} = \mu_0 \mathbf{H}$ at a second critical field H_{c2}, instead of showing a discontinuous disappearance of superconductivity at the thermo-dynamical field H_c. Later it was discovered that the behaviour of these materials is not simply due to impurities in their chemical composition; they possessed entirely new properties and were termed thereafter *type-II superconductors*.

While the class of type-I superconductors is composed entirely of metallic chemical elements, type-II superconductors may be metal alloys or even some pure metals, such as Niobium (Nb) and Vanadium (V), and also different oxide compounds (see Section 2.2.4). All metals and metal alloys have their T_c below 30K and are referred to as *low temperature superconductors* (LTS), while the oxide superconductors have their T_c above 30K and are referred to as *high temperature superconductors* (HTS).

Magnetization of type-II superconductors

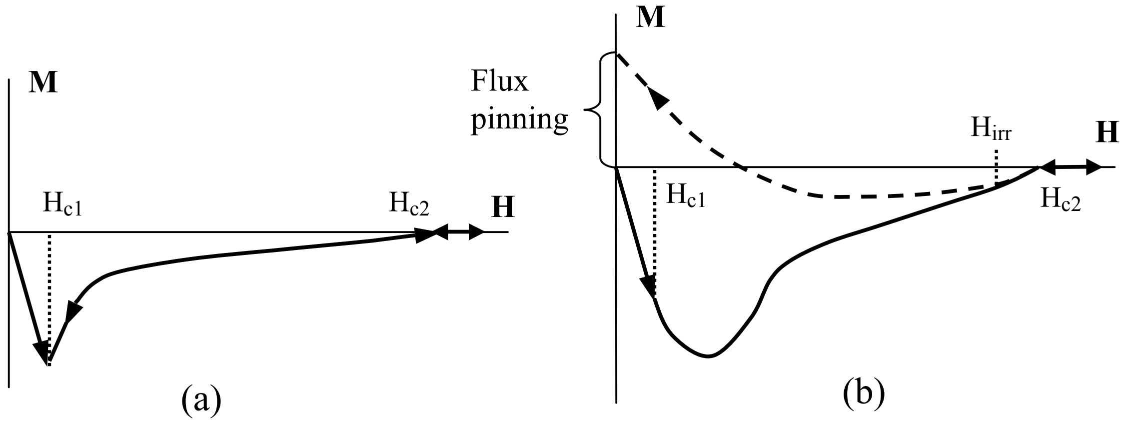

Figure 2-3 (a) Magnetization of ideal type-II superconductor. The state of perfect diamagnetism exists below H_{c1} and above H_{c2} the material is in normal state. (b) Magnetization of real type-II superconductor The curve is reversible only above H_{irr}. The magnetic flux at H = 0 is 'trapped' or 'pinned' in the material. *after [She94].*

The sketch in Fig. 2-3a shows that in an idealized type-II superconductor **B**, **H** and **M** are uniquely related to one another and the magnetization curve is reversible. The state of perfect diamagnetism, $\mathbf{B} = \mu_0 (\mathbf{M}+\mathbf{H}) = 0$, exists only below H_{c1}, afterwards the flux starts to penetrate, and above H_{c2} there is no magnetization at all and the material returns to its normal state. As the magnetic field is decreased below H_{c2}, the reverse magnetization path will exactly retrace the forward one. However, no real material exhibits the exact retracing of the idealized curve. Structural imperfections or chemical impurities act as barriers for flux movement into the crystal; this is referred to as *flux pinning*. As a matter of fact, it is the practical goal of material engineers to introduce as many pinning sites as possible in order to allow high currents to flow under high magnetic fields. A real type-II superconductor has a more complicated magnetization path, which is depicted in Fig 2-3b. Noticeable difference is the absence of sudden change in magnetization **M** as **H** passes through H_{c1}. Only the slight deviation from linearity conveys that the diamagnetic state is no longer perfect, and that flux has started to penetrate into the material. The increase of **H** leads to more extensive flux penetration, and at H_{c2} the state of full penetration is achieved, $\mathbf{B} = \mu_0 \mathbf{H}$ and the material becomes normal. In the superconducting state, some of the flux is trapped within the material. After reaching H_{c2}, when **H** is reduced, flux lines are free to move at first, and so the **H-M** curve retraces its path until a point H_{irr}, the *irreversibility field*, when flux pinning becomes stronger, **B** declines slower than **H**, and **M** deviates from the forward curve. As **H** is further decreased, **B** remains high and since $\mathbf{B} = \mu_0 (\mathbf{H}+\mathbf{M})$, **M** rises to a positive value. At the end of the reverse cycle, when $\mathbf{H} = 0$, the value of **B** remains finite due to the flux trapped by the superconductor [She94].

The mixed state

Apart from the normal and superconducting states, Type-II superconductors exhibit a new state, which is called the *mixed state*, which allows the existence of normal regions in the material. In the mixed state, Meissner effect is no longer present and magnetic flux may partially penetrate the superconductor; the superconductivity, however, is not lost. The existence of the mixed state can be explained by the fact that the material always tends to assume the state with lowest total free energy and when the surface energy between normal and superconducting regions is negative, the appearance of normal regions will reduce the total free energy and lead to a more favorable energy state [Inn78]. It turns out that the configuration in which the ratio of surface to volume of normal material is a maximum is cylindrical normal regions, parallel to the external field and threading the superconductor, as shown in Fig. 2-4. These cylindrical normal cores are arranged in a regular pattern, forming a lattice, sometimes called *fluxon lattice*. Within each core the magnetic flux has the same direction as that of the applied field and is shielded from the neighboring superconducting regions by a vortex of induced current. These supercurrents together with the surface current, circulating at the perimeter of the specimen, maintain the bulk diamagnetism, see Fig. 2-4.

The mixed state is an intrinsic feature of type II superconductors and exists for magnetic fields such that $H_{c1} < H_a < H_{c2}$. It was predicted by Abrikosov that the magnetic flux would penetrate in a regular array of flux tubes, named fluxons, each one having the quantum of flux $\Phi_0 = h/2e = 2.6678\times10^{-15}$ Wb (h = Planck's constant and e = electron charge).

Several years after Abrikosov, the magnetization of type-II superconductors was experimentally described by Bean [Bea62], [Bea64]. He presented a macroscopic model of the current and magnetic flux distribution, and showed that the flux penetration in such materials is not uniform – there is a flux density gradient and a flux-free region in the center of the specimen. Bean's model has been named the *critical state model*. It is widely used in the modelling of type-II superconductors and is presented in more details in Section 4.2.1.

Flux pinning, creep and flow

In a perfectly pure material, the flux lines would be able to easily move and adjust their density according to the applied field. However, due to impurities and inhomogeneities in type-II superconductors, the fluxons are pinned and an energy barrier is created that has to be overcome in order to move them. Flux pinning can be imagined as if the fluxons are situated in pinning wells of depth F_0 (pinning strength) and placed at a given distance, which the fluxons need to jump to move from one well to another, see Fig. 2-5.

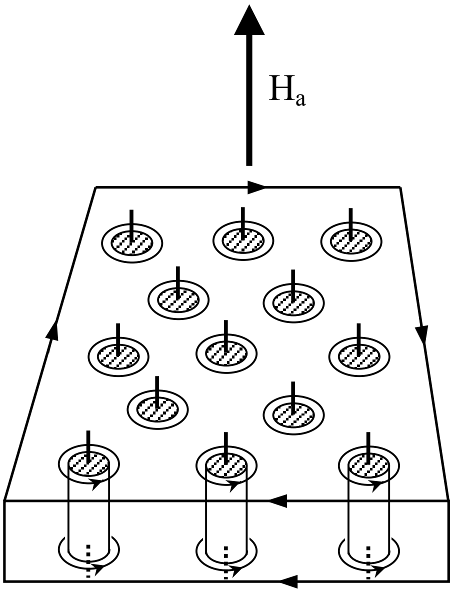

Figure 2-4 The mixed state, showing normal cores and encircling supercurrent vortices. The vertical lines represent the flux threading the cores. The surface current maintains the bulk diamagnetism. *after [Inn78]*

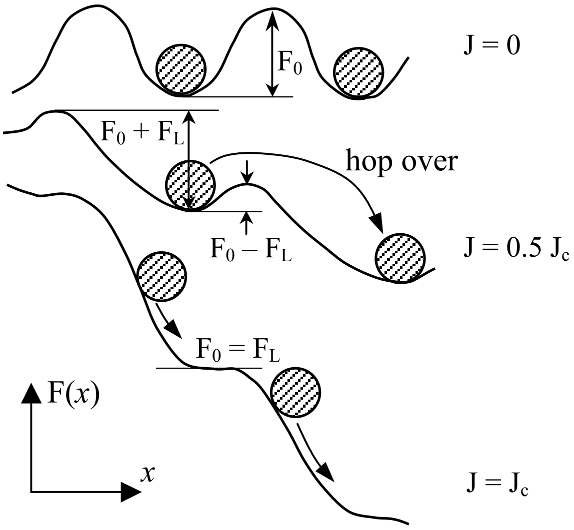

Figure 2-5 Mechanism of flux-flow. The presence of current in a magnetic field generates a Lorentz force, which tilts the staircase, allowing flux lines to hop out of their pinning wells more easily. *after [She94]*

When electric current with density J is carried by a type-II superconductor, it passes the flux lines and creates a Lorenz force $\mathbf{F}_L = \mathbf{J} \times \mathbf{\Phi_0}$ upon each vortex. The fluxons will remain in place as long as their pinning strength F_0 is larger than the Lorenz force F_L, even if the depth of the pinning wells is gets smaller with the increase of J. At a certain value J_c, the Lorentz force will become greater than the pinning strength, and all fluxons will start to move, see Fig. 2-5. This movement is referred to as *flux-flow*. J_c is called the *critical current density* and is very important characteristic, since it gives the maximum current the superconductor can carry, and above which the material becomes normal again. In HTS, certain flux motion may be activated by thermal fluctuation of the fluxon lattice; this motion is slower and more sporadic and has been named *flux-creep*.

Lower and upper critical fields

For type-II superconductors, Abrikosov defined the relation of the lower (H_{c1}) and upper (H_{c2}) critical field to the thermodynamical critical field H_c as follows:

$$\begin{aligned} H_{c1} &\simeq H_c / \kappa \\ H_{c2} &\simeq \sqrt{2}\kappa H_c \end{aligned} \tag{2.3}$$

where κ is the Ginzburg-Landau constant of the material. It is equal to λ/ξ, where λ is penetration depth, at which the magnetic flux enters a superconducting specimen and ξ is the coherence length, which corresponds to the distance between the super electrons according to the Ginzburg-Landau theory [Gin50].

The value of κ for type-II superconductors can be experimentally obtained from the magnetization curves. For LTS materials it is usually between 4 and 34, so that H_{c2} is much larger than H_{c1} [Inn78]. For example, $\kappa = 34$ in Nb_3Sn and $H_{c2} \sim 1600 \times H_{c1}$.

The flux penetration (B-H) curves in type-I and type-II superconductors are depicted in Fig. 2-6. Since the value of H_{c1} is very low, the approximation $B = \mu_0 H$ is often used for modelling purposes of type-II superconductors.

The values of H_{c2} and B_{c2} for several type-II superconductors are given in Table 2-2. A great advantage of type-II superconductors is the large magnetic fields, which they can support without losing their superconducting properties, compared to type-I superconductors, for which the values of H_c are very low, see also Table 2-1.

TABLE 2-2. T_c, H_{c2} and B_{c2} in type-II metal alloy superconductors

Compound	T_c *(K)*	H_{c2} *(A/m)*	B_{c2} *(Tesla)*
Nb-Ti alloy	10.2	$\sim 0.9\times10^7$	~ 12
Nb_3Sn	18.3	$\sim 1.6\times10^7$	~ 22
Nb_3Ge	23.0	$\sim 2.2\times10^7$	~ 30
Nb_3Al	18.9	$\sim 2.3\times10^7$	~ 32
$PbMo_6S_8$	14.0	$\sim 3.3\times10^7$	~ 45

The superconducting transition temperatures and the critical magnetic fields at 4.2K.
Sources [Inn78] and [Lar00].

The H-T phase transition of high-T_c superconductors is presented in Fig. 2-7. Unlike low-T_c superconductors, H_{c2} is not the real phase boundary, since thermal fluctuations make the dissipation line well below H_{c2} at the irreversibility field H_{irr} [Lar00].

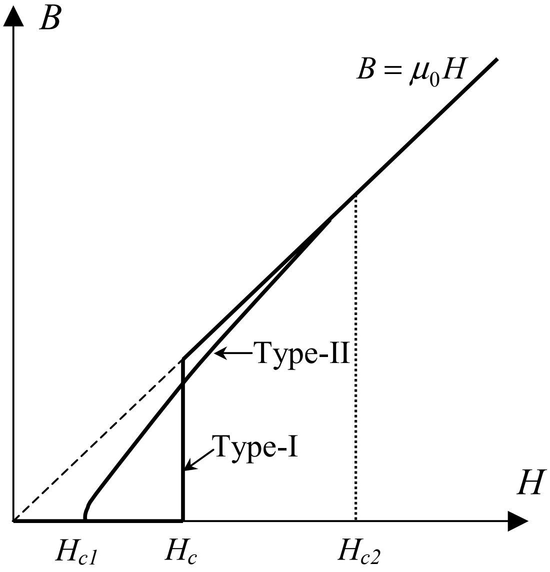

Figure 2-6 Comparison of flux penetration behaviour of type-I and type-II superconductors with the same thermo-dynamic critical field H_c. *after [Tin75]*

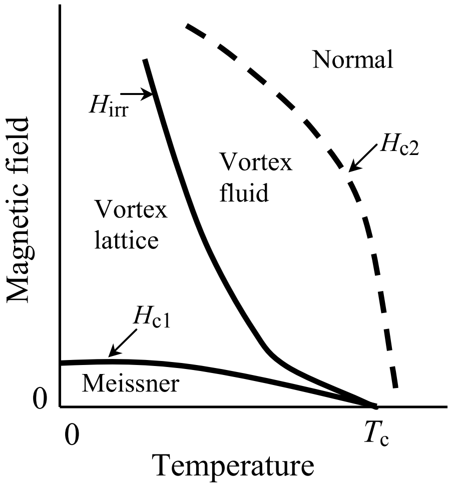

Figure 2-7 Phase diagram of high-T_c superconductors. *after [Lar00]*

2.2.3 Critical currents in high-T_c superconductors

The Anderson-Kim model of flux creep relates the measured critical current density J_c in type-II superconductors to the pinning strength F_0 and voltage criterion E_c in the following manner [And62], [Kim63]:

$$J_c(T) = J_{c(0)}[1-(k_B T / F_0)\ln(Bd\Omega / E_c)] \tag{2.4}$$

where $J_{c(0)}$ *is* J_c at zero temperature, Ω is the frequency of a flux-hopping event, d is the hopping distance, B is the magnetic induction, and E_c is the voltage criterion (usually the smallest discernible electric field, V/m). Since parameters d and Ω depend on the temperature and the magnitude of the applied magnetic field, Eq. (2.4) must be solved numerically.

It is clear that for any volt-per-meter criterion E_c, there will be either a given magnetic field or a temperature for which a certain value of J gives a discernible voltage drop per unit length of the superconducting sample [She94]. Therefore, the concept of critical current J_c in type-II superconductors is no longer well defined, and there is a significant discrepancy of the J_c values obtained with the different voltage criteria. If one uses a high sensitivity SQUID magnetometer to define the current at which electric field appears, a low J_c will result. A less sensitive E-criterion, typical of transport current measurements, will give correspondingly a higher value of J_c; the 1 μV/cm is the most commonly used voltage criterion.

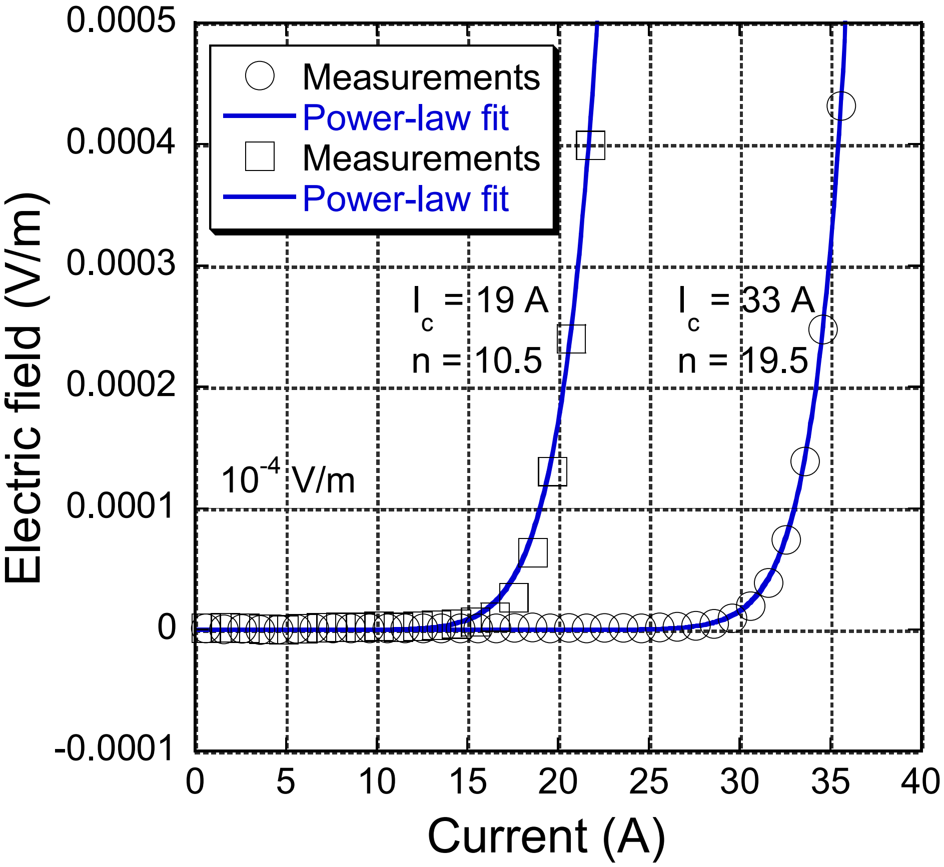

Figure 2-8 V-I characteristics of two Bi-2223 tapes, obtained in DC transport current measurements at 77 K. Given are also the power-law parameters from Eq. (2.5).

An example of the measured voltage-current characteristics of two HTS tapes, obtained with DC transport current and the 1 μV/cm criterion, is shown in Fig. 2-8. The HTS material is Bi-2223, see Section 2.2.4. The effect of flux movement on the DC characteristics of silver sheathed Bi-2223 tapes has been well studied and seen in the *E-J* plots for this material [Hug97].

For the purpose of routine characterization of LTS and HTS materials, power-law voltage-current dependence seems to be best suited because of both its simplicity and excellent fit to the experimental data. In this power-law model the electric field E is proportional to the current I of power n in the following way:

$$E = E_c \left(\frac{I}{I_c} \right)^n \tag{2.5}$$

where E_c is the voltage criterion, I_c is the corresponding critical current, and the n-value defines the steepness of the transition curve. Figure 2-8 shows the different values of I_c and the power index n fitted from Eq. (2.5) for the two measured samples.

Typical values of n for Bi-2223 tapes in self-field at 77 K are between 10 and 30, while for LTS the transition to normal state is usually sharper and n-values in Nb-Ti may reach 50 [Iwa95].

The *critical current density* J_c is then calculated from the measured value of I_c:

$$J_c = \frac{I_c}{S} \tag{2.6}$$

where S is the cross-section of the superconducting core in mono or multifilamentary conductors. The values of not only J_c but also n vary if E_c different from 1 μV/cm is used.

2.2.4 Advanced HTS materials

High-T_c superconductors are chemical compounds, consisting of repeating patterns of atoms of different elements, called unit cells. The unit cell of one HTS superconductor – $Bi_2Sr_2Ca_2Cu_3O_x$ – is depicted in Fig. 2-9. Trillions of unit cells form a very small crystal, known as a *grain*. Millions of grains are needed to make a macroscopic sample. HTS are brittle ceramic materials, most of which are oxides – their resistivity at room temperature is about 100 times higher than that of copper [Tix95].

TABLE 2-3. Critical parameters of HTS superconductors for power applications

	YBCO	*Bi-2212*	*Bi-2223*
T_c (K)	93	87	110
B_{irr} @ 4.2 K (T)	> 30	>30	> 30
B_{irr} @ 77 K (T)	> 5	0.005	0.5
J_c @ 4.2 K (A/mm^2)	> 100,000	5,000	3,000
J_c @ 77 K (A/mm^2)	> 10,000	100	500

The J_c values are obtained for short samples in self-field. *Source [Rab01a].*

The first high-T_c superconductor, discovered by Bednorz and Müller, was lanthanum copper oxide $(La,Ba)_2CuO_4$, which has a T_c just above 30 K. The HTS material with highest T_c = 134 K, discovered so far, is $HgBa_2Ca_2Cu_3O_8$. The first superconductor with $T_c > 77$ K is yttrium barium copper oxide $YBa_2Cu_3O_x$, known as YBCO or Y-123, which together with the bismuth oxides $Bi_2Sr_2CaCu_2O_x$ and $Bi_2Sr_2Ca_2Cu_3O_x$, mentioned as Bi-2212 and Bi-2223, are at present the most advanced HTS materials. The latter two compounds are also referred to as BSCCO, which stands for bismuth strontium calcium copper oxide.

Table 2-3 presents the critical parameters of YBCO, Bi-2212 and Bi-2223 – the most widely used HTS.

BSCCO

BSCCO conductors represent the basis for all present large-scale applications of HTS. They are called conductors of 1st generation. BSCCO has a well-established manufacturing technology, and commercial conductors are available in long lengths (up to 1 km).

Transport current applications are among the main targets for BSCCO conductors. They are produced by the Oxide-Powder-In-Tube (OPIT) process, a simple sketch of which is shown in Fig. 2-10. The current in BSCCO conductors has to pass through the grain boundaries, which obstruct current except when at low angle. Therefore, strong texture is necessary and the better the grains are aligned, the higher the critical current density of the conductor is. In order to obtain texture and alignment of the grains in the oxide powder, which are initially randomly oriented, rolling is required in the manufacturing process and the superconductors are made in the form of thin tapes; usually having width of 2-4 mm and thickness 0.2-0.4 mm. HTS compounds are very brittle materials. To improve substantially the mechanical characteristics of the tapes, the superconducting core is placed in a tube, made of Ag, which is selected for its good mechanical and oxygen diffusion properties. The tapes can have mono or multifilamentary BSCCO core.

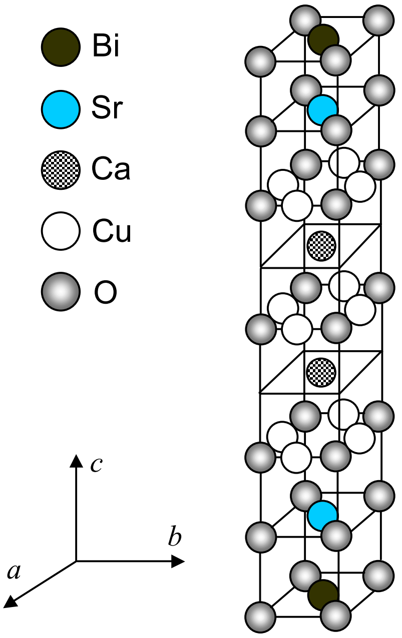

Figure 2-9 Unit cell of $Bi_2Sr_2Ca_2Cu_3O_x$.

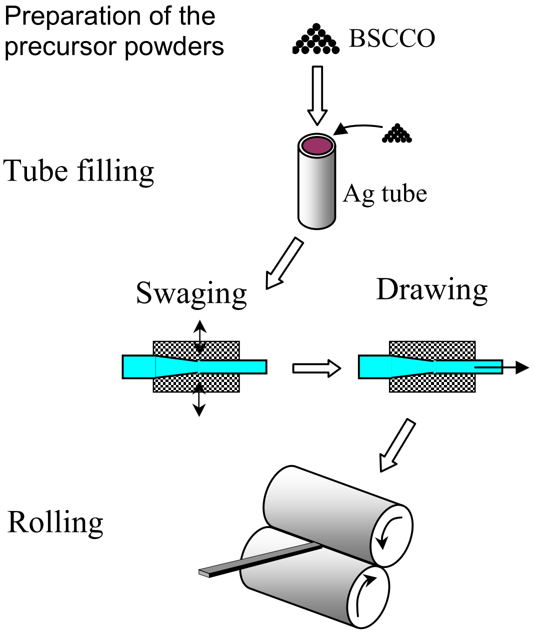

Figure 2-10 Schematic presentation of the OPIT technique. Intermediate and final heat treatment is not shown.

Because of the layered structure of the unit cells, BSCCO has intrinsic anisotropy along the *c*- and *a*,*b*- planes of its crystals, and as a result of the rolling during the manufacturing process the produced tapes have anisotropic properties. A very important characteristic of BSCCO materials is the strong anisotropy of the critical current density – for applied magnetic field perpendicular to the wide side of the tape ($B_{//c}$), J_c decreases quickly, while for applied parallel magnetic field ($B_{//a,b}$), the decrease of J_c is much more moderate. The anisotropy of J_c in Bi-2223 tapes for modelling purposes is dealt with in Chapter 5.

BSCCO has a double Bi-O layer (see Fig. 2-9), which is almost insulating, making the compounds a superconductor-insulator-superconductor stack, which is very convenient for electronics applications [Lar00].

The irreversible field at 4.2 K is very large both for Bi-2212 and Bi-2223. The critical current density of Bi-2223, however, decreases faster in applied field than for Bi-2212. At 4.2K Bi-2212 can carry up to 1,000 A/mm^2 in fields of 26 T, while the corresponding current density of Bi-2223 is lower. That is why Bi-2212 is preferred for HTS magnet applications at 4.2 K. At temperatures above 20 K, however, the performance of Bi-2212 is strongly degraded due to important flux creep, and at 77 K its irreversible field is only 0.005 T. On the other hand, Bi-2223 at 77 K has its irreversible field of 0.5 T, which is not of interest for magnet design but is good enough for transport current applications. Therefore, Bi-2223 is at present the most widely used material for wires and cables, operated at 77 K.

YBCO

One of the main structural differences between BSCCO and YBCO is that the charge reservoir layer of the latter is metallic and not insulating like the one of the former. Therefore, YBCO is less anisotropic.

Another important advantage of YBCO is the very large current densities, which have been obtained in YBCO conductors – above 10,000 A/mm^2 at 77 K. These conductors, however, are produced in laboratory samples only in short lengths of 1 m at most.

The difficulty in obtaining long YBCO conductor is intrinsic to its manufacturing technology, which is completely different from that of BSCCO. YBCO is a coated conductor, which consists of a thin film of a few μm of HTS material deposited on a flexible substrate. One variation of this process is the Ion Beam Assisted Deposition, called IBAD. In this process, films of HTS material are deposited on an aligned buffer layer (the IBAD layer), which is placed on a flexible substrate. This process improves the alignment of the HTS films and consequently their electrical performance. There are other two competing processes – the Rolling Assisted Textured Substrate (RABiTS) and the Inclined Substrate Deposition (ISD).

YBCO is considered the most suitable material for conductors of 2nd generation. However, obtaining long lengths of YBCO conductors for the moment is not achievable and lots of research efforts are dedicated to this problem.

2.3 AC loss mechanisms in high-T_c superconductors

Superconductors have zero resistance and no power is dissipated only when DC current below the critical one is passed through. As it was briefly explained in Section 2.2.1, any applied AC current or changing magnetic field would inevitably lead to losses as heat is being dissipated in the superconductor. For example, at liquid helium temperature (4.2 K), 1 single watt of dissipated heat would require, following Carnot-cycle theory, at least 70 watts of refrigerating power for its removal. In practice, this amount is considerably larger and may reach hundreds of watts since refrigerators never get very close to Carnot's efficiency [Car83]. At liquid nitrogen temperature (77 K) the necessary refrigerating power is lower by more than a factor of 20 than at 4.2 K, and this is the main reason that in most applications HTS materials are intended to be operated at 77 K or at intermediate temperatures (20-60 K).

2.3.1 AC losses in the superconductor

Hysteresis loss

The origin of the main type of AC loss in a type II superconductor is a *hysteresis*. As an external magnetic field is applied, flux starts partially penetrating into the bulk of the superconductor, and currents are induced at the surface, much like the skin effect in a copper conductor. There are, however, two differences in this analogy. Firstly, due to the initial state of infinite conductivity, the superconductor exhibits a skin-effect even at zero frequency, and secondly, the induced current density has a critical value J_c, which is a decreasing function of the magnetic field at a given temperature, in contrast to the normal skin effect, where the induced current density is proportional to the field amplitude for a fixed frequency [Car83]. Figure 2-11 shows the depth of flux penetration into the superconductor (a-b) up to a point where it is completely penetrated (c). Now, if the field starts to reverse, the flux will not recede in the same way since it is pinned by defects in the material; see also Fig. 2-3. As a consequence, when the applied field is decreased (d), and the surface electric field changes its direction, a new region with reversed current density is formed at the surface, and starts to propagate inwards as the applied field is further reduced. It is namely this irreversibility and the flux pinning that cause the hysteresis loss.

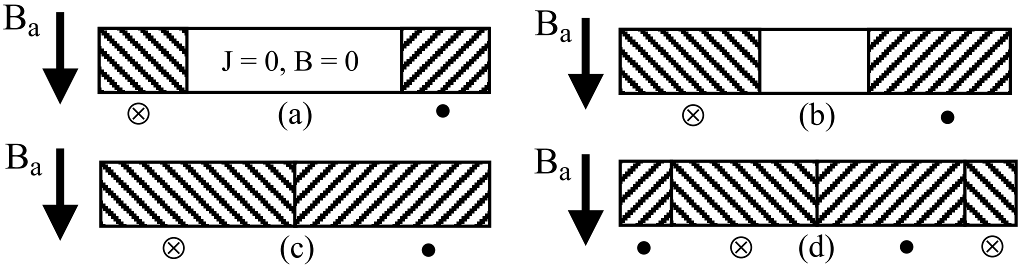

Figure 2-11 Zones of magnetic flux and current penetration into the cross-section of type-II superconductor. B$_a$ is the applied external field. Shown is the penetration starting from the edges of the superconductor, while the central area is current and flux-free. The opposite directions of the induced currents are denoted by ⊗ and •.

Stationary, non-moving flux lines are not harmful to superconductivity. In principle, the energy dissipation occurs by means of two different mechanisms: electric resistance or changing magnetic flux. In superconducting materials, conventional electric resistance is absent, but Faraday's law $\nabla\times\boldsymbol{E} = -\partial\boldsymbol{B}/\partial t$ continues to hold. In type-II superconductors, the existence of hysteresis causes energy dissipation and a voltage is needed to sustain the current. For DC applications, $\partial\boldsymbol{B}/\partial t = 0$, flux is pinned, and consequently no loss appears. For AC applications, the hysteresis loop in the **M**-**H** plane determines the energy loss in the superconductor. A detailed description of hysteresis in HTS is given in [Sjö01].

The hysteresis loss in self-field (transport current application with no external field) for superconductors with strip and elliptical geometry has been theoretically calculated by Norris [Nor70]. Norris's equations are given in Section 3.3.1.

The hysteresis loss in applied external magnetic field is most often referred to as *magnetization loss*. Analytical solutions for the magnetization loss in type-II superconductors have been found only for simple geometries, such as cylindrical wire [Wil83], thin rectangular tape in parallel field (slab) or in perpendicular field (strip) [Cam82], [Mül95]. The magnetization loss in Bi-2223 tapes is treated in more details in Chapter 4 and Chapter 5.

Flux-creep and flux-flow loss

The motion of flux lines in the mixed state of type-II superconductors gives rise to energy dissipation in the material, and therefore the term *flux-flow resistivity* has been coined. The origin of energy dissipation is the Lorenz force, which applies to a fluxon with single flux quantum Φ_0 when a current is passed: $\mathbf{F}_L = \mathbf{J} \times \mathbf{\Phi_0}$. If the flux line is not well pinned, it will then move in a direction transverse to the current under the effect of $\mathbf{F}_L$. The movement of the flux line with velocity $\mathbf{v}_\varphi$ will induce an electric field $\mathbf{E} = \mathbf{B} \times \mathbf{v}_\varphi$, which is parallel to $\mathbf{J}$ and acts like a resistive voltage causing power dissipation.

If there is no flux pinning and the vortex lines are free to move, the viscous drag force on a flux line is given by $(-\gamma \mathbf{v}_\varphi)$, where γ is a drag coefficient. For the steady state this force is balanced by the Lorenz force and so their magnitudes are equal: $J\Phi_0 = \gamma v_\varphi$. Combining this equality with the equation for $\mathbf{E}$, one obtains the flux-flow resistivity [She94]:

$$\rho_f = \frac{E}{J} = B\frac{\Phi_0}{\gamma} \tag{2.7}$$

By definition, the electric resistivity is the slope of electrical field E vs. current density J curve. When the E-J relationship becomes nonlinear, the resistivity is no longer constant.

The E-J plot for a type-II superconductor at absolute zero is shown in Fig. 2-12. At that temperature, the variation of E with J is simple. The solid lines show that below $J_c(B,T)$ $E = 0$, because the flux vortices are fully pinned and immobile (perfect superconductivity). Above J_c, flux flow begins, and E increases proportionally to $|J - J_c|$; the constant slope is the flux-flow resistivity ρ_f defined above. With the increase of the applied magnetic field, J_c diminishes and the slope of the E-J plot in the flux-flow regime gets steeper. Ultimately, in a very high field, the material becomes normal and J_c reaches the zero value, which means the slope is simply the normal resistivity ρ_n.

At temperatures, higher than 4.2 K, the effect of thermally activated movement of flux vortices, known as flux-creep, becomes more pronounced and at 77 K it definitely has to be taken into account [She94]. Figure 2-13 shows the E-J plot at 77 K. By defining a certain threshold value of the current density J_{th} it is possible to identify the regions corresponding to thermally activated resistance, flux creep, and flux flow in the E-J plot. The $J_{c(0)}$ is defined as the J_c value that would have been obtained in the absence of flux creep. The prominent excursion away from the solid lines justifies the term *giant flux creep* used to describe the behaviour of HTS. In either flux creep or flux flow, a flux line or a whole flux bundle is imagined to hop over the pinning barrier from one pinning well to another. Fortunately, the anisotropy, chemical and manufacturing impurities of real HTS create many pinning sites in the material, and therefore flux motion at 77 K is much more restricted than the above conventional model and the excursion from the E-J curve at 0 K is less emphasized. However, due to the thermally activated flux-flow at 77 K, and also because of the grain boundaries, the effective resistivity of a HTS is always finite (never reaches zero), so the state of perfect conductivity is never achieved.

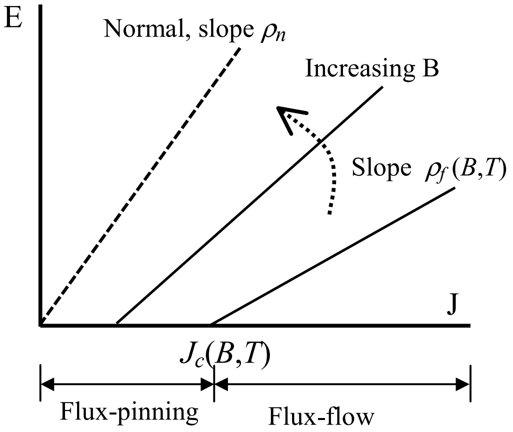

Figure 2-12 Plot of electric field as a function of the current at absolute zero. Below J_c all flux vortices are pinned; above J_c flux flows with energy dissipated as $E = \rho_f(J–J_c)$, where $\rho_f = \rho_n[H/H_{c2}(T)]$. *after [SHE94]*

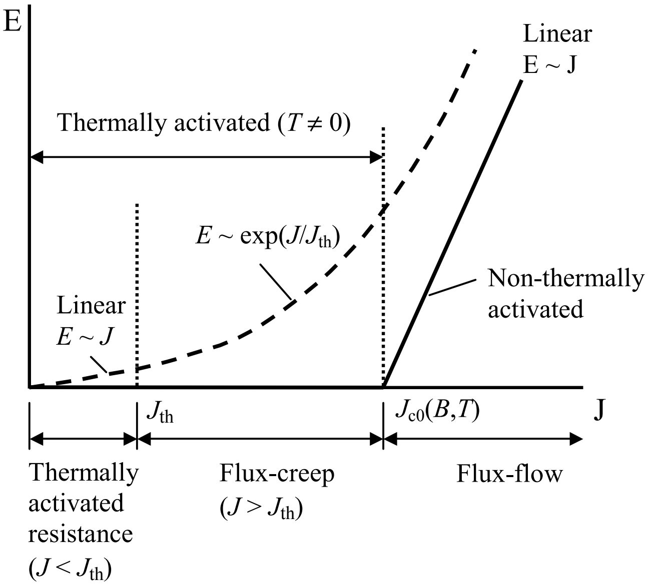

Figure 2-13 E-J plot at 77 K, showing the effect of thermally activated flux motion. The flux creep causes energy dissipation (equivalent to resistance) at currents well below J_c. *after [SHE94]*

2.3.2 AC losses in the metal matrix

Eddy current loss

For reasons of mechanical stability and AC loss reduction, HTS are manufactured from fine filaments embedded in normal metal matrix, made of Ag or Ag-alloys.

Eddy current loss is the loss occurring as a result of induced currents in the normal metal matrix by the applied external magnetic field or by the self-field of the applied transport current. This loss deserves special attention for HTS applications, since the resistivity of the normal matrix is orders of magnitude higher than the resistivity of the superconducting core, and the undesired flow of eddy currents leads to heat (Ohmic) dissipation due the friction and motion of electrons in the metal lattice of the sheath.

When a sinusoidal AC current is applied to a metal wire, the resulting changing self-field has its magnetic flux lines in the form of concentric ovals around the conductor (e.g. circles around a cylindrical wire) in a plane perpendicular to the direction of the current.

Figure 2-14 shows a simplified sketch of a Bi-2223 monocore cylindrical wire, as well as the directions of the applied transport current I_t and the resulting self-field $\boldsymbol{B}$. Faraday's law states that a voltage is created or induced in a region of space when there is a changing magnetic field:

$$V_e = -\frac{d\Phi}{dt} \tag{2.8}$$

where $\Phi = \Phi_m \cos \omega t$ is the magnetic flux around the wire.

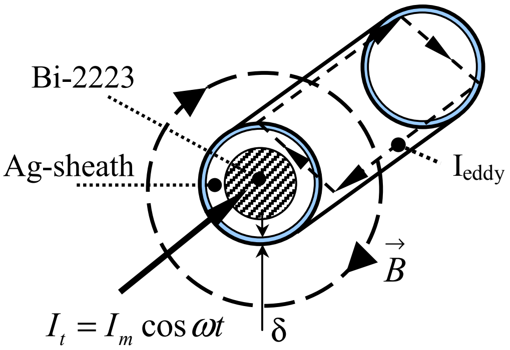

Figure 2-14 Generation of eddy currents in a cylindrical superconductor by the self-field of applied transport current I_t. Shown is the penetration depth δ, at which they circulate.

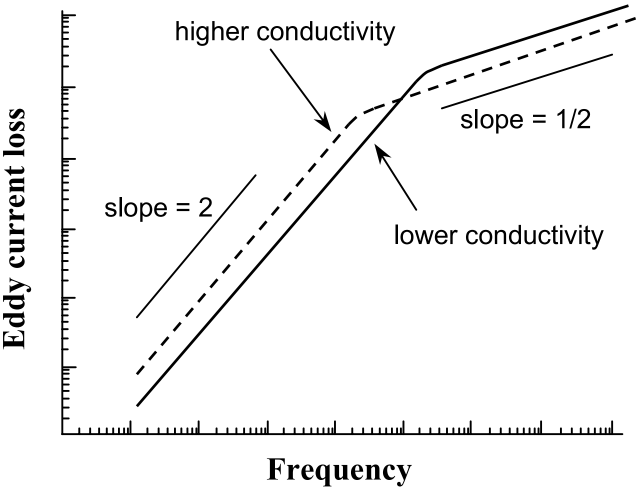

Figure 2-15 The frequency dependence of the eddy current losses for two sheets of thickness 2*b* but different conductivity. The transition between the ω^2 and $\omega^{1/2}$ dependence occurs at the frequency where $b = \delta$. *after [Hug97]*

The induced voltage also varies sinusoidally with time; following Ohm's law for a driving voltage (V_e) and a finite value of the wire's Ag-sheath impedance (Z_{Ag}), a current will flow, $I_e = V_e / Z_{Ag}$. These induced currents are known as *eddy currents* because of their circulatory paths.

Eddy currents are closed loops circulating in planes perpendicular to the magnetic flux. When there is an applied AC transport current or field, they travel parallel to the tape surface and also transversely crossing the Ag-matrix, as shown in Fig. 2-14. The eddy current flow, however, is limited to the area of the inducing magnetic field. The depth of their penetration decreases with the transport-current frequency ω and is a function of the electrical conductivity σ and the relative magnetic permeability of the material μ_r. This dependence has been termed '*skin effect'*. The penetration, or skin depth, is calculated as:

$$\delta = \sqrt{\frac{2}{\omega\sigma\mu_0\mu_r}} \tag{2.9}$$

The frequency dependence of eddy current loss is plotted in Fig. 2-15 for two metal sheets of different conductivity. There are two distinct regions with different frequency dependence: at low frequency the losses are proportional to ω^2, while at high frequencies, proportional to $\omega^{1/2}$. The transition between the two regions takes place at a 'critical' frequency ω_c where the sheath half-thickness b equals δ. For a sheath thickness of 100μm, conductivity of Ag equal to 3.3×10^8 Sm^{-1}, and taking $\mu_r = 1$, this transition should occur at:

$$f_c = \left[\frac{2}{2\pi b^2 \mu_0 \sigma}\right] \approx 75 \text{ kHz} \tag{2.10}$$

This critical frequency f_c is far above the range of interest for power applications of Bi-2223 tapes and therefore the square frequency dependence of the eddy current loss is valid.

The eddy current self-field loss in Bi-2223/Ag tapes is studied in detail in Chapter 3.

Coupling current loss

The calculation of AC losses in external perpendicular magnetic field, based on the critical state model, shows that the losses are proportional to the aspect ratio (width/thickness) of the superconductor [Cam82]. This has been also confirmed by experimental results [Kwa01]. For this reason HTS tapes made for AC applications are nowadays manufactured of a number of fine filaments, which have an aspect ratio lower that of the whole tape. The filaments are embedded in a silver (silver alloy) matrix, which is chosen for its good mechanical properties and permeability to O_2 during the annealing process. The presence of applied magnetic field induces layers of screening currents in the superconductor, trying to shield the interior from the external field, see also Fig. 2-11. On the one hand, the good electrical conductivity of the metal matrix is useful in promoting dynamic stability against flux jumping. On the other hand, it has the extremely undesirable effect of coupling the separate filaments in changing magnetic fields [Wil83]. The interaction between two neighbouring filaments is sketched in Fig. 2-16. In low external field with amplitude B_a (a), the filaments are not coupled. Each filament carries its own ‘go and return’ screening currents. None of these screening currents is crossing the silver matrix, and the field between the filaments is the same as the external one. This is not the case in (b), where B_a is strong enough so that the coupling between the filaments is complete and the screening currents are crossing the Ag matrix to form their return paths. It follows from the Lenz’s law that the coupling pattern will always take priority if the induced voltage at the extremities of the tape is sufficient to overcome the resistive drop across the matrix. This induced voltage is proportional to the length l – the longer the conductor it is, the faster complete coupling will appear. The induced voltage depends also on the rate of field change and on the filament arrangement. The resistance across the matrix will depend on the metal resistivity and the transverse distance over which the coupling currents must flow.

Coupling between the filaments is highly undesirable for two reasons. Firstly, the magnetization losses in the superconductor are proportional to the field penetration profile (the shaded triangular area in Fig. 2-16.). This area in multifilamentary tapes will be much larger in the coupled than in the uncoupled case for fields above the full penetration (around 10-20 mT for Bi-2223 tapes). The effective size of the superconductor as regards the AC losses is no longer the filament but rather the bundle of filaments, so that the multifilamentary tape now behaves as one single body. Secondly, the flow of coupling currents across the metal matrix results in Ohmic (heat) dissipation, referred to as *coupling current loss*. It is due to the finite value of the matrix resistivity ρ_m, which for the silver is $2.5\text{-}3\times10^{-9}$ Ωm at 77 K and because of the high density of the coupling currents, this loss has very important contribution to the total AC loss in multifilamentary HTS.

Fortunately it is possible to reduce considerably the coupling by twisting the filaments, see Fig. 2-17. A changing external field will now induce an electric field between the filaments, which reverses every half twist pitch. If the twist pitch length L_p is small enough there will be insufficient distance for coupling currents to flow between reversals and the filaments will remain uncoupled. The coupling current loss is proportional to L_p^2 / ρ_m.

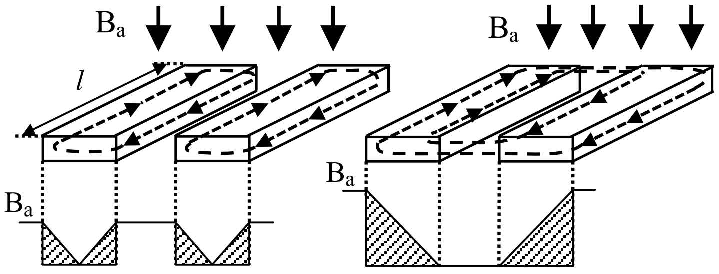

(a) (b)

Figure 2-16 Filaments free of coupling (a) and completely coupled (b).

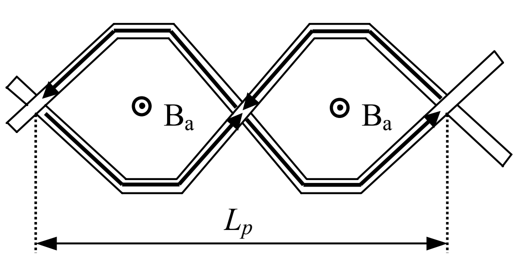

Figure 2-17 Schematic drawing of induced currents in two twisted filaments (top view). *after [Rab01a*]

Although twisting has full effect in uniform fields and partial effect in non-uniform fields, it is rather ineffective with respect to the self-field of the transport current. The magnetic self-field lines take the form of concentric ovals around the superconducting wire see Fig. 2-14. The most important effect of the self-field is to make the transport current flow as near the surface as possible – quite like the classical skin effect for AC current in copper conductors. A sheath of current flows starting from the outside filaments and penetrates only as far as needed to carry the transport current. This could be thought of as a screening current distribution, which shields the internal filaments from the self-field. Twisting makes almost no difference because it does not change the self-field flux linked between the inner and outer filaments. For this reason the self-field effects in twisted or untwisted multifilamentary tapes and monofilamentary tapes are practically equivalent [Wil83].

Another innovative way for reducing the coupling current loss is the introduction of thin layers of highly resistive materials around the individual filaments [Hua98a], [Kwa97]. These resistive barriers decrease considerably the flow of coupling currents in the metal matrix and appear to be very effective not only in external magnetic field applications, but also in self-field [Zha99].

2.4 Power applications of high-T_c superconductors

More than 15 years after their discovery, a great progress has been done in the development of HTS conductors, on the one hand, and the design and testing of various HTS devices and prototypes for power applications, on the other. Different companies and institutions have contributed to the achievements in the development of HTS technology in the last decade – from research institutes and universities to large manufacturers of electric power equipment and utility companies.

This section gives a general overview of some of the most important applications of HTS in power systems without any pretensions for exhaustiveness of the presentation.

2.4.1 Cables

The use of HTS for power transmission cables was among the first large-scale applications that were envisaged after the discovery of high-T_c superconductivity. Utility companies exhibited great interest in the development of HTS cable technology because of the advantages, which HTS conductors offered compared to conventional cables – larger current and power capacity up to a factor of 3 to 5 and reduction of size up to 50% [DoE98]. These two factors are especially important in large urban areas, where the constant increase in demand of electric power is in contrast to the limitations and congestions in the available aerial and underground space. The Tokyo metropolitan area is expected to be among the first to start large-scale utilization of HTS cables to replace the conventional electric ones in the existing underground ducts.

Different projects have been undertaken for the design, manufacturing and testing of superconducting cables, made of Bi-2223/Ag tapes. Among these, the Sumitomo – Tokyo Electric Power Co. (TEPCO) project of 100m, 66 kV, 1 kA rms 3-phase cable in Japan [Mas01], the NKT – NST project of 30 m, 36 kV, 2 kA rms 3-phase cable in Denmark [Wil01] and the Pirelli – Detroit Edison project of 120 m, 24 kV, 2.4 kA rms 3-phase cable in the USA [Ste01]. The last two projects have culminated in 2001 with the successful commissioning and installation of the cables in the power energy grids of Copenhagen and Detroit, respectively. The cables are now running at real load operating conditions as part of HTS field demonstration programs.

The structure of the 66 kV cable of Sumitomo – TEPCO is shown in Fig. 2-18.

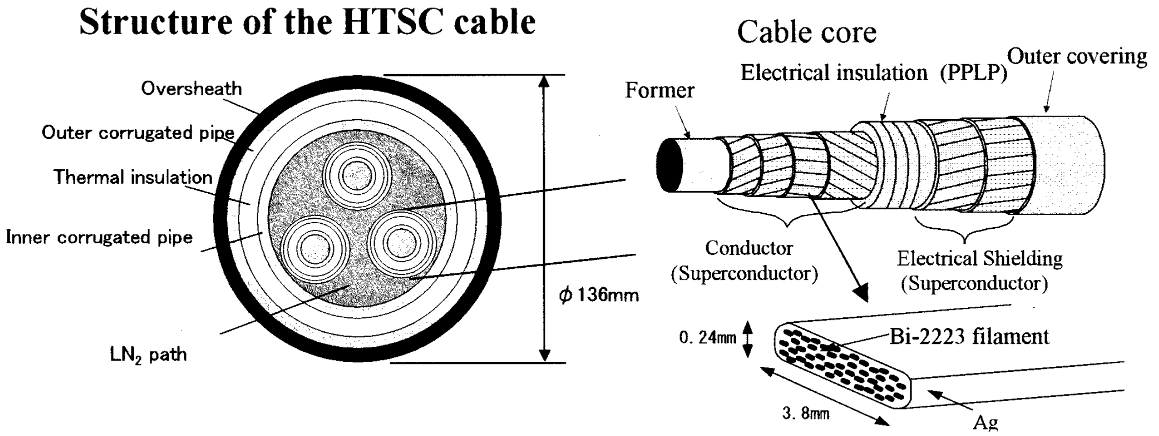

Figure 2-18 Structure of a 3-phase HTS cable. *from a TEPCO brochure*

2.4.2 Fault Current Limiters

All pieces of equipment in electric power networks have to be designed to withstand the thermal and mechanical stress arising from potential short-circuit or 'fault' currents, whose value may exceed the nominal current by a factor of 100. The reduction of these currents leads to significant cost savings and optimization of the workload design. Among the different available current limiting devices, superconducting fault current limiters (SCFCL) offer ideal performance because in normal operation the SCFCL is in superconducting state and has negligible impedance, while in the case of fault event, the quick transition to normal state passively limits the current [Pau01].

YBCO films, Bi-2223 wires or Bi-2212 bulk have been used for construction of different prototypes. Bi-2223 wires are not very suitable for SCFCL in their standard form because of the low matrix resistance. YBCO films are, for the moment, not feasible in long-length or large-area production. Nevertheless, in 2000 Siemens demonstrated a resistive 300 kVA SCFCL with meander configuration of YBCO plates. To date, the largest HTS based SCFCL prototypes use Bi-2212 bulk material (rods or tubes of Bi-2212 ceramic). The first-ever SCFCL was made by Asea Brown Boveri (ABB) of Switzerland in 1996. It was a 3-phase 1.3 MVA prototype, made of Bi-2212 tubes, which was installed in a Swiss hydropower plant and successfully tested during 12 months operation. Recently, ABB have developed and tested a single phase 6.4 MVA SCFCL [Che01].

SCFCL allow novel and unconventional design of power systems. For example, coupling of grids can be achieved with a rather simple SCFCL configuration. The technical benefits have been confirmed with prototype tests and detailed simulations. Significant economic benefits can be achieved by increasing the cost-effectiveness of new power systems and by upgrading the existing ones. Because of the advanced level of the SCFCL technology, they are expected to be the first large-scale applications of HTS.

2.4.3 Transformers

The efficiency of conventional transformers may exceed 99 % but there is still room for improvement. They are purchased with excess capacity to meet maximum power and temperature limits and the average workload is below the optimum design level. Power transformers account for 25 % of the total transmission and distribution losses of electricity and this costs around $2 billion annually in the US alone [Meh97].

A key advantage of HTS transformers is the capability to work continuously in over-load conditions without any lifetime loss because of the ultra-cold operating range of 20 to 77K, even if this is done at the expense of increased used of liquid nitrogen. Another advantage is the reduction of size and weight, which can go down to 30-50% of the ones of conventional transformers. Worth mentioning is the potential environmental hazard of oil used in conventional transformers, while in HTS ones the only substance present in large volume is non-flammable and environmentally benign liquid nitrogen. Last but not least the zero resistance of the HTS windings will lead to reduction of the total losses in the transformers, thus improving their initial capital cost / lifetime efficiency ratio.

For economic viability of HTS transformers, the engineering critical current densities must be higher than 400 A/mm^2 to provide the necessary ampere-turns of the conductor [Meh97].

The world's first operational HTS transformer was made in a project lead by ABB of Switzerland. It was connected to the electric power grid of Geneva in 1997. This 3-phase transformer had an output of 630 kVA and was designed to convert power from 18.7 kV to 420 V. It was made of Bi-2223 windings cooled in liquid nitrogen. The transformer was in operation for 12 months and its performance under power network conditions was quite successful with only minor problems encountered during the test-period.

Currently, there are different ongoing projects for HTS transformers. Siemens is building a 1-MVA transformer in Germany and has started a program for development of on-board transformers for electric rail vehicles [Leg01]. A project, lead by Waukesha Electric Systems in the USA, is currently working on a 5/10-MVA transformer, whose operational tests are scheduled for 2002, with plans for scaling up to 30/60-MVA units [Gra01].

Utilities are also interested in HTS transformers of higher ratings, at which the expected economic gains become even more favourable. A conceptual study performed by ABB suggests that more than 20 % reduction in capital cost, more than 50 % reduction of weight, and more than 70 % decrease of AC losses can be obtained for 100-MVA HTS transformers compared to conventional ones.

2.4.4 Magnetic energy storage devices

Power disturbance problems cost US manufactures between $12 and $26 billion annually [Par97]. For example, a power blackout can cost car manufactures up to $500,000 an hour. Voltage sags and momentary outages of short duration are another serious power quality problem that may affect sensitive electronic equipment like process controllers, CPU units, medical care monitors and many others.

New superconducting technologies offer solution to this problem – superconducting energy storage systems have significant advantages over conventional power quality equipment, such as uninterruptible power supplies (UPS), batteries and diesel generators. Reduced environmental impact, low maintenance and operation costs, small size and weight, increased safety and reliability are characteristic features of the new superconducting energy storage systems.

Two technologies are currently under development: one based on flywheels and the other on magnetic fields [DoE98]. Flywheel energy storage devices are based on rotating discs that float on superconducting magnets and store energy in their spinning motion. Once charged, these discs will spin almost indefinitely, without losing any of their energy due to complete lack of friction. Flywheels can be used in commercial and industrial applications for utility companies, telecommunications, trains and electric vehicles; in aeronautic applications for energy storage in satellites, space stations, launch vehicles and mission control centers, as well in military applications for energy directed weapons, satellites, ships and command centers. A 10 kW flywheel project is near completion in the USA and a 100 kW UPS unit is at design level [Gra01].

Another storage technique, superconducting magnetic energy storage (SMES), relies on large superconducting coils to store energy in a loss-less manner as a powerful magnetic field. The first commercial SMES systems have been constructed in the 1990's. A SMES for small and mid-size substations must provide power above 2 MW in order to guarantee the critical load. Larger, 10 MW SMES will be required to protect critical loads at almost any distribution station in the USA [Par97]. At present, smaller SMES (micro-SMES or μ-SMES) are being developed for power quality use, too, which demand rather little energy storage but quite a lot of power delivery – for example an energy storage of 0.3 kWh with power rating of 1 MW.

If the SMES and flywheel technologies are advanced to perfection, the energy storage industry will be revolutionized.

2.4.5 Other applications

Motors and generators

Magnetic fields in conventional motors and generators are created by large coils of copper or aluminum wire. HTS wires have much higher current capacities, which means considerably smaller and more powerful motors and generators can be built. For instance, a 1,000 horsepower HTS motor can be 50% smaller than a conventional one of the same power rating. In addition, the substitution of conventional with HTS conductors will eliminate the losses due to electrical resistance, and the efficiency of motors and generators can be increased up to 98 % and 99.5 %, respectively. Today's standard generators operate at an efficiency rate of 97-98%, while typical motors at 90-96% [DoE98].

Magnetic Resonance Imaging equipment (MRI)

The heaviest and most expensive part of an MRI scanner is a powerful magnet. While nowadays all MRI machines (single unit price of $1 million to $3 million) are using LTS technology, the MRI systems built with HTS magnets would be smaller and more powerful than their LTS counterparts. At the moment, however, only LTS magnets are able to work in persistent mode and to provide a perfectly stable magnetic field, required for the MRI operation. The further advance of HTS technology would possibly lead to achievement of persistent mode in HTS and this will reduce manufacturing and maintenance costs, making sophisticated medical imaging more accessible and would expand substantially the market and utilization of such equipment.

Magnetic separators

Numerous industries, such as pharmaceutical and chemical, need the ability to selectively separate certain materials. Magnetic separation techniques, using superconducting technologies, purify mixed materials with different magnetic properties. Magnetic separators made with HTS coils would be more efficient and cheaper than LTS units because of reduced cooling needs and simpler cryogenic systems.

A project, lead by Dupont Superconductivity is currently underway in the USA for the construction of magnetic separator using 2.2-3 T magnet with reinforced Bi-2223 wire, current rating of 130 A, and operating temperature of 30 K [Gra01].

2.5 Major issues for full-scale industrial applications

On a 1-to-1-substitution basis, HTS devices will save around 50 % of the present energy losses in cables, electric motors, generators and transformers. Comparing the critical current capabilities of HTS with copper and aluminum wires indicates that the superconductors can carry up to 100 times more current at virtually no resistance in the same cross section. However, the HTS material in superconducting devices occupies only 10-20 % of the engineering cross section. These devices require refrigerating systems having additional thermal losses and that is why the calculated result for the savings falls in the range of 50% of the currently wasted energy, which is lost in the transmission and distribution process and amounts to approximately 10% of total production of electricity [Law01].

2.5.1 Development of the superconductivity market

Different studies, which assess the potential of the market for superconducting devices are available, for example the US Department of Energy study [Mul01] and the online report of the Consortium of European Companies Determined to use Superconductivity, Conectus [Con01]. The estimates for the worldwide market for superconductor applications, recently made by Conectus, are shown in Fig. 2-19. These figures are rather conservative in comparison to the other reports, made mainly by US institutions.

As can be seen in Fig. 2-19, almost all of the present commercial superconducting products still use LTS materials, which have well-established applications, mainly for magnet technology – ranging from small magnets for laboratory purposes to super-powerful magnets used in particle physics. The largest share of the LTS market is taken by magnets for advanced medical diagnosis (MRI equipment).

A boom of the utilization of HTS in different areas, such as electric power systems, industrial processing, transportation, (new) medical and magnet technology, communication and information systems, and electronics, is expected in the second half of this decade, so that the worldwide market of HTS would reach \$1.6 billion by 2010 and would increase exponentially in the next decade, reaching \$40 billion by 2020.

The earliest HTS equipment to achieve large-scale commercialization is predicted to be fault current limiters (market entry in the 2003-2004 period), followed by cables and transformers in 2005, and by electric motors in 2006. The final market entry is expected for generators in 2010 [Law01].

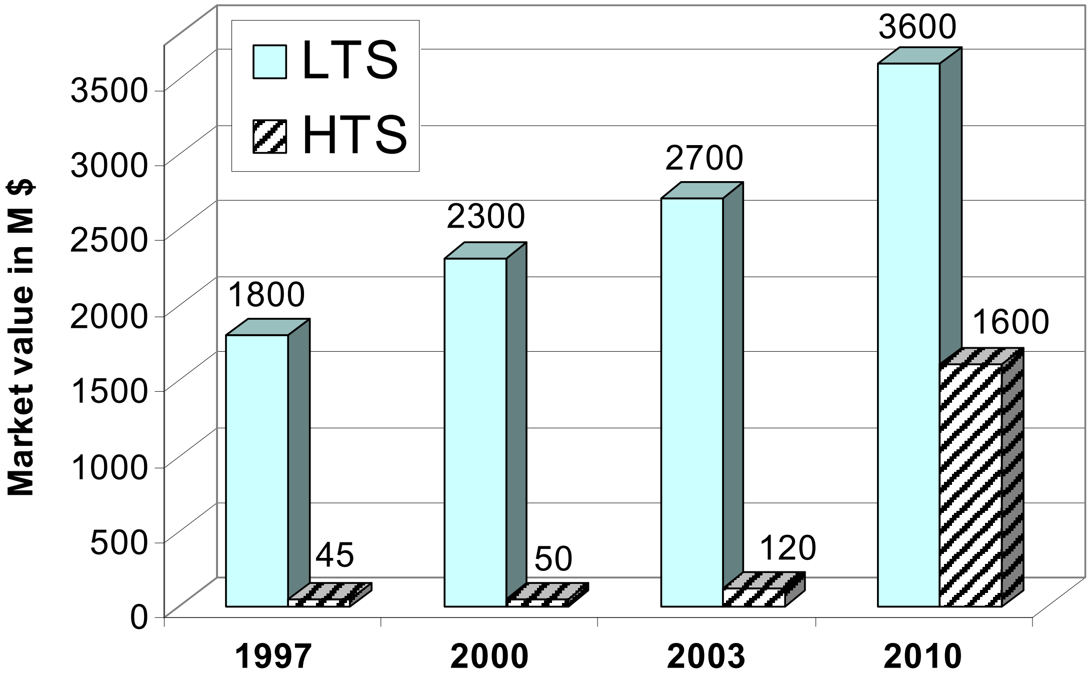

Figure 2-19 Worldwide markets of superconductor applications. *source Conectus, Dec. 2001*

2.5.2 Necessary improvements in BSCCO conductors

The market potential of HTS in the next 5-15 years has promoted rigorous competition between Europe, Japan and the USA. Different research institutions and industrial companies on a worldwide scale are developing novel competitive configurations for wires and cables from the 1st generation conductors (BSCCO) and currently investigating the possibilities for long-length production of the 2nd generation conductors (YBCO).

The manufacturing, operation and maintenance costs of cryogenic systems at 77 K are considerably lower than those at 4.2 K. In addition, the cooling agent of the latter (liquid helium) is much more expensive than the cooler of the former (liquid nitrogen). Therefore, applications at 77 K have a promising future and since Bi-2223 technology is most advanced at this stage, the first industrial applications will use primarily Bi-2223.

For the full utilization of the potential of Bi-2223, however, various improvements must be achieved in the next a few years along with development of reliable and inexpensive cryogenic systems [Fri99].

Critical currents

Given the critical current I_c, the critical current density J_c is obtained after dividing I_c by the cross-section of the superconductor, while the engineering critical current density J_e is equal to I_c divided by the cross-section of the entire conductor. For any application, high I_c and J_e values in long-length conductors are required. The best Bi-2223 tapes available in lengths of a few hundred meters are manufactured by American Superconductor Corporation (ASC) with I_c = 100-125 A, J_c = 300-400 A/mm^2 and J_e = 120-150 A/mm^2. Short-length tapes have been made also by ASC with J_c = 800 A/mm^2 with special geometry using thin filaments and thick matrix, so the corresponding I_c and J_e are not so high. The best 1-km tape was made by Nordic Superconductor Technologies (NST) with J_c = 230 A/mm^2.

The potential of Bi-2223 has been demonstrated by high J_c values on short-length tapes and by the J_c values of thin Bi-2223 films being a factor of 10-100 higher. Unfortunately, cracks, secondary phases and other macroscopic defects appear in the manufacturing process of long-length tapes and limit their performance. Furthermore, for the need of AC reduction, multifilamentary tapes (almost exclusively manufactured nowadays) must be twisted, which results in additional decrease of J_c.

For the successful implementation of large-scale applications with Bi-2223 conductors, the competitive J_e values at 77 K must be in the range 500-800 A/mm^2 and I_c must be 200-300 A.

Cost reduction

The economic viability of Bi-2223 conductors is a very important factor taken into consideration by the end-users. Currently, the manufacturing cost of Bi-2223/Ag tapes is \$200-400/kA-m. With large-scale tape manufacturing and an increase of I_c, this cost can be reduced to \$40-50/kA-m plus some profit margin. Around 50 percent of the manufacturing cost is attributable to the sliver (silver alloy) matrix, so by replacing, say 50 % of the silver with a cheaper metal or alloy, the cost could be reduced by a further 20-25 %.

For acceptable device application cost, the manufacturing cost of a Bi-2223 conductor must be reduced by a factor of 10-15, so that the sale price amounts possibly to \$20-30/kA-m, in order to compete with the current prices of copper wire, which are around \$20-25/kA-m.

AC losses

The aspect of AC loss reduction is another key issue for improving the function/cost ratio of Bi-2223 conductors. The removal of every single watt of cold power dissipated in superconducting applications may cost up to $50 to the utilities. It is, therefore, essential to obtain as low AC losses as possible, especially in magnetic field applications, in which the magnetization losses are much higher than transport current losses.

It is difficult to quantify the desired AC reduction in Bi-2223 conductors. A common target for AC losses in cable applications is 1 W/m per phase. There is no much room for AC reduction in transport current applications, where a decrease of 30-40% would be welcome, while in magnetic field applications there is a need of greater AC loss reduction.

Mechanical strength

Bi-2223 as a ceramic material is hard and brittle. It may well withstand high pressure but has low strength in bending, twisting and tension. Improvements are required in the manufacturing process so that to keep the strain on the tape as low as possible – a total strain above 0.2% is undesired since it may cause severe degradation of the superconducting properties.

A considerable decrease in the I_c of the tapes results when bending with radius below the critical one (with 95 % of I_c retention) is applied. A low critical bending radius, which is now around 25-30 mm for tapes manufactured by NST and 35-50 mm for tapes manufactured by ASC may be useful considering, for example, that retrofitting in the existing underground cable ducts may lead to sharp curvatures in some places.

The maximum values of the strain and stress Bi-2223 conductors can support may be increased up to a factor of 2 by special mechanical reinforcement.

2.6 Conclusions

As far as AC power applications are concerned, HTS are expected to enter during the next years the large market of electric power equipment that is currently using conventional copper and aluminium wire, such as cables, transformers, motors and generators. Electric devices using HTS will be half the size of conventional machines with the same power rating, and will save half the energy loss. This will be of great benefit with respect to the increasing demand of electricity in the world, and will represent a new progressive step in the way electricity is generated, transported, and utilized.

Bi-2223 conductors are nowadays produced commercially in long lengths; their manufacturing technology is much more advanced than that of YBCO and Bi-2223 is not completely ruled out as 2nd generation conductor. YBCO has a major disadvantage for AC magnetic field applications and flexible device configurations – it needs to be made in the form of a thick film with high aspect ratio, which is unfavourable both in terms of AC losses in applied magnetic fields, and for manufacturing of long-length conductors.

Continuous improvements in the performance of Bi-2223 conductors are required, among which the aspect of AC losses is of particular significance and is a leading thread in the contents of the next chapters.

Chapter 3. Modelling and AC Losses of Bi-2223 Tapes with Applied Transport Current

---

Abstract

Presented is the principle of the electrical characterization technique with digital lock-in for measurements of AC losses in self-field. The main theoretical derivations for different types of losses in self-field are outlined. An overview is made on the frequency dependence of the self-field loss components in related studies.

Based on measurements in a broad frequency range (59–2500 Hz), a model for dissociating the different AC loss contributions is proposed. The model is based on the different frequency dependence of the hysteresis, eddy current and resistive (near I_c) losses in self-field. A detailed analysis for 14 mono and multifilamentary tapes, produced by BICC Cables, has been made for these three loss contributions, whose relative weight depends on the amplitude and the frequency of the applied current.

A simple electromagnetic model of Bi-2223 tapes has been used in order to simulate the eddy currents in the silver sheath and matrix with finite element method software. The effect of the tape geometry and sheath resistivity on the eddy current losses has been investigated. A comparison is presented between the measured, simulated and theoretically derived eddy current losses.

Described is an original method for estimating the performance of Bi-2223 tapes in over-critical current excursions. The current waveform is triangular, sinusoidal or with arbitrary shape, and is applied for several consecutive cycles. The generator frequencies are selected to be 0.05, 0.1, 0.5, 1, 10 and 59 Hz. The amplitude of the applied current is varied from 2 to 20 times the value of I_c. The resistive behaviour of the superconducting tapes and the temperature rise in the over-I_c regime have been evaluated.

Original contributions of this thesis

- the modelling and dissociation of hysteresis, eddy current and resistive flux-creep losses in HTS tapes and their quantitative analysis in the frequency range 59–2500 Hz
- the numerical simulations and analysis of eddy current losses in Bi-2223 tapes
- the characterization and modelling of Bi-2223 tapes in over-critical current regime

3.1 Introduction

Most of the power applications of HTS would require applied DC or AC magnetic field, and for this reason the greater part of the research on AC losses in HTS tapes, wires, and cable prototypes in recent years has been directed to combined application of transport current and/or external magnetic field.

However, one of the large-scale industrial applications of HTS, for which Bi-2223 is considered to be the most promising material at 77 K [Fri97], will be their usage in transmission lines for electric power systems where AC transport current is conducted without the presence of external field. Therefore, most of the related work on AC losses in Bi-2223 silver sheathed tapes in the self-field of applied transport current has been confined to the power frequency range 40–180 Hz, where the dominating loss is the hysteresis one in the superconductor – for example in [Ash94], [Glo97] and [Paa95]. The eddy current loss, which occurs in the Ag sheath, is known to contribute negligibly in this low frequency range, and is shown to have an increasing contribution as the frequency goes beyond several hundred Hz [Fuk95]. However, no detailed work on eddy current loss in self-field has been published so far to the best of our knowledge. One of the reasons for that is the impossibility to measure it separately from the other self-field loss contributions in HTS tapes.

This chapter presents a systematic study of self-field loss in Bi-2223/Ag and Ag-alloy tapes by quantitatively describing the different loss contributions at various applied currents up to I_c in the range of 59–2500 Hz. Characterized is also the behaviour of Bi-2223 tapes in over-critical current regime.

The chapter is structured as follows. Section 3.2 describes the electrical characterization technique with digital lock-in that has been used for all performed measurements in self-field; Section 3.3 provides the background theory including a review of the relevant calculations of hysteresis and eddy current self-field loss in HTS conductors; Section 3.4 contains the results of AC loss measurements in a broad frequency range and the model for AC loss dissociation; Section 3.5 describes finite element method model for simulation of eddy current loss in the metal sheath and the effect of the geometry and matrix composition in reducing this loss component; Section 3.6 presents a characterization of the stability and resistive behaviour of Bi-2223 tapes in the occurrence of over-critical current excursions; and Section 3.7 gives the conclusions from this chapter.

3.2 Measurement of transport current losses

Different experimental techniques have been developed for AC loss measurements in HTS. Magnetization methods detect the changes in the magnetic moment of the sample and employ a system of pick-up (search) coils [Cis95], [Oom97], [Rab01a]. They are used in applied external magnetic field. Calorimetric methods, used for both magnetization and self-field applications, involve the measurement of the temperature increase of the sample or the rate of cryogen boil-off [Dol96], [Mag98].

The measurement of transport current loss is most often done by means of the electrical characterization technique, which is described in more details in [Mül97b] and [Sjö01]. The electrical measurements require a complicated experimental set-up and high-precision equipment, since the quantities being measured often differ by several decades of magnitude. For example, in a typical transport current set-up, the driving current is between

10^0 and 10^2 Amperes, while the corresponding voltage that must be measured, is of the order of 10^{-7}–10^{-8} Volts.

The experimental set-up at the Laboratory of Nonlinear Systems at the Swiss Federal Institute of Technology or Lausanne, where all measurements used in this thesis have been made, is presented diagrammatically in Fig. 3-1. Two digital, large-bandwidth, multiple-channel dual lock-in amplifiers [Pro94] are used, which can compute simultaneously the amplitude and the phase of up to 8 harmonics of the signal. The two low-noise, low-distortion amplifiers should operate at the same temperature and have identical temperature behaviour.

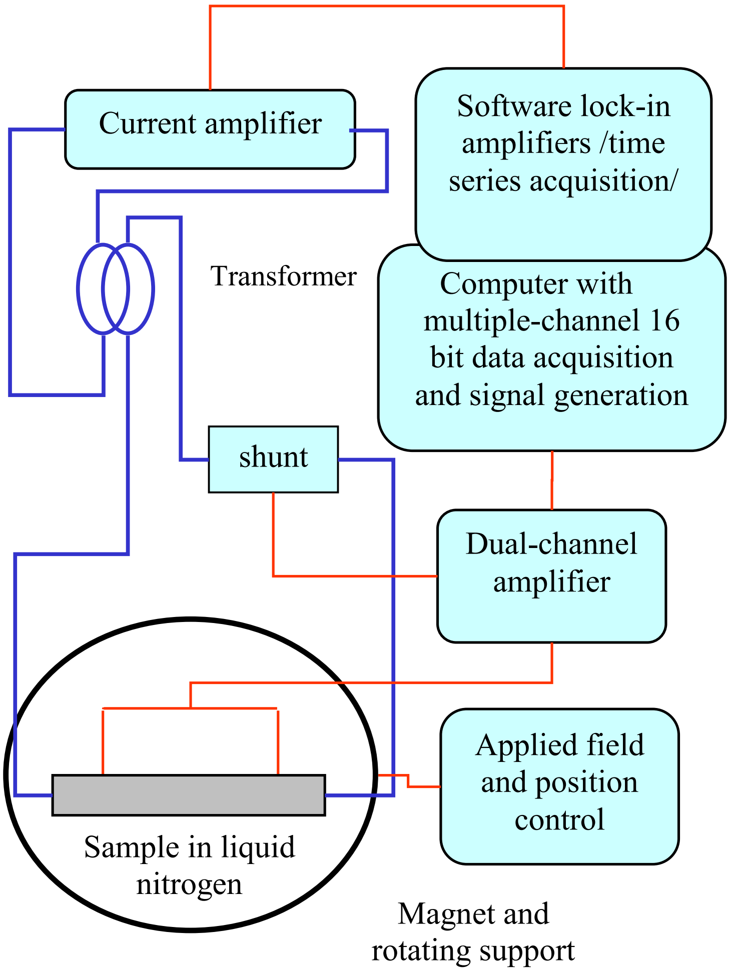

Figure 3-1 Experimental set-up for electrical AC loss measurements with digital lock-in.

The software lock-in allows its integration into a specially designed complete measurement system with easily controlled frequency (set of frequencies), amplitude (set of amplitudes), as well as an applied DC magnetic field amplitude and angle. For a perfect reference, the same clock signal is used both for signal generation and for data acquisition on the different channels. Another advantage is the possibility to generate arbitrary waveforms for the driving current *I(t)*. Once correctly tuned and calibrated, the system allows almost automatic measurements.

A typical configuration for measurements on a sample tape of length *l* (usually 5-10 cm) is depicted in Fig. 3-2.

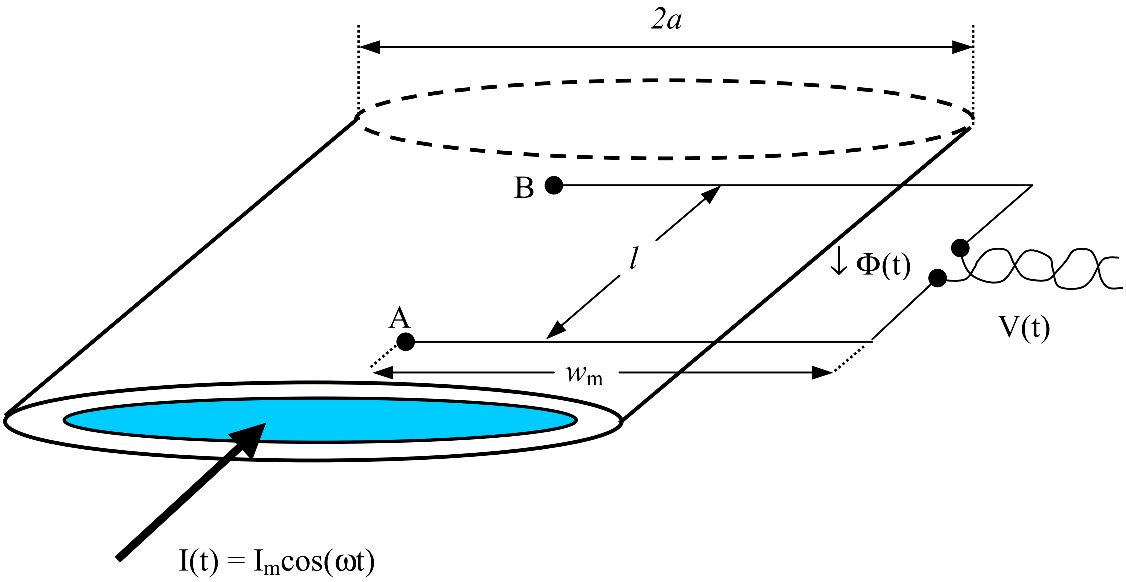

Figure 3-2 Tape configuration for electrical self-field loss measurements with voltage taps soldered onto the tape's surface.

The measured voltage *V(t)* is the sum of an AC loss (in-phase) component and an inductive (quadrature) component. For currents below I_c, the inductive component is much larger than the loss component, therefore it is extremely important to accurately determine the phase of the current passing through the sample. The first lock-in amplifier measures the amplitude and the phase of both the in-phase and quadrature components of the voltage across the sample with reference signal taken from the reference output of the sine current generator. The phase shift φ_I between the current *I(t)* and the reference output of the sine current generator is measured by the second lock-in amplifier. The amplitudes of the first harmonic of the in-phase voltage V_1^{in} and the driving current I_m, as well as their phase-difference ($\varphi_{V_1}^{in} - \varphi_I$) are then used for the calculation of the self-field power loss per unit length l at given frequency:

$$P_{sf}(I_m) = \frac{V_1^{in} I_m \cos(\varphi_{V_1}^{in} - \varphi_I)}{2l} \quad [\mathrm{W/m}] \tag{3.1}$$

For precise AC loss measurements, the lead extensions must be parallel, must form a large flux loop and be far enough from the tape before the twisting (see Fig. 3-2). In practice, for $w_m \geq 6a$ the recorded magnetic flux Φ(t) accounts for 95% of the flux produced by the superconductor, so the measured loss is sufficiently accurate [Sjö01, Mül97b]. The measurement results are extremely sensitive to the phase-angle error of the digital lock-in.

The configuration of Fig. 3-2 is most often used in electrical measurement set-up. In this configuration all voltage contributions between the points A and B will be measured, i.e. resistive, hysteretic, eddy current, and purely inductive ones, so the measured loss is the total self-field loss with applied transport current.

3.3 Calculation of AC losses of HTS in self-field

In some of the main AC applications of HTS, such as fault current limiters and power cables, transport current will be conducted without the presence of external magnetic field. The AC losses occurring in this case are also referred to as *self-field losses*. The self-field AC loss, obtained from the electrical characterization technique, most often used for transport current measurements, is a composite loss with contributions from hysteresis and resistive loss in the superconductor (near I_c), as well as from eddy current loss in the silver matrix. Since the separation of these loss contributions is not feasible by means of such measurements, a possible way of self-field AC loss dissociation is based on the different frequency dependence of the hysteresis, eddy current and resistive loss, as outlined in this section.

3.3.1 Hysteresis loss in self-field

Bi-2223 Ag-sheathed tapes have a cross-sectional geometry, which is best approximated by an elongated ellipse or thin rectangle of aspect ratio (width/thickness) of usually 10-15. A method of calculation of the hysteresis loss in a Bi-2223 tape based on transport current measurements is presented in Appendix A. The original derivation of the hysteresis loss in type-II superconductors with strip and elliptical cross-section has been done by Norris with the assumptions of the critical state model [Nor70]. He used two methods for the calculation of hysteresis loss in superconductors carrying AC current – by integrating the instantaneous product of the electromagnetic field and the current over a cycle, and by evaluating the flux distribution for all points within the conductor at peak current.

Norris calculated the self-field hysteresis loss flat superconductors of infinitely thin rectangular (strip) cross-section:

$$P_{hyst} = f\,\frac{I_c^2\mu_0}{\pi}\left[(1-i)\ln(1-i)+(1+i)\ln(1+i)-i^2\right] \qquad (3.2)$$

where f is the frequency of the transport current and $i = I_m / I_c$ is the peak-to-critical current ratio. For low applied transport current ($i << 1$), P_{hyst} varies as i^4 .

For a superconductor with elliptical cross-section, the hysteresis loss calculated by Norris is:

$$P_{hyst} = f\,\frac{I_c^2\mu_0}{\pi}\left[(1-i)\ln(1-i)+(2-i)\frac{i}{2}\right] \qquad (3.3)$$

In this case, P_{hyst} varies as i^3 for $I_m / I_c << 1$.

The hysteresis loss in Eq. (3.2) and Eq. (3.3), expressed in W/m, is linearly proportional to the frequency of the applied transport current.

The loss calculated by Eq. (3.2) and (3.3) for either geometry is entirely determined by the critical current and does not depend on the aspect ratio. The reason for the higher loss in the elliptical conductors is that the loss level is set mainly by the depth of flux penetration. For the same transport current the flux penetration in the ellipse is always greater than in the strip [Yan96].

When the current amplitude I_m becomes larger than I_c, Norris's formulas are no longer valid, since any excess current has to flow in the Ag-sheath, causing resistive power dissipation and strongly non-sinusoidal voltage waveform [Mül97b].

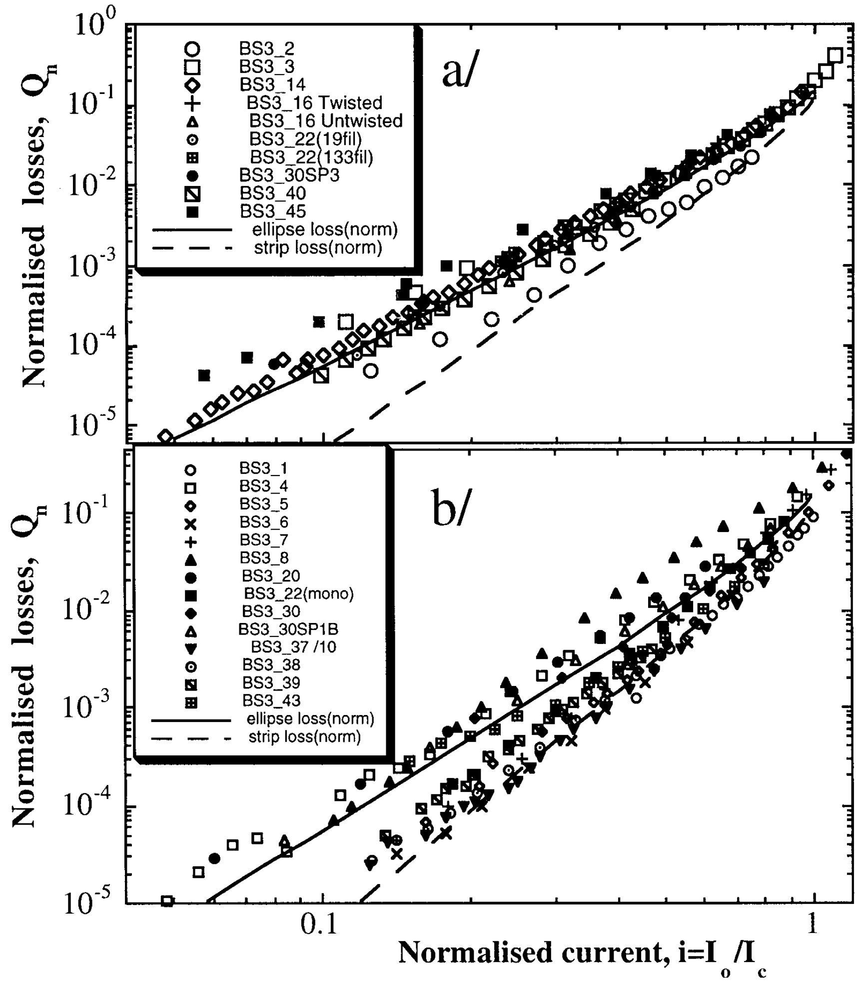

Figure 3-3 Self-field AC losses reported by Glowacki *et al.* for multifilamentary (a) and monofilamentary (b) Bi-2223 tapes. The experimental data are from different sources. *from [Glo97]*

Dresner has applied dimensional analysis in order to obtain analytical expressions for the hysteresis loss in HTS with B-dependent power-law current-voltage characteristics [Dre96a], [Dre96b]. His work is aimed also at explaining why the experimental results for AC losses in HTS match quite well the theoretical predictions based on the critical state model (CSM). In other words, to answer the question why the predictions of a theory (CSM), whose conditions (constant and B-independent J_c) are violated in HTS with broad resistive transition, should be valid for HTS materials both in applications with driving current or external magnetic field. The main result for the case of incomplete penetration ($I_m < I_c$) with applied transport current and Kim's dependence of $J_c(B)$, see Section 5.3.1, is that the hysteresis loss is proportional to the frequency and the amplitude of the driving source as follows:

$$P_{hyst} \sim \omega^{(n+1)/(n+2)} I_m^{(4n+4)/(n+2)} \qquad (3.4)$$

where n is the value of the power index in the E-J relation.

Typical values of n for Bi-2223 tapes fall in the range 10 – 30, so that $(n+1)/(n+2)$ is between 0.92 and 0.97, compared to 1 for the CSM, and $(4n+4)/(n+2)$ is between 3.67 and 3.82, compared to 3 and 4 for Norris's elliptical and strip predictions, respectively. Thus the dependence of the hysteresis loss on the frequency and the amplitude of the transport current is found to be rather insensitive to power index values, higher than 10, and for this reason the CSM predictions appear to match well the experimental results.

There have been various publications for the self-field AC loss in Bi-2223 tapes – for example in [Ash94], [Glo97], [Fri97], [Hug99], [Mül97b], [Yan96]. Practically in all references the experimental results are always compared to Norris's strip and elliptical predictions. It has been found that at power frequencies (50 – 60 Hz) below I_c the hysteresis loss is the main AC loss contribution and $P_{hyst}/(\omega I_c^2)$ as universal functions of I_m / I_c predict fairy well the loss in Bi-2223 tapes. However, the question which of the strip or elliptical prediction fits better the experimental results has not been unanimously answered. In most cases, the experimental results on self-field AC loss in Bi-2223 tapes fall somewhere between the strip and elliptical curves. Considerable differences may be observed between different samples, as reported in [Glo97] and shown in Fig. 3-3.

3.3.2 Theoretical and empirical derivations of eddy current loss

In general, a 2-D analysis of eddy current flow and associated Ohmic losses is rather complicated and no comprehensive analytic solution is available [Hug97]. Nevertheless, some configurations can be calculated with relative ease. Most of the theoretical work on eddy current effects in superconducting media has been done for the case of applied magnetic field – for example in [Car83], [Fum95], [Jil94], [Mül97a].

The effect of cladding material on AC losses of commercial Nb_3Sn tapes has been reported in an early paper by Bussière *et al.* [Bus74]. Eddy current losses are found to be proportional to the square of the frequency and the surface current density:

$$P_{eddy} \sim \alpha f^2 j^2 / \rho \qquad (3.5)$$

with increased contribution at low currents (ρ is the metal resistivity).

The eddy current loss in a multifilamentary cylindrical wire has been calculated by Murphy [Mur77] for small peak transport current I_p $(i = I_p / I_c \leq 0.3)$. Below the critical frequency ω_c, the eddy current loss per unit volume is approximately given by:

$$\frac{P_{eddy}}{v} = \frac{I_c^2 \omega^2}{4\rho} \left(\frac{2\pi R_0}{L} \right)^2 \left[i^2 + 2i^3 \right] \qquad (3.6)$$

Fukunaga *et al.* have used the following empirical formula to calculate the eddy current loss in a rod-form wire with applied AC transport current [Fuk95]:

$$P_{eddy} \approx \frac{\pi \mu_0^2 f^2 I_c^2}{2\rho} R_{Ag}^2 i^2 F(\Gamma) \qquad (3.7)$$

where ρ is the resistivity of Ag, $i = I_p / I_c$ and $F(\Gamma) = \ln(\Gamma)^2 + \ln(\Gamma) - \Gamma^2 / 2 - 1/2$ with $\Gamma = R_0 / R_{Ag}$ (ratio of the outer radius of the ceramic core to the radius of the Ag-sheath).

Müller has calculated analytically the eddy current AC power loss in the metal and the hysteresis loss in the superconductor of a metal-superconducting strip, such as the hastelloy-Y123 flexible tape [Mül97a]. The analysis is valid for the low-frequency limit (i.e. $\omega/2\pi \ll 0.4$ MHz) and the result for the eddy current loss in self-field is:

$$P_{eddy} = \frac{4\mu_0^2}{\pi^3} \frac{I_c^2 \omega^2}{\rho} abh\left(\frac{I_p}{I_c}\right) \tag{3.8}$$

where a and b are the metal strip half-width and thickness, respectively, and

$$h\left(\frac{I_p}{I_c}\right) = \int_0^{I_p/I_c} du \sqrt{\frac{I_p}{I_c}u - u^2}\left[1 - \sqrt{1-u^2} - \frac{u}{2}\ln\frac{1+u}{1-u} + \frac{1}{8}\left(\ln\frac{1+u}{1-u}\right)^2\right] \tag{3.9}$$

where the integration variable u is the current ratio, increasing from 0 to I_p / I_c.

Ishii *et al.* have studied the hysteresis and eddy current loss in Bi-2223 Ag-sheathed mono and multifilamentary tapes [Ish96]. They have calculated the eddy current loss with applied peak transport current I_p with the following empirical approximation:

$$P_{eddy} \approx \frac{(\mu_0 \omega I_p)^2}{2\rho} \frac{d^3}{L} \tag{3.10}$$

where d is the sheath thickness and L is the outer filament-layer perimeter.

The only theoretically derived formula for the expected self-field eddy current loss in a metal-superconductor strip, applicable to the geometry of Bi-2223/Ag tapes, is the one given by Eqs. (3.8) and (3.9). Müller has obtained also the analytical solution of the integral in Eq. (3.9), which leads to a formidable expression in terms of fast converging series. The eddy current loss in Eq. (3.8) is found to have a I_p^6-dependence. In most of the other derivations, however, the eddy current loss is found to be proportional to the square of the peak current, c.f. Eqs. (3.5), (3.7) and (3.10).

In order to obtain an idea about the orders of magnitude of the expected self-field eddy current loss in Bi-2223 tapes, we have solved numerically the integral in Eq. (3.9), taking for example $a = 1.5$ mm, $b = 50$ μm and $I_c = 20$ A, and compared the results from Eq. (3.8) to the Ishii's empirical approximation in Eq. (3.10). This is shown in Fig. 3-4, where a difference of order(s) of magnitude between the eddy current loss calculated from the two equations is observed, except for current ratio $i = I_p / I_c \sim 0.8$. This difference is due to the I_p^6 vs. I_p^2-dependence in the two formulae. Apart from their current dependence, Eqs. (3.8) and (3.10) differ considerably in the geometric factors as well.

The common features of the theoretically or empirically derived formulae for the calculation of eddy current loss in self-field – Eqs. (3.5) to (3.10) – are that the eddy current loss has quadratic dependence on the frequency of the applied current and is inversely proportional to the resistivity of the metal sheath. These derivations, however, differ from each other in the geometric parameters to be taken into consideration, as well as in the order of magnitude of the calculated loss, as we have shown. Therefore, it is necessary to evaluate the level and the contribution of the self-field eddy current loss in other ways than by theoretical or empirical calculations only.

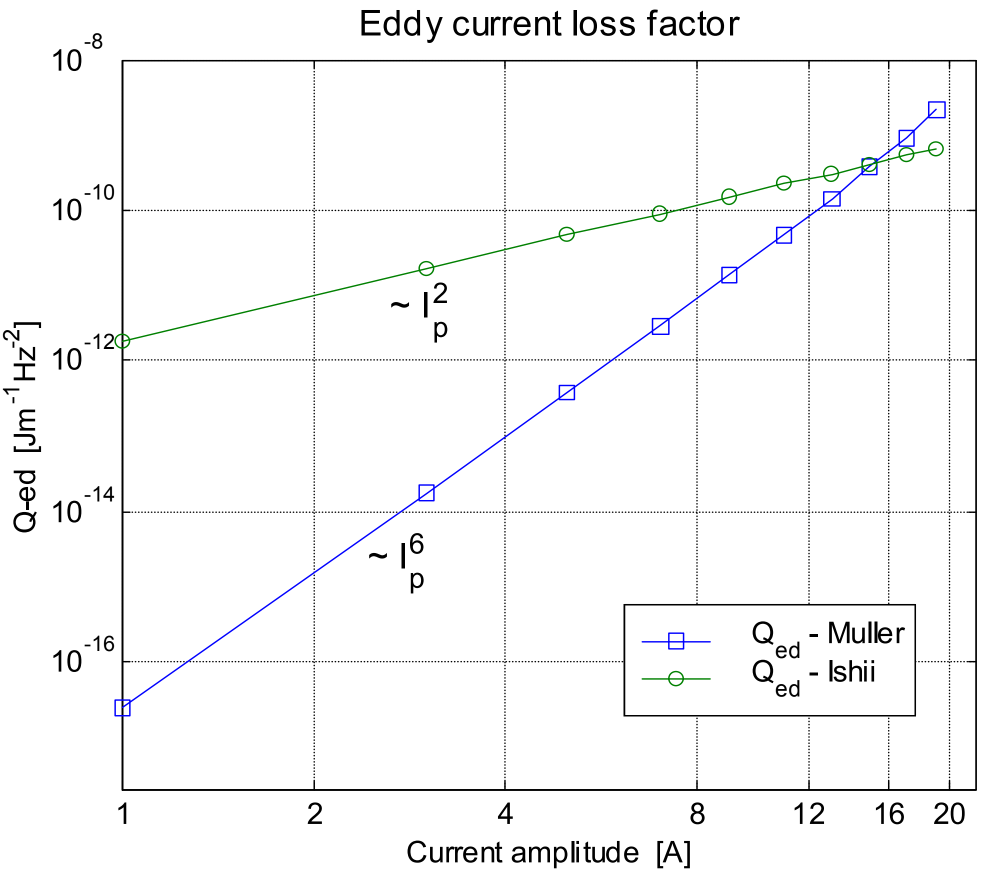

Figure 3-4 Comparison between the eddy current loss factors (P_{eddy}/ω^2) from Eq. (3-8) and Eq. (3-10). The value of I_c used in the calculations is 20 A.

3.4 Frequency-dependence modelling of transport current AC losses in self-field

3.4.1 Frequency behaviour of self-field AC losses in related studies

Frequency-dependent losses (hysteresis and eddy-current loss)

The qualitative assessment of the type of dominating loss when measurements are made for a small frequency set – e.g. at 10, 100, 1000 Hz – is usually done by evaluating the current-dependence of the measured losses, see for example [Fuk94]. In the range 10–100 Hz, the AC loss is proportional to I_m^3, therefore it is concluded that hysteresis losses (Q_{hyst}) is of major contribution. At 1 kHz, however, the total loss is larger and is proportional to I_m^2; this is due to eddy current loss, which is concluded to be dominating at such frequencies.

Similar conclusions have been reached by Fukunaga *et al.*, who have described the hysteresis and eddy current loss (per cycle) of wires with cylindrical cross section (rods) in the range 10–1000 Hz [Fuk95]. At 50/100 Hz the losses are proportional to $I_m^{3-3.5}$ and independent on *f*, i.e. the main contribution is from Q_{hyst}. Around 500 Hz the loss current-dependence starts changing to ~ I_m^2, which comes from the eddy current loss in the silver sheath. The total loss gradually increases with the frequency above 100 Hz due to the growing contribution of the eddy current loss, which varies with f^2.

Ishii *et al.* have studied the AC loss in Bi-2223 mono and multifilamentary silver sheathed tapes by means of AC transport current technique [Ish96]. They have used Eq. (3.10) to estimate the expected eddy-current loss in the silver sheath. At 50 Hz the eddy current loss is found to be much less than 10 % of the total self-field loss, which below I_c is found to be directly proportional to the frequency as in the CSM.

In some papers, presenting numerical results for transport current loss in the range of 10–120 Hz, the self-field AC loss per cycle is found to decrease slightly with the frequency. This has been reported in [Ame98b] and [Fuk01]. The difference with the CSM has been explained by the higher current density at the edges of the tapes, which hinders the penetration of the self-field with the increasing frequency and results in reducing the self-field loss per cycle (skin-like effect).

Indeed, in HTS with smooth *E-J* characteristics, the hysteresis loss does not increase linearly with the frequency. The power loss goes with *f* to the power of (n+1)/(n+2), as it has been shown by Dresner, see Section 3.3.1. Similar dependence – *f* to the power of n/(n+1) – has been theoretically derived by Rhyner [Rhy93]. However, for *n*-values larger than 15 both (n+1)/(n+2) and n/(n+1) are very close to unity, and that is why in most literature sources it has been reported that the self-field AC loss in Bi-2223 tapes is (*quasi) linearly* proportional to the frequency of the applied current, e.g. in [Hug94], [Hug97], [Mül97a], [Ore92], [Yan95]. The quasi-linear frequency dependence of the hysteresis loss has been also demonstrated in [Nib99] by means of numerical simulations.

Frequency-independent losses (flux-creep and flux-flow loss)

The critical state model assumes very steep *E-I* characteristics for the superconducting material with zero electric field, respectively no resistance below I_c and immediate transition to normal state above I_c. In Section 2.2.3 it was discussed that this is not the case in type-II superconductors at 77 K, see also Fig. 2-8. Since the *E-I* characteristics of HTS materials are quite broad, this leads to the appearance of resistive loss mechanisms in Bi-2223 tapes due to flux-creep (below I_c) and flux-flow (above I_c).

Paasi *et al.* have investigated the influence of the thermally activated creep of the self-flux on the transport current loss in a single-layer coil made of BSCCO-2223/Ag multifilamentary tape [Paa95]. It was found that the voltage due to the wide resistive transition gives rise to frequency independent loss with significant contribution even well below the critical current (i > 0.7–0.8), which explains why the total loss near I_c does not follow the expected I_p^{3-4}- behaviour for the classical self-field loss based on the CSM. Because of the linear frequency dependence of the self-field loss it is concluded that coupling and eddy current losses do not have any dominating role at $f \leq 250$ Hz.

Several other authors have also found that as the applied current approaches the DC critical current, there appear to be additional resistive losses due to flux-creep and flux-flow in the superconducting filaments [Ash94], [Fri97], [Paa96], [Yan94]. Due to the broad *E-I* characteristics of Bi-2223 tapes, the boundary between flux-creep and flux-flow is not well defined, since the I_c depends on the employed voltage criterion.

A noticeable contribution of flux-creep losses has been observed not only with transport current measurement techniques. Dolez *et al.* have used a calorimetric method to measure self-field losses in Bi-2223 /Ag tapes, and have found that in addition to the linear term of the hysteresis loss, there appears a loss part independent on the frequency and increasing with the AC current amplitude [Dol96].

3.4.2 Model for AC loss dissociation in a broad frequency range

Self-field AC loss measurements in a wide frequency range (59–2500 Hz)

As it was discussed in the previous section, in a narrow frequency range, or with a small set of measurement frequencies it is possible to distinguish the type of predominating loss only qualitatively, mainly by observing the current dependence of the measured loss. For quantitative analysis of the self-field AC losses, we have made transport current measurements in a relatively broad frequency range: 59–2500 Hz.

The loss measurements have been performed on 14 Bi-2223 tapes, produced by BICC Cables Energy Technology. Table 3-1 shows the specification of the BICC tapes with the relevant technical characteristics and Fig. 3-5 displays micrographs of typical cross-sections of tapes with different filament number.

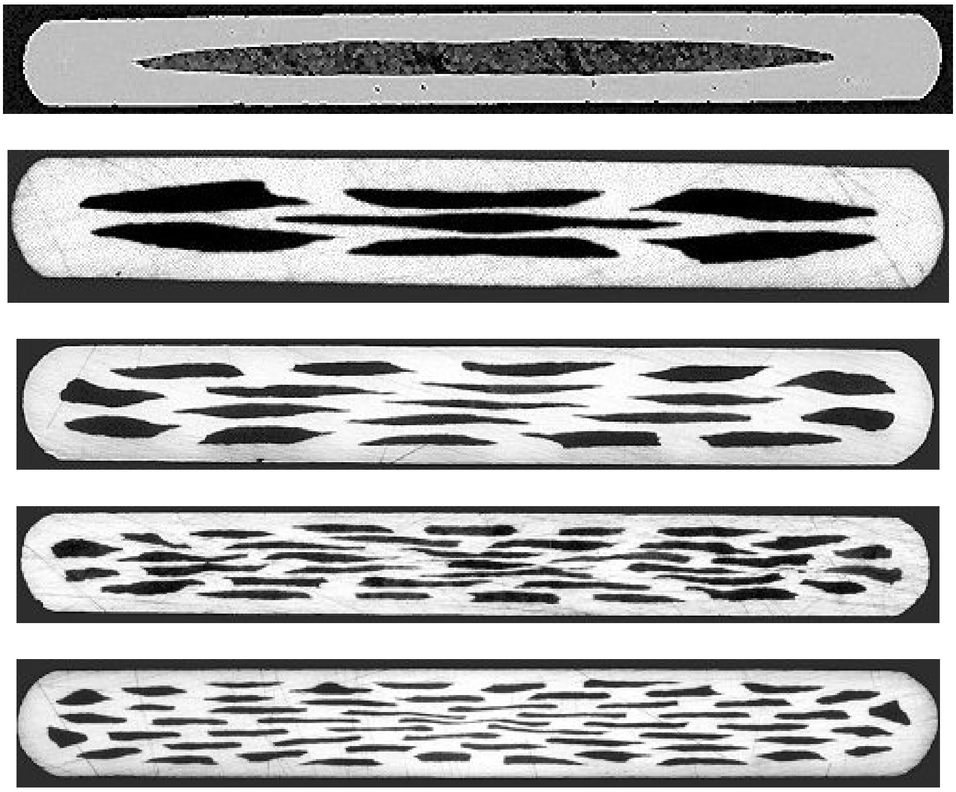

Figure 3-5 Micrographs of cross-sections of 1, 7, 19, 37 and 55-filamentary tapes made by BICC Cables.

TABLE 3-1. BICC tape specification

Tape designation	#	I_c (A)	2b (mm)	d (μm)	2a (mm)	w (μm)	Sheath material	n	λ
BICC-19	7	17.1	0.30	125	2.80	400	AgMgNi *	17.3	0.23
BICC-23	7	12.4	0.28	100	2.90	415	Ag	21.4	0.23
BICC-34	19	27.4	0.25	80	2.85	250	Ag	18.5	0.31
BICC-36	37	28.7	0.31	100	2.85	270	Ag	16.3	0.33
BICC-41	55	23.1	0.35	90	3.00	250	Ag	18.2	0.33
BICC-44	1	15.5	0.28	95	2.80	350	Ag	14.8	0.40
BICC-45	55	23.8	0.36	90	3.00	270	Ag	18.6	0.33
BICC-46	19	10.4	0.34	100	3.35	300	AgMgNi **	9.7	0.27
BICC-47	19	33.1	0.28	80	3.70	330	AgAu **	19.7	0.27
BICC-49	37	26.4	0.36	100	2.95	270	Ag	11.1	0.33
BICC-51 [1]	37	24.7	0.36	100	2.75	50	Ag	13.3	-
BICC-53	19	18.3	0.30	85	2.80	280	Ag	14.6	0.33
BICC-55 [2]	19	17.4	0.30	85	2.30	50	Ag	17.4	-
BICC-56	1	19.2	0.32	160	2.75	380	Ag	19.1	0.40

Legend:

#	number of filaments
I_c	DC critical current
2b	tape thickness
d	sheath thickness
2a	tape width
w	combined width of the two sheath edges
n	power index from the fit $E/E_c = (I/I_c)^n$
λ	filling factor (S_{BSCCO}/S_{TOTAL})
BICC-51 [1]	the same tape as BICC-49 with the edges polished out
BICC-55 [2]	the same tape as BICC-53 with the edges polished out
AgMgNi *	outer sheath tube made of alloy
AgMgNi **, AgAu **	entire sheath made of alloy

The self-field loss measurements have been performed at 90 logarithmically distanced frequencies between 59 and 2500 Hz. The applied transport current is a sine wave with peak value I_p varied between 1 A and the DC critical current, i.e. $0.05 < I_p/I_c < 0.99$. The update rate is 200 kHz for the signal generation and 50 kHz for the simultaneous sampling acquisition on the two channels with 16-bit resolution. To avoid windowing, the data block length is chosen to have k complete cycles of the measured frequency and m complete cycles of the line frequency, thus ensuring the best rejection of the 50 Hz mains noise.

Model for AC loss dissociation

The conclusions from Section 3.3 and Section 3.4.1 for the expected frequency comportment of self-field AC losses for Bi-2223/Ag tapes can be summarized as follows. At low frequencies ($f \leq 200$ Hz) the *hysteresis loss* (Q_h) should have a main contribution; afterwards a gradual increase with the frequency has to be seen due to the growing contribution of *eddy current loss* (Q_e), which will presumably dominate at high frequencies. Some additional *resistive loss* due to flux-creep (Q_r) may contribute for applied currents close to I_c.

We have proposed the following loss-model for dissociating the contributions of the eddy current, hysteresis, and resistive losses in Bi-2223 tapes, which is based on a least-squares fit of a second order polynomial to the power loss curves [Sta98a]:

$$P_{meas} = Q_e . f^2 + Q_h . f^1 + Q_r . f^0 \tag{3.11}$$

where the first term corresponds to the eddy current loss with a square dependence on *f*, the second term comes from the (quasi) linear increase of the hysteresis loss with frequency, and the last one is the resistive loss, being constant with *f*. A very small fitting error is introduced by assuming a linear dependence of the hysteresis loss with *f*, see Section 3.4.1.

Figure 3-6 shows the measured AC loss per cycle for one sample tape (BICC-23). Plotting the loss per cycle allows an easy qualitative assessment of the dominating loss contribution. A flat loss segment in the plot corresponds to hysteresis loss; a positive slope is due to eddy current loss, while the appearance of a negative slope at high currents is due to resistive flux-creep loss.

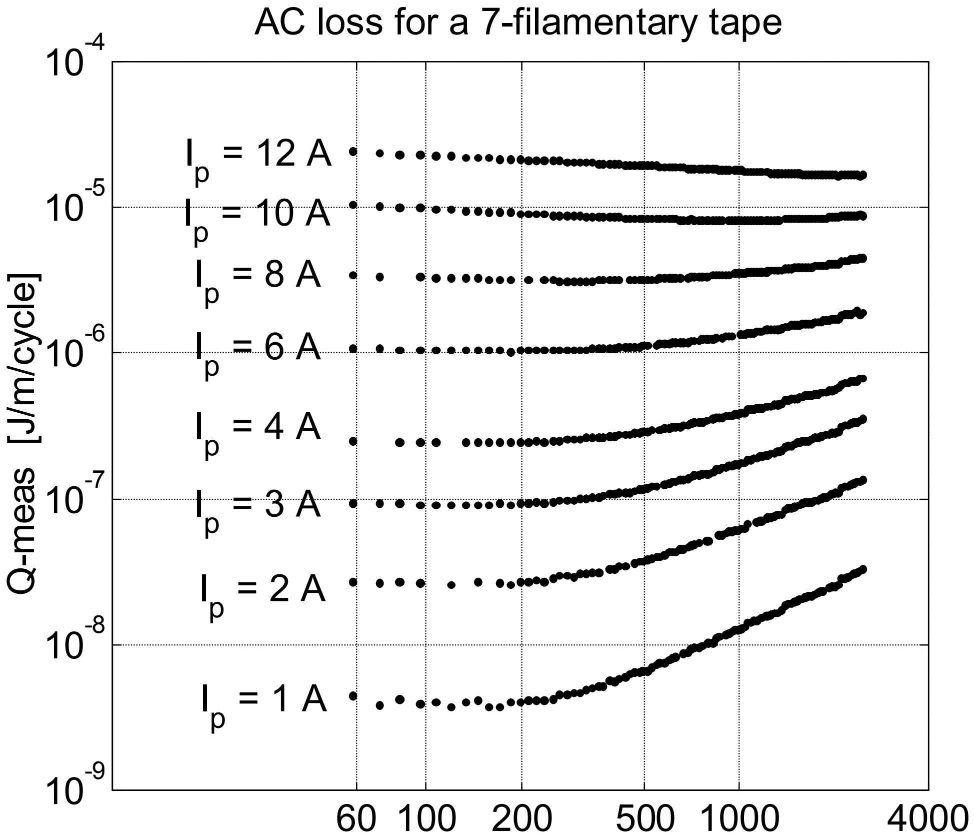

Figure 3-6 Frequency dependence of measured self-field AC loss (per cycle) in BICC-23 tape for different peak currents. The DC critical current is 12.4 A.

Next, Fig. 3-7 and Fig. 3-8 show the frequency dependence of the AC losses, given in $\mu J / m / cycle$, for one monofilamentary and one 7-filamentary tape for different reduced current ratio $i = I_p / I_c$. Plotted are also the fit curves with the respective loss coefficients as in Eq. (3.11).

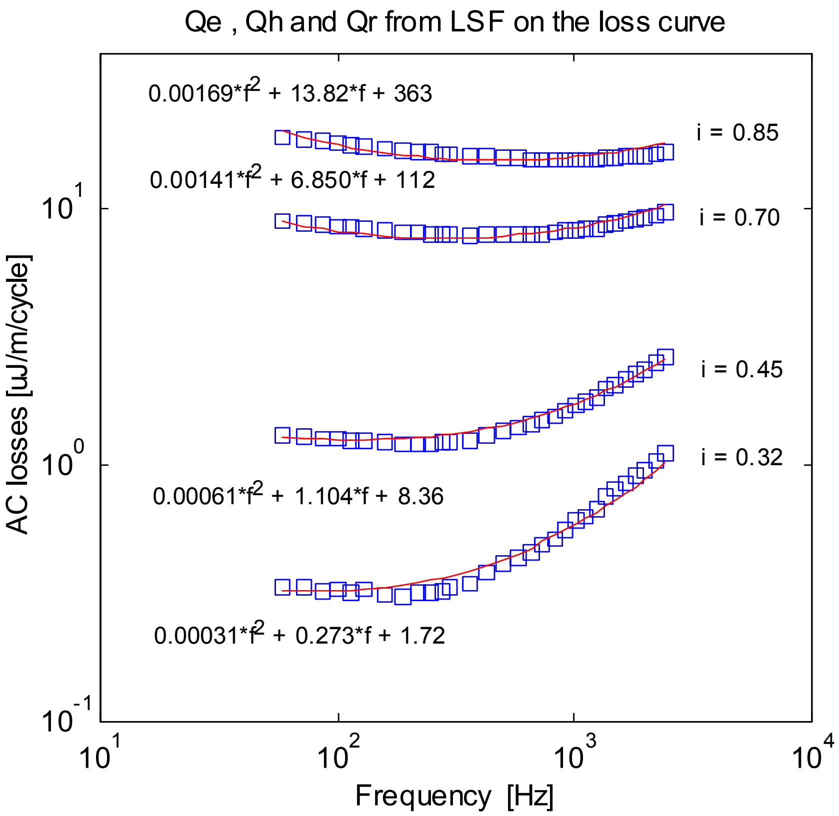

Figure 3-7 Least-squares fit (solid line) to the experimental loss data (square symbols) for different values of *i* for BICC-44, a monofilamentary/Ag tape with $I_c = 15.5$ A.

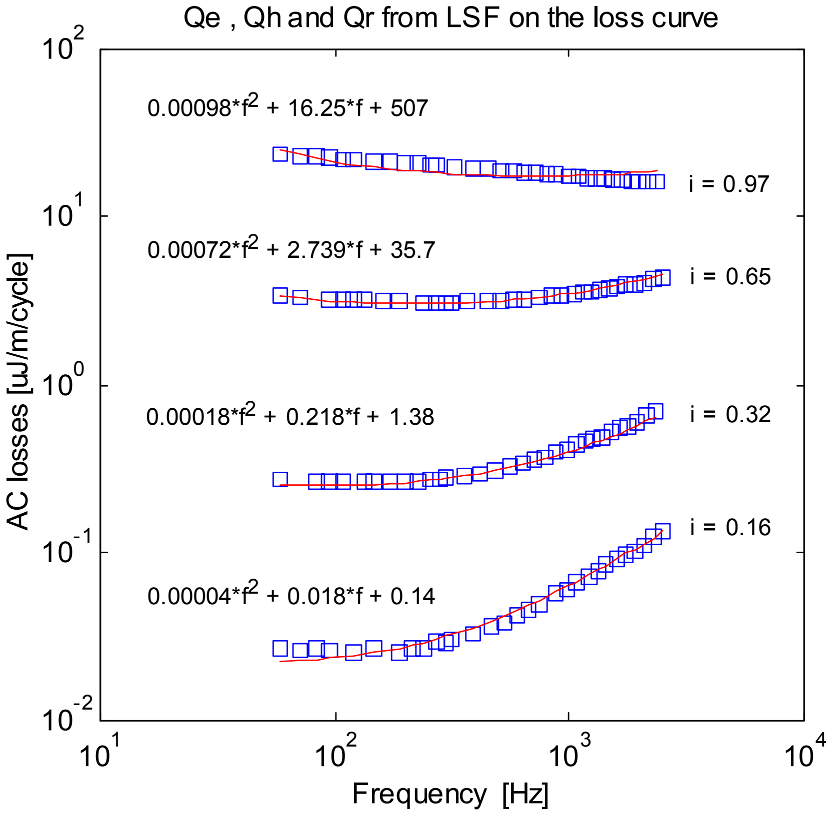

Figure 3-8 Least-squares fit (solid line) to the experimental loss data (square symbols) for different values of *i* for BICC-23, a 7-filamentary/Ag tape with $I_c = 12.4$ A.

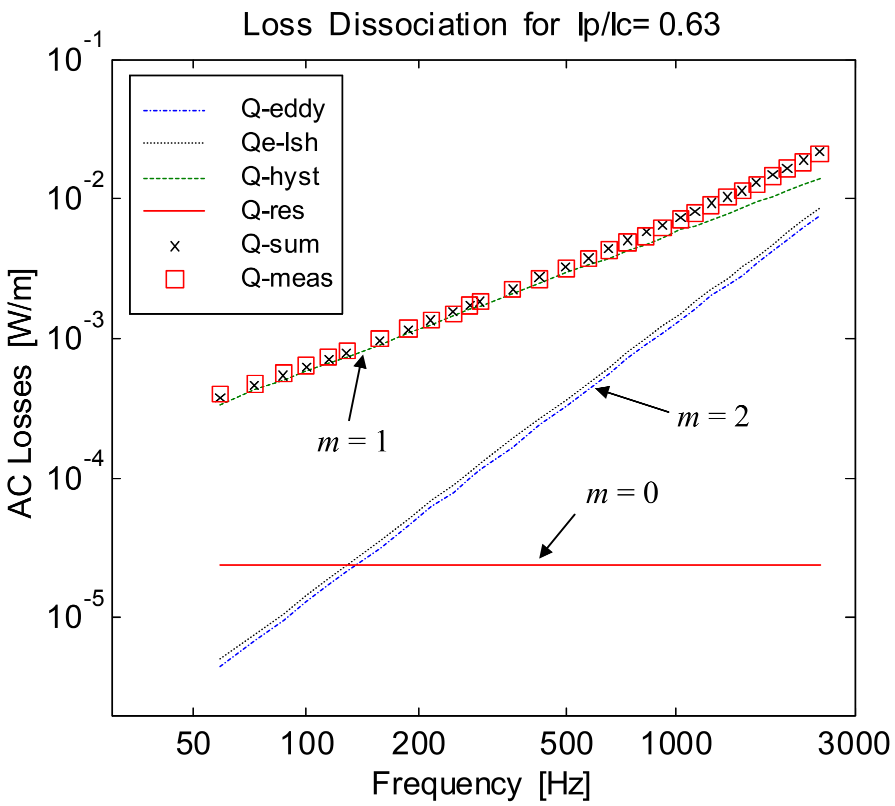

Figure 3-9 Dissociated loss contributions for BICC-56, a monofilamentary/Ag tape with I_c = 19.2 A. *m* indicates the slope of the hysteresis, eddy current and resistive losses.

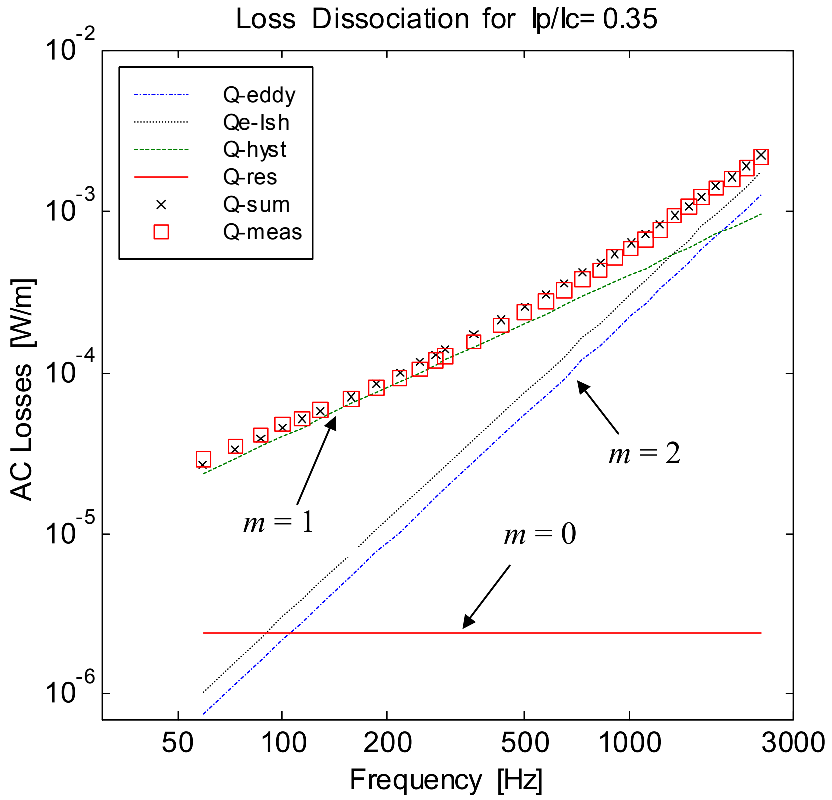

Figure 3-10 Dissociated loss contributions for BICC-19, a 7-filamentary/AgMgNi tape with I_c = 17.1 A. *m* indicates the slope of the hysteresis, eddy current and resistive losses.

The principle of loss dissociation is also illustrated in Fig. 3-9 and Fig. 3-10, where plotted are the hysteresis loss (Q-hyst), the eddy current loss (Q-eddy), and the resistive loss (Q-res) as obtained by the least-squares fit. Shown is the sum of the three contributions (Q-sum) and the measured loss (Q-meas) as well, for comparison with the model. In addition, plotted is also the eddy current loss (Qe-Ish) as calculated from Ishii's approximation $Q_e = (\mu_0 \omega I_p)^2 d^3 / 2\rho L$, where I_p, d and L are respectively the transport current amplitude, sheath thickness, and the length of the perimeter of the outer filament layer, see Eq. (3.10). The graphs are plotted for a given reduced current ratio *i*.

The average fitting error between the measured and the modelled loss for all 14 BICC tapes is around 10 %, which is well within the measurement accuracy (range of the methodological and instrumentation errors) of the AC loss electrical characterization technique [Fri97].

3.4.3 Hysteresis loss

An important advantage of our loss-dissociation model is that we are able to separate the hysteresis loss in the tapes from the total self-field loss that is in principle measured by means of the electrical characterization technique.

In order to assess the significance of the modelled loss dissociation, Fig. 3-11 and 3-12 show the hysteresis loss for the tapes with the same number of filaments, compared to the Norris's predictions for elliptical and strip cross-section. The loss is normalized to the quantity ($\mu_0 I_c^2 / \pi$) to make it independent of the critical current for each tape.

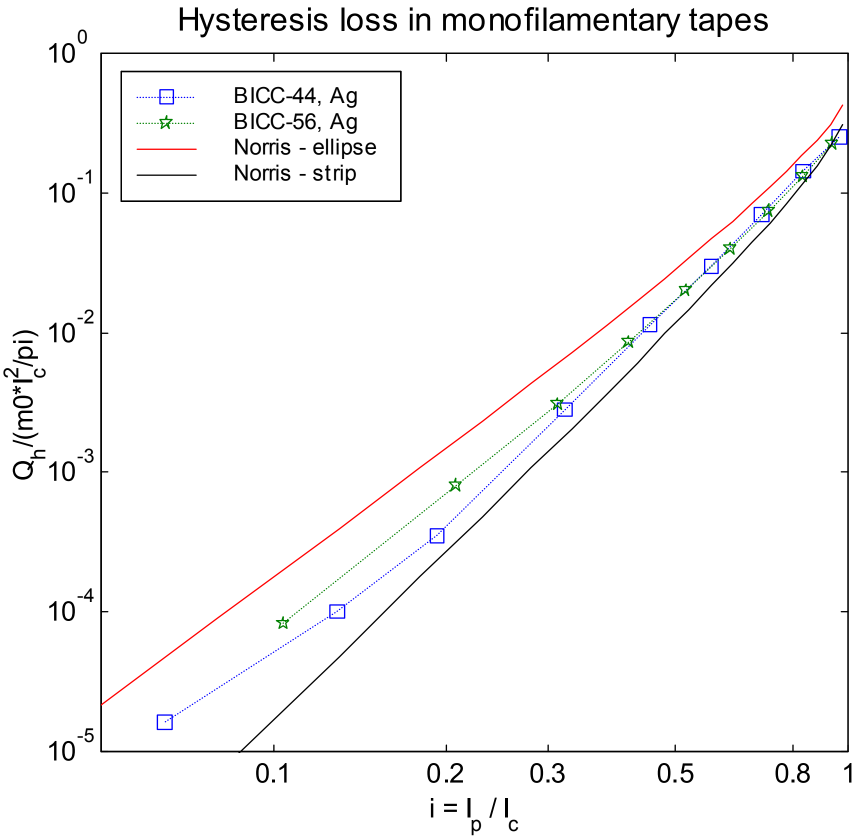

Figure 3-11 Hysteresis loss for monofilamentary tapes, normalized by $\left(\mu_0 I_c^2 / \pi\right)$.

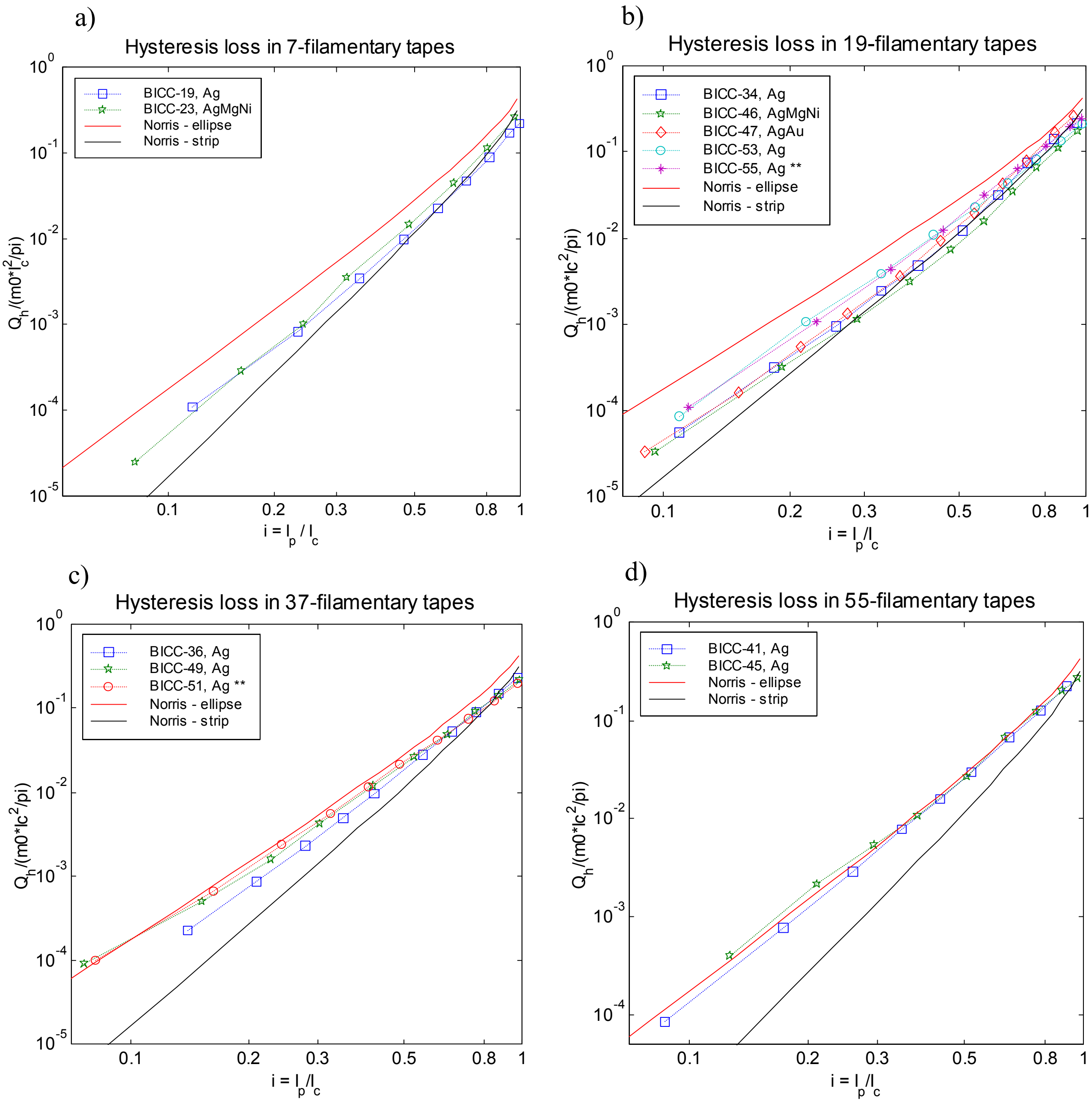

Figure 3-12 Hysteresis loss for multifilamentary tapes, normalized by $\left(\mu_0 I_c^2 / \pi\right)$. BICC-53/55 and BICC-49/51 are samples from the same batch of tapes.

Figures 3-12b and 3-12c show excellent agreement between the compared hysteresis losses in tapes from the same batch (within each batch and for identical heat treatment, the critical currents of the individual tapes vary by no more than 10%). BICC-53/55 and BICC-49/51 are samples from the same batch of 19- and 37-filamentary tapes. BICC-55 and BICC-51 have their sheath's edges polished, which should affect only the eddy current and not the hysteresis loss in these tapes. Indeed, as it is shown in Fig. 3-12b and Fig. 3-12c, the dissociated hysteresis losses for the two pairs of samples from the same batch are practically identical.

Figures 3-11 and 3-12 show no major difference in the hysteresis loss for the sets of 1, 7, 19, 37 and 55-filamentary tapes, so that it is possible to compare the tapes with different number of filaments as shown in Fig. 3-13. In general, the hysteresis loss for the measured BICC tapes cannot be exactly matched by either of Norris's predictions. The only exception is the higher hysteresis loss in the 55-filamentary tapes. Both BICC-41 and BICC-45 (55-Ag tapes) fall very closely on the Norris curve for elliptical cross-section for all values of *i*. In a review of the influence of the conductor architecture on the transport AC loss, Glowacki *et al.* have shown that most of the published and their own data for multifilamentary tapes fall closer to and onto the higher-loss elliptical prediction, see Section 3.3.1 and [Glo97]. On the other hand, the preferred operating current most power applications would be around 0.6-0.7 of I_c, where the loss for a strip is nearly 50 % of that for an elliptical geometry. It is readily seen from the plots in Fig. 3-12a and Fig. 3-12b that for $i > 0.5$ the hysteresis loss for the 7- and 19-filaments is closer to the lower-loss strip prediction, while the losses for the 37-filamentary tapes (Fig. 3-12c) remain between the two Norris's curves. Lower self-field loss for 7-filamentary tapes in comparison with 19- and 37-filamentary tapes have been reported in [Ina99] and [Fri97], which has been explained by the filament configuration in multifilamentary tapes. In some 7-filamentary tapes, three almost disconnected sections can be created (see Fig. 3-5 as well), while in 19, 37 and 55-filamentary tapes the filaments interleave and form a bundle, which is completely coupled in self-field and behaves like a monocore tape.

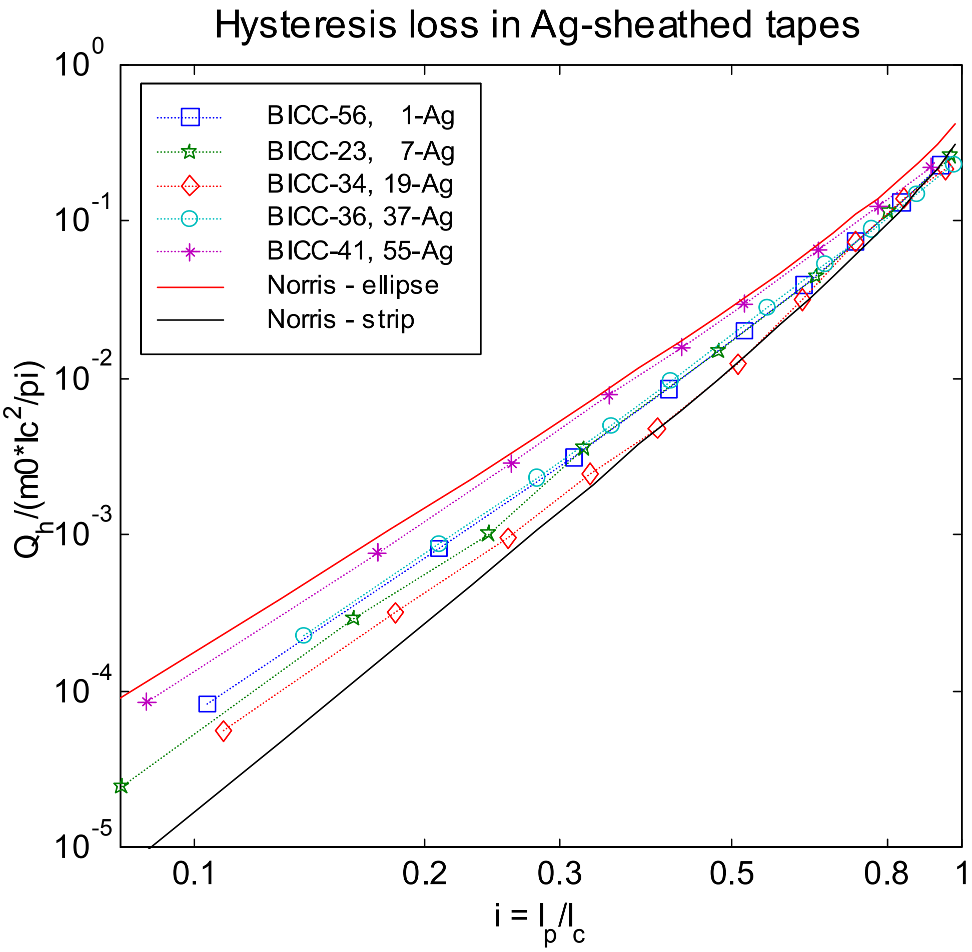

Figure 3-13 Normalized hysteresis loss for tapes with different number of filaments.

The reasons for which the measured hysteresis self-field losses do not appear to match exactly either of the CSM-based Norris's strip and elliptical predictions, but rather fall in-between, can be summarized as follows [Fri97]:

(a) The CSM assumes J_c is constant along the whole width of the superconductor. This is not the case in Bi-2223 tapes. The influence of the lateral J_c distribution on AC losses in multifilamentary tapes is described in details in Section 4.8.

(b) Powder-in-tube Bi-2223 tapes have a cross-sectional geometry, which is not exactly elliptical neither rectangular in shape. The influence of the geometry on self-field AC losses is treated in details in [Yan96].

(c) A very small phase-angle error in the lock-in calibration may result in a large measurement error in the AC loss, especially at low values of i.

(d) The loss equation for a thin strip in self-field assumes an infinitesimally small thickness of the sample. As mentioned by Norris, there may be additional loss for low currents for samples of finite thickness.

(e) In certain filament configurations, the filaments are never completely coupled and some of the inner filaments may carry current independently of the others. In other configurations, where the coupling is full, the inner filaments are effectively screened by the outside ones from the self-field, and strong skin-like effects may be observed.

3.4.4 Flux-creep resistive loss near I_c

The relative weight of the frequency independent loss term in Eq. (3.11), attributed to resistive flux-creep loss is shown in Fig. 3-14 for several BICC tapes with different number of filaments. As can be seen from the figure, the relative weight of the resistive loss for each tape at 59 Hz is almost constant for $i < 0.8$ and is around 5-10 %. The general model of loss dissociation from Eq. (3.11) 'forces' a second-order fit to the loss curve. Therefore, the frequency-independent term Q_r appears even at low values of i. The weight of this loss-term disappears quickly as the frequency is increased (c.f. Figs. 3-9 and 3-10) and is negligible above 100 Hz. The resistive loss has no physical meaning for low currents at 59 Hz, which is the lowest frequency in the fitting procedure, thus with highest proportion of Q_r in the total loss. At values of i around 0.7-0.8 at 59 Hz, however, there starts an increase in the contribution of the resistive loss component, which reaches 35-40 % near I_c. This loss at high currents has a physical meaning, since when I_p is close to I_c flux lines start to move in the BSCCO crystals, and resistive voltage is induced. The appearance of flux-creep and flux-flow loss at currents near and above I_c has been explained in Section 2.3.1 and discussed also in Section 3.4.1.

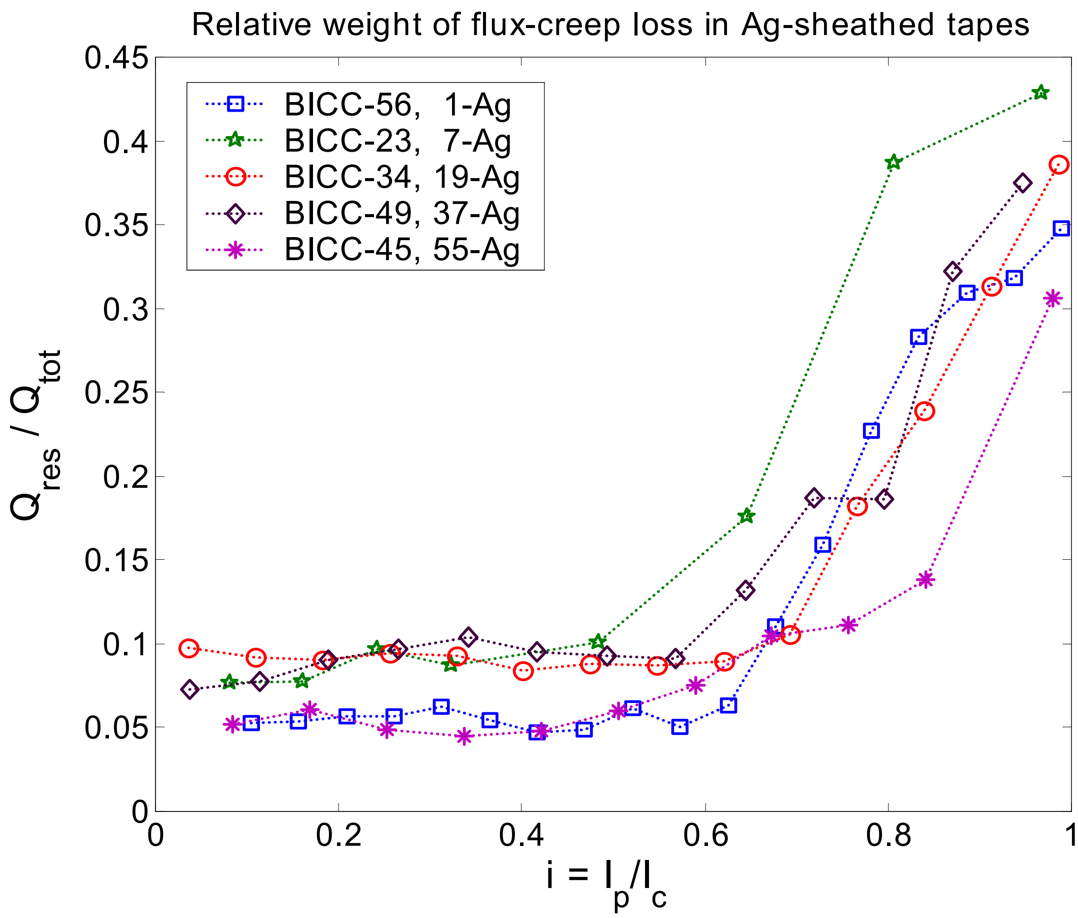

Figure 3-14 Relative weight of the flux-creep resistive loss with respect to the total self-field loss at 59 Hz for several Ag-sheathed tapes.

3.5 Eddy current loss in self-field

3.5.1 Measured eddy current loss in Bi-2223 tapes

An overview of the theoretical and empirical derivations for eddy current loss in self-field was given in Section 3.3.2. The measured eddy current loss, obtained from the AC loss dissociation model in Eq. (3.11) for all BICC tapes is of the same order of magnitude as the approximation, given by Ishii, $Q_e = (\mu_0 \omega I_p)^2 d^3 / 2\rho L$, see Fig. 3-9 and Fig. 3-10. That is why we have compared the dissociated eddy-current loss component with Ishii's empirical formula.

Figures 3-15 and 3-16 show the eddy current loss for the mono and multifilamentary tapes, respectively. In fact, plotted is the eddy current loss-factor Q_{ed} (Jm^{-1}Hz^{-2}), which multiplied by f^2 yields the eddy current loss in W/m. The measured eddy current loss has the same I_p^2-current dependence as in Ishii's approximation. A deviation from the I_p^2-

dependence is observed only when $I_p \to I_c$, where other loss mechanisms are dominating and the superconductor is in transition to its normal state.

The relative weight of the eddy-current loss with respect to the total self-field loss in the range 59–2500 Hz for 5 tapes with different filament number is shown in Fig. 3-17 for increasing values of *i*. The proportion of the eddy current loss strongly depends on the applied-to-critical current ratio – the lower *i*, the higher the relative eddy-current contribution. Fig. 3-17a shows that for very low *i*, the eddy currents have a significant contribution (more than 10 % of the total loss) even below 100 Hz for some of the tapes. For $i \sim 0.3$ the loss is more than 20 % only for $f > 300$ Hz (see Fig. 3-17b); for $i \sim 0.6$ the loss is completely negligible (less than 5 %) at $f < 200$ Hz for all tapes (see Fig. 3-17c); and for $i > 0.8$ the eddy current loss does not have a dominating role in the whole frequency range – less than 25 % even at 2.5 kHz.

The reason for the decreasing contribution of eddy current loss with *i* is in fact the increasing contribution of the hysteresis loss at higher applied currents – $Q_{hyst} \sim I_p^{3-4}$ between Norris's strip and elliptical predictions, while $Q_{eddy} \sim I_p^2$ in the theoretical calculations and the measured loss. In addition, there is an increasing contribution of resistive flux-creep loss near I_c (see Fig. 3-14).

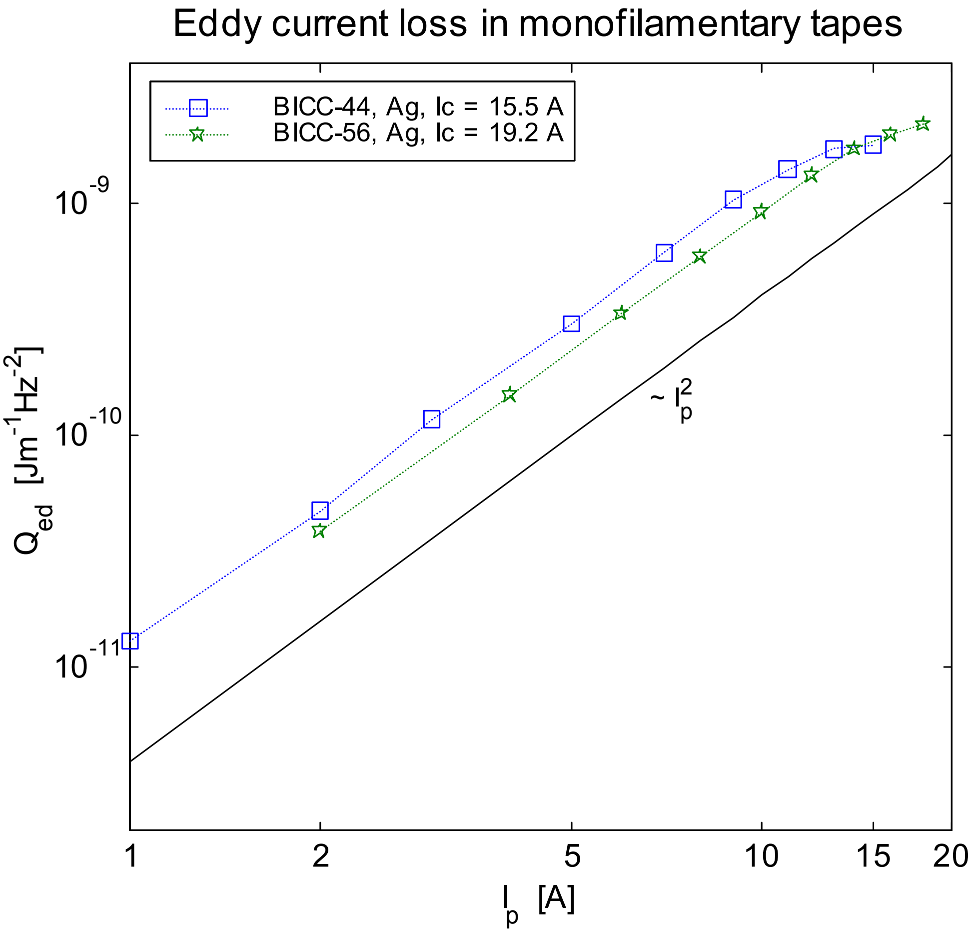

Figure 3-15 Eddy current loss factor for monofilamentary tapes.

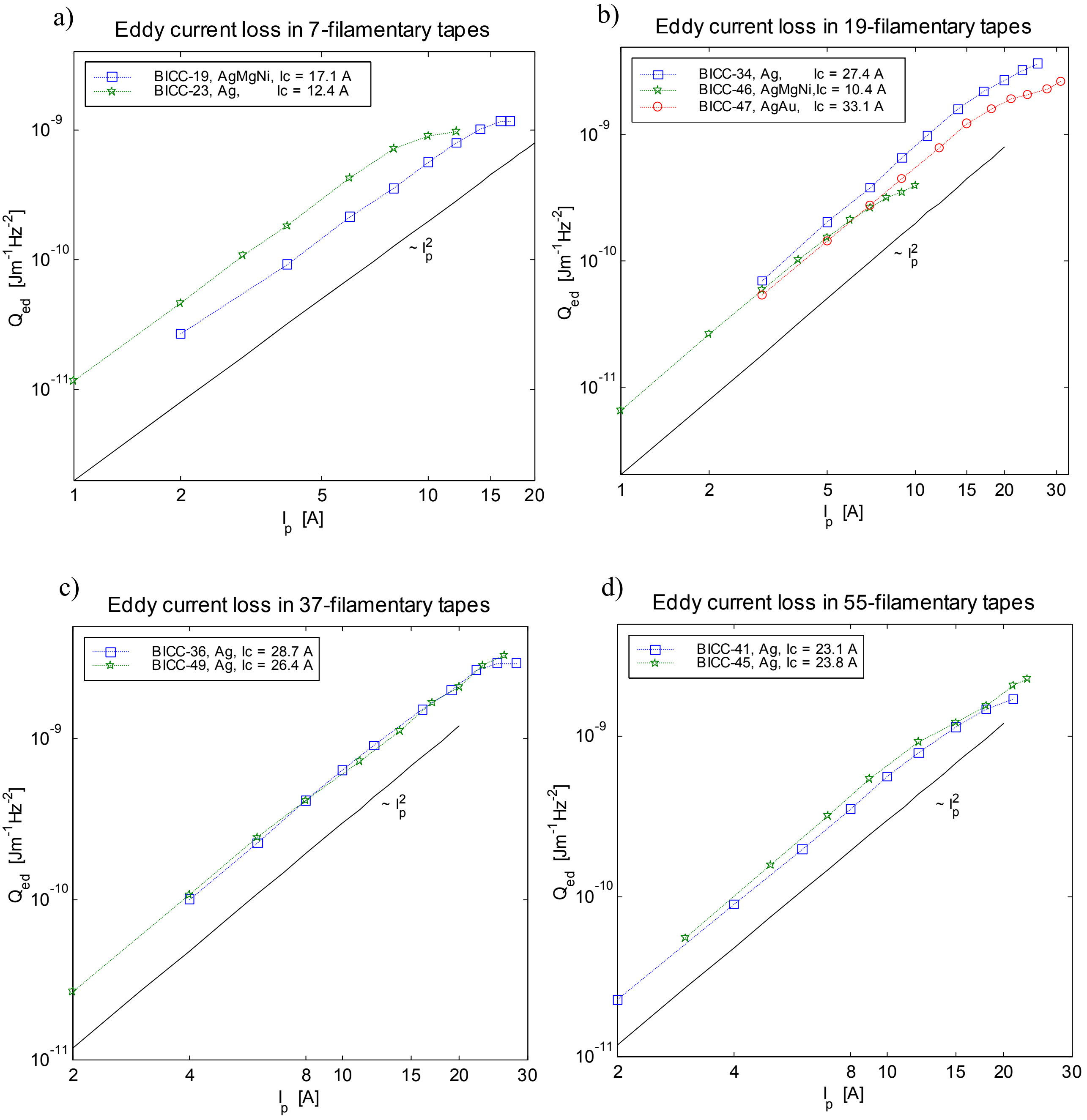

Figure 3-16 Eddy current loss factor for multifilamentary tapes.

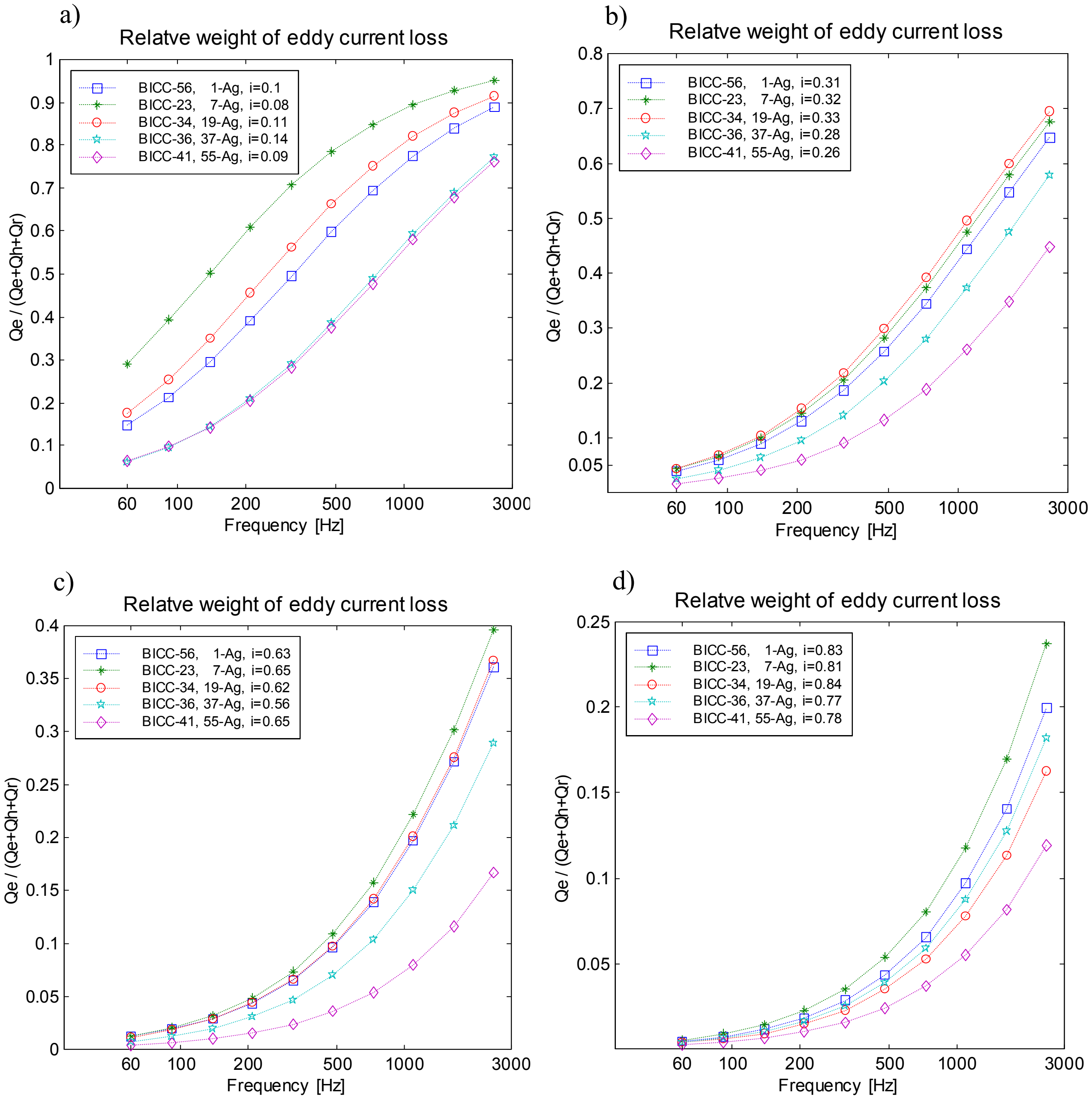

Figure 3-17 Frequency dependence of the relative weight of eddy current loss for different values of *i:* (a) *i* ~ 0.1, (b) *i* ~ 0.3, (c) *i* ~ 0.6, (d) *i* ~ 0.8.

3.5.2 Numerical modelling of eddy current loss

In order to evaluate the magnitude of the eddy current loss by other means, in addition to the method of the loss-dissociation model from self-field measurements, we have made electromagnetic simulations of eddy currents in BSCCO tapes.

Basic electromagnetic equations for HTS

The general Maxwell's equations express the electromagnetic properties of a given material and describe the relations between the electrical field **E**, magnetic field **H**, magnetic flux density **B,** and the current density **J**:

Ampere's law, $$\nabla \times \mathbf{H} = \mathbf{J} + \frac{\partial \varepsilon_0 \mathbf{E}}{\partial t} \tag{3.12}$$

Faraday's law, $$\nabla \times \mathbf{E} = -\frac{\partial \mathbf{B}}{\partial t} \tag{3.13}$$

Gauss's law, $$\nabla \cdot \varepsilon_0 \mathbf{E} = \rho_c \tag{3.14}$$

and $$\nabla \cdot \mathbf{B} = 0 \tag{3.15}$$

where ρ_c is the free charge density and ε_0 is the permittivity of vacuum, 8.85×10^{-12} F/m.

The constitutive properties of the material are added to the above equations:

Ohm's law: $$\mathbf{J} = \sigma \mathbf{E} \tag{3.16}$$

and $$\mathbf{B} = \mu \mathbf{H} \tag{3.17}$$

where $\mu = \mu_r \mu_0$ with μ_r the relative permeability of the material and $\mu_0 = 4\pi\times10^{-7}$ H/m. For type-II superconductors (see also Fig. 2-6), Eq. (3.17) can be approximated above H_{c1} by:

$$\mathbf{B} = \mu_0 \mathbf{H} \tag{3.18}$$

and the electrical displacement current in Eq. (3.12) can be neglected [Bra96b].

The current continuity condition then follows from Ampere's law (3.12):

$$\nabla \cdot \mathbf{J} = 0 \tag{3.19}$$

Finite element method modelling of HTS

As it was explained in Section 2.3.2 and Section 3.3.2, eddy currents are induced by time-varying magnetic fields, and the exact solution for the eddy current loss is available only for simple geometries. The equation of flow of induced currents is:

$$\nabla^2 \mathbf{J} = \sigma \mu \frac{\partial \mathbf{J}}{\partial t} \tag{3.20}$$

For the 2D solution of Eq. (3.20) and the calculation of eddy current loss in HTS tapes we have employed numerical analysis [Nib97]. The finite element method (FEM) software package Flux2D has been used [Flux2D]. The numerical computation is performed using the **A**-V formulation of Maxwell's equations, in which the introduction of the magnetic vector potential **A**, defined from $\mathbf{B} = \nabla\times\mathbf{A}$, in Ampere's laws leads to the following state equation to be solved:

$$\nabla\times\left(\frac{1}{\mu}\nabla\times\mathbf{A}\right)=\mathbf{J} \tag{3.21}$$

The main difficulty in the numerical modelling of HTS is the nonlinear conductivity in Ohm's law of such materials. An introduction to the finite element method is given in Appendix B, and more details about FEM modelling and the **A**-V formulation in Flux2D are given in Section 4.4 and Section 4.5, respectively.

Simplified electrical model of BSCCO tapes with applied transport current

The primary goal of this study was the evaluation of eddy current loss in the metal sheath/matrix of Bi-2223 tapes. For this reason the nonlinear hysteretic behaviour of the BSCCO core was not taken into account. We have used the simplified electrical model shown in Fig. 3-18 for the simulation of applying a transport current through a Bi-2223 tape and the resulting self-field effects [Nib98].

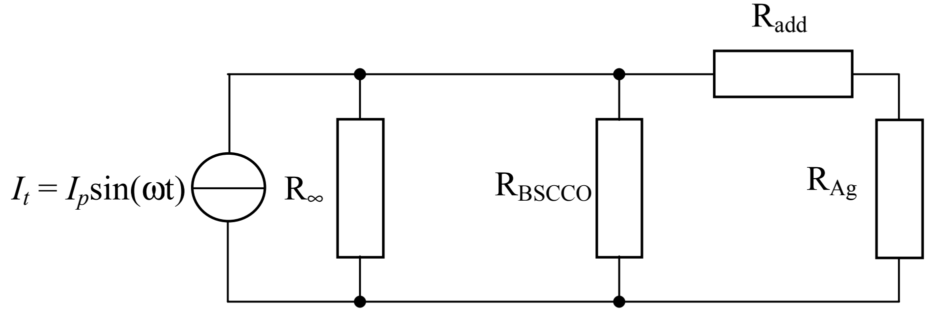

Figure 3-18 Electrical model of a BSCCO tape used in FEM simulations.

The simulated system is a Bi-2223 tape. The model consists of a superconducting core (mono or multifilamentary) in parallel with the Ag (Ag-alloy) sheath. The tape is characterised by means of the resistivity for each material (Ag and BSCCO). The simulation set-up consists of a current source, which is connected to two parallel massive conductors, respectively the BSCCO core and the Ag sheath. Both materials are assumed to be isotropic. The main parameters of the electromagnetic simulation are the resistivity ρ of each material, as well as the amplitude and the frequency of the transport current. There is neither a current nor a magnetic field inside the tape prior to applying the AC transport current (zero initial conditions). The relationship between **B** and **H** is considered linear – $\mathbf{B} = \mu_0\mathbf{H}$, i.e. the relative permeability of the superconductor has been given the value of 1. The effective resistance of the tape is calculated from the total measured loss in genuine Bi-2223 tapes for different values of the applied current:

$$\mathrm{R_{eff}} = \frac{P_{total}}{I_{rms}^2} \tag{3.22}$$

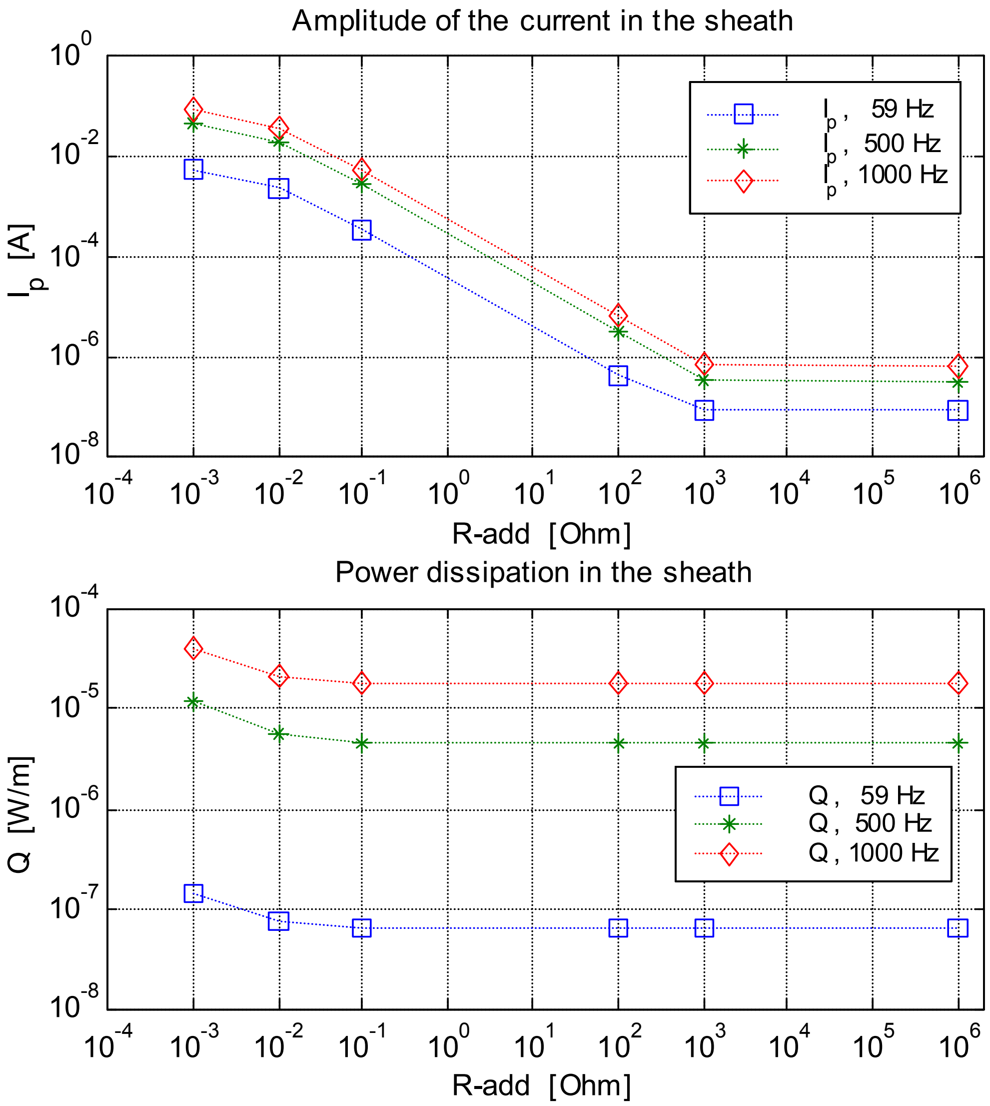

Figure 3-19 Current amplitude and power dissipation in the metal sheath at frequency of 59 Hz, 500 Hz and 1000 Hz for increasing values of R_{add}. The peak transport current is 10 A.

Knowing the cross-sectional geometry of the tape, as well as the measured resistivity of the Ag sheath at 77 K, the effective resistivity of the superconductor is then calculated from the simple model of two resistors in parallel and the basic relation $\rho = RS / l$. Thus the superconducting core is modelled as a conductor with very low resistivity calculated from the measured total AC loss for a given value of the current amplitude at a given frequency. For example, from the above equation, for a monocore tape of dimensions 2.75×0.32 mm with filling factor 0.40, the effective resistance of the superconductor at 59 Hz and I_p of 4A is calculated to be 1.12 μΩ, while the resistance of the Ag-sheath is 5.3 mΩ. There is a difference of 3 orders of magnitude between the resistance of the superconducting core and the metal sheath. In this way the portion of the transport current flowing through the sheath would be around 1/1000 of the applied transport current. Although in reality there indeed exists a partitioning of the transport current between the core and the sheath, it may be of a smaller magnitude. The calculated power dissipation in the sheath would then inevitably include a resistive portion resulting from the transport current flow. To avoid that, an additional resistance R_{add} with a value much higher than R_{Ag} was included in the simulation model (see Fig. 3-18) to make sure that practically no transport current flows in the Ag sheath and all the calculated loss in the metal sheath and matrix comes from the eddy currents only:

$$Q = \int_0^{1/f} dt \int_v \mathbf{E} \cdot \mathbf{J} dv \tag{3.23}$$

where v is the volume of Ag.

The effect of the additional resistance R_{add} on the amplitude of the current flowing in the metal and the corresponding power dissipation is shown in Fig. 3-19. Increasing the value of R_{add} from 1 mΩ to 1 MΩ leads to a decrease in the current amplitude in the metal from the mA to µA-range. The power dissipation, however, ceases to depend on the current amplitude at $R_{\mathrm{add}} = 0.1\ \Omega$. That is why selecting a value of $R_{\mathrm{add}} \geq 0.1\Omega$ assures that the total power dissipation in the sheath and matrix, calculated by Eq. (3.23), is due to eddy current flow only and does not result from any transport current in the Ag.

Current density and magnetic field profiles in the BSCCO core

The eddy current loss distribution in the sheath depends on the current density and magnetic field profiles in the BSCCO tape. In order to evaluate the relevance of the obtained power loss distribution, we have made a comparison between the simulated current density and magnetic field distributions in the BSCCO core with the analytical expressions for a HTS strip of infinitesimal thickness and constant J_c with applied transport current, given by Brandt *et al.* [Bra93]:

$$J(x) = \begin{cases} \dfrac{2J_c}{\pi} \arctan\left(\dfrac{a^2 - c^2}{c^2 - x^2}\right)^{1/2} & for \quad |x| < c \\ J_c & for \quad c < |x| < a \end{cases} \tag{3.24}$$

and

$$H(x) = \begin{cases} 0 & for \quad |x| < c \\ \dfrac{H_c x}{|x|} \arctan\mathrm{h}\left(\dfrac{x^2 - c^2}{a^2 - c^2}\right)^{1/2} & for \quad c < |x| < a \\ \dfrac{H_c x}{|x|} \arctan\mathrm{h}\left(\dfrac{a^2 - c^2}{x^2 - c^2}\right)^{1/2} & for \quad |x| > a \end{cases} \tag{3.25}$$

where a is the half-width, c the penetration depth of the self-field in the strip and $H_c = J_c / \pi$.

Brandt's analysis is one-dimensional and the quantity J_c is given in A/m. In order to obtain the same dimension, the current density J (A/m^2), computed in our FEM simulations, has been integrated along the thickness of the tape. The results of the comparison between the simulated and analytical current and field profiles are shown in Fig. 3-20 for reduced current ratio $i = 0.25$ and $i = 0.5$. As can be seen, the results from the simulations are very close to the theoretical current density and magnetic field distributions and this has confirmed the aptitude of using the simplified electrical tape model from Fig. 3-18. However, for values of $i \geq 0.5$, even though the magnetic field profile remains close to the analytical one, there is an increased current density at the edge of the superconductor because of the skin-effect and the fact that J_c is not defined in this FEM model; J exceeds J_c (I_c / S) near the edge and the normalized current density curve has a peak much higher than 1.

Therefore, the value of the transport current amplitude, which has been used in all simulations presented further on, is 4 A; this means i is always < 0.5, i.e. the simulated field and current density in the BSCCO core is close to the analytical ones, since all simulated tapes have critical currents higher than 10 A.

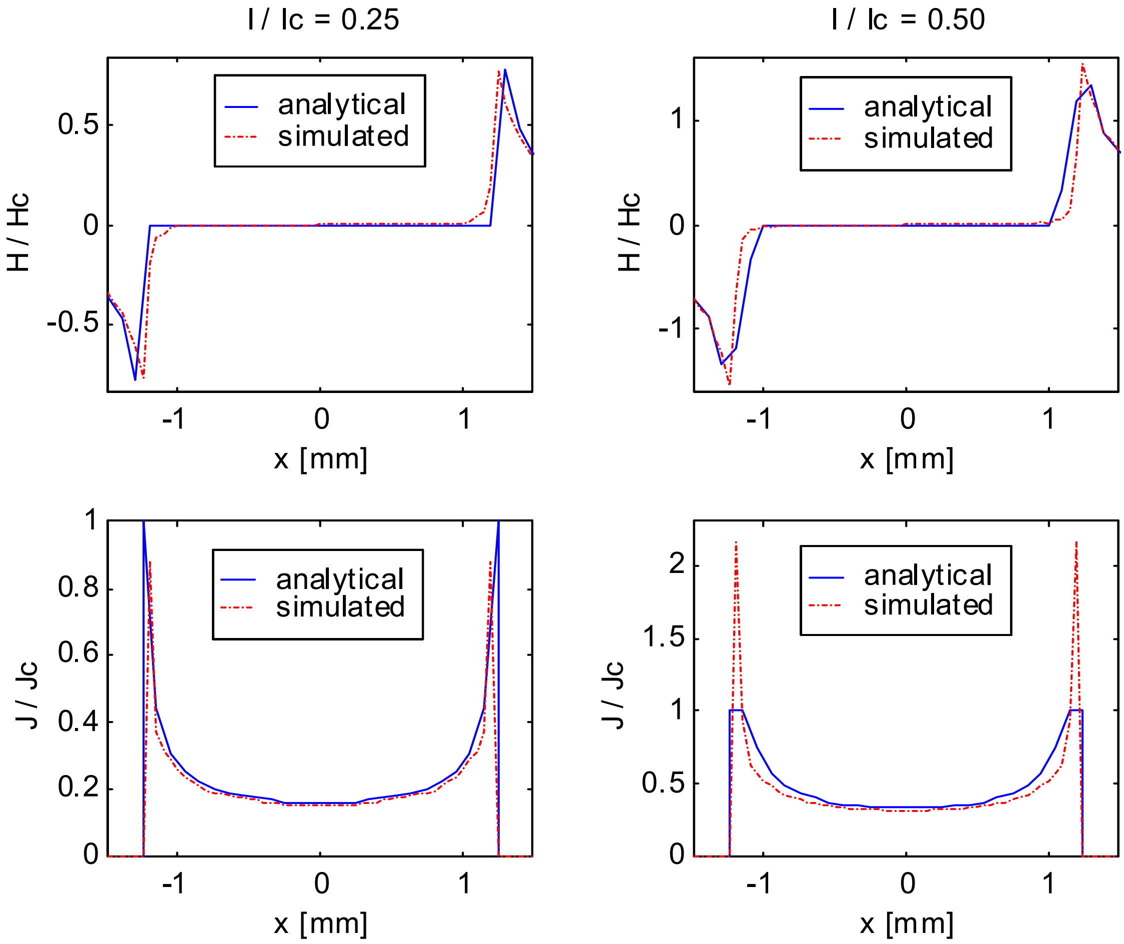

Figure 3-20 Comparison between Brandt's (analytical) and FEM (simulated) magnetic field and current density distributions for two values of the reduced current ratio.

Simulated eddy current loss in Bi-2223 tapes

The effect of eddy currents inside the Ag sheath and matrix has been evaluated for several frequencies – 59 Hz, 500 Hz and 1 kHz. FEM simulations have been performed on 1, 7, 19 and 37-filamentary tapes, which have dimensions and cross-sectional geometry similar to the real tapes whose AC loss has been measured and described in Section 3.4. Cross-sections of tapes used in the FEM simulations are shown in Fig. 3-21.

a) monofilamentary tape

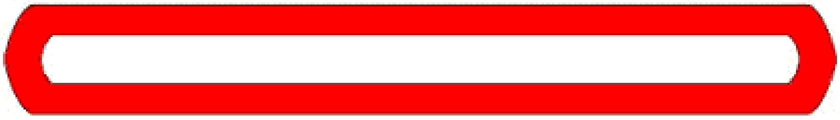

b) 7-filamentary tape

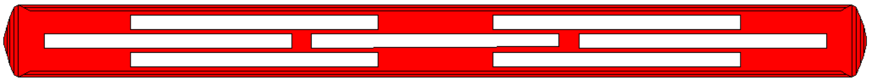

c) 19-filamentary tape

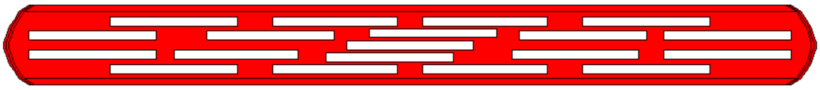

d) 37-filamentary tape

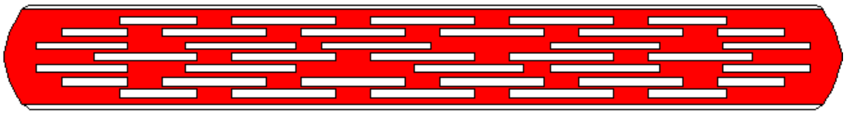

Figure 3-21 Cross-sectional geometry of BSCCO tapes used in the FEM simulations.

Figure 3-22 shows the density distribution of the dissipated power (eddy current loss) in the metal sheath for the simulated monofilamentary BSCCO tape at 59 Hz and 1 kHz. The eddy current loss is much higher at 1 kHz. Most of the power is dissipated in the sheath edge, close to the Ag-BSCCO interface, where the magnetic self-field has highest amplitude. This suggests that the width of the tape's edge is probably one of the important geometric parameters for the eddy current loss magnitude.

a) f = 59 Hz

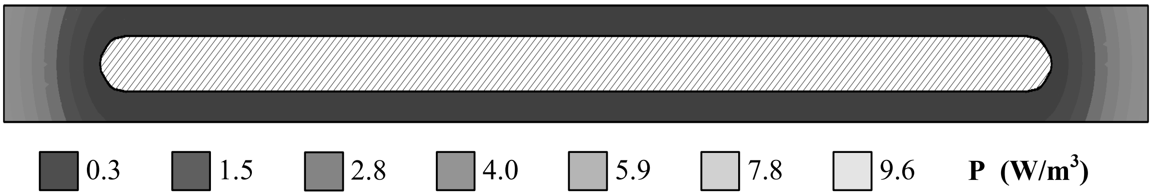

b) f = 1 kHz

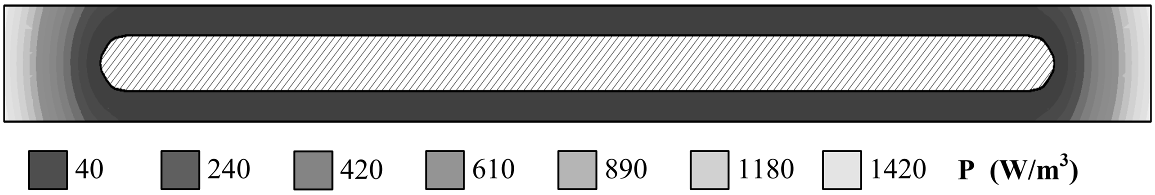

Figure 3-22 Power dissipation due to eddy currents in the Ag-sheath in a monofilamentary tape at peak applied current at 59 Hz (a) and at 1 kHz (b).

3.5.3 Comparison between measured, simulated and empirically derived eddy current loss

Effect of the tape geometry on the eddy current loss

The eddy current loss, calculated with Ishii's approximation – $Q_e = (\mu_0 \omega I_p)^2 d^3 / 2\rho L$ – has a very strong dependence on the sheath thickness *d*. For those BICC tapes, whose sheath thickness is 120 – 160 μm (see Table 3-1), the measured eddy current loss falls in accord with Ishii's empirical approximation within a factor of two, which is a relatively good match (c.f. Fig. 3-9 and Fig. 3-10). For the tapes with thinner sheath, however, the dissociated eddy current loss differs considerably from the calculated one.

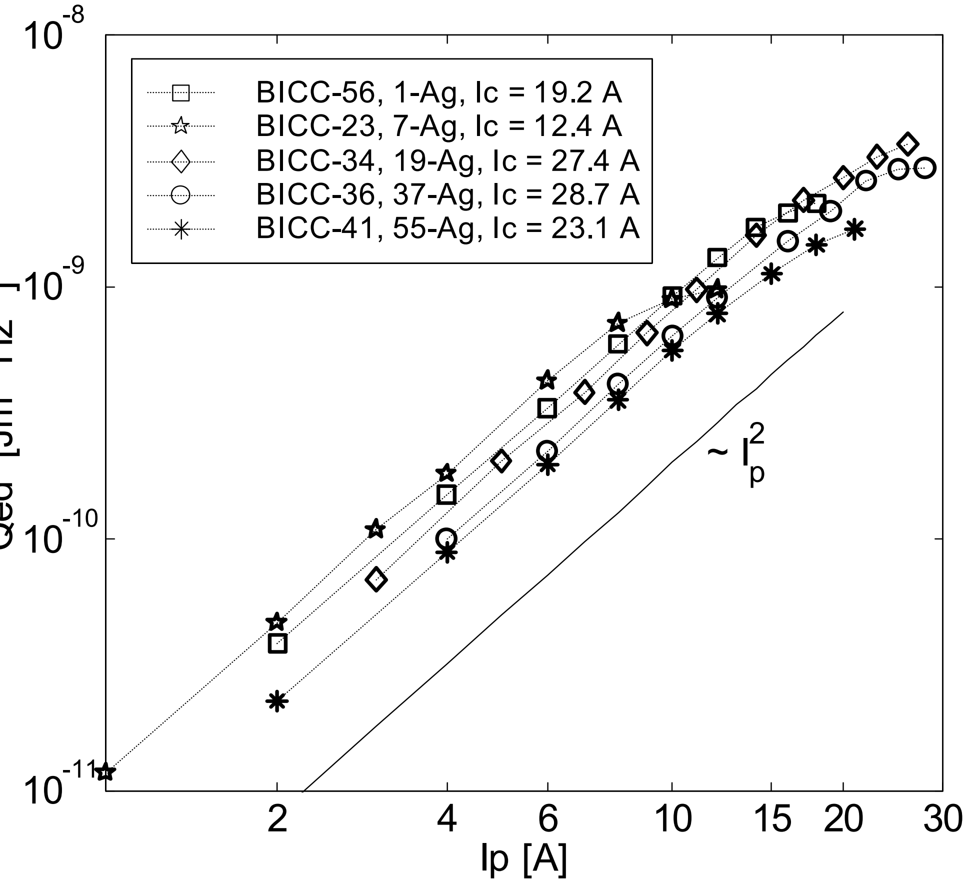

Figure 3-23 Eddy current loss factor, obtained from measurements of Ag-sheathed tapes with different number of filaments.

The measured eddy current loss for five Ag-sheathed tapes with different filament number is plotted in Fig. 3-23 as a function of the transport current amplitude. BICC-23 has similar sheath thickness as BICC-41, but exhibits much higher eddy current loss factor, which leads to the conclusion that the most important geometric parameter for the eddy current loss is not the thickness of the sheath. As suggested by the power density distribution, shown in Fig. 3-22, it is the width of the sheath edge, which influences most significantly the eddy current loss in the Bi-2223 tapes. Indeed, as shown in Fig. 3-23, BICC-23 and BICC-56 tapes, which have the largest edge-width of the sheath, exhibit the highest eddy current loss; see also

Table 3-1. This is also in accord with results from the FEM simulations, shown in Fig. 3-24 for 1, 7, 19 and 37-filamentary tapes. Note also that all simulated losses have a slope of 2 on a log-log frequency-loss plot, which is exactly the expected f^2-dependence, and proves that the power dissipation in the sheath in the FEM simulations is a result from eddy current flow and not from transport current flow (any resistive loss from the latter would have been frequency independent).

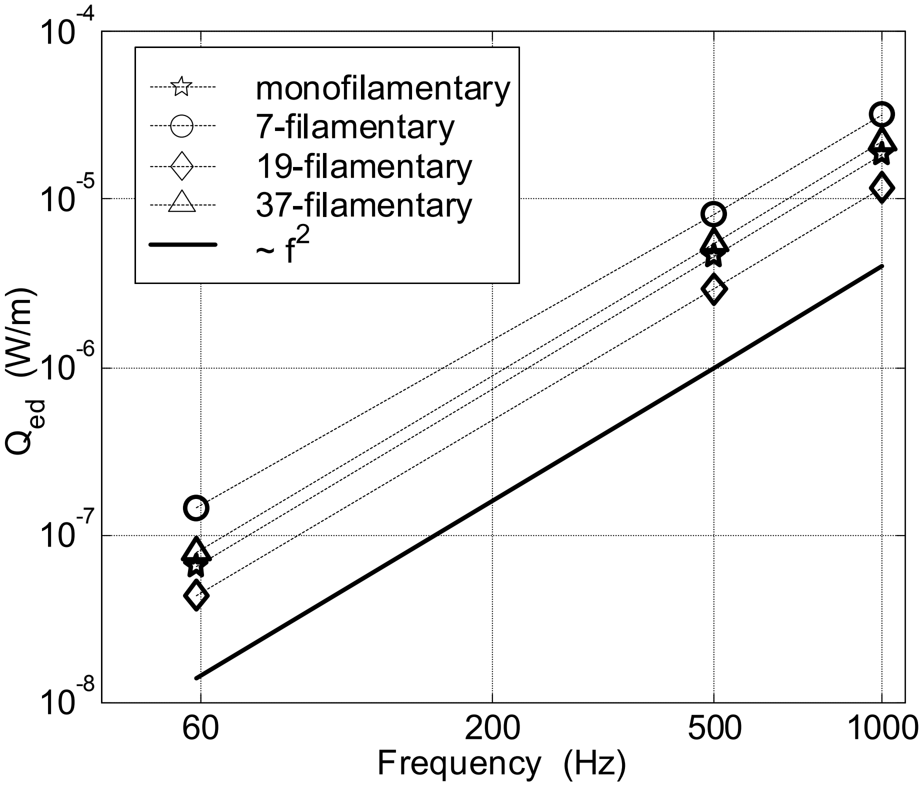

Figure 3-24 Frequency dependence of the eddy current loss, obtained from FEM simulations of Ag-sheathed tapes with different number of filaments.

In order to evaluate quantitatively by FEM simulations the influence of the sheath geometry on the eddy current loss, we have varied the edge width and the thickness of the sheath for the 37-filamentary tape. The effect of this geometry variation on the density of the eddy current loss dissipation is shown in Fig. 3-25. The 'thin' and 'thick' tapes are obtained by decreasing and increasing the sheath thickness respectively by 1/2 and by 2. And the 'narrow' and 'wide' tapes – by decreasing and increasing the edge width by the same factors (1/2 and 2). The FEM simulation results show clearly that, as in the monofilamentary tape, most of the power dissipation in the sheath occurs at the edges. The highest power dissipation is observed in the tape with a wide edge, see Fig. 3-25e.

The results for the eddy current loss for the 37-filamentary tape with different sheath geometry are shown in Fig. 3-26. Indeed, the edge width is the most important geometry parameter of the tape, determining the magnitude of the eddy current loss. The tape with the large edges has the highest loss, while the tape with the narrow edges has the lowest loss. The decrease/increase of the edge width by a factor of 2 leads to a decrease/increase of the eddy current loss by approximately 200%, while the corresponding effect of decreasing/increasing the sheath thickness is only 20%.

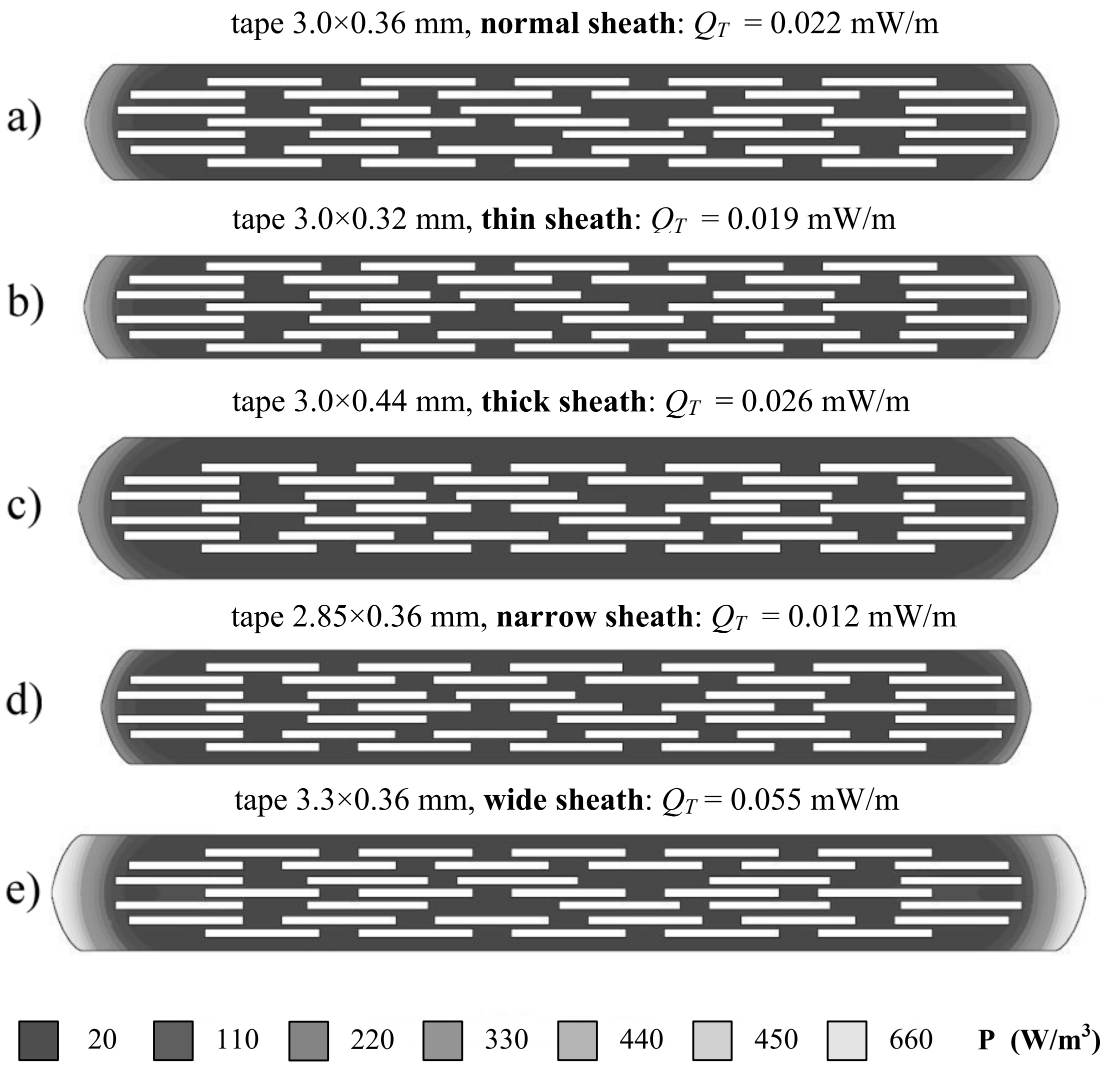

tape 3.0×0.36 mm, **normal sheath**: Q_T = 0.022 mW/m

tape 3.0×0.32 mm, **thin sheath**: Q_T = 0.019 mW/m

tape 3.0×0.44 mm, **thick sheath**: Q_T = 0.026 mW/m

tape 2.85×0.36 mm, **narrow sheath**: Q_T = 0.012 mW/m

tape 3.3×0.36 mm, **wide sheath**: Q_T = 0.055 mW/m

Figure 3-25 Density of the power dissipation (W/m^3) in the Ag sheath for a 37-filamentary tape at peak transport current. Given is also the calculated power loss Q_T (mW/m).

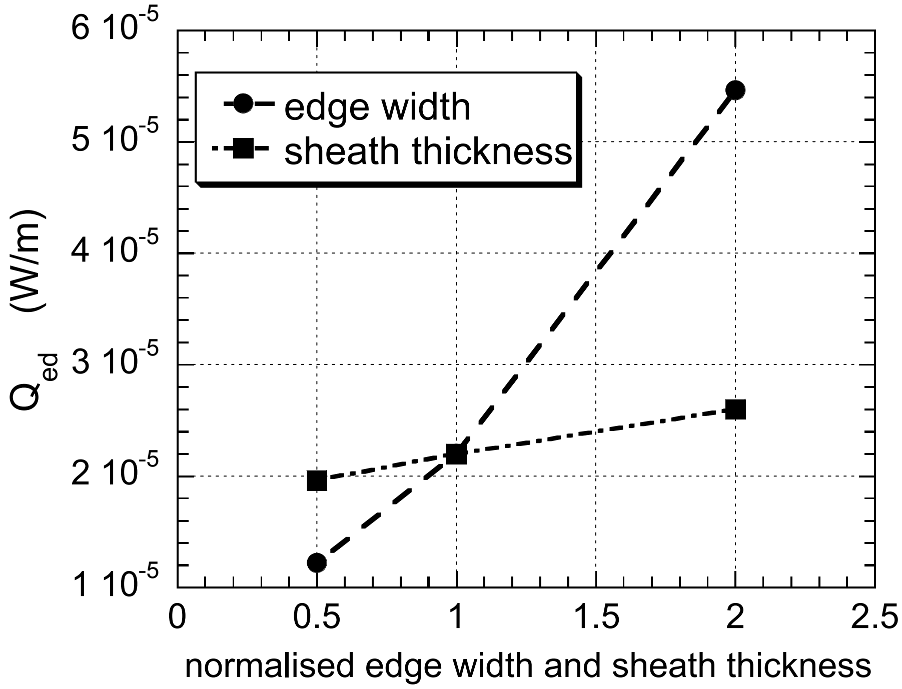

Figure 3-26 Effect of the sheath thickness *d* and the edge width *w* on the eddy current loss in the Ag. The normalized value of the abscissa at 0.5 and 2 correspond respectively to decreasing and increasing the reference tape's *d* and *w* by a factor of 2. See also Fig. 3-25.

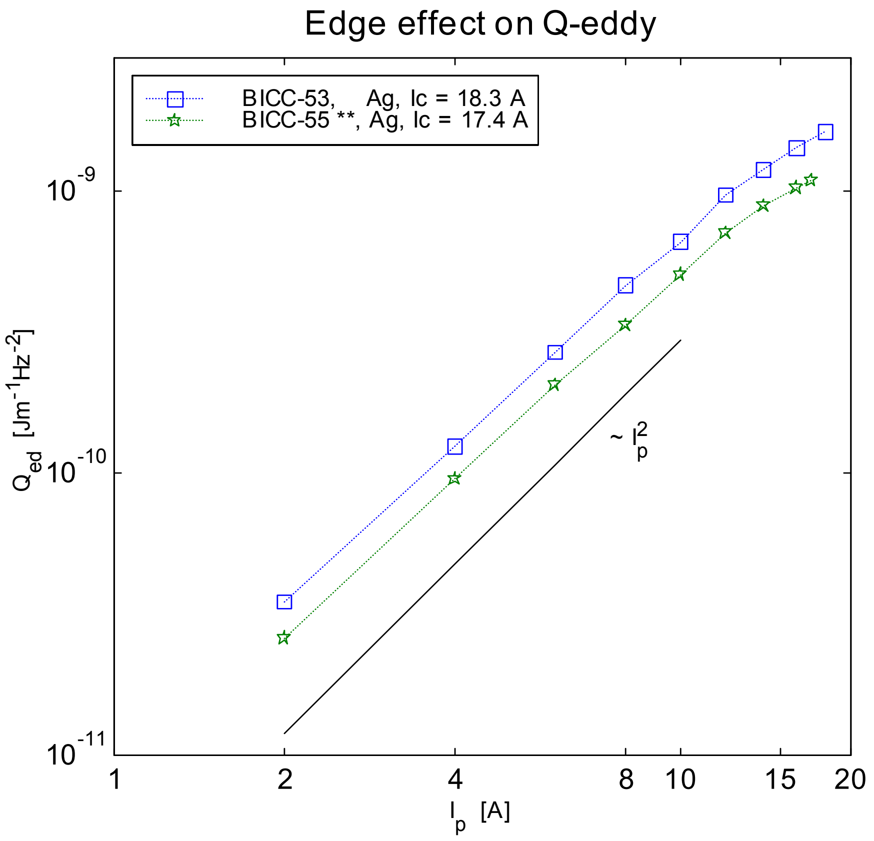

Figure 3-27 Effect of the edge width on the measured eddy current loss in two 19-filamentary tapes of the same batch. BICC-55 has its two edges polished out.

The effect of the sheath's edge-width reduction on the measured eddy current loss is shown in Fig. 3-27 and Fig. 3-28, where the losses for two samples from the same batch are compared (one has the two silver edges polished out). There is a visible loss reduction – a factor of 1.4 for the two pairs, which is somewhat less than the factor of 2, expected from the simulations.

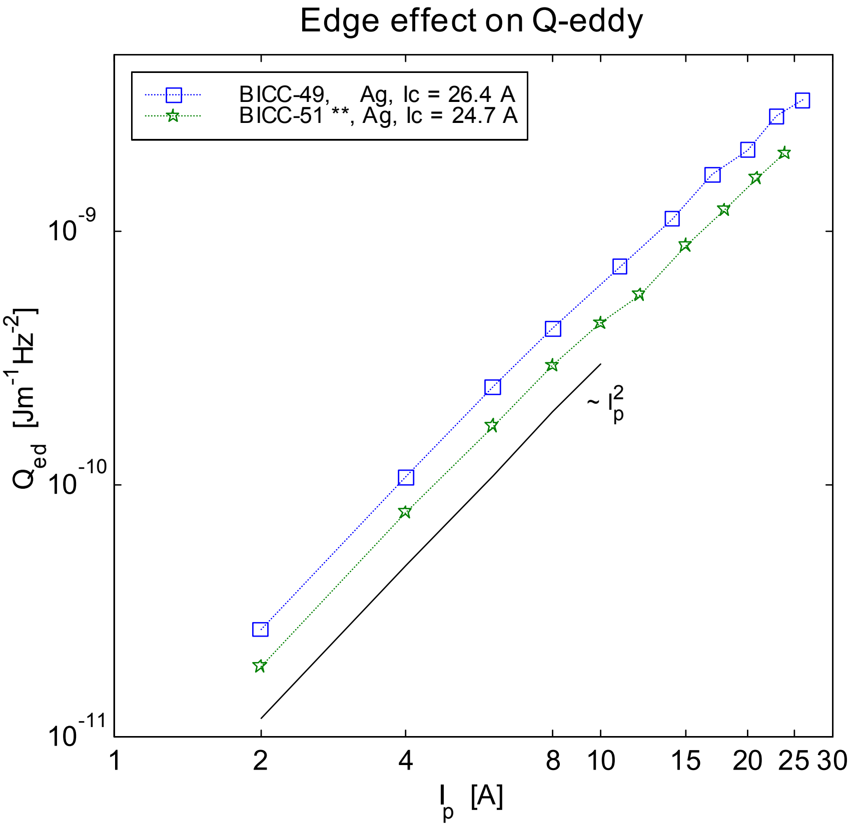

Figure 3-28 Effect of the edge width on the measured eddy current loss in two 37-filamentary tapes of the same batch. BICC-51 has its two edges polished out.

Effect of the sheath resistivity on the eddy current loss

The resistivity ρ of three different annealed materials, used for making the sheath of the Bi-2223 tapes, has been measured by BICC at 77 K: it is $2.6\times10^{-9}\,\Omega\text{m}$ for pure Ag, $12.8\times10^{-9}\,\Omega\text{m}$ for the AgMgNi alloy, and $15.1\times10^{-9}\,\Omega\text{m}$ for the AgAu alloy.

Figure 3-29 displays the results from FEM simulations for the dependence of eddy current loss on the metal sheath resistivity for the 19-filamentray tape. The obtained $1/\rho$ -dependence (inverse proportionality) is in accord with the theoretical and empirical formulae for eddy current loss calculations from Section 3.3.2, where the sheath resistivity is in the denominator of all equations.

The effect of the sheath composition and resistivity on the measured eddy current loss for tapes with the same number of filaments is shown in Fig. 3-30. The 7-filamentary AgMgNi-sheathed tape (BICC-19) has eddy current loss, which is two times lower than that of the Ag-sheathed tape (BICC-23), which is less than half the expected loss reduction since $\rho_{Ag} : \rho_{AgMgNi} \approx 1/5$. The loss reduction in the 19-filamentary alloy tapes is even lower – 30 % instead of 500 % for the AgMgNi-sheathed tape (BICC-46) and 40 % instead of 600 % for the AgAu-sheathed tape (BICC-47) since $\rho_{AgAu} : \rho_{AgMgNi} : \rho_{Ag} \approx 6:5:1$.

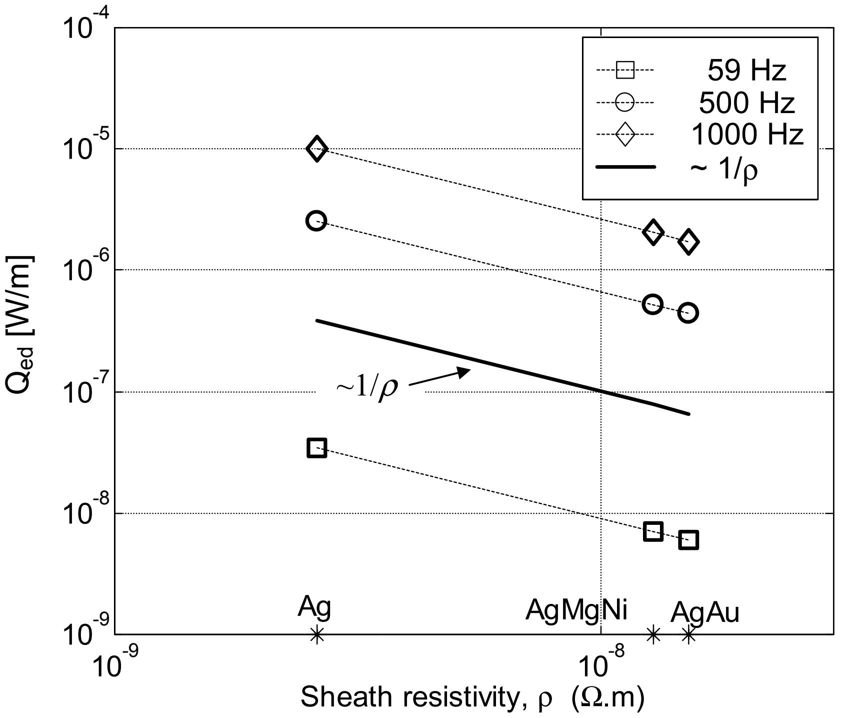

Figure 3-29 Eddy current loss, obtained by FEM simulations with the 19-filamentary tape, using different values of the metal sheath resistivity.

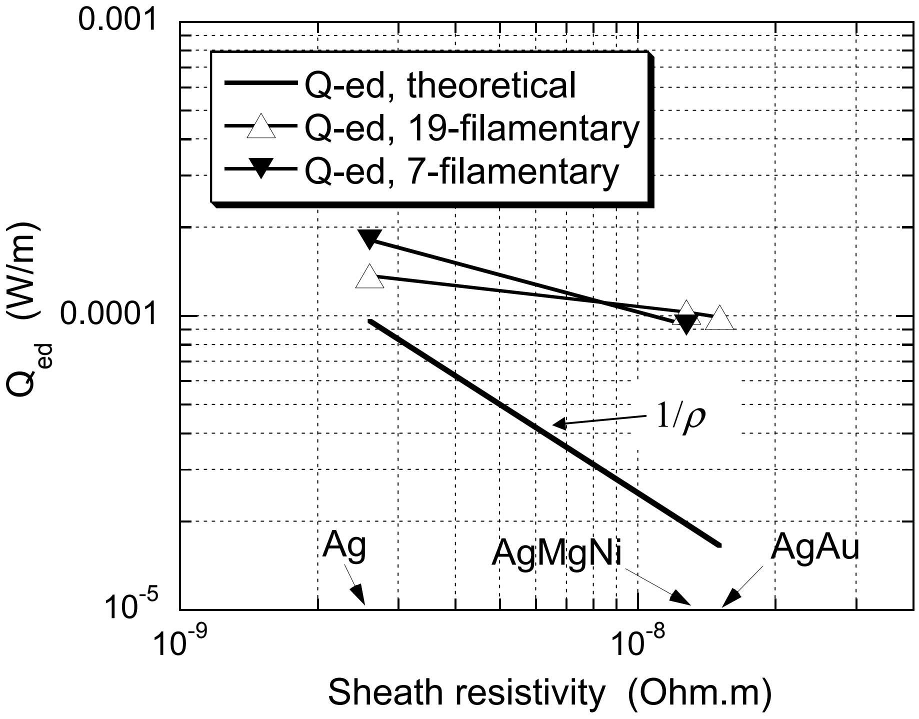

Figure 3-30 Measured eddy current loss at 1.5 kHz in 7-filamentary and 19-filamentary tapes with different sheath composition and resistivity. The solid line indicates the theoretical slope (1/ρ-dependence).

Discussion

Table 3-2 presents a comparison between the measured eddy current loss for five ordinary Ag-sheathed tapes, the FEM simulation results and the calculated loss from Ishii's empirical approximation.

TABLE 3-2. Eddy current loss comparison

Tape	*d (μm)*	*w (μm)*	Q_{meas}/Q_{Ish}	Q_{meas}/Q_{sim}
BICC-56 (1)	160	380	0.9	8.1
BICC-23 (7)	100	415	6.8	5.6
BICC-34 (19)	80	250	5.0	10.6
BICC-36 (37)	100	270	2.7	4.8
BICC-41 (55)	90	250	3.8	–

Comparison between the ratios of the measured (Q_{meas}) and the empirical (Q_{Ish}) and simulated (Q_{sim}) eddy current loss for Ag-sheathed tapes at 1kHz and 4A peak value of the transport current. The number of filaments is given in brackets. *d* and *w* are the thickness and the edge width of the metal sheath.

The FEM simulations have shown that the edge-width, and not the thickness of the sheath, is the governing geometric parameter, which determines the eddy current loss in the normal metal. In Ishii's approximation, however, the eddy current loss depends on the cube of the sheath thickness. This can explain the difference between calculated and measured eddy current loss. The monocore tape has the thickest sheath (~ 160 μm) and for such sheath thickness Ishii's approximation gives a result very close to the measured loss. Most of the other tapes have considerably thinner sheaths (80–100 μm), so that Q_{Ish} is lower, therefore the ratio Q_{meas} / Q_{Ish} is higher than for the monocore tape by a factor between 2 and 5. Exception is the higher ratio for the 7-filamentary tape – $Q_{meas} / Q_{Ish} = 6.8$. This is due to the large edge-width of this tape, which is the reason for the higher measured and simulated eddy current loss.

In other words, the empirical calculation for the eddy current loss has been made for a metal strip without taking into consideration the concentrated power dissipation in the sheath edge due to the higher magnetic field in that region, resulting from the specific self-field distribution in the superconducting core. This may well account for the difference between calculated and measured losses.

In the simulations, however, the current density and magnetic field in the whole tape have been included into the finite-element calculations. Although in the same order of magnitude, there is a difference by a factor of 5–10 between the measured and the simulated eddy current loss (see Table 3-2). In addition, as shown in the previous sections, the effect of the sheath resistivity and the edge-width on the eddy current loss in the measured tapes is lower than it is expected from the theory and the simulations.

All this leads us to the conclusion that the f^2 – dependent loss, which is measured in the tapes, does not come only from eddy currents in the sheath and has another, additional contribution [Sta98b]. This additional loss could possibly come from electromagnetic coupling and associated current flow between the filaments for the multifilamentary tapes. The use of high-resistivity alloy sheaths, however, should have decreased considerably these coupling losses, which was not observed in the measured loss. Nor can coupling explain the considerable difference between measured and simulated f^2 – dependent loss in the monocore tape since this phenomenon occurs only in multifilamentary tapes.

Therefore, if the measured f^2 – dependent loss does not come from the metal sheath/matrix only – in the form of eddy current or coupling loss – then it should come from the BSCCO core. More precisely, because of its f^2 – dependence it must be of the same origin (type) as the eddy current loss in the sheath – that is, from the induced currents by the self-field in the BSCCO material. It is important to note that values of the f^2 – dependent loss factor from the AC loss dissociation model, Eq. (3.11), decrease if a narrower frequency range is used for the fit, 59–500 Hz for example. In other words, the magnitude of the eddy-current-type loss factor is due mainly to the high-frequency data from the measured AC loss in self-field. At low frequency, for example in the power frequency range of 50–200 Hz, the induced currents in the BSCCO core can be completely neglected – when the applied current is low, the self-field is negligible; when the applied current is near I_c, the self-field cannot be neglected but because of its low frequency, the induced eddy-current voltage is insignificant, which follows from Faraday's law. At high frequency, however, the effect of the induced currents by the self-field appears to be non-negligible.

As it will be demonstrated in Chapter 5 and Chapter 6, the critical state model is not fully applicable to HTS materials. One of the main effects of the self-field in BSCCO/Ag tapes is that the current density is higher near the edges of the superconductor, where locally J may exceed J_c even at low applied currents, when there are still current-free zones in the center. In such regions with $J > J_c$ flux-flow resistance is developed. At high frequency, due to the strong skin-effect the induced currents in the BSCCO core tend to flow as close to the edge as possible, and because of the increasing value of the finite resistivity of the BSCCO core where J approaches J_c, these induced currents produce an additional, f^2 – dependent loss, which will be definitely non-negligible above 1 kHz. This additional loss in the BSCCO makes the effect of decreasing the edge width or using an alloy sheath on the reduction of what is measured as a f^2 – dependent loss in the tapes noticeably slighter than expected, and accounts for the higher measured eddy-current-type loss compared to the simulated and empirically derived ones.

3.6 Response of Bi-2223 tapes to over-critical current excursions

Fault current limiters (FCL) are devices, which are triggered when an over-critical current perturbation in the power grid occurs with value several times higher than the nominal current of the FCL. With view towards the utilization of Bi-2223/Ag tapes for FCL, a study of the over-I_c behaviour of such tapes, subject to sinusoidal transport currents up to $100 \times I_c$ for up to 50 ms (2.5 cycles at 50 Hz), is reported in [Lay99]. A necessity has been discovered for improvements of the tapes' critical current and/or sheath's resistivity.

Another promising application of Bi-2223 tapes at 77 K, as outlined in Chapter 2, is their usage for power cables in superconducting transmission lines [Fri97]. In power systems nowadays, current perturbations may occur with amplitude up to 20 times the nominal value, and for duration up to 10 to 20 cycles at most.

In this section we present a study of the over-I_c behaviour of Bi-2223 tapes, subject to current perturbations with various form and frequency, amplitude up to $20 \times I_c$, and duration up to 15 cycles [Sta00].

Table 3-3. BICC tape specification

Tape	λ	I_c *(A)*	*Dimensions (mm)*	*Sheath material*	*n-value*
BICC-A (1)	0.40	19.2	2.75 × 0.32	Ag	19.1
BICC-B (7)	0.23	14.5	3.00 × 0.25	AgMgNi	19.2
BICC-C (19)	0.27	10.6	3.34 × 0.34	AgMgNi	16.1
BICC-D (19)	0.27	19.7	2.71 × 0.32	Ag	17.8

Table 3-3 shows the specification of the Bi-2223 tapes, manufactured by BICC General Superconductors. The filament number is given in brackets; λ is the filling factor; and I_c is the DC critical current (1 μV/cm criterion). The last column contains the power index of the DC V-I characteristics $V = V_c(I/I_c)^n$. We have selected tapes with a good power index (15-20), and not very high critical current, which allows us to reach the 20-I_c amplitude with the capacity of our existing power supply and transformer.

3.6.1 Over-I_c voltage-current waveforms

BICC-A tape was subjected to over-critical current experiments with a current waveform shown in Fig. 3-31. The current with amplitude of 64 A (3.3 × I_c) was applied for the duration of 10 complete cycles with different frequency: 0.05, 0.1, 0.5, 1 and 10 Hz. No significant difference has been discovered between the V-I waveforms for the 10 different cycles (Fig. 3-31 shows the average values). The implication is that the tape shows a very good stability in response to such over-critical-current perturbations.

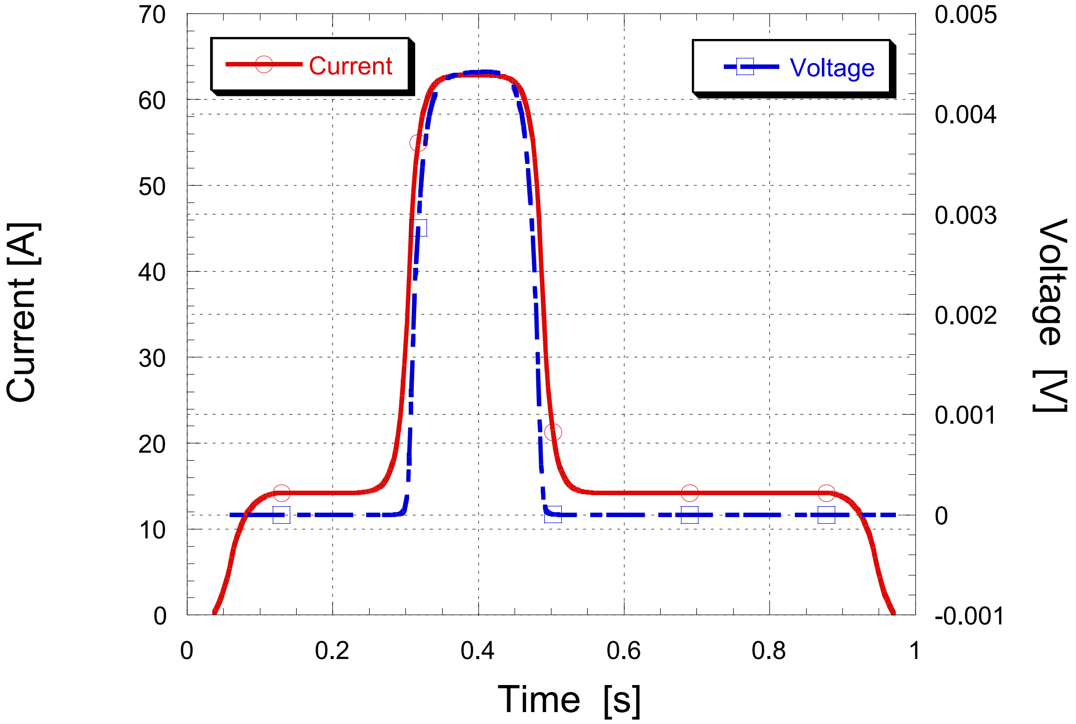

Figure 3-31 Arbitrary over-critical current waveform and measured voltage across the sample (BICC-A). The tape's I_c is 19.2 A.

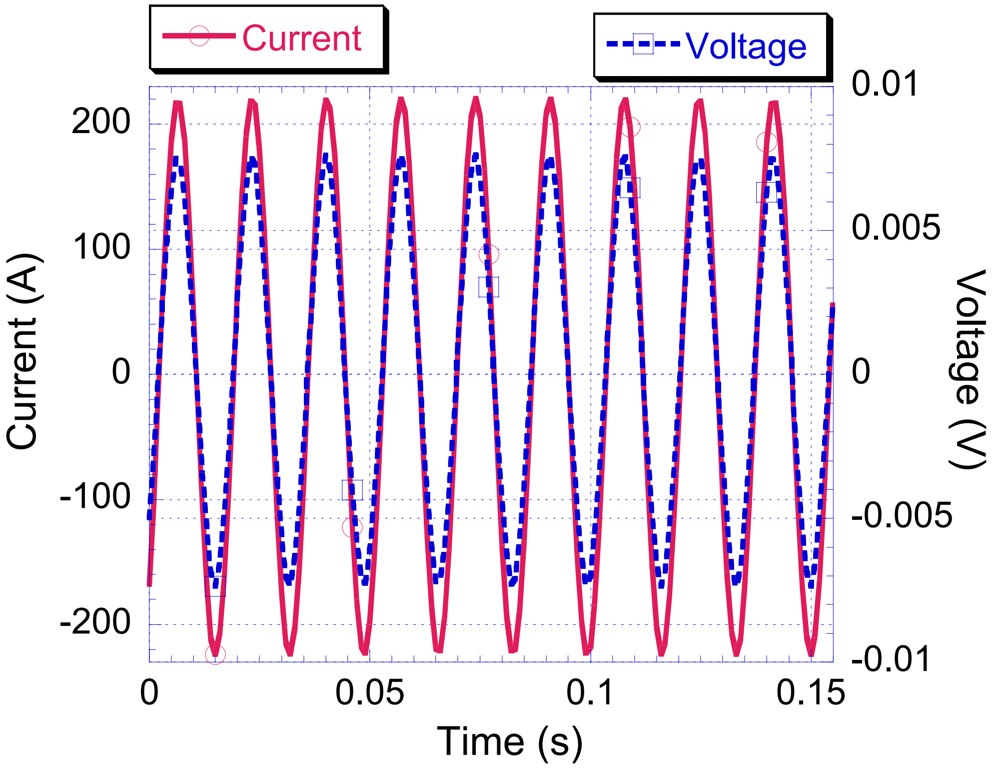

Figure 3-32 Over-critical sinusoidal current and voltage waveforms at 59 Hz for 10 consecutive cycles (BICC-D).

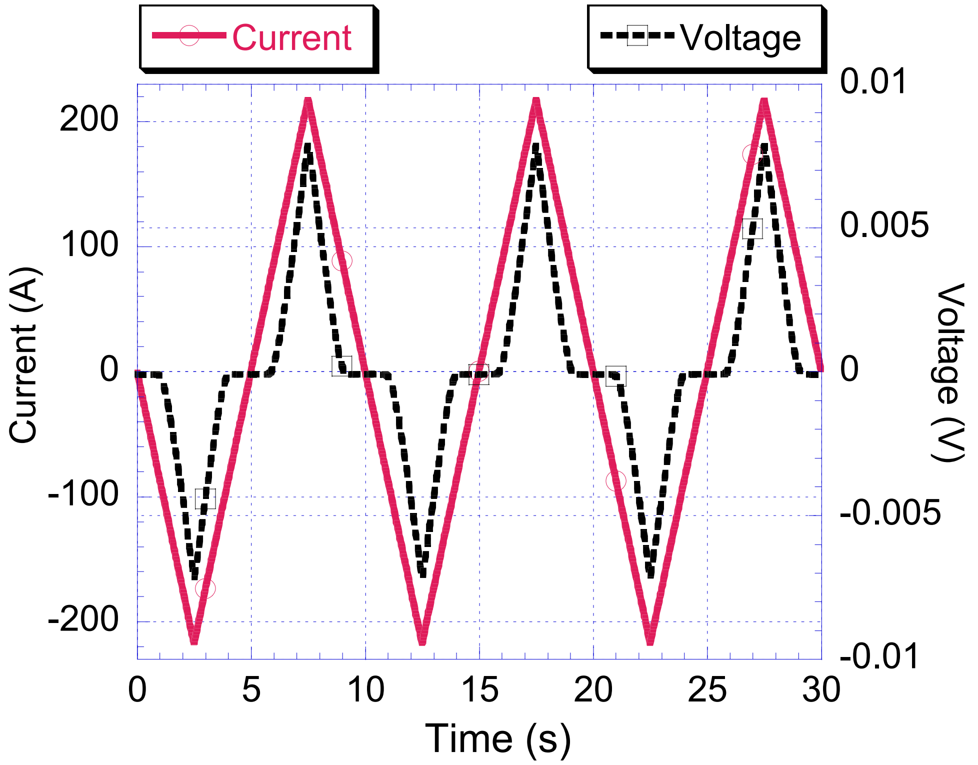

Figure 3-33 Over-critical triangular current and voltage waveforms at 0.1 Hz for 3 consecutive cycles (BICC-B).

BICC-B, BICC-C and BICC-D tapes were subjected to triangular and sinusoidal over-critical currents at 0.1, 1, 10 and 59 Hz with amplitude up to 200/300 A (~ $15 \times I_c$). The current was driven through the tapes for at least 10 cycles at 0.1, 1 and 10 Hz, and for 1 second at 59 Hz. Fig. 3-32 and Fig. 3-33 show the recorded *V-I* waveforms, for a 59-Hz sine and a 0.1-Hz triangular current respectively.

It is readily seen that the waveforms are identical for the different cycles, which means that the Bi-2223 tapes enter and exit the superconducting state, as the current amplitude goes below and above I_c, without deterioration of their superconducting properties.

One of the samples (BICC-D) was destroyed when the same experiment (10 cycles) was tried for a current amplitude of 400 A (~ $20 \times I_c$) at low frequency (10 Hz).

3.6.2 Resistive behaviour in the over-I_c regime

The higher the frequency of the transport current excursion, the shorter the tape is subjected to continuous over-I_c perturbation during the cycle. Low-frequency perturbations have been selected for the following analysis, since it is more convenient to evaluate the tapes' response to slow changing perturbations due to the absence of reactive component, which appears at high frequencies. Conclusions for the stability of the tapes remain valid for higher frequencies, too, as it will be shown later.

Figure 3-34 shows the effective resistance $R = V/I$ of a tape, subject to a sinusoidal over-I_c perturbation. Discontinuities are due to the current's passage through zero. Better insight into the non-linear resistive behaviour of the tapes can be achieved if a triangular input current is applied (more measurement data below I_c are obtained).

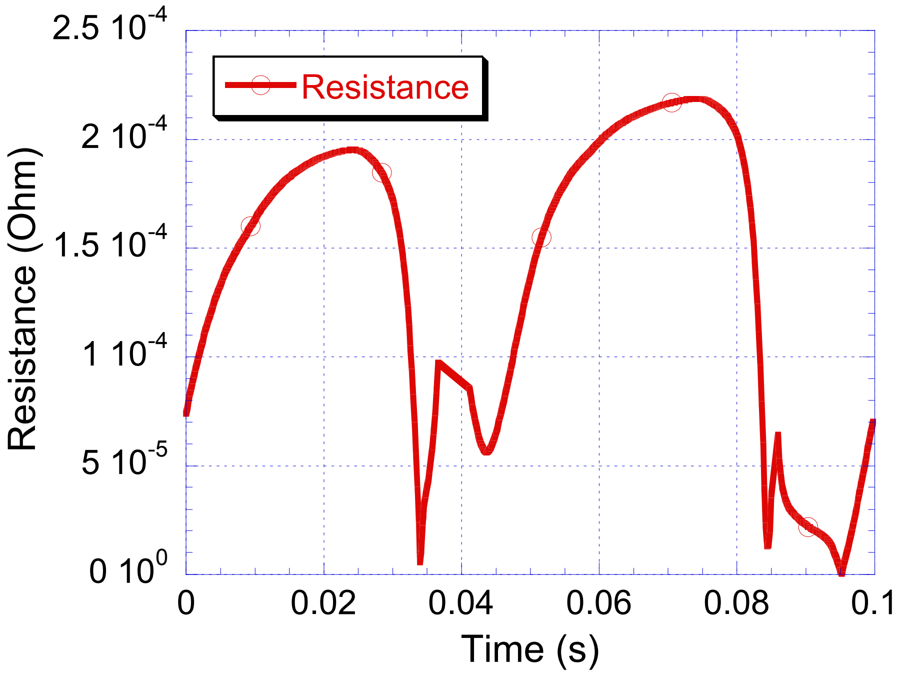

Figure 3-34 Effective resistance of the tape for one cycle at 10 Hz. I_{max} = 200 A (BICC-D).

The cycle of the triangular perturbation can be divided into four parts of the same duration: as the current goes consecutively from 0 to + I_m, from + I_m to 0, from 0 to – I_m, and from – I_m to 0, where I_m is the current's amplitude. For each of these 4 parts, the resistive behaviour of the tape can be observed by plotting the measured current-voltage dependence, as in Fig. 3-35. The *I-V* relation can be modelled with the following equation:

$$I = \frac{V}{R_0} + I_c \times \left(\frac{V}{V_c} \right)^{1/n} \qquad (3.26)$$

where I_c is the tape's critical current (A) and V_c is the I_c-determination voltage criterion (V). Equation (3-26) is then fitted to measurement data, where the fit-variable is R_0 (Ω), the linear term of the over-I_c resistance. Figure 3-35 shows an example of the R_0 fit as well.

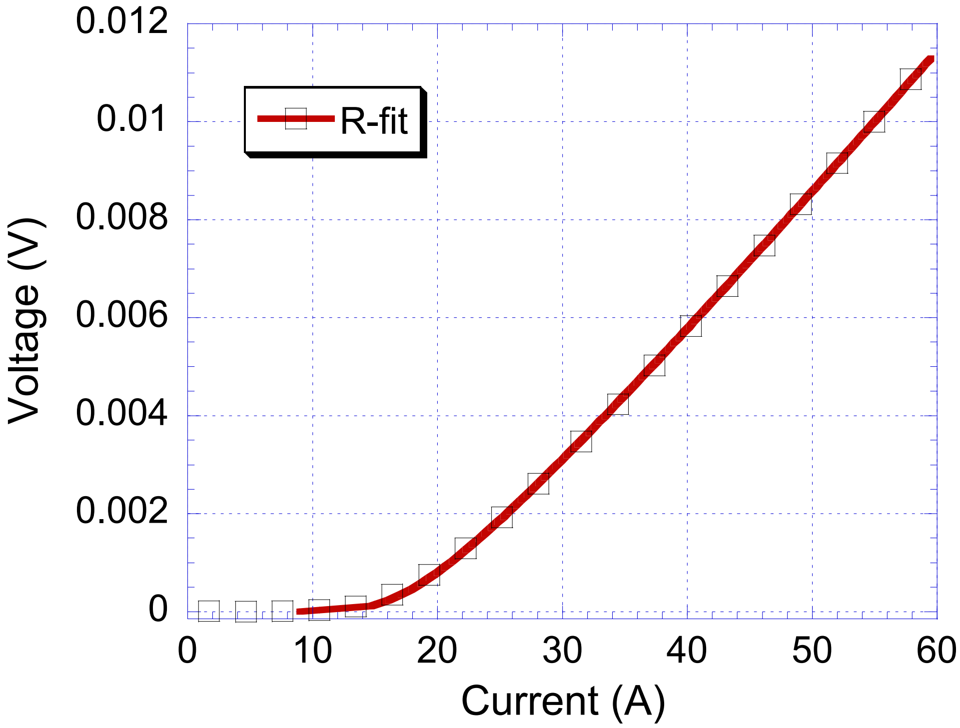

Figure 3-35 *V-I* dependence, measured – square symbols, and fitted from Eq. (3.26) – solid curve (BICC-C).

A value of R_0 has been obtained for each part of the cycle at 0.1, 1 and 10 Hz, for BICC-B and BICC-C tapes. The R_0 values for these two tapes are respectively close to 3.3×10^{-4} Ω and 3.1×10^{-4} Ω. The consistent R_0 values, of ± 5% deviation for all frequencies and for all cycle parts, signify that no change in the linear part of the over-I_c resistance has occurred.

3.6.3 Models for temperature-rise estimation

Figure 3-36 shows a comparative plot of the tape's effective resistance, $R = V/I$, for the four different parts of the over-I_c cycle.

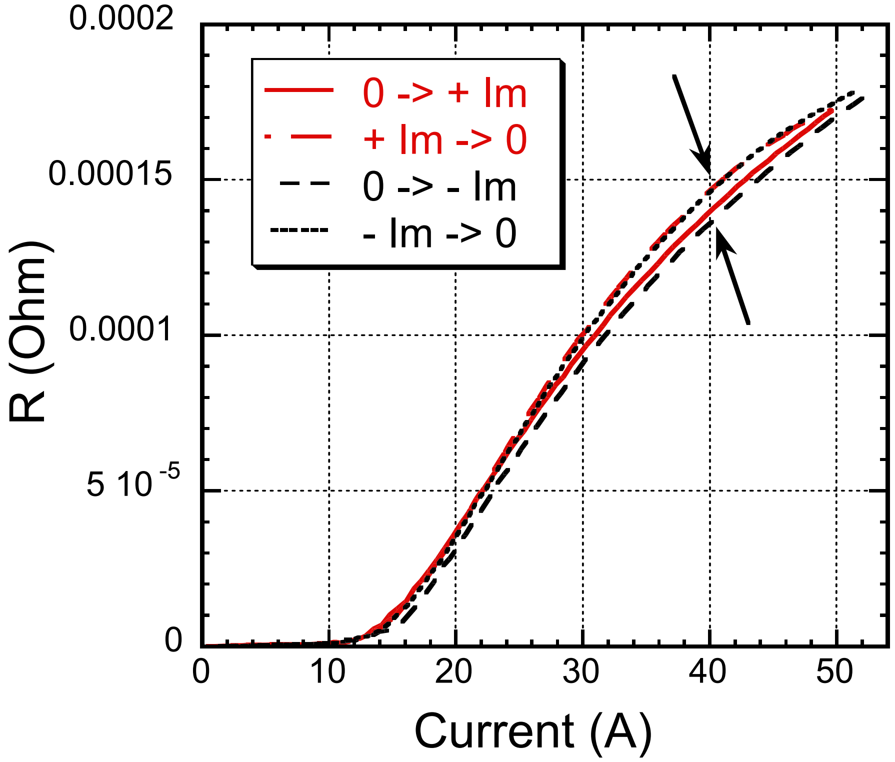

Figure 3-36 Effective resistance for the different parts of the over-I_c cycle (BICC-C).

The value of R in the over-I_c regime is slightly higher when the current goes down to 0 from its peak value ($+I_m$ or $-I_m$), see the arrows in Fig. 3-36. This can be explained by a slight heating of the tape as the over-I_c current reaches its amplitude. Exact measurements of the temperature increase in the Bi-2223 tapes are not feasible; however, an evaluation of the temperature rise can be achieved in two ways.

First, one may assume that if the frequency is high enough, the heat transfer in the system is adiabatic (i.e. no heat is transferred to the liquid nitrogen). Such an approach has been used in [Lay99]. The temperature increase can then be calculated from the dissipated energy as follows:

$$E = \int V(t)I(t)dt = v\int C_p dT \tag{3.27}$$

where V is the voltage, I is the current, t the time, v the sample volume and T the temperature. C_p is the specific heat for pure silver at T = 100 K and is equal to 1.96 J/cm^{3}K. Table 3-4 contains the calculated energy dissipation in Joule and the corresponding temperature increase for BICC-A, B, C tapes (ΔT_1).

Table 3-4. Temperature increase in Bi-2223 tapes in over-I_c regime

Tape	*Frequency (Hz)*	*Energy (J)*	ΔT_1 (K)	ΔT_2 (K)
BICC-A	10	0.55	7.5	4.5
BICC-B	10	0.41	4.8	3.1
BICC-C	10	1.12	10.1	5.7

The temperature increase in the three tapes, given in Table 3-4, is maximized due to the assumption for adiabatic situation. Since it may be argued that this is hardly the case in the liquid nitrogen bath, we have attempted to evaluate the temperature rise in another way.

The resistivities of the metal, composing the tape's sheath/matrix - pure Ag or AgMgNi alloy - have been measured at various temperatures by BICC Superconductors and are shown in Fig. 3-37.

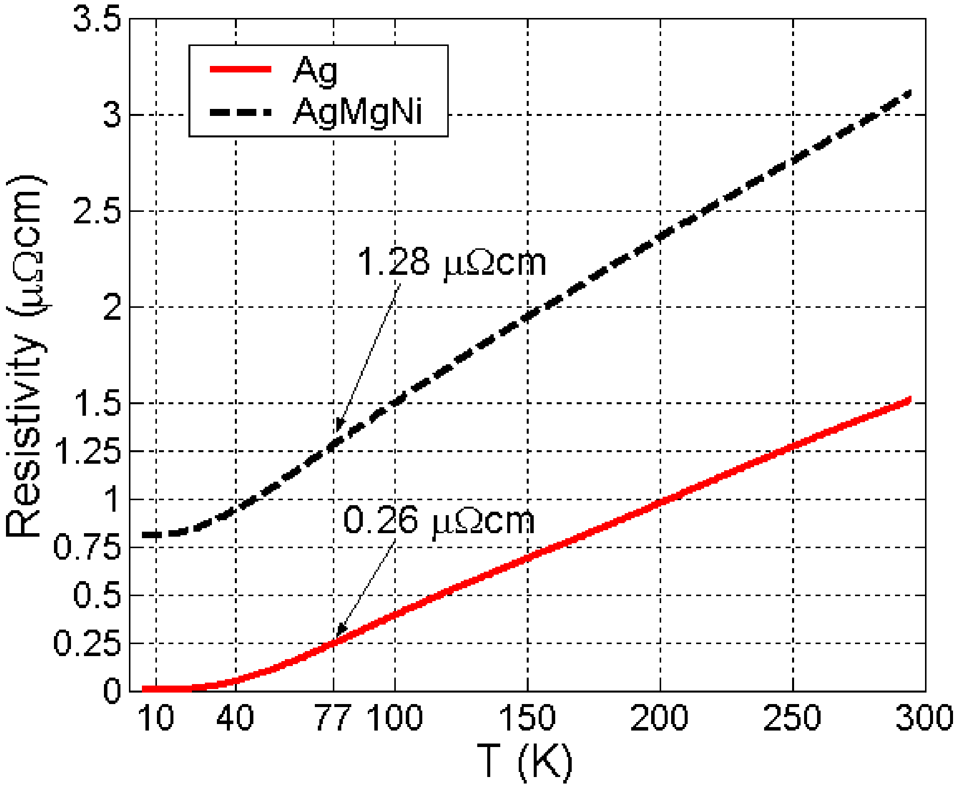

Figure 3-37 Resistivity of pure Ag and AgMgNi alloy (annealed).

As shown in the figure, the resistivity of pure Ag at 77 K is 0.26 μΩcm, while that one of AgMgNi alloy is 1.28 μΩcm. These values are by a factor of 100 lower than the resistivity of Bi-2223 bulk superconductor at high-pulsed currents with amplitude 10-15 × I_c, which is within the range 100-300 μΩcm [Nou97]. For this reason we conclude that in a strong over-I_c ($I_m >> I_c$) regime the current in the tape is conducted mainly through the metal sheath and matrix, be it a Ag or a AgMgNi one, rather than through the Bi-2223 filaments, which have much higher resistivity. Therefore, any increase in the temperature of the tape should be attributed primarily to heating of the normal metal. In other words, the increased resistance of the tape in the over-I_c regime is due to heat dissipation in the normal metal, where the larger part of the current goes through.

The difference in the tape's effective resistance as the current goes down to zero from its peak value can be easily calculated. For example, in Fig. 3-36, this difference is largest when the applied current is 40 A (indicated by arrows in the figure), and is equal to 25 μΩ. By using the simple formula $\rho = RS/l$, we can then calculate the increase of the resistivity of the normal metal, which for the given geometry of this tape is 0.057 μΩ cm. That corresponds to a 5.7 K increase of the temperature of the tape, since the slope of the $\rho_{\mathrm{AgMgNi}} - T$ curve near 77K is 0.01μΩ cm/K.

The results of the evaluation of the temperature rise in the three tapes, using the measurement data for the ρ–T dependence of the normal metal (shown in Fig. 3-37), are presented in Table 3-4 (ΔT_2). As can be seen, both ways of evaluating the temperature increase in the tapes lead to similar results (compare ΔT_1 and ΔT_2). All values for ΔT are between 3 K and 10 K, which indicates very slight heating of the tapes. The corresponding amount of dissipated Joule energy in the tapes, as calculated from Eq. (3-27), is also shown in Table 3-4.

Finally, Fig. 3-38 shows a comparison between the tape's effective resistance ($R = V/I$) for 3 different frequencies – 0.1, 1 and 10 Hz. As can be seen, the R-curves practically coincide, which confirms that conclusions about the resistive behaviour in the over-I_c regime, made from measurements at one frequency, are in general valid for the other selected frequencies as well.

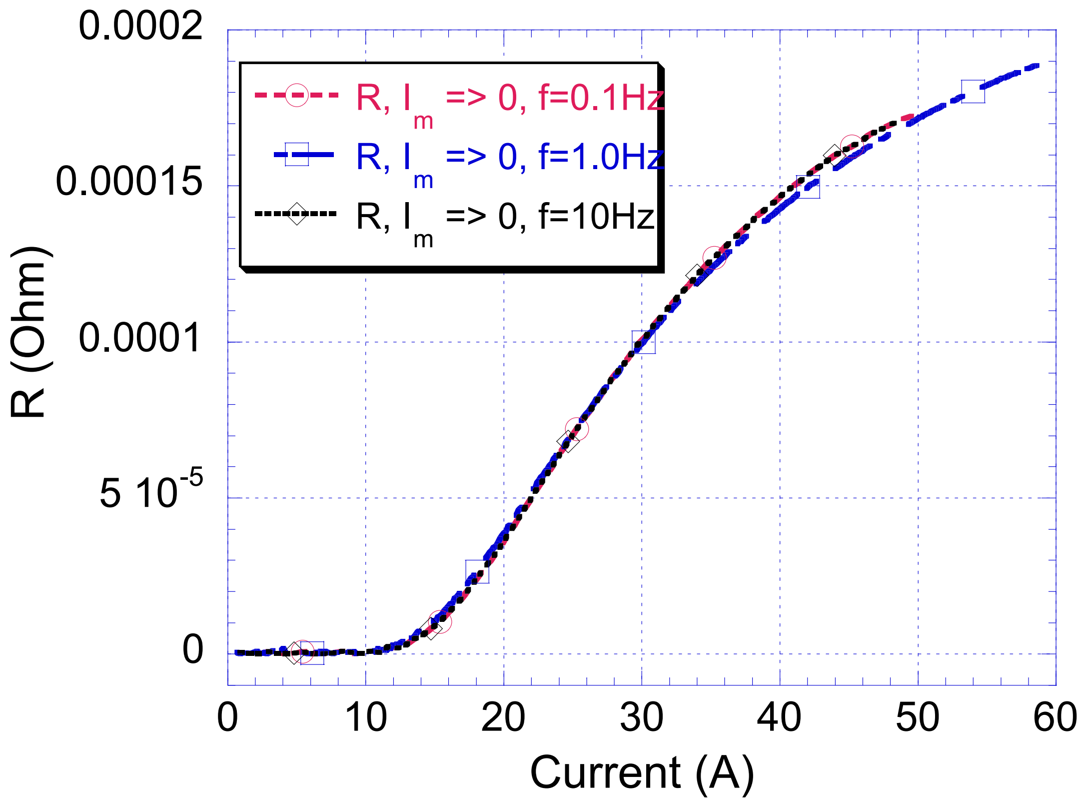

Figure 3-38 Effective resistance at different frequencies as the current amplitude goes from $+I_m$ to zero (BICC-C).

3.7 Conclusions

Frequency dependent modelling of self-field AC losses in Bi-2223 tapes

Using the electrical characterization technique it is not possible to measure separately the hysteresis, flux-creep and eddy current loss in any frequency range of interest when AC transport current is applied to HTS tapes, and the evaluation of the dominating loss component by measurements at fixed frequency or in a narrow frequency range can be only qualitative. We have achieved AC loss dissociation of measured self-field losses by fitting a second order polynomial to the experimental loss curves, assuming a square frequency dependence for the eddy current contribution, a linear frequency dependence for the hysteresis loss, and frequency independent flux-creep contribution at high applied currents. This loss-model is in compliance with the conclusions from related previously published work on self-field loss in HTS tapes. The loss dissociation was rendered possible thanks to the sufficiently broad frequency range of the measurements, whereby the loss frequency-dependence can be clearly observed and the fitting errors are minimized.

The eddy current loss in Bi-2223 tapes has been also evaluated by means of FEM simulations. The effect of sheath's resistivity and geometry has been studied and compared to the measured and theoretical eddy current loss. The simulations have shown that there is a considerable concentration of power dissipation (eddy current loss) in the edges of the sheath due to the large values of J, therefore H, close to the Ag-BSCCO interface. For this reason the edge width is the most important geometric factor in determining the value of the eddy current loss in the metal sheath, whereas the sheath thickness has much lower effect on the power dissipation. The eddy current loss in the metal sheath and matrix can be decreased by reducing the edge width and/or by using alloys with increased resistivity, such as AgMgNi.

The measured f^2 - dependent loss in the Bi-2223 tapes was found to be higher than the calculated and simulated eddy current loss. We have explained this difference with a suggested additional contribution of screening current loss in the superconducting core due to the non-negligible effect of induced currents by the self-field at high frequencies ($f \geq 1$ kHz) near the edges of the tapes, where $J > J_c$ and the resistivity of the BSCCO is finite.

However, the main conclusions of our work on frequency modelling of measured self-field AC losses are related to the dependence of the eddy-current-type loss contribution on the applied-to-critical current ratio. For the intended current ratio in power applications ($i > 0.4$), the eddy-current-type loss in Bi-2223 tapes does not have significant contribution below 500 Hz, and starts dominating in the total self-field AC loss for frequencies well above 1 kHz.

The main self-field loss in the measured Bi-2223 tapes is the hysteresis loss. For the power frequency-range applications ($f \leq 200$ Hz), the eddy-current-type loss does not have any significant contribution, except for low applied currents (i < 0.2). The relative eddy current contribution to the total AC loss is inversely proportional to the current ratio – the higher i, the less significant is this contribution. The main reason for such inverse proportionality is the different current dependence of the hysteresis and eddy current losses – $Q_{hyst} \sim I_p^{3-4}$ between Norris's strip and elliptical predictions, while $Q_{eddy} \sim I_p^2$ in the theoretical calculations and the measured loss. Therewith comes the increasing contribution of hysteresis loss with higher applied currents.

At low frequency ($f \leq 100$ Hz), and high applied currents ($i > 0.8$), resistive flux-creep loss contribution appears, whose relative weight may reach up to 30-40 % of the total loss.

Since this loss is independent of *f*, with the increase of the frequency $(Q_{eddy} \sim f^2, Q_{hyst} \sim f)$, the resistive loss contribution from flux-creep becomes quickly completely negligible.

Over-critical current behaviour of Bi-2223 tapes

Four Bi-2223 tapes were subjected to over-critical-current excursions of different waveform (arbitrary, sinusoidal and triangular), frequency (0.05, 0.1, 1, 10 and 59 Hz) and amplitude, reaching 20 times the value of I_c. Even after 10 consecutive cycles of over-critical-current perturbation at frequency up to 10 Hz, and 1-second perturbations at 59 Hz, with amplitude up to 15 × I_c, the samples did not deteriorated their superconducting properties (when I goes repeatedly below I_c). One sample was destroyed only when 10 cycles at 20 × I_c were applied at low frequency (10 Hz).

The performed experiments lead to the conclusion that Bi-2223/Ag and Ag-alloy tapes show very good stability (no deterioration of their superconducting properties) when over-critical-current perturbations occur for up to 10 consecutive cycles at frequencies up to 10 Hz, 60 consecutive cycles at 59 Hz, and current amplitudes up to 15 × I_c. The overall stability of the tapes was also demonstrated by the identical response to over-I_c perturbations at different low frequencies, repeated for up to 10 cycles.

The estimated temperature increase (ΔT) in the over-I_c regime, evaluated in two different ways, showed a ΔT of maximum 10 K. This small rise is due to the fact that in the over-I_c regime ($I_m >> I_c$), the larger part of the current is conducted by the normal metal sheath/matrix, and the heat resulting from the energy dissipation in the tape, is transferred from the Ag to the nitrogen bath (quick cooling).

Thus we can sustain a conclusion that Bi-2223 tapes are apt for use in future power transmission lines, as far as over-I_c transport current grid perturbations are concerned.

Chapter 4. Numerical Modelling of High-T_c Superconductors with B-independent J_c and n

---

Abstract

This chapter starts with presenting the two most commonly used models of type II superconductors – the critical state model and the power-law *E-J* model, together with a discussion on the applicability and limitations of each model for high-T_c superconductors. Follows a description of the most popular numerical techniques for modelling of HTS materials, among which are the algorithms based on Brandt's method, as well as the finite element method.

All results from numerical modelling of Bi-2223 conductors presented in this thesis have been obtained with the finite element method software package Flux2D. The implementation of the power law E-J model in Flux2D is described. A discussion is made on the intrinsic difficulties in the numerical simulations of highly non-linear materials such as high-T_c superconductors. Given are a number of considerations to be taken into account, for example the effect of the finite residual resistivity, the mesh optimization and CPU time, and also the boundary conditions for different applications.

The Flux2D implementation has been validated by a multi-comparison approach – comparison with electrical measurements in self-field, with Brandt's algorithm and theoretical predictions in self-field, parallel and perpendicular magnetic fields, as well as with the implemented models in another FEM software package (Flux3D).

The results presented in the last sections of this chapter are for models with B-independent J_c and power index n, used for evaluating the significance of the finite n-value on the current distribution and AC losses in multifilamentary Bi-2223 tapes. More advanced models with lateral $J_c(x)$ dependence have been used in order to quantify the effect of the locally varying J_c along the width of multifilamentary tapes in self-field, as well as in applied parallel and perpendicular magnetic fields.

Original contributions of this thesis

- the work on optimization of FEM parameters in Flux2D
- the validation of the Flux2D implementation by a multi-comparison approach
- the study of the significance of the n-value in HTS tapes by FEM simulations
- the modelling of multifilamentary tapes with lateral $J_c(x)$ dependence

4.1 Introduction

The level of AC losses in transport current or combined current and magnetic field applications is still a major obstacle for large-scale power utilization of HTS materials. For example, depending on the amplitude of the transport current and/or the external field, the AC loss at 77 K in single Bi-2223/Ag tapes at power frequencies may vary from several μW/m to tens or even hundreds of mW/m. For the design and implementation of any HTS device, the expected loss levels must be calculated or evaluated in advance with a certain precision for different applications.

Modelling tools for HTS superconductors are required since theoretical solutions for current and field equations have been found for simple geometries only and are based on the assumptions of Bean's critical state model, which is not fully applicable to superconductors with smooth current-voltage characteristics. Numerical methods are, therefore, at the forefront of AC loss modelling and analysis in the field of high-T_c superconductivity.

The chapter is structured as follows. Section 4.2 defines the different basic models of type-II superconductors; Section 4.3 gives an overview of some engineering approaches for AC loss modelling; Section 4.4 describes the most common numerical methods for modelling of HTS; Section 4.5 presents the nonlinear model of HTS implemented in the FEM software Flux2D; Section 4.5 contains the validation of the Flux2D implementation; Section 4.7 and 4.8 present original results from modelling of multifilamentary tapes with different n-values and models of lateral J_c distribution; and Section 4.9 gives the conclusions from this chapter.

4.2 Basis for modelling of type-II superconductors

4.2.1 The critical state model

A great advance in the theoretical modelling of superconductors was triggered in 1957 by a paper from Abrikosov [Abr57], who presented a theory for the magnetization of hard (type-II) superconductors, in which he showed that the flux enters the specimen in quantized flux lines, starting at very low field H_{c1} and completing its penetration at a much higher field H_{c2}. Several years afterwards, in order to obtain the virgin magnetization curves in hard superconductors, which exhibited magnetic hysteresis, Bean introduced a model, later referred to as the critical state model (CSM), a basic premise of which is the existence of a limiting macroscopic superconducting current density J_c that the superconductor can carry [Bea62], [Bea64]. In Bean's model only two states are possible to occur in the superconductor, zero current for regions with no magnetic flux penetration, and full current with density J_c in regions with partial or complete flux penetration.

Along the width of a superconducting specimen, the current density is:

$$J(x)=\begin{cases} 0, & H(x)=0 \\ \pm J_c, & H(x)\neq 0 \end{cases} \tag{4.1}$$

In Maxwell's equations, this can be also written as:

$$\nabla \times \mathbf{B} = \mu_0 \mathbf{J}$$
$$\nabla \times \mathbf{E} = -\frac{\partial \mathbf{B}}{\partial t} \tag{4.2}$$

with $J = \pm J_c$ or zero.

Even though experiments had shown that the critical current density is a function of the magnetic field, Bean assumed that J_c is independent of B, which in his early paper was equivalent to the assumption that the magnetic field is much less than the critical field of the filaments H_c.

Slab in a parallel field

The critical state model is illustrated in Fig. 4-1, which shows the current and field distribution along the x-axis of a superconducting slab of width $2a$ with infinite length along the y- and z-directions. The external field is applied parallel to its long side.

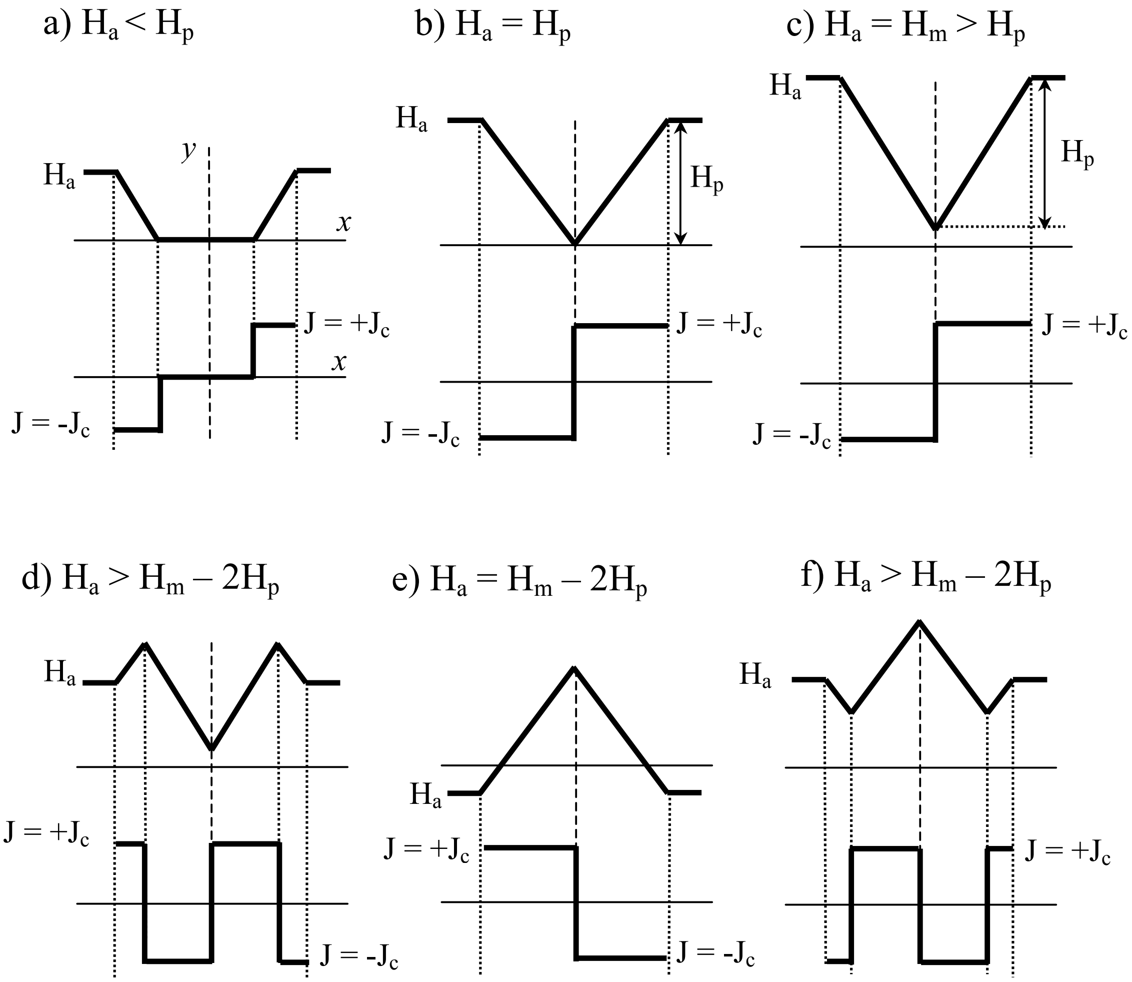

Figure 4-1 Current and field distribution in a superconducting slab in the CSM model.

Let us suppose the external field has amplitude H_a and is increasing. Following Lenz's law, screening currents will be induced at the edges of the slab. These induced currents will have direction such as to oppose the variation of the field and will try to screen the interior of the slab. Since the field has only y-component, and the current flows in the z-direction, the curl of H in Ampere's law is reduced to one term. The field penetration profile is a straight line, whose slope is defined by J_c:

$$\partial H_y / \partial x = \pm J_c \tag{4.3}$$

The field will partially penetrate the slab and the current density will be ± J_c in the penetrated region, see Fig. 4-1a). As the field amplitude is further increased until a certain value H_p, the flux will penetrate to the center of the slab and the whole width will carry current with density ± J_c as shown in Fig. 4-1b). The value H_p of the external field is referred to as the *penetration field*. When the external field has amplitude $H_m > H_p$, since the screening currents' density cannot exceed J_c, they will not oppose any further to the increase of the field inside the superconductor, and the penetration pattern will simply shift upwards, see Fig. 4-1c). The difference between the field at the edge and the center of the specimen remains constant and equal to H_p.

Let now the external field start to diminish. The screening currents have to oppose this decrease and near the edges of the slab areas with inversed current will appear. In the rest of slab, the field and the current density remain unchanged, as shown in Fig. 4-1d). When the external field has decreased with $2H_p$ from its peak value, the field and current patterns have completely reversed, compare Fig. 4-1b) and Fig. 4-1e). When the external field starts to increase, new regions with inverse currents appear again at the edges, see Fig. 4-1f).

It is to be noted that once the field has penetrated (partially or completely) the slab, there always exist screening currents in the superconductor, even when the external AC field passes through zero during the cycle.

Strip with transport current

The analytical solutions for the current and field distributions in a superconducting strip (rectangle with width $2a$, infinitesimal thickness and infinite length) with applied transport current and/or perpendicular magnetic field have been obtained by Brandt *et al.* [Bra93]. The exact equations were given in Section 3.5.2, see Eqs. (3.24) and (3.25). The critical current density is assumed constant as in the CSM. However, two differences are observed in the strip geometry compared to the CSM in a slab: firstly, due to the crucial demagnetising effects in a superconducting strip, the screening currents flow along the entire width of the specimen, even when the flux penetration has not reached the centre yet. Secondly, the flux penetration is rather quadratic and not linear along the x-axis.

The analytical current and field profiles in superconducting strip with applied transport current are shown in Fig. 4-2. The current is flowing across the whole width of the strip even for very low values of i, at which the field penetrates only near the edges.

The current and field distributions in a strip in perpendicular field are quite similar to the ones in Fig. 4-2, since both the self-field and the external field start penetrating the specimen from the edges. The main difference is that the induced currents flow in opposite directions in the two halves of the strip, because the perpendicular field has the same direction at both edges.

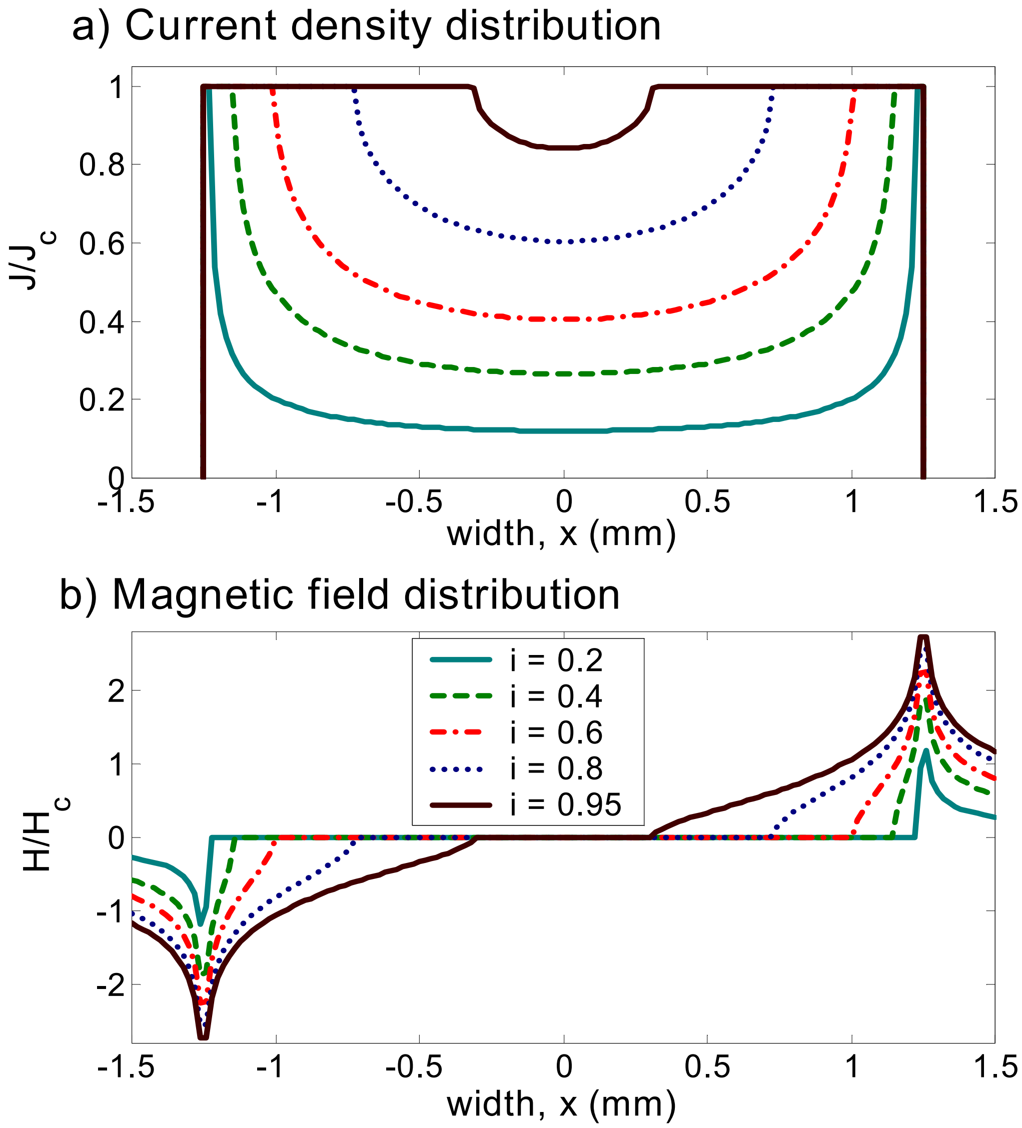

Figure 4-2 Current density J(x) and magnetic field H(x) in a superconducting strip of half-width a = 1.25 mm, carrying transport current increasing from zero from virgin state. *i* is the reduced current ratio I_p / I_c.

4.2.2 The constitutive equations of type-II superconductors

The constitutive equations of any material compliment Maxwell's equations and give the relation between **B** and **H** on the one hand, and **E** and **J**, on the other. In SI units the magnetic flux density is expressed in the form $\mathbf{B} = \mu_0(\mathbf{H} + \mathbf{M})$, where M is the magnetisation. In type-II superconductors the definition of **M** is not straightforward. The magnetization serves rather as a useful auxiliary variable since it does not have the physical significance as in standard magnetic materials [Paa98]. Thus the expulsion of magnetic flux ($\mathbf{B} = 0$) in a type-II superconductor can be formulated in two completely different ways. For obtaining $\mathbf{B} = 0$ inside the superconductor, one can set $\mathbf{H} = -\mathbf{M}$, or one can use the convention $\mathbf{H} = \mathbf{M} = 0$.

In this thesis we shall use the convention that **H** = **M** = 0 in the flux-free regions of the superconductor and the employed **B**-**H** constitutive equation will be written as:

$$\mathbf{B} = \mu_0 \mathbf{H} \tag{4.4}$$

As it was mentioned in Chapter 2, Eq. (4.4) can be used as good approximation for the **B**-**H** relation in type-II superconductor (c.f. Fig. 2-6), provided that $H > H_{c1}$, which is the case for all practical applications. This form of the **B**-**H** relation has been used in all references for modelling of HTS, found by the author.

The other constitutive equation gives the relation between the current density and the electric field and is most often written in the form of Ohm's law, **E** = ρ**J**, where ρ is the resistivity of the material.

The main problem in the modelling of type-II superconductors is the definition of the resistivity, which is not constant and consequently Ohm's law is nonlinear.

The E-J relation in the critical state model and its mathematical formulation is shown in Fig. 4-3a). It is a discontinuous, step-like function with zero electric field below J_c. Because of its simplicity, the CSM is widely used for theoretical derivations of losses in simple geometries, such as strip, slab and cylinder, for example in [Car83] and [Wil83]. Recently, a vector potential theory based on the CSM has been developed for AC loss calculation in superconductors [Rhy02]. The CSM can be extended with the introduction of the B-dependence of J_c [Kum89], [Pri97].

Because of its mathematical simplicity, the CSM does not fully apply to HTS, where the superconducting-to-normal state transition is rather broad and flux-flow resistance is developed near I_c. Instead of the sharp transition of the CSM, one can introduce a linear part above J_c that takes into account the flux-flow resistance, see Fig. 4-3b). Such extension of the CSM has been used in [Has98], [Sok98] and [Yam97].

Another possible extension of the CSM is the introduction of the material's transition to the normal state at a point, where the superconductor's resistivity becomes equal to the one in the normal state, as shown in Fig. 4-3c). This generalization of the CSM makes it more realistic, and has been applied in numerical modelling [Mas97], [Del01]. For faster convergence of the nonlinear solving algorithm, a piecewise linear approximation is used for the superconducting and transition states with ρ_0 and ρ_c having very small and very large values, respectively.

The CSM and any of its extensions, however, do not match very well the experimental current-voltage characteristics of HTS materials, which are better fitted by a power-law relation, such as the one in Fig. 4-3d). The power-law model was introduced in Chapter 2, see Fig. 2-8 and Eq. (2.5). The limiting cases of $n = 1$ and $n = \infty$ correspond, respectively, to the linear Ohm's law and the CSM. In practice, for values of n > 50 the power-law model is very close to the CSM, as it will be shown in Section 4.7. At first, the power-law model was considered simply as a phenomenological description of the broad superconducting-to-normal state transition in HTS, but later it has been sustained by theoretical arguments of flux-creep [Bra96a], [Vin91].

The power-law model is most commonly used for numerical modelling of HTS, which is described in Section 4.4. In addition to the fact that it matches better the experimental E-J characteristics of HTS, it is a smooth function and is more convenient to use in certain numerical formulations, based on Maxwell's equations, which cannot deal with infinite conductivity of the material or derivatives of discontinuous functions.

Both the CSM and the power-law model have been used for modelling of HTS, and comparisons with measurements and experimental data for AC losses have been reported to be satisfactory in the two cases. However, as far as the limits of applicability of these models are concerned, it shall be noted that for transport current applications above I_c the CSM does not hold since the current density cannot exceed J_c, and for $I_p >> I_c$ the power-law model is not convenient either, because the electric field goes as $\left(J/J_c\right)^n$ and rises to extremely large values, whereas the point of transition to normal state is not well defined.

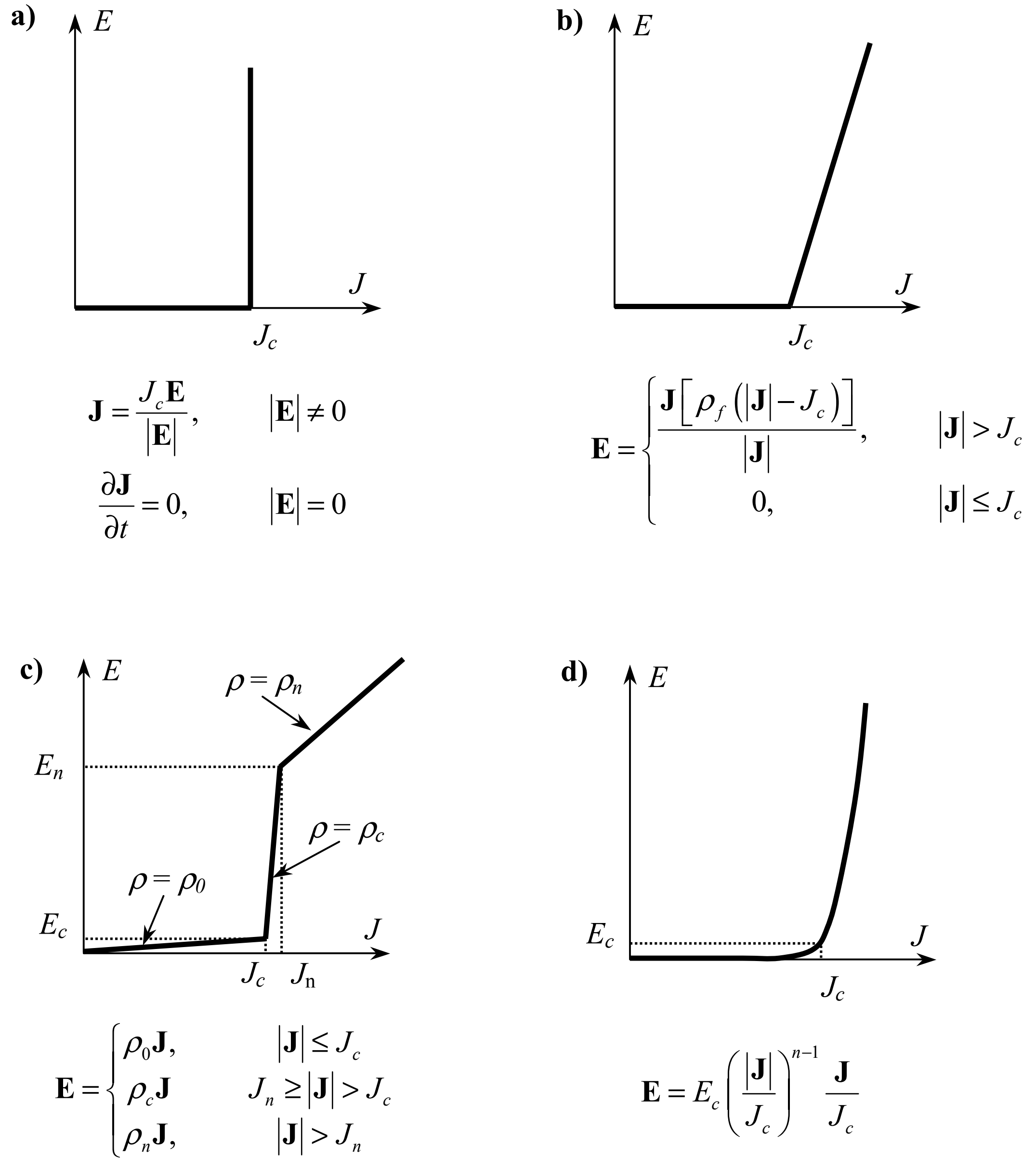

$$\mathbf{J} = \frac{J_c \mathbf{E}}{|\mathbf{E}|}, \quad |\mathbf{E}| \neq 0$$

$$\frac{\partial \mathbf{J}}{\partial t} = 0, \quad |\mathbf{E}| = 0$$

$$\mathbf{E} = \begin{cases} \dfrac{\mathbf{J}\left[\rho_f \left(|\mathbf{J}| - J_c\right)\right]}{|\mathbf{J}|}, & |\mathbf{J}| > J_c \\ 0, & |\mathbf{J}| \leq J_c \end{cases}$$

$$\mathbf{E} = \begin{cases} \rho_0 \mathbf{J}, & |\mathbf{J}| \leq J_c \\ \rho_c \mathbf{J} & J_n \geq |\mathbf{J}| > J_c \\ \rho_n \mathbf{J}, & |\mathbf{J}| > J_n \end{cases}$$

$$\mathbf{E} = E_c \left(\frac{|\mathbf{J}|}{J_c}\right)^{n-1} \frac{\mathbf{J}}{J_c}$$

Figure 4-3 The *E-J* relation in Bean's models (a), its flux-flow extension (b), its piecewise linear generalization (c), and in a power-law model (d).

4.3 Engineering approaches for modelling of HTS

Before starting the actual device design for different power applications of HTS, the expected AC loss levels need to be calculated in advance. Analytical derivations of AC losses exist only for simple geometries, most often under the assumptions of the CSM. Even if these analytical calculations provide at least the order of magnitude of the AC loss in some applications, for example in applied magnetic field or transport current only, for the combined transport current and external field case analytical solutions are available only for a slab in parallel field.

One possibility is to use numerical analysis in order to calculate the AC loss in various applications. The existing numerical methods are described in the next section. They are in general time consuming and require special modelling software. Therefore, some general approaches have been recently developed in order to express the total AC loss in HTS for different applications with simple engineering formulas. For example, it has been demonstrated that the AC loss of a HTS tape in the combined current and field applications can be modelled as the sum of a magnetisation and transport current contribution [Rab01a], [Rab01b]:

$$Q_{tot}(B_a, I_t, \alpha) = Q_m(B_a, \alpha) + Q_{tr}(B_a, I_t, \alpha) \tag{4.5}$$

where I_t, B_a, and α are respectively the transport current amplitude, the amplitude and the angle of orientation of the external magnetic field. The total loss can be expressed to a satisfactory precision as follows:

$$Q_{tot}(B_a, I_t, \alpha) = \frac{C_1(\alpha)B_a^p \cdot C_2(\alpha)B_a}{C_1(\alpha)B_a^p + C_2(\alpha)B_a} + C_3 I_t^q + C_4(\alpha)B_a I_t^2 \tag{4.6}$$

where the parameters of the model $C_1 \div C_4$, p and q account for the difference between the CSM and the BSCCO tapes and are identified from measurements.

A somewhat different modelling approach, based on the CSM, is described in [Mag01] and [Sch01], where the total loss in the combined current and field application depends on the amplitude and frequency of the transport current and the external field, as well as on the temperature, and is given as:

$$P = P(I_t, B_a, T, f) = P_{//} + P_{\perp} + P_{ff} \tag{4.7}$$

where the parallel and perpendicular hysteresis loss components and the flux-flow loss have been derived on a semi-empirical basis for various cases.

Another type of macroscopic modelling of HTS is necessary when the superconducting components of a single device or of many devices have to be considered in a system with other conventional electric power elements. In this case it is the global characteristics of the superconductor, such as voltage, current and AC loss, which are required. A description of superconducting components as parts of the libraries in the simulation software PSICE is given in [She97].

Recently, the idea of representing the superconductor with an equivalent electric circuit has been exploited by different authors – [Cri01], [Göm01], [Ich01] and [Sjö01].

Figure 4-4 shows the generalised equivalent circuit model, which has been proposed in [Sjö01]. The model is based on the consequences of Maxwell's equations, measurement results, as well as on the physical structure of BSCCO tapes. The incorporated circuit elements have been described in mathematical expressions. The superconducting material is described by a nonlinear resistance $R_{dc}(T_{sc})$, identified from DC measurements, in series with a hysteretic inductance $L_h(T_{sc})$, and a by-pass material (Ag) expressed by a linear resistance $R_{bp}(T_{bp})$ in parallel. These elements depend all on their internal temperatures T_{sc} and T_{bp}, whose evolutions are modelled with parallel heat diffusion equations. In addition, a conventional inductance L_0 is placed in series with the other elements, see Fig. 4-4.

The simplicity of this type of model makes it fast and easy to apply. Further elaborations are, however, necessary for larger applications of such models in power system simulations.

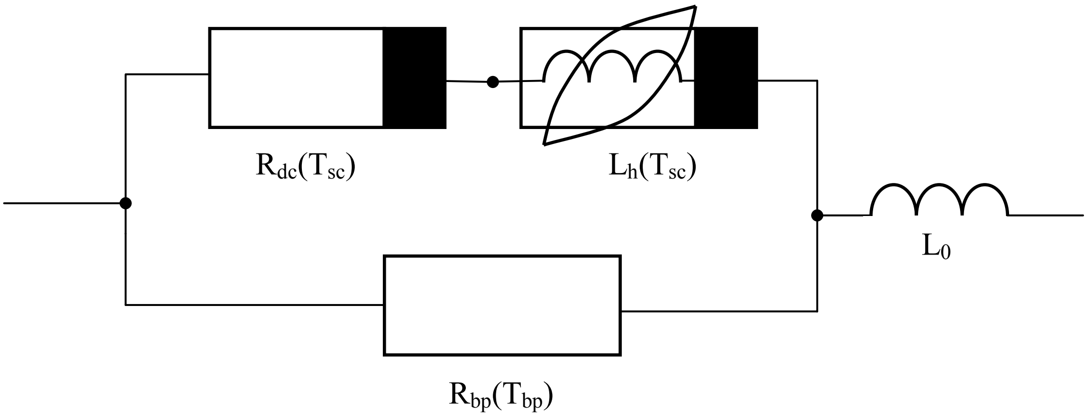

Figure 4-4 General equivalent circuit of a superconducting tape. *from [Sjö01]*

4.4 Numerical methods for 2D modelling of HTS

Numerical modelling of HTS has received considerable attention during the last several years. Numerical techniques have become very popular method for analysis of 2D problems in superconductors with various geometry under different operating conditions, where analytical solutions are either not available, or are based entirely on the CSM, which is not fully applicable for materials with smooth current-voltage characteristics.

Different numerical implementations for 2D modelling of HTS have been proposed, among which are the algorithms based on the analytical method of Brandt, outlined in Section 4.4.1, and the finite element method (FEM), which is described in Section 4.4.2. Apart from these, the finite difference method has been used [Mas98], [Syk97], as well as a hybrid finite element – boundary element method [Sig91], and a non-linear diffusion method [Tam99], [Mah99].

4.4.1 Brandt's method and its numerical implementations

In 1996 Brandt devised a scheme for calculating the 2D analytical solution of the magnetic moment, flux and current penetration in type-II superconductors with arbitrary voltage-current characteristics, expressed by a power-law relation $E = E_c(J/J_c)^n$ [Bra96b].

The starting point of Brandt's analysis is the 2D Laplace equation:

$$\nabla^2(A + xB_a) = -\mu_0 J \tag{4.8}$$

with $J(x,y,t)$ and $A(x,y,t)$ oriented in the z-direction, where the magnetic vector potential A is defined from $\mathbf{B} = \nabla \times \mathbf{A}$ and the electric field from $E = -\partial A / \partial t - \nabla_z \phi$, where $\nabla_z \phi$ is the voltage gradient.

The general solution of Eq. (4.8) is given as:

$$A(\mathbf{r}) = -\mu_0 \int_c Q(\mathbf{r}, \mathbf{r}') J(\mathbf{r}') d^2\mathbf{r}' - xB_a \tag{4.9}$$

with $\mathbf{r} = (x, y)$, $\mathbf{r}' = (x', y')$ and the integral kernel

$$Q(\mathbf{r}, \mathbf{r}') = \frac{\log|\mathbf{r} - \mathbf{r}'|}{2\pi} \tag{4.10}$$

Following the definition of the vector potential, and taking the E-J relation into account, the time-derivative of Eq. (4.9) can be written as:

$$E_c \left(\frac{J(\mathbf{r})}{J_c} \right)^n + \nabla_z \phi - x\dot{B}_a = \mu_0 \int Q(\mathbf{r}, \mathbf{r},') \dot{J}(\mathbf{r}') d^2\mathbf{r}' \tag{4.11}$$

Equation (4.11) needs to be integrated numerically. This can be done by tabulating the functions E and J on a 2D grid with equidistant points along the x- and y-axis, as shown in Fig. 4.5 for a rectangular superconductor with thickness $2b$ and width $2a$. The discretized version of Eq. (4.11) for the i-th point on the grid is then written as:

$$E_c \left(\frac{J_i}{J_c} \right)^n + \nabla_z \phi - x\dot{B}_a = \mu_0 \sum_j^N Q_{ij} \frac{J_j^{t+\Delta t} - J_j^t}{\Delta t} \Delta x \Delta y \tag{4.12}$$

In order to obtain the 2D solution for the current density, Eq. (4.12) is then inverted as follows:

$$J_i^{t+\Delta t} = J_i^t + \frac{\Delta t}{\mu_0 \Delta x \Delta y} \sum_j^N \mathbf{Q}_{ij}^{-1} \left[E_c \left(\frac{J_j}{J_c} \right)^n + \nabla_z \phi - x_j \dot{B}_a \right] \tag{4.13}$$

where Δt, Δx and Δy are the time step and axes grid distances, and Q^{-1} is the inverted geometric kernel, which in fact represents the mutual inductances between the grid elements.

Equation (4.13) is solved iteratively for each point on a k × m grid, starting from zero initial conditions.

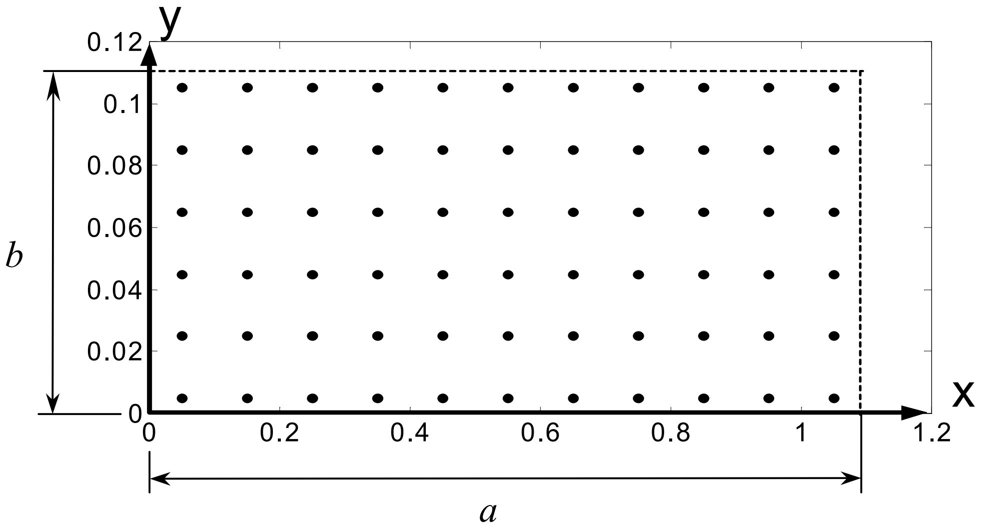

Figure 4-5 Grid for numerical calculations based on Brandt's method. Only 1/4 of the geometry needs to be calculated with symmetry exploitation in self-field or external field.

The numerical solution of Eq. (4.13) is performed on the conductor only and does not require boundary conditions as in the finite element or finite difference methods. In addition, the numerical algorithm is not very complicated and can be implemented in different programming languages. For these reasons, Brandt's method has become quite popular. In particular, it has been employed by the group at the University of Twente, which has improved the model by including the field dependence of J_c for modelling of monofilamentary HTS with various aspect ratios in different applications [Yaz98], [Yaz99]. Another implementation of Brandt's method has been performed by the group at the University of Southampton, which has done certain modifications in order to allow modelling of multifilamentary conductors. Their refined algorithm uses step-forward solving method with improved computation speed and obtains sufficient accuracy even for a rather coarse mesh [Yan99].

4.4.2 The finite element method

Another numerical technique with increasing popularity for modelling of HTS is the finite element method (FEM), an introduction to which is given in Appendix B. However, for FEM modelling of HTS sophisticated software is needed. It is possible to develop homemade software as different Japanese groups have done, for example [Ame97], [Ame98a], [Ame98b], [Fuk99], [Kaj01]. Another possibility is to use commercial FEM software for electromagnetic field computation, such as Flux2D [Nib99], [Nib00], Flux3D [Vin00a], [Vin00b] or OPERA-2d [Paa97], and to develop special subroutines for simulation of superconductors. The implementation of the Flux2D model is described in the next section.

Any FEM software is based on Maxwell's equations, see Section 3.5.2. However, there exist different ways to formulate Maxwell's equations depending on the auxiliary variables used. The most frequently employed are the **T**-Φ and the **A**-V formulations.

The T-Φ formulation

This formulation is based on the current vector potential **T** and the magnetic scalar potential **Φ**, which are defined as follows:

$$\begin{aligned} \nabla\times\mathbf{T} &= \mathbf{J} \\ \mathbf{H} &= \mathbf{T}-\nabla\Phi \end{aligned} \qquad (4.14)$$

Using the constitutive equation $\mathbf{B}=\mu_0\mathbf{H}$, the Faraday's and Gauss's laws must be satisfied, so that:

$$\begin{aligned} \nabla\times\mathbf{E} = -\frac{\partial\mathbf{B}}{\partial t} \quad &\Leftrightarrow \quad \nabla\times\mathbf{E}+\frac{\partial}{\partial t}\big(\mu_0(\mathbf{T}-\nabla\Phi)\big)=0 \\ \nabla\cdot\mathbf{B}=0 \quad &\Leftrightarrow \quad \nabla\cdot\big(\mu_0(\mathbf{T}-\nabla\Phi)\big)=0 \end{aligned} \qquad (4.15)$$

In order to insure uniqueness of the solution of Eqs. (4-15), a gauge condition $\nabla\cdot\mathbf{T}=0$ must be also added [Vin00a].

The A-V formulation

This formulation is based on the magnetic vector potential **A** and the electric scalar potential V. **A** has no physical meaning but is a suitable auxiliary variable, defined from:

$$\mathbf{B}=\nabla\times\mathbf{A} \qquad (4.16)$$

Introducing **A** in Faraday's law, the electric field is then expressed as:

$$\mathbf{E}=-\frac{\partial\mathbf{A}}{\partial t}-\nabla V \qquad (4.17)$$

where ∇V is a voltage gradient (scalar).

The general equation to be solved is Ampere's law:

$$\nabla\times\frac{1}{\mu_0}\nabla\times\mathbf{A}+\sigma\left(\frac{\partial\mathbf{A}}{\partial t}+\nabla V\right)=0 \qquad (4.18)$$

More details about the **A**-V formulation are given in the next section.

4.5 FEM modelling of HTS with Flux2D

4.5.1 Implementation of the E-J power law model in Flux2D

All numerical results for modelling of HTS, presented in this thesis, have been obtained with Flux2D, which is finite element method software package for 2D electromagnetic problems [Flux2D]. Flux2D uses the Galerkin method for formulating the FEM equations, the basic principle of which is given in Appendix B and more details can be found in [Bin92] and [Sal95]. The implementation of the nonlinear model of HTS materials in Flux2D was done by Nadia Nibbio during her Ph.D. thesis, realized in our laboratory at the Swiss Federal Institute of Technology – Lausanne [Nib99].

The constitutive equations of HTS used in the Flux2D implementation are:

$$\begin{aligned}\mathbf{B} &= \mu_0 \mathbf{H}\\ \mathbf{J} &= \sigma(E,B)\mathbf{E}\end{aligned} \tag{4.19}$$

where the electric field is linked to the current density by the power-law model,

$$\mathbf{E} = E_c \left(\frac{|\mathbf{J}|}{J_{c(B)}} \right)^{n(B)-1} \frac{\mathbf{J}}{J_{c(B)}} \tag{4.20}$$

with the possibility to include a dependence of J_c and n on the magnetic flux density.

The nonlinear conductivity of the superconductor can be expressed from Ohm's law and Eq. (4.20) as:

$$\sigma(E,B) = J_c(B) \frac{|E|^{\frac{1-n(B)}{n(B)}}}{E_c^{1/n(B)}} \tag{4.21}$$

In 2D, the electric field *E(x,y)* and the current density *J(x,y)* are parallel and directed along the z-axis, i.e. in the FEM simulations they are always perpendicular to the cross-section of the conductor. The material properties along the *z*-direction in this 2D model are assumed to be isotropic.

The numerical computation in Flux2D is performed with the **A**-V formulation, whose general state equation is Ampere's law, Eq. (4.18), written in 2D as follows:

$$\nabla \frac{1}{\mu_0} \nabla A_z + \sigma(E,B) \frac{\partial A_z}{\partial t} = -\sigma(E,B) \nabla V \tag{4.22}$$

where $A_z(x,y)$ is the *z*-component of the magnetic vector potential and ∇V is a voltage source, applied uniformly to the cross-section of the conductor.

The material properties of the superconductor are introduced by means of a special user-subroutine [Nib99]. The nonlinear resistivity of the HTS is defined using Eq. (4.21) as follows:

$$\rho(E,B)=\frac{E_c^{1/n(B)}}{J_c(B)}\left|E\right|^{\frac{n(B)-1}{n(B)}}+\rho_0 \tag{4.23}$$

where ρ_0 is a finite residual resistivity, which is added for numerical stability of the algorithm, see Section 4.5.3 below. When the value of ρ_0 is properly selected, it does not influence the current and field distribution or AC loss calculation.

The AC loss per cycle in the volume v of the superconductor, expressed in Joules, is calculated as follows:

$$Q_{sc}=\int_0^{1/\mathrm{f}} dt\int_v J\cdot E dv \tag{4.24}$$

where f is the frequency of the applied current or magnetic field.

Equation (4.24) gives the total loss (hysteresis and Ohmic) in the superconductor in the case of applied current and/or magnetic field [Rhy93].

All simulations are performed for two complete AC cycles with 80 time steps per cycle. Processed and presented are the results from the second cycle.

4.5.2 Newton-Raphson algorithm for nonlinear problems

The numerical algorithm used in Flux2D for finding the solution of Eq. (4.22) is shown with a flow chart in Fig. 4-6. The solution is simultaneously calculated for all the nodes on the FEM mesh for a given time step. For a nonlinear problem, which is the case of superconducting materials, a system of nonlinear algebraic equations must be solved. The solution of this nonlinear system cannot be obtained with one single step and a certain number of iterations are required. There are different iterative methods, among which the so-called Newton-Raphson method is commonly used [Bin92], [Sal95].

We shall briefly remind the main principle of the Newton-Raphson algorithm, applied for the simulation of HTS in Flux2D [Nib00]. The state equation for any node to be solved is Eq. (4.22), which can be summarized with the operator

$$R(A)=0 \tag{4.25}$$

Equation (4.25) can be expanded around the starting value A_0 in a Taylor series, keeping only the first order terms:

$$R(\mathrm{A}_0+\Delta\mathrm{A})=R(\mathrm{A}_0)+\frac{\partial R}{\partial A}\Delta\mathrm{A}=0 \tag{4.26}$$

$$\Rightarrow\frac{\partial R}{\partial A}\Delta\mathrm{A}=-\mathrm{R}(\mathrm{A}_0) \tag{4.27}$$

From the initial estimate we can find

$$\mathrm{A}_1=\mathrm{A}_0+\Delta\mathrm{A} \tag{4.28}$$

and so forth until it converges to the solution. The iteration procedure is stopped when the vector ΔA_k is negligible compared to the solution A_k, which is defined by the precision criterion ε, see Fig. 4-6. It is to be noted that if the derivative term is not updated at each iteration, the solution will still converge. More iterations will be required, but since the algorithm continues until the precision criterion is met, the result is still valid.

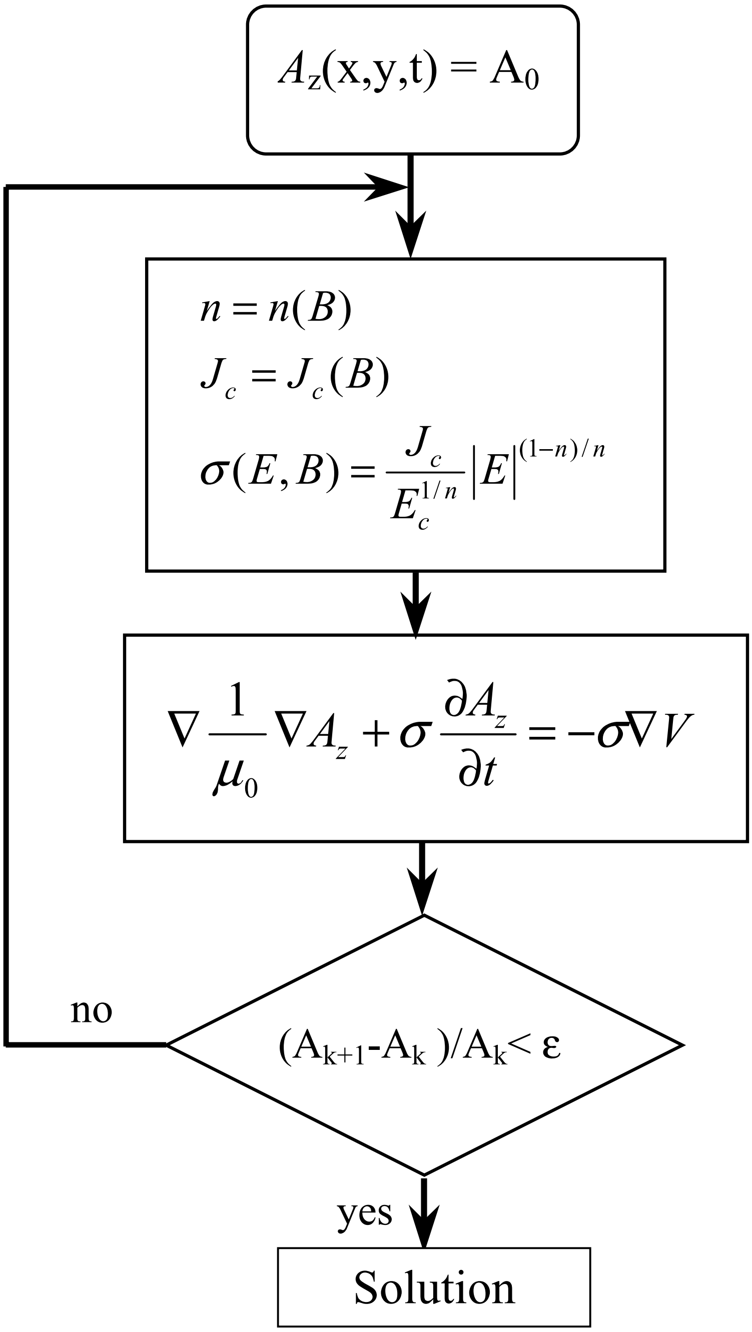

Figure 4-6 Algorithm for finding the solution of Ampere's law using the special subroutine for HTS in Flux2D. The nonlinear solver uses the Newton-Raphson method. A_0 are the initial conditions and ε is the required precision criterion.

The method provides fast convergence provided that sufficiently good starting values are used. An example of the iterative process for finding a solution using the Newton-Raphson algorithm is shown in Fig. 4-7. The algorithm may converge or diverge depending on how close to the exact solution the starting value is.

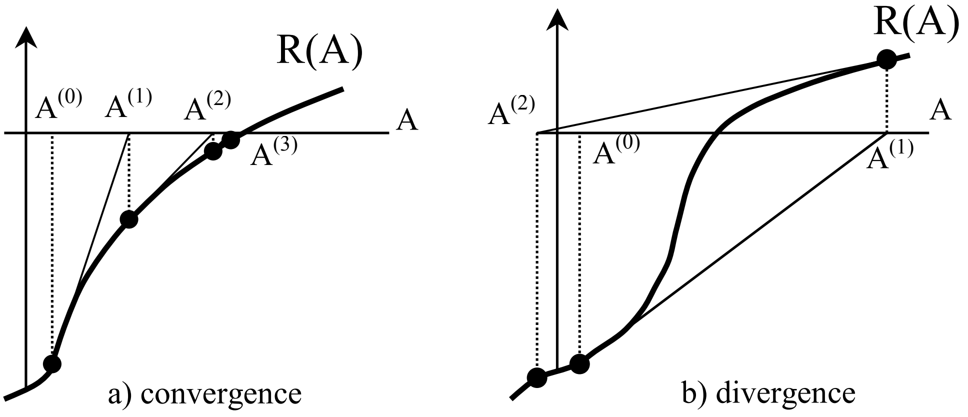

a) convergence

b) divergence

Figure 4-7 Finding the solution of a nonlinear equation by Newton-Raphson algorithm.

Different convergence problems may arise when simulating HTS materials with nonlinear *E-J* characteristics, especially for higher *n*-values [Vin00a]. The Flux2D implementation has been tested with *n*-values up to 100, and convergence has been achieved. However, the higher *n*, the longer it takes for the Newton-Raphson algorithm to converge. The CPU time for different *n*-values is shown in Fig. 4-8; see also Section 4.5.5.

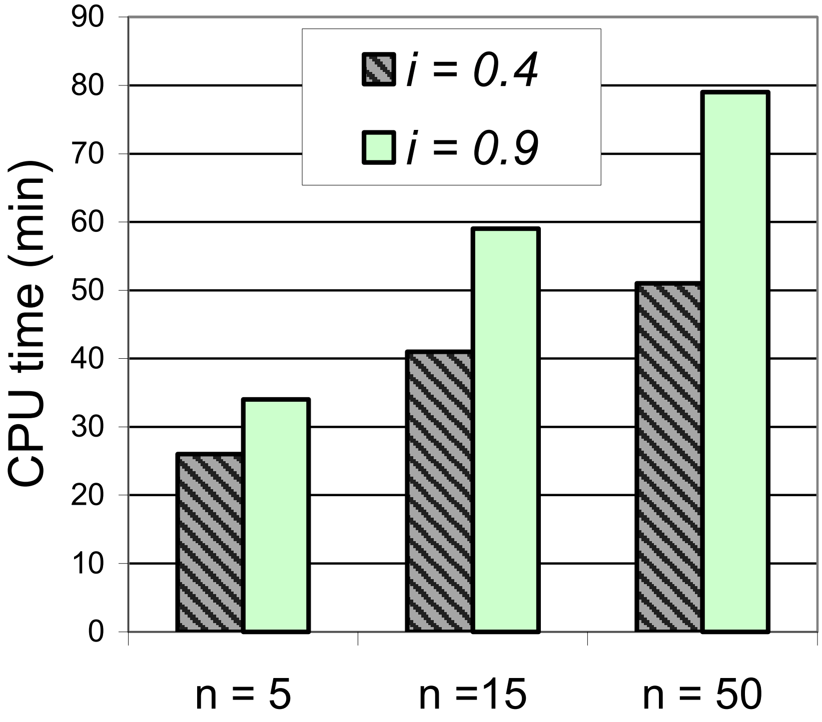

Figure 4-8 CPU time needed for simulation of 2 cycles (160 time steps) on a mono-filamentary tape with reduced current ratio of 0.4 and 0.9. The simulation is performed on a Pentium III, 800 MHz PC.

4.5.3 Effect of the residual resistivity ρ_0

The nonlinear solver with the Newton-Raphson method calculates in each node the values of the electric field *E* and the current density *J*. With the power-law current-voltage characteristics of HTS, expressed by Eq. (4.20), taking $J_c = 1\times10^8$ A/m^2 and $n = 10$, the values of *E* are of the order of 1×10^{-14} V/m for $|J| < 0.2\ J_c$, while *J* is of the order of 1×10^7 A/m^2, which means that these two physical quantities differ by more than 20 orders of magnitude. This enormous difference creates additional problems in the numerical simulations, especially in the regions with low current density, where the electric field is very close to zero. A critical point is the passage of *E* through zero, when *J* changes directions, which means that the local value of the conductivity σ becomes infinite at this instant. In such regions the algorithm may never converge.

For reasons of numerical stability of the algorithm in the passage through zero, a finite residual resistivity ρ_0 has been added in Eq. (4.23). From a physical point of view, this additional linear term may be interpreted as the thermally activated resistance at 77 K, see Fig. 2-13. The *E-J* characteristics with different values of the residual resistivity are displayed in Fig. 4-9 and the effect of ρ_0 on the AC loss in self-field is shown in Fig. 4-10.

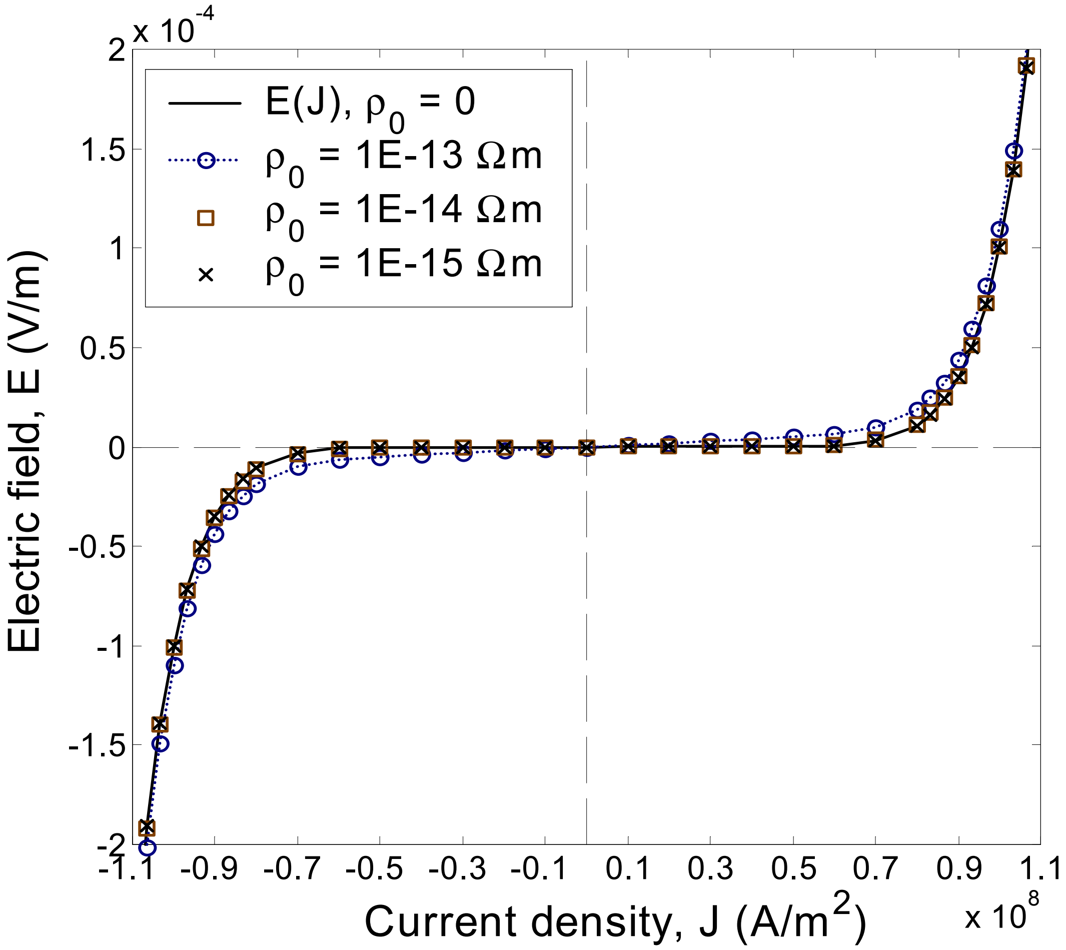

Figure 4-9 Influence of the residual resistivity ρ_0 on the power-law E-J characteristics with *n* = 10, $J_c = 1\times10^8$ A/m^2 and $E_c = 1\times10^{-4}$ V/m.

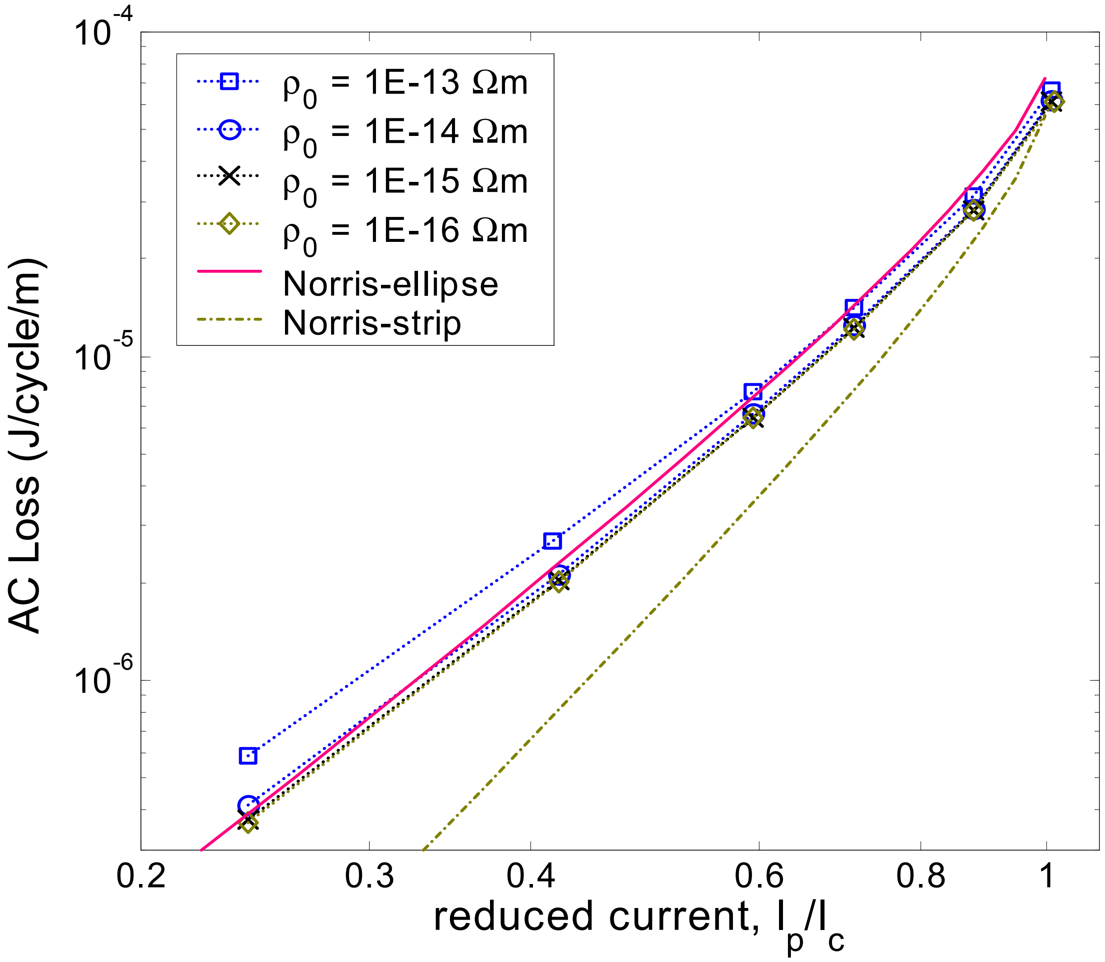

Figure 4-10 Effect of the residual resistivity ρ_0 on the AC loss of a monofilamentary tape in self-field with n = 15 and $J_c = 5\times10^7$ A/m^2.

As can be seen in Figs. 4-9 and 4-10, the value of 1×10^{-13} Ωm is obviously too large and results in excessive calculated AC loss. On the other hand, when taking a very low value, for example 1×10^{-16} Ωm, even though the AC loss computation is correct, there may be numerical oscillations in the calculation of the current density, as shown in Fig. 4-11. These oscillations may be reduced by refining the mesh at the expense of CPU time, as demonstrated in Section 4.5.5.

In conclusion, the value of ρ_0 must be carefully selected. It depends on the parameters J_c and E_c of the material. The optimal value of ρ_0 has been found to be in the range $0.001\times E_c/J_c - 0.01\times E_c/J_c$.

Similarly, in the numerical formulations, which use the conductivity σ in the non-linear Ohm's law, a maximum value of σ is set at $1\times10^{13} - 1\times10^{15}$ S/m in order to enhance the efficiency of the calculations [Ame98a].

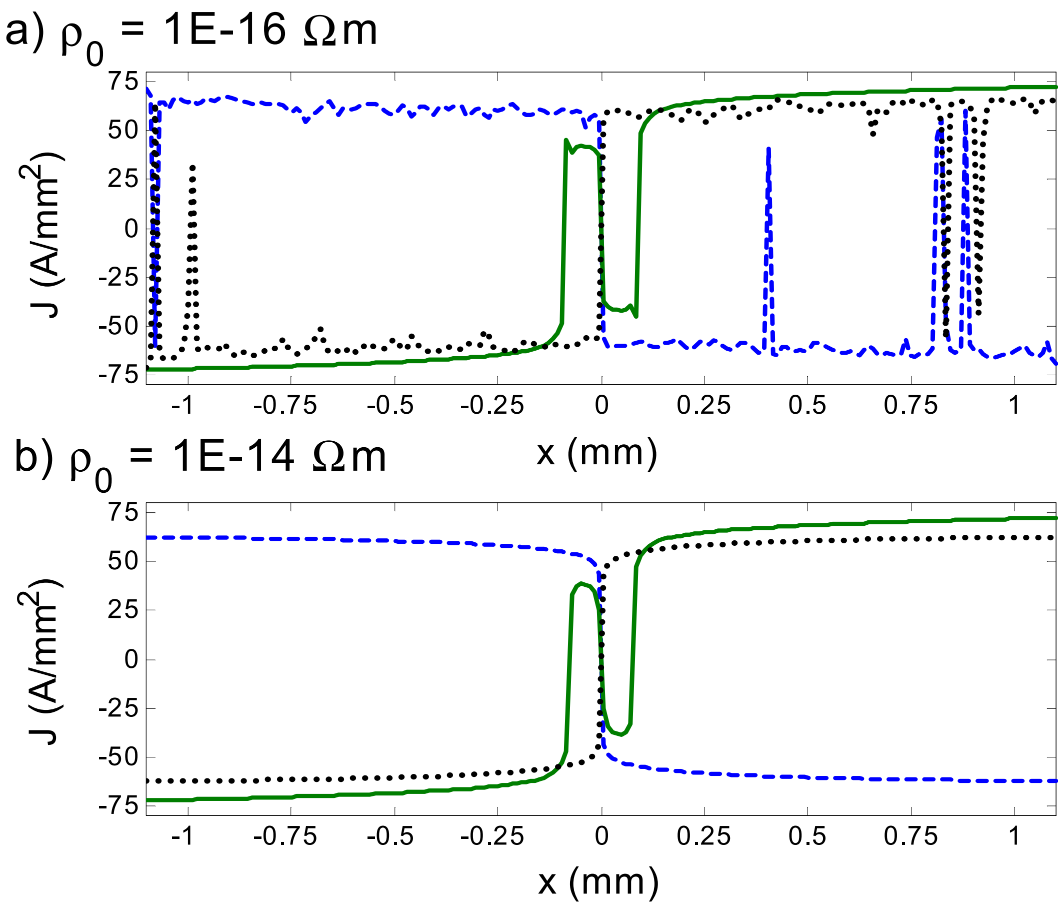

Figure 4-11 Numerical oscillations in the current density due to a very low value of the residual resistivity (a) and a smooth J-profile (b). Shown are the J-profiles at ωt = –π/2, π, +π/2 in perpendicular magnetic field of 20 mT along the central line-segment of the tape.

4.5.4 Boundary conditions for different applications

The simulation of different operating conditions, for example applied external field of a given orientation, is performed by setting the appropriate values for the magnetic vector potential A on the domain boundary, see Fig 4-12. Examples for the type of boundary conditions needed for certain applications are given in Table 4.1. For applying an external magnetic field of orientation other than parallel or perpendicular to the x-axis, the domain boundaries must be rotated with respect to the x- and y-axis by the desired angle or orientation of the applied field. It is also possible to rotate the whole conductor but for complex geometries this is rather cumbersome and time consuming.

For simulations of applied transport current to a HTS, Flux2D uses a voltage source – the voltage gradient ∇V in Eq. (4.22), which is defined during the description of the physical properties of the material and represents a constant voltage applied to the cross-section of the conductor. Because of the almost 90° phase-difference between the voltage and current in a superconductor, the voltage source $V = V_{max}\cos(\omega t)$ is a cosine wave, thus ensuring a resulting sine current. This is equivalent to starting the simulations from zero-current initial conditions. Two complete cycles are always simulated and the results from the second cycle are processed.

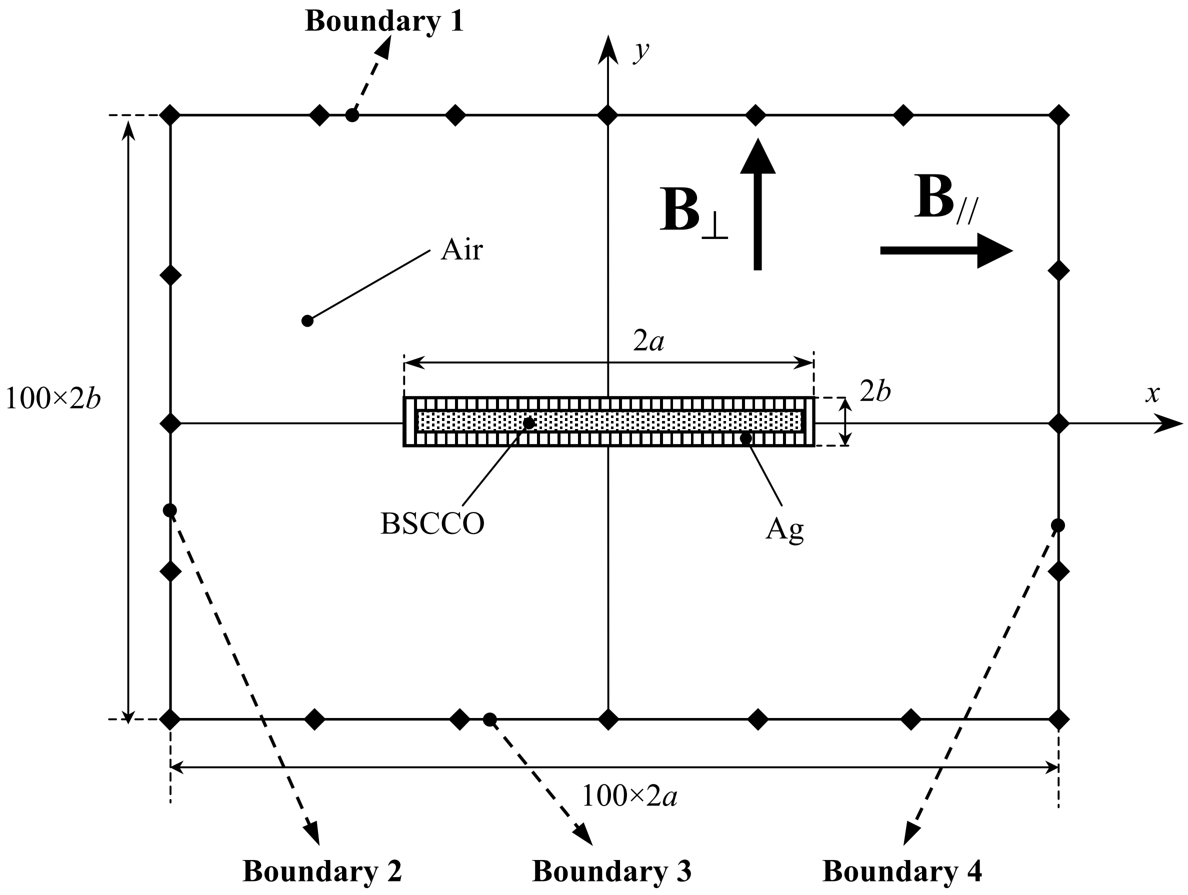

Figure 4-12 Problem domain and boundaries in FEM simulations.

For simulations in AC magnetic field, sinusoidal boundary conditions of the magnetic vector potential A are used, which is equivalent to the application of sine magnetic field with zero amplitude at t = 0.

Table 4.1 Boundary conditions for different applications in Flux2D

Boundary	self-field ($B_{ext} = 0$)	Perpendicular field ($B_\perp$)	Parallel field ($B_{//}$)
1	Dirichlet: A = 0	Neumann: ∂A / ∂n = 0	Dirichlet: A = A_0sin(ωt)
2	Dirichlet: A = 0	Dirichlet: A = A_0sin(ωt)	Neumann: ∂A / ∂n = 0
3	Dirichlet: A = 0	Neumann: ∂A / ∂n = 0	Dirichlet: A = -A_0sin(ωt)
4	Dirichlet: A = 0	Dirichlet: A = -A_0sin(ωt)	Neumann: ∂A / ∂n = 0

A Dirichlet boundary condition indicates that the magnetic flux lines are parallel to the boundary (A = constant), while a Neumann boundary condition indicates that the field lines are perpendicular to the boundary (∂A / ∂n = 0).

4.5.5 Mesh optimization and CPU time

In any FEM simulation, the problem domain is divided into regions, which in turn are subdivided into small elements of different shape, the *finite elements*, see Appendix B. The arrangement of the finite elements is referred to as *FEM mesh*. The fineness of the mesh is defined by the required computation precision in each region, determined by the expected relative difference of the electromagnetic quantities (E, J, A) in two adjacent elements.

An example of the FEM mesh used for the simulation of a superconducting tape of rectangular geometry is shown in Fig. 4-13.

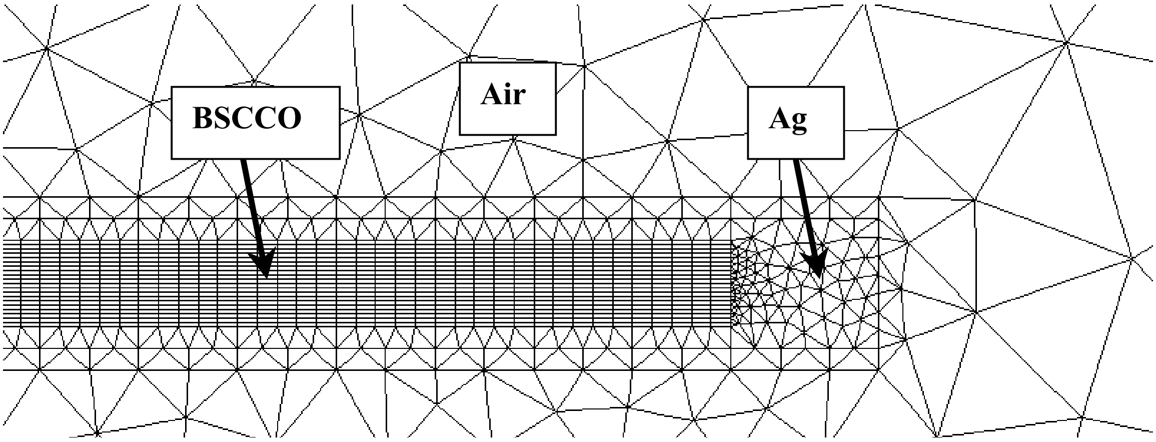

Figure 4-13 FEM mesh used for simulations of a HTS tape with rectangular geometry (2.7 mm × 0.32 mm). The finest mesh is in the BSCCO region (1200 elements).

The finer the mesh in the superconductor, the higher the numerical precision obtained. However, a fine mesh requires a great number of finite elements, and consequently considerable CPU time and hard disk memory.

In order to define the optimal mesh for simulations of HTS, we have used a rectangular tape with different number of elements. The mesh details are given in Table 4.2. The elements in the BSCCO region are of brick (rectangular) type, while in the silver and in the air the default triangular elements are used.

Table 4.2 Mesh with different number of finite elements in a BSCCO tape.

Mesh	Elements in BSCCO	Total number of elements	Total number of nodes
20 × 5	100	1074	2273
60 × 5	300	1618	3561
60 × 10	600	1964	4553
60 × 20	1200	2708	6641
120 × 10	1200	3358	7941
120 × 20	2400	4692	11809

The 3rd and 4th column indicate the total number of elements and nodes in the whole problem domain, including the Ag and air regions.

The calculated AC losses in the rectangular tape with different applied current ratio are shown in Fig. 4-14. As can be seen in the figure, the calculated AC loss even with a rather coarse mesh of 20 × 5 elements in the BSCCO produces the same results as the finest mesh of 120 × 20 (the difference is less than 2 %) The CPU time and hard disk memory, necessary for simulation and storage of the results of 2 cycles for mesh with different fineness, are displayed in Fig. 4-15.

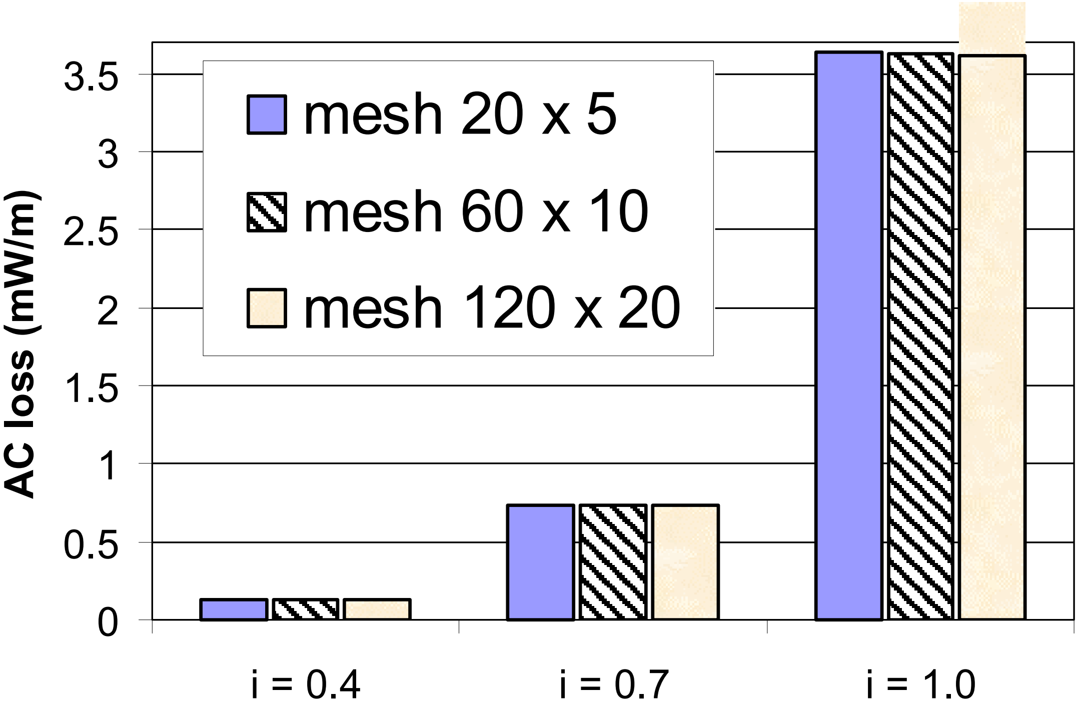

Figure 4-14 AC loss in self-field for mesh with different fineness. *i* is the reduced applied current ratio I_p/I_c.

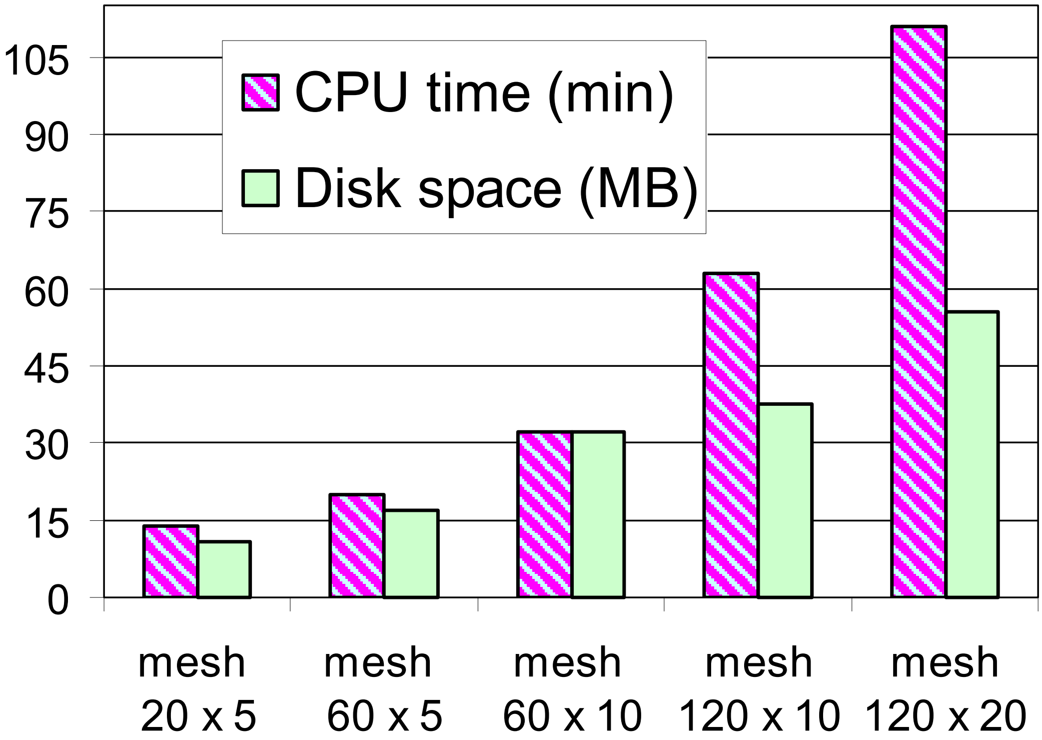

Figure 4-15 CPU time and disk memory for simulation of 2 cycles (storage of every other time step out of 80 per cycle). The simulation is performed on a Pentium III, 800 MHz PC

Figure 4-15 indicates the advantages of using a coarse mesh – lower CPU time and memory consumption. However, while useful for quick computation of AC losses in certain applications, the course mesh may result, for example, in inaccurate interpolation of the current density between neighboring elements. The influence of the mesh on the current density profile along a straight line in the center of the rectangular tape is shown in Fig. 4-16. The numerical oscillations in a course mesh are stronger for lower applied currents and/or lower value of the additional resistivity ρ_0.

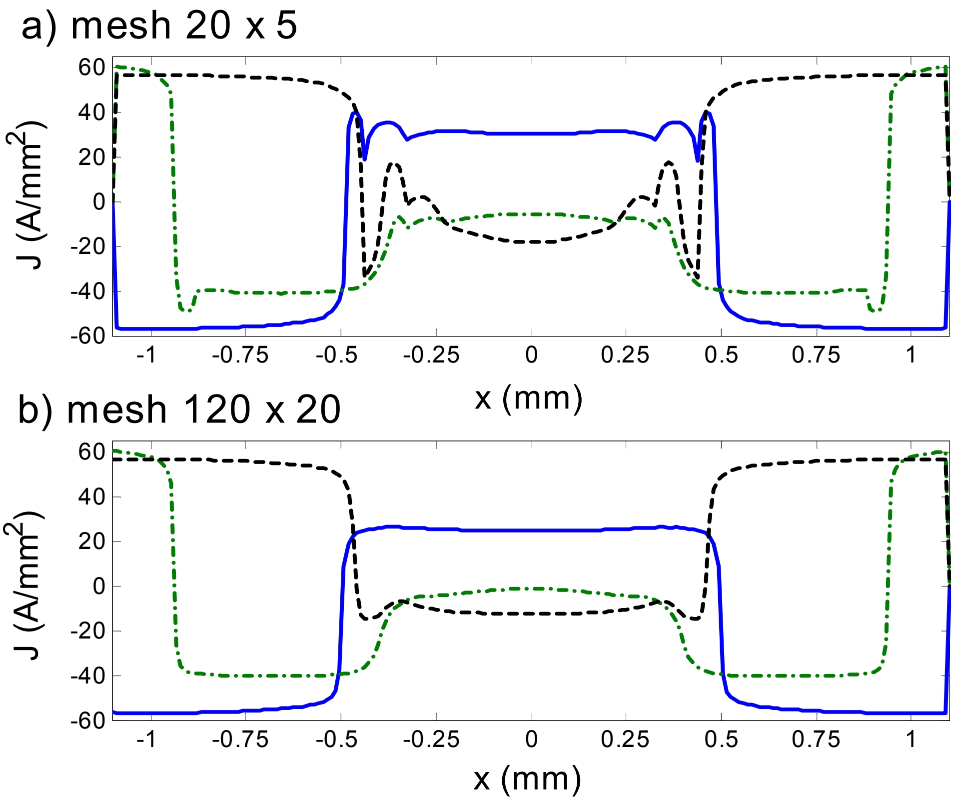

Figure 4-16 Oscillations in the current density profile due to the coarse mesh (a), compared to a smooth J-profile with fine mesh (b). Applied is a transport current with peak value 0.9 I_c. Shown are the J-profiles at $\omega t = -\pi/2, \pi, +\pi/2$. The residual resistivity ρ_0 is $1\times10^{-14}\ \Omega$m.

4.6 AC losses and current distribution in HTS tapes – validation of the Flux2D implementation

In shall be noted that in the 2D simulations with Flux2D the length *l* of the conductor is given as a parameter, usually $l = 1$ m, which is used only for calculating the volume loss. Otherwise, the current return takes place at 'infinity', which is equivalent to having a twist pitch of infinite length. Therefore, the superconducting filaments in applied field or transport current conditions are always coupled regardless of the values of the field. The coupling currents in the matrix, however, are not taken into account by the **A**-V formulation in 2D, in which the current is always parallel to the *z*-direction, and the coupling current loss in the silver is not calculated.

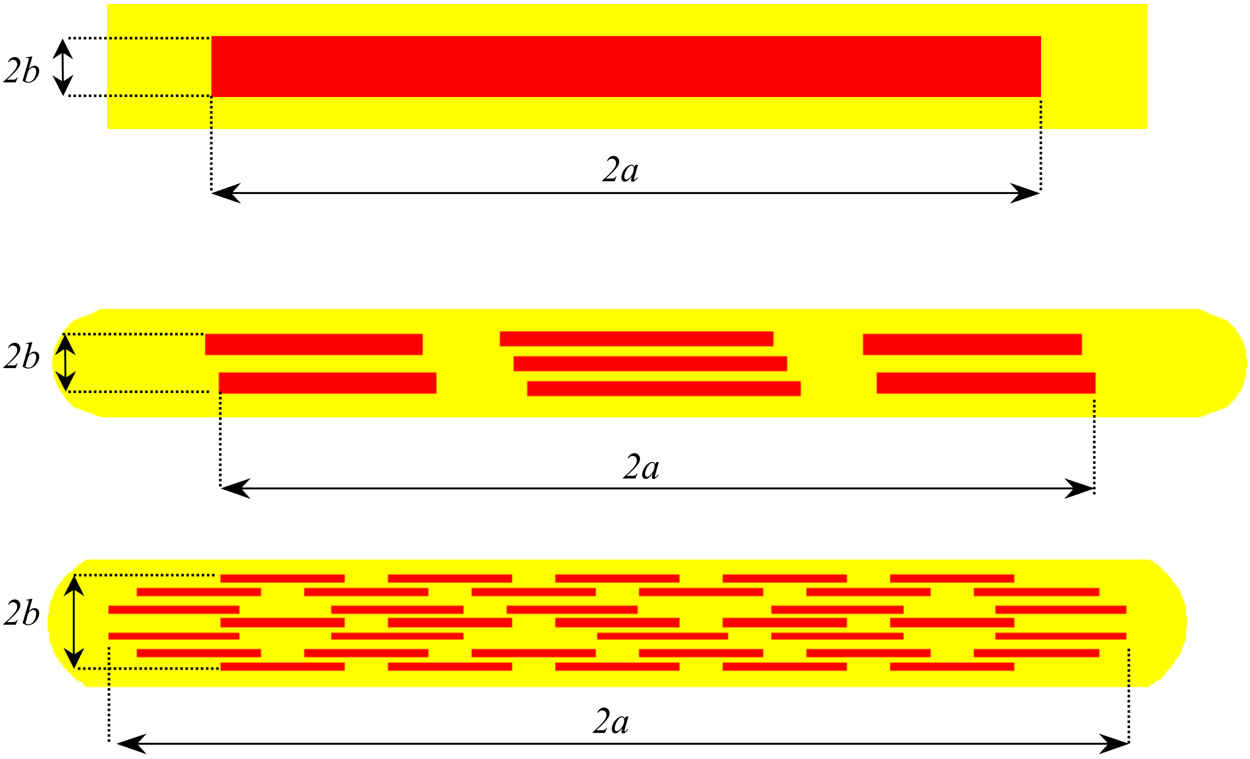

Figure 4-17 Geometries of tapes used in the Flux2D simulations. The dimensions of the tape and the filament arrangement are similar to the ones of genuine Bi-2223 tapes.

In order to validate the implementation of the nonlinear model of HTS in Flux2D, we have made a series of simulations and made comparison with measurements and analytical results. The simulations were performed on a monofilamentary, a 7-filamentary and a 37-filamentary BSCCO tape with power-law *E-J* characteristics, whose geometries are shown in Fig. 4-17 and are similar to the ones of the experimental samples.

Table 4.3 Geometry of the BSCCO tapes used for numerical simulations

tape	**fill-factor**	**width, 2*a* (mm)**	**thiskness, 2*b* (mm)**	**aspect ratio *a*/*b***	***n*-value**
monofilamentary	0.40	2.2	0.16	13.8	19
7-filamentary	0.27	3.2	0.24	13.3	21
37-filamentary	0.34	2.8	0.28	10	13

Given are the dimensions and the aspect ratio of the BSCCO core. For the multifilamentary tapes, these are the dimensions of the filament region. The *n*-value is the same as in the genuine tapes.

4.6.1 Comparison with measurements and Norris's losses in self-field

The current distribution based on the CSM in superconductors with rectangular cross-section has been described by Norris in his original paper [Nor70]. The determination of the current contour depends on the aspect ratio (width/thickness) of the conductor – for infinitely wide flat sheets the contours are straight lines parallel to the surface, while for rectangular conductors with finite thickness the current contours are of elliptical shape.

Figures 4-18 and 4-19 display respectively the current penetration profile in a rectangular superconductor in the CSM, as given by Norris, and in the simulated by Flux2D HTS tape with power-law *E-J* characteristics. Note the similarity in the shape of the current-carrying and current-free regions. The difference between the analytical and simulated current distribution is that in the CSM the current density is either $\pm J_c$ or zero everywhere, while in a HTS tape with finite *n*-value the current density is not uniform – the reversed current density near the edges of the tape exceeds (although slightly) J_c and at the same time in the internal contour with positive current J is well below J_c.

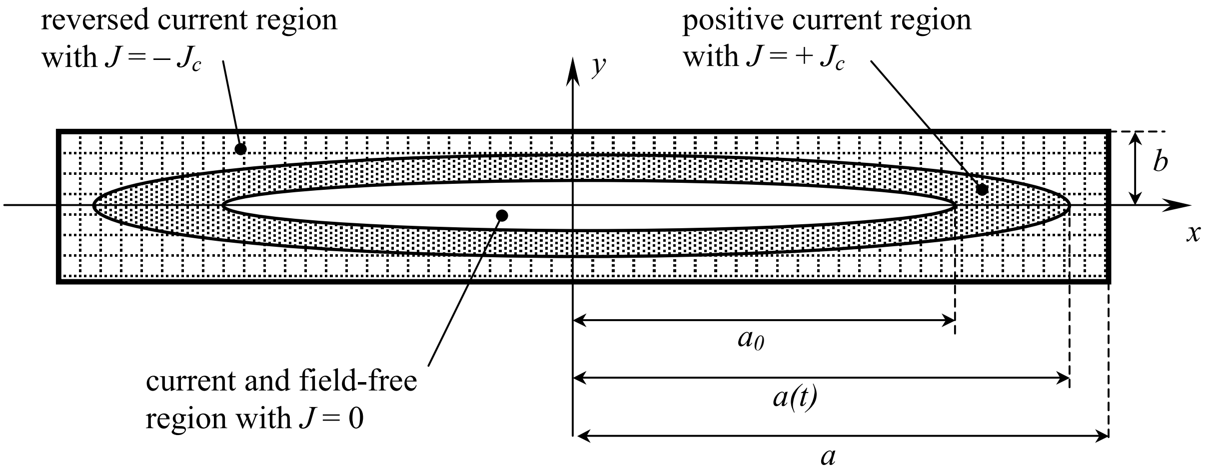

Figure 4-18 The current penetration profiles for a superconductor with rectangular cross-section of half-thickness *b* and half-width *a*, as described by Norris. a_0 represents the limit of the field and current free region and *a*(*t*) defines the current reversal contour.

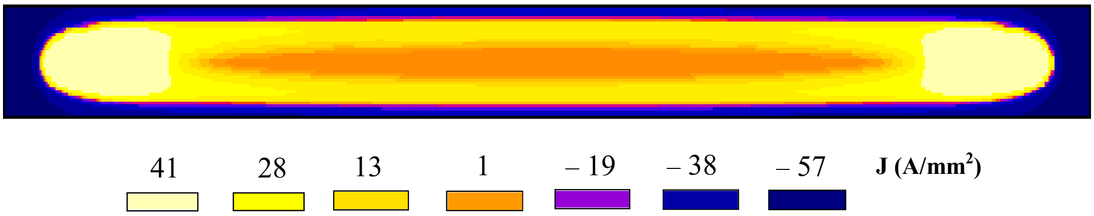

Figure 4-19 Current density profile in the superconducting core obtained with Flux2D at $\omega t = \pi$ with peak transport current of 0.6 I_c. J_c = 54 A/mm^2 is constant and *n* = 19.

A comparison between the simulated and measured AC losses in self-field for the monofilamentary, 7- and 37-filamentary tapes is shown in Fig. 4-20. Plotted are also Norris's predictions for elliptical and strip geometry. The simulation results are quite close to the measured AC loss in all cases.

Note that the simulated loss for the monocore tape is close to Norris's elliptical rather than the strip prediction. The main reasons for this are threefold. Firstly, as commented by Norris, in a conductor of finite thickness there will be additional loss, compared to the strip geometry, where the thickness is infinitesimal. Secondly, the CSM does not fully apply to HTS with broad *E-J* characteristics. Close to the edges of the tape there are regions, where locally $J > J_c$ even if there is a current-free zone in the center. These are regions with high power dissipation, contributing to the increased AC loss compared to the one calculated with the CSM model. Last but not least comes the influence of the finite n-value – the lower n, the higher the AC loss is in the region $I_p < 0.8\ I_c$, see also Section 4.7.

Another interesting point is that the AC loss in the 7-filamentary tape (both measured and simulated) is lower than in the other two tapes. The main reason is the filament arrangement of the 7-filamentary tape, where 3 separate stacks are formed, see Fig. 4-17, while in the 37-filamentary tape the filaments are interleaved in a bundle and behave like a monocore tape in self-field.

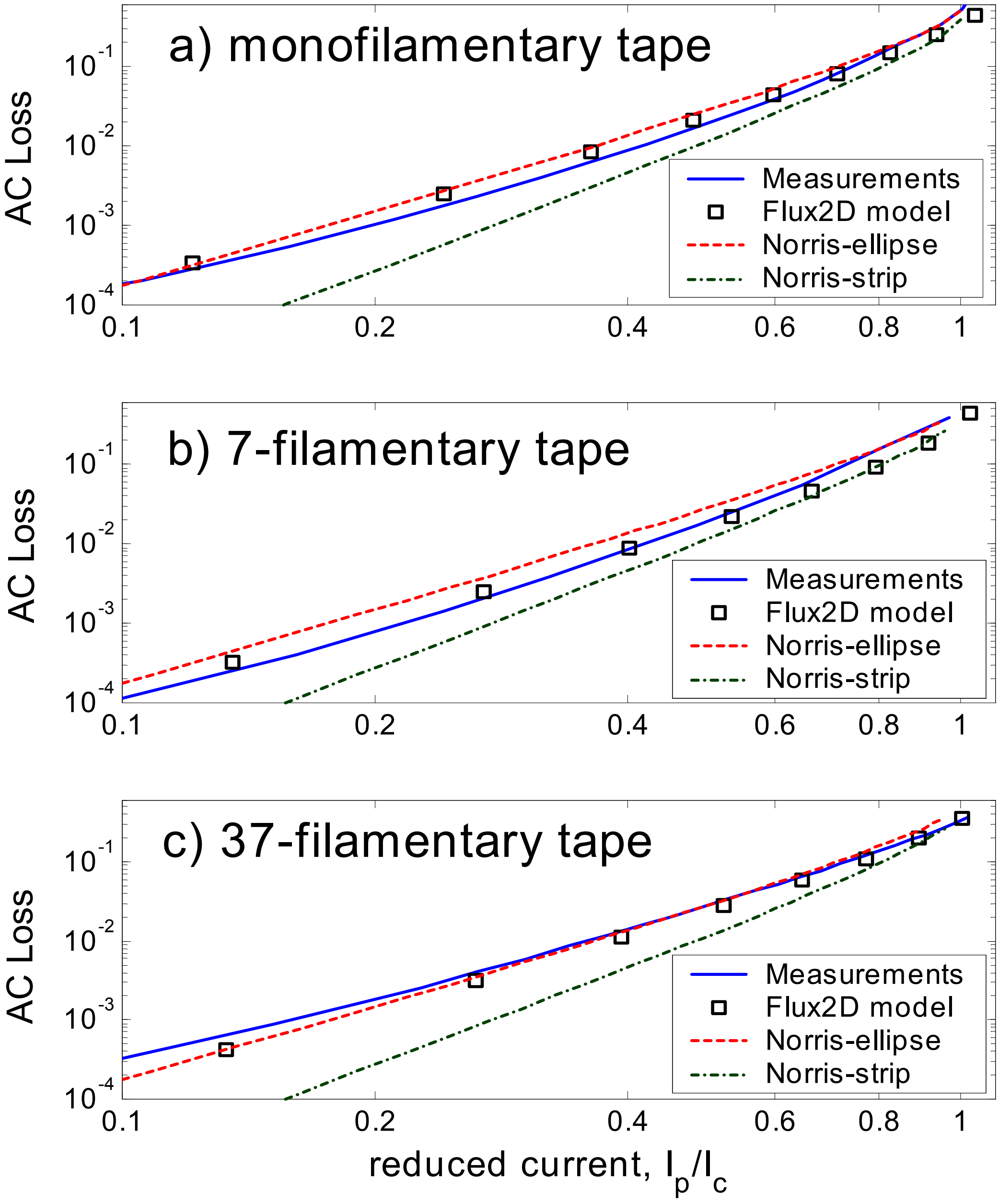

Figure 4-20 Comparison of simulated, measured and theoretical AC loss in self-field. The loss is normalized by $\left(\mu_0 I_c^2/\pi\right)$ to make it independent of the critical current of each tape.

4.6.2 Comparison with Brandt's model and the CSM in applied field

We have made a quantitative comparison between the current distribution and AC loss obtained in the monofilamentary tape with Flux2D, and with the numerical algorithm based on Brandt's method, described in Section 4.4.1. The application of transport current, as well as external magnetic field of parallel and perpendicular orientation has been simulated. In all numerical simulations, a constant J_c of 54 A/mm^2 and n-value of 15 were used.

Figure 4-21 shows comparative plots of the current density distribution in a HTS rectangular tape for two different time steps ($\omega t = \pi$ and $\omega t = 2\pi$) with peak transport current 0.95 I_c. At such amplitude, the current penetration is complete and there is no current-free zone in the centre of the tape. The AC losses in self-field are compared in Fig. 4-22. The numerically calculated AC losses with Flux2D and Brandt's algorithm fall very close to Norris's elliptical prediction.

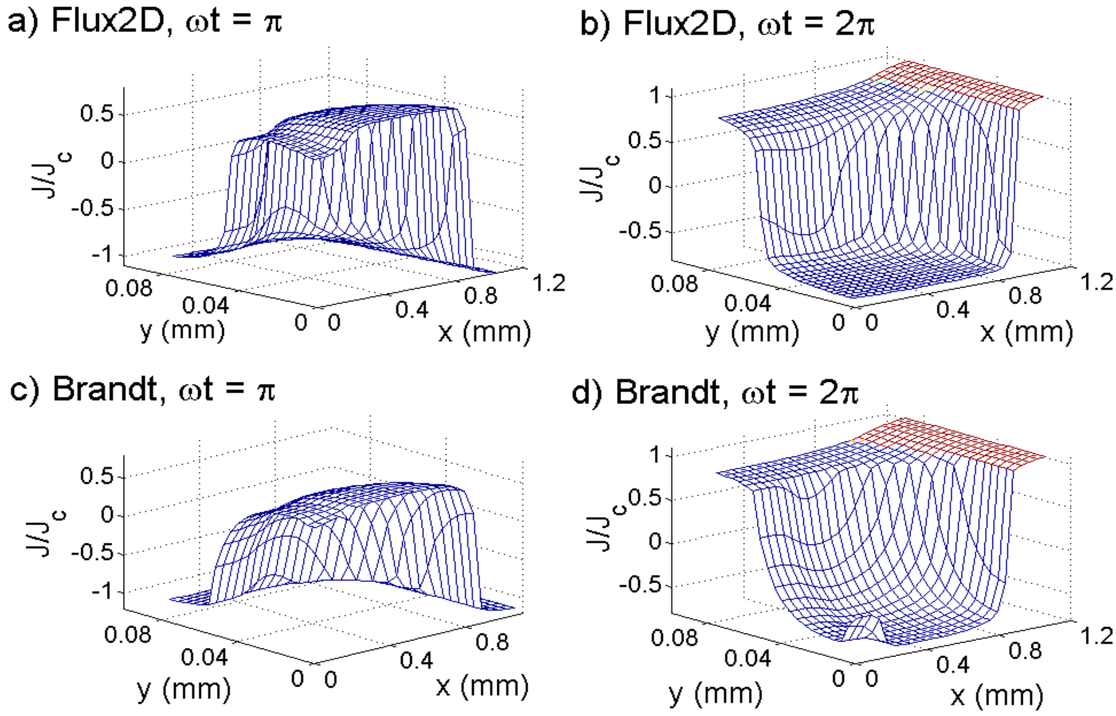

Figure 4-21 Current density profile in one quarter of a rectangular HTS tape with applied peak transport current of 0.95 I_c, calculated numerically with Flux2D and Brandt's algorithm.

The current density profiles in applied external magnetic field of 5 mT, perpendicular to the broad side of the tape, are compared in Fig. 4-23. This amplitude is below the full penetration field (B_p) and there is a current (and flux) free region in the center of the tape, obtained with both numerical simulations.

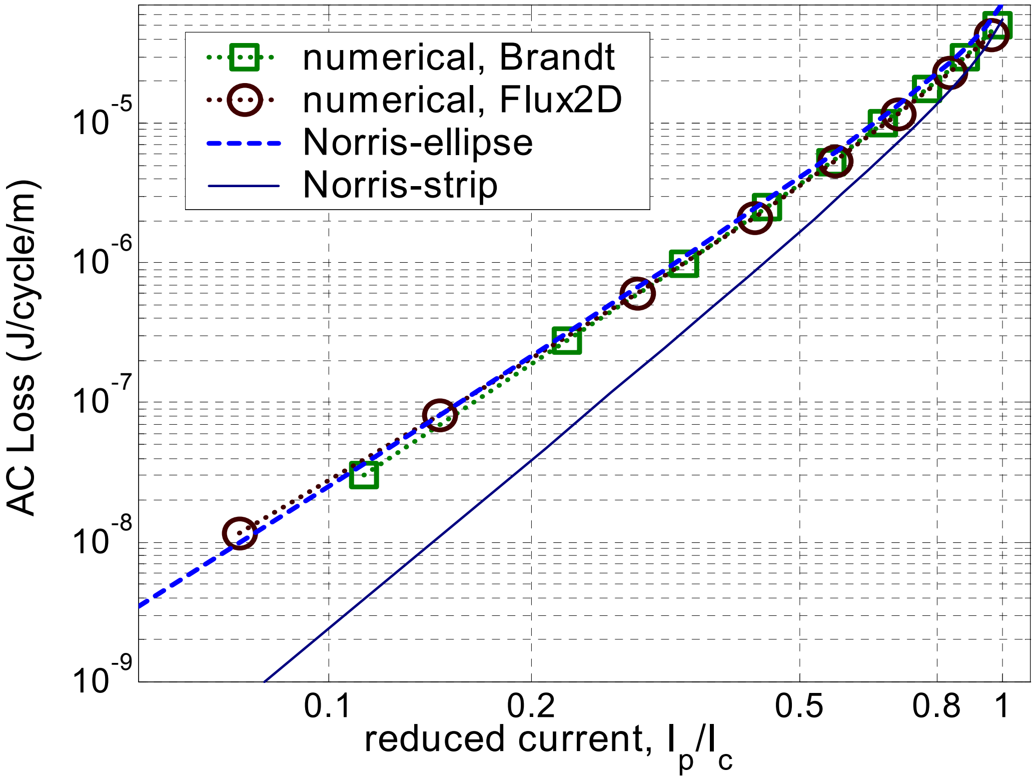

Figure 4-22 AC loss in self-field for a monofilamentary tape of rectangular cross-section, calculated numerically with Flux2D and Brandt's algorithm.

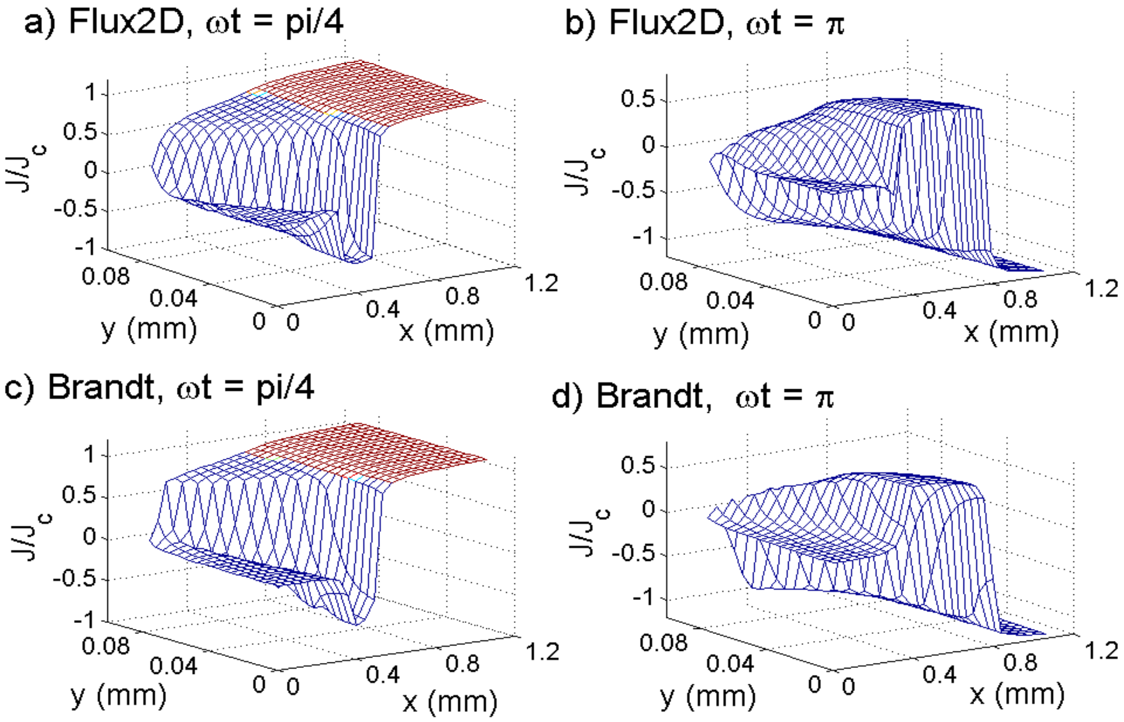

Figure 4-23 Current density profile in one quarter of a rectangular HTS tape with applied perpendicular field of 5 mT, calculated numerically with Flux2D and Brandt's algorithm.

The magnetization loss in a superconducting slab in the CSM has been calculated theoretically; see for example [Cam82] or [Wil83]:

$$Q_m = \frac{2B_a^2}{\mu_0}\left[\frac{\beta}{3}\right] \qquad for \quad \beta \le 1$$
$$Q_m = \frac{2B_a^2}{\mu_0}\left[\frac{1}{\beta} - \frac{2}{3\beta^2}\right] \qquad for \quad \beta \ge 1 \tag{4.29}$$

where Q_m is given in J/cycle/m^3 and β is the ratio of the applied field B_a to the full penetration field B_p. The latter is equal to $\mu_0 J_c a$, where a is the half-thickness of the slab.

A comparison between the numerically calculated magnetization loss with Flux2D and Brandt's algorithm in a rectangular tape in parallel field, and the theoretical loss for a slab from Eq. (4.29), is shown in Fig. 4-24. The numerically calculated losses are practically identical. They are very close to the theoretical loss for fields above 10 mT and slightly higher than the theoretical one for fields below 10 mT.

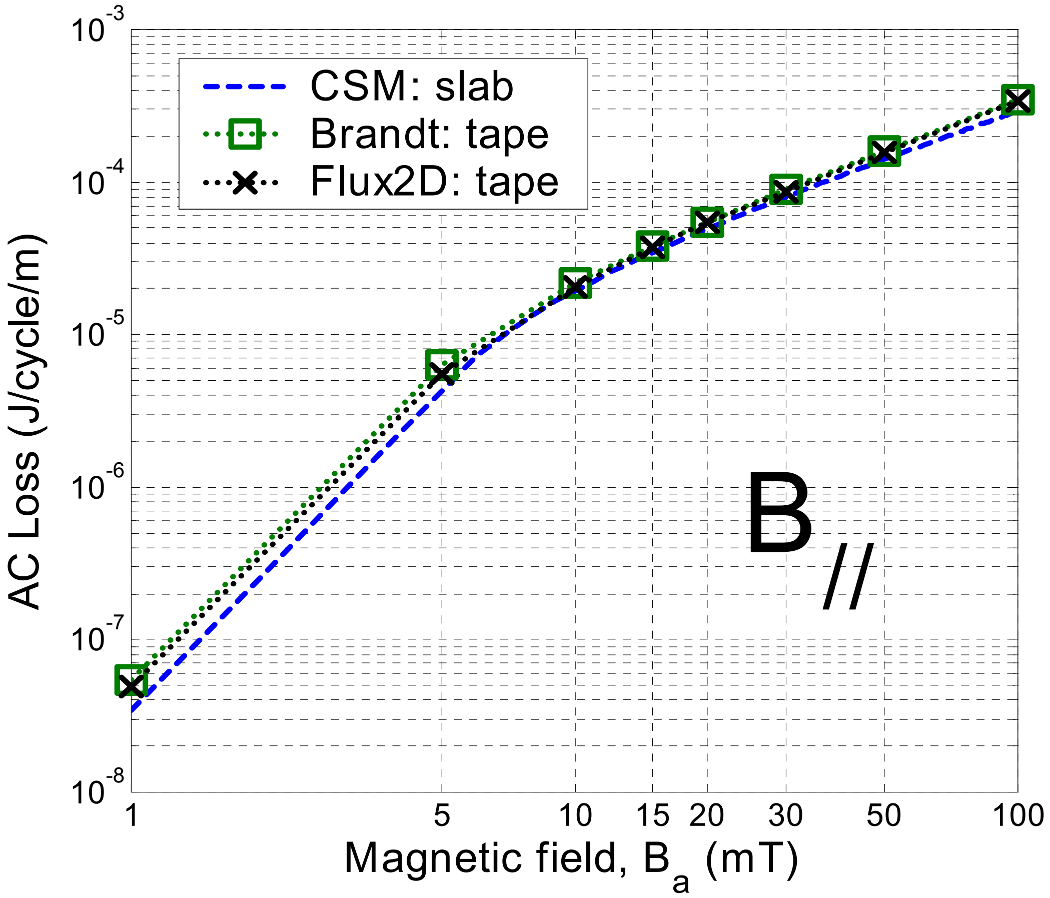

Figure 4-24 AC loss in parallel field for a monofilamentary tape of rectangular cross-section, calculated with Flux2D and with Brandt's algorithm. Given is also the analytical loss for a slab from Eq. (4.29).

The hysteresis loss, based on the magnetization of a superconducting strip with constant J_c in perpendicular field has been calculated by Müller *et al.* [Mül95]:

$$Q_h = \frac{2B_a^2}{\mu_0}\frac{\pi a}{2\beta b}\left(\frac{2}{\beta}\ln(\cosh\Gamma) - \tanh\Gamma\right) \tag{4.30}$$

where a is the strip width, b is its thickness and Γ is defined as B_a / B_d with B_d being a characteristic field at which the strip is halfway penetrated, equal to $\mu_0 J_c b / \pi$.

A comparison between the calculated magnetization loss with Flux2D and Brandt's algorithm of a rectangular tape in perpendicular field, and the theoretical loss for a strip from Eq. (4.30), is shown in Fig. 4-25. The numerically calculated losses in this case are also practically the same. The difference between numerical and theoretical loss is larger than for a slab – it is 25-35% for fields above 5 mT and increases for lower field, reaching a factor of 3.5 at 1 mT. This can be explained by the difference in the current penetration profiles in superconducting tapes with aspect ratio of 10-15, on the one hand, and an infinitely thin strip, on the other. Therefore, the analytical model for a strip in perpendicular field does not account very well for the AC losses of BSCCO tapes in perpendicular field, especially for low field amplitudes.

Similar results for numerical and analytical AC loss calculations have been presented in [Rab01a].

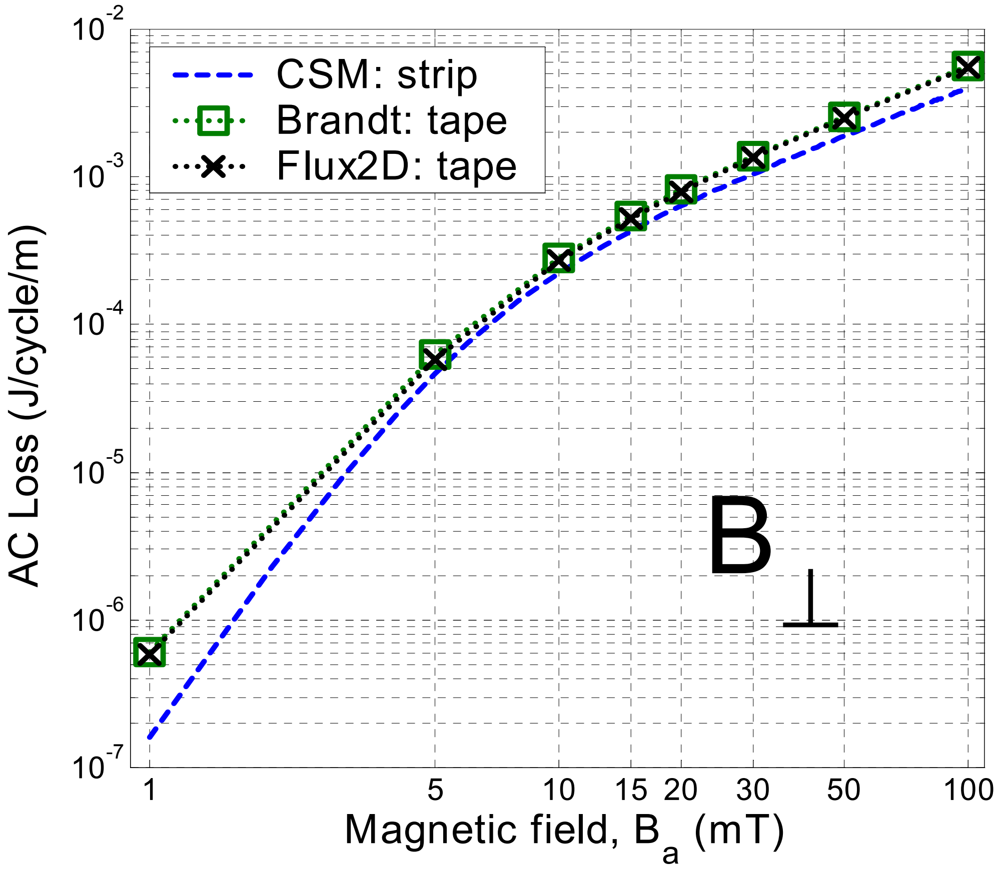

Figure 4-25 AC loss in perpendicular field for a monofilamentary tape of rectangular cross-section, calculated with Flux2D and with Brandt's algorithm. Given is also the analytical loss for a strip from Eq. (4.30).

4.6.3 Comparison with other FEM models

Within the framework of the European Project BIG-POWA, a comparison has been made between the numerical models of HTS, developed by three of the partners – the University of Southampton (SOTON), the National Polytechnic Institute of Grenoble (INPG), and the Swiss Federal Institute of Technology - Lausanne (EPFL). SOTON uses a refined algorithm based on Brandt's method with voltage source [Yan99]; INPG has developed different formulations with voltage and current source in the FEM software package Flux3D [Vin00b], [Vin00c]; and EPFL uses the Flux2D implementation with voltage source, described in Section 4.5.

The simulations have been made on the 37-filamentary tape, shown in Fig. 4-17 with I_c = 40 A, constant J_c = 108 A/mm^2 and n = 15. Different amplitudes (I_p) of the transport current for the current source model at 59 Hz have been used – 16 A, 24 A, 32 A and 38 A, which correspond to $0.4\times I_c$, $0.6\times I_c$, $0.8\times I_c$ and $0.95\times I_c$, respectively. The voltage gradients of the voltage source models have been selected such that to produce the same target currents in the tape. Transport current simulations were made in self-field and with applied parallel AC magnetic field (in-phase with the current) with B_a = 3 mT and B_a = 70 mT [Sta01a].

AC transport current without external magnetic field

For simulations with transport current, the formulation in Flux3D allows application of both current and voltage sources, while the Flux2D and Brandt's formulations use a voltage source.

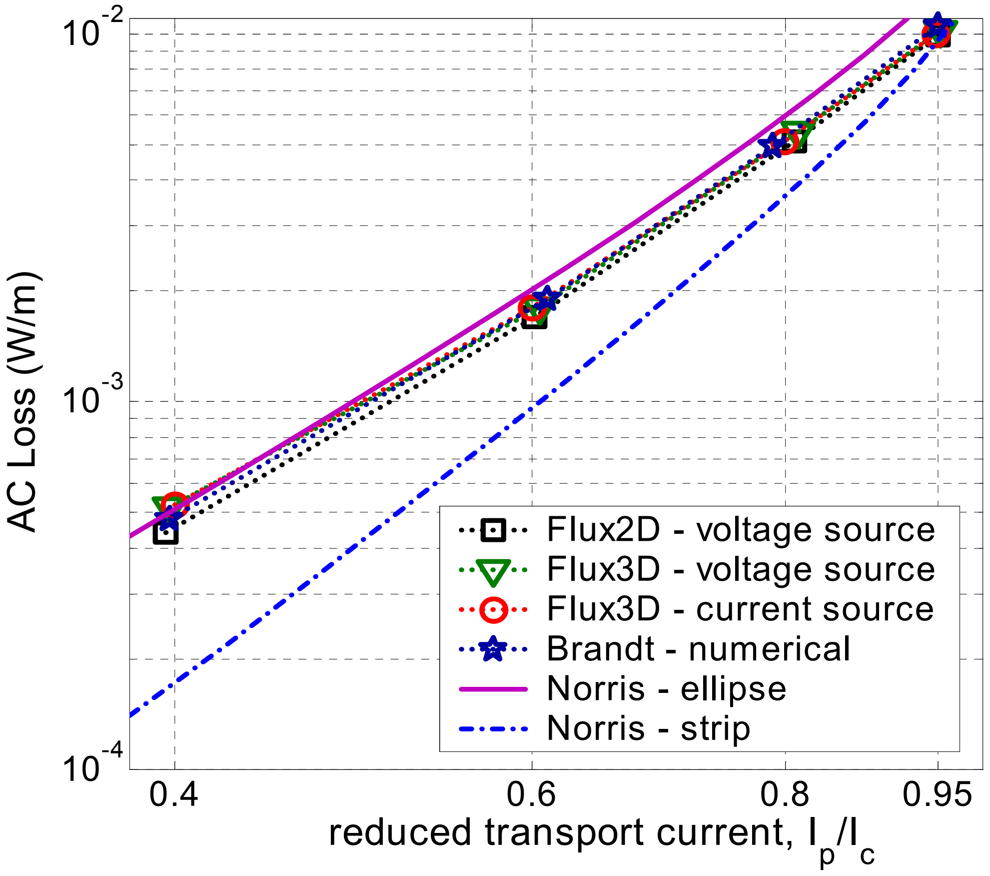

Figure 4-26 AC loss in self-field for different reduced transport currents.

The obtained self-field AC losses with the different models are shown in Fig. 4-26 for different reduced currents. Plotted are also Norris's theoretical elliptical and strip predictions. The results from the different models are very similar and fall closer to the elliptical prediction, since an ellipse is a more appropriate approximation of the geometry of multi-filamentary HTS tapes than a strip and losses occur mostly at the edges of the tapes, while there is no such edge effect in a strip. The self-field AC losses are proportional to $I_p^{3-3.5}$.

The current and magnetic field distributions were calculated at 6 different time instants (ωt = π/2, 3π/4, π, 5π/4, 3π/2 and 2π), and they turned out to be very similar between the four models. Examples of the current density distribution for $I_p = 0.6\ I_c$ and ωt = 2π are shown in Fig. 4-27.

In self-field (B_a = 0 mT), the integral of the transport current density at ωt = 2π is zero. The outer filament layer carries positive current and gets saturated first – even when I_p is as low as 0.6 I_c the current density exceeds locally J_c (108 A/mm^2) in some parts of the outmost filaments (see Fig. 4-27). The inverse current is carried by the inner filaments, which do not saturate completely even at $I_p \sim I_c$. The central filaments are current-free at $I_p < 0.8\ I_c$.

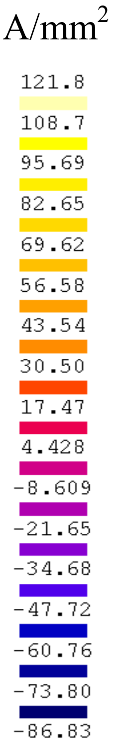

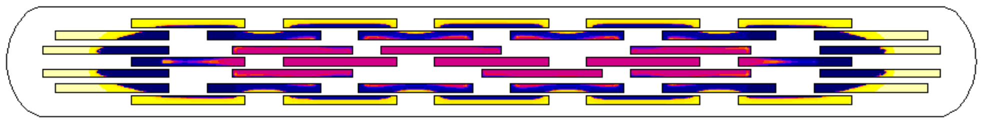

Voltage source (Flux2D)

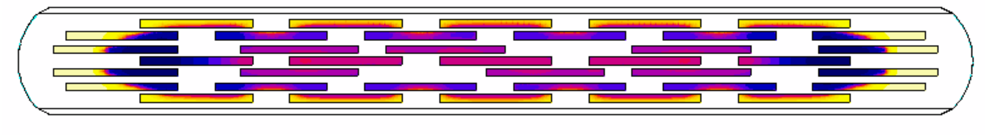

Voltage source (Flux3D)

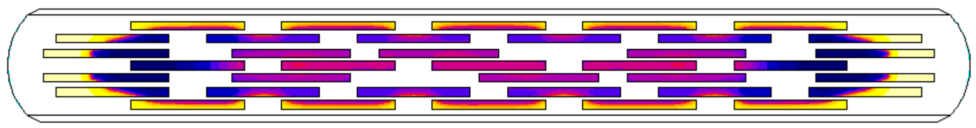

Current source (Flux3D)

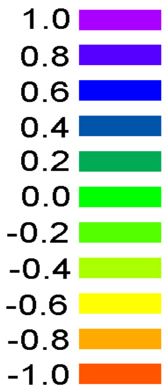

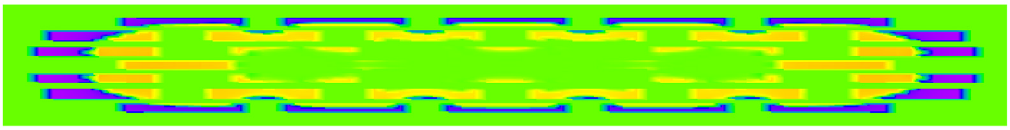

Voltage source (Brandt)

Figure 4-27 Current density distribution at ωt = 2π for $I_p = 0.6\ I_c$. J_c = 108 A/mm^2.

AC transport current in parallel external AC magnetic field

The results for the AC loss calculations are shown in Fig. 4-28 for applied AC magnetic field, parallel to the wide side of the tape with amplitude 3 mT and 70 mT. The losses for B_a = 3 mT are very close for the four models. They are higher than the self-field AC loss and are proportional to I_p^2, which shows that even at such low fields there is already a considerable contribution from the resulting magnetization losses in the superconductor. The losses for B_a = 70 mT, computed from the FEM simulations practically coincide, and are by 10% lower than the losses computed with Brandt's method. At such values of B_a, the magnetic field has completely penetrated the superconductor and the magnetization loss is dominating the total loss. That is why the losses are almost independent of the applied transport current.

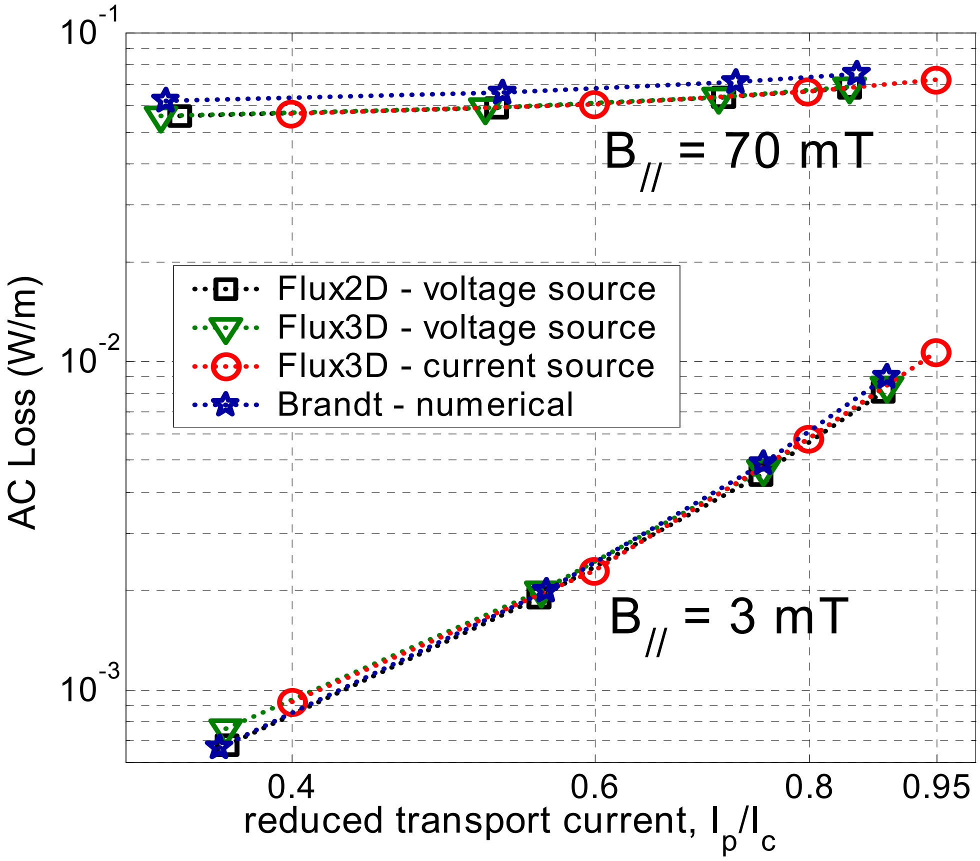

Figure 4-28 AC loss in parallel magnetic field with B = 3 mT and 70 mT.

The voltage gradients that produce the target current in self-field for the voltage-source models have been kept the same in the simulations with applied field. The induced currents, which increase as the field becomes stronger, however reduce the transport current capacity of the superconductor. Therefore, when a voltage source is applied, the resulting total current in the tape is decreased. In the model with a current source the total current through the superconductor is equal to the driving (source) current regardless of the applied magnetic field. For this reason, the AC loss points in Fig. 4-28 for the voltage-source models are situated to the left of the ones for the current-source model, yet on the same loss curves (see the FEM results).

The obtained current density distributions with the FEM models in applied external field are very similar. An example is plotted in Fig. 4-29 for $I_p = 0.6\ I_c$ at $\omega t = 2\pi$ and external field with $B_a = 3$ mT and 70 mT.

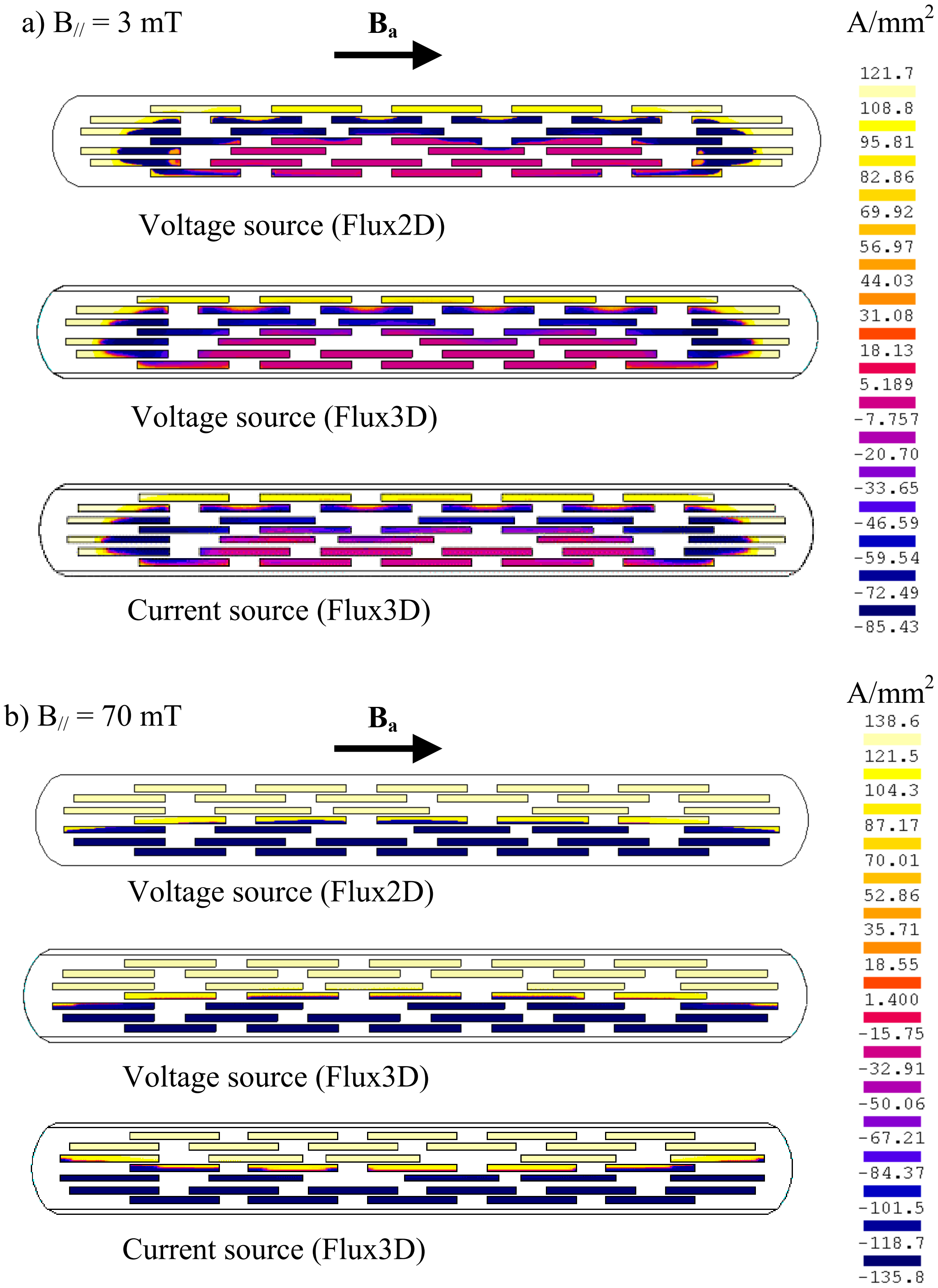

Figure 4-29 Current density distribution at $\omega t = 2\pi$ for $I_p = 0.6\ I_c$ with $B_a = 3$ mT (a) and $B_a = 70$ mT (b). $J_c = 108$ A/mm^2.

Similarly to the effect of Faraday's law in normal conductors, an AC magnetic field applied to a superconductor generates currents trying to screen the tape from the field. In applied parallel field, these induced currents circulate in opposite directions in the top and bottom halves of the tape. Therefore, the total current through the tape, which is a superposition of the transport and induced currents, has a specific asymmetric pattern with respect to the line dividing the tape in two halves along its width, see Fig. 4-29a. At high values of the applied field, when the magnetic field has totally penetrated the superconductor, the induced currents dominate the transport one at this instant and the current density locally exceeds J_c in all filaments, see Fig.4-29b.

4.7 Influence of the finite *n*-value of Bi-2223 tapes

The influence of the finite *n*-value of high-T_c superconductors has been studied by FEM simulations on a 37-filamentary tape with constant J_c of 108 A/mm^2.

Figure 4-30 displays the *E-J* characteristics for several values of the power-law index. The limiting cases of $n = 1$ and $n = \propto$ correspond to the linear Ohm's law $E = \rho J$ and the critical state model, respectively. For HTS, *n* usually varies between 5 and 30. We have made simulations with $n = 5$ (strong flux creep), $n = 15$ (weak flux creep) and $n = 50$, a value more typical of LTS materials. The *n*-value may vary if different voltage criterions E_c are used for the calculation of J_c. The form of the *E-J* relation in Fig. 4-30, however, is independent of E_c.

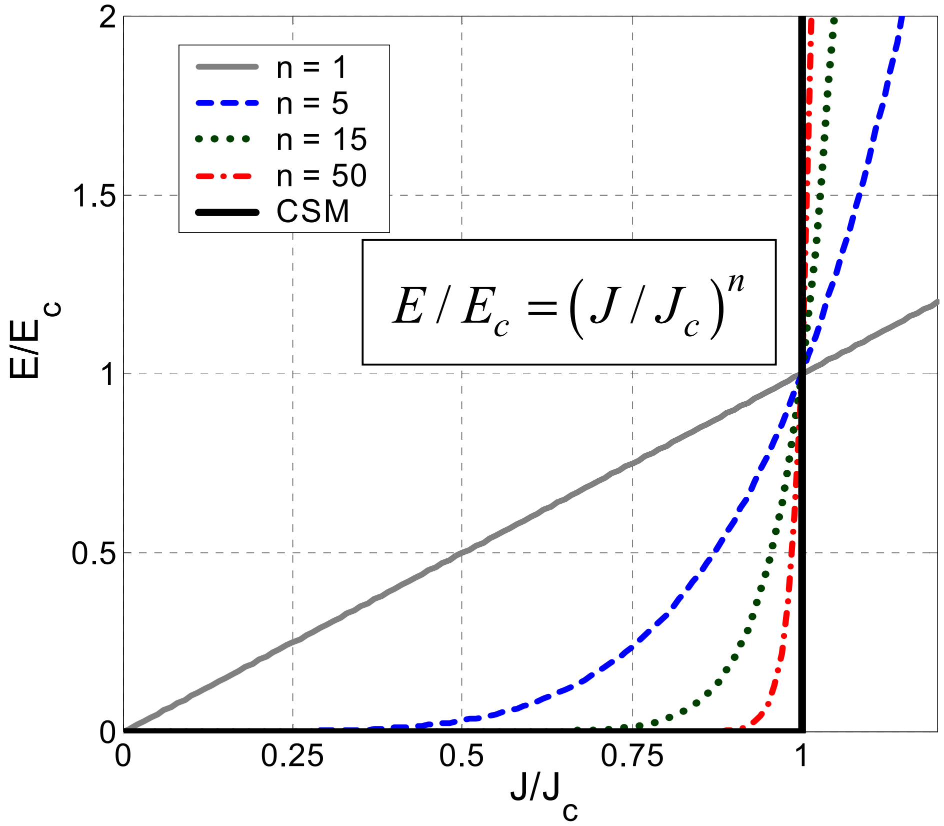

Figure 4-30 *E-J* characteristics for different values of the power-law index.

4.7.1 Influence of the *n*-value on the current density distribution

The effect of the n-value on the current density distribution in the tape is demonstrated in Figs. 4-31 to 4-33. In self-field, for I_p below 0.4 I_c the current is concentrated near the edges of the tape and there is a large current-free zone in the center. With the increase of I_p, the outer filaments saturate first with current density $J_{max} \geq J_c$, and the current contour moves into the inner filaments.

As shown in Fig. 4-31, even for applied peak current as low as 0.4 I_c, the saturating current density (J_{max}) in the outer filaments of the tape with $n = 5$ is well above J_c; for the tape with $n = 15$, J_{max} is slightly above J_c, and for n = 50, J_{max} is very close to J_c.

When $I_p = 0.95\ I_c$, the current has penetrated all the filaments and there is no current-free zone in the center of the tape, see Fig. 4-32. The outer filament layer is completely saturated ($J \geq J_c$ everywhere). When $n = 5$, $J_{max} \sim 1.6\ J_c$, when $n = 15$, $J_{max} \sim 1.2\ J_c$, and when $n = 50$, $J_{max} \sim J_c$.

In self-field, the saturating current density of the inner filaments, carrying inverse current, remains always lower than J_c, see J_{min} in Fig. 4-31 and 4-32. However, the higher the n-value, the closer J_{min} is to $-J_c$.

In external parallel field of 70 mT, the influence of the n-value is even more emphatic, see Fig. 4-33. When $n = 5$, the saturating current density in the outer filaments at this instant is more than 2 times J_c, when $n = 15$, $J_{max} \sim 1.3\ J_c$, and when $n = 50$, $J_{max} \sim J_c$.

To summarize, for a low n-value ($n = 5$), the current density distribution is highly non-uniform and J_{max} always exceeds largely J_c. For an intermediate n-value ($n = 15$), the current distribution is more uniform, and J_{max} is closer to J_c. For a large n-value ($n = 50$), the current distribution is most uniform and the outer and inner filaments saturate with the same $|J_{max}| \approx |J_{min}| \approx J_c$. In fact, for such large n-values, the current distribution corresponds well to the critical state model, in which J is either zero or $\pm J_c$.

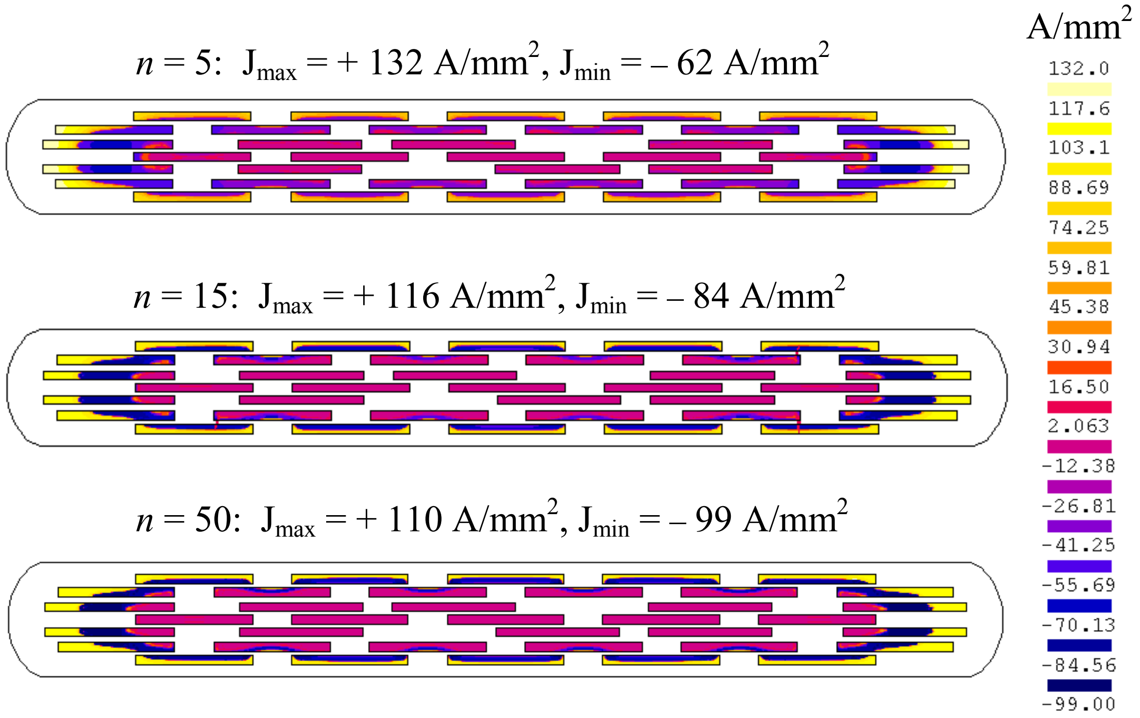
$n = 5$: $J_{max} = +\ 132$ A/mm^2, $J_{min} = -\ 62$ A/mm^2

$n = 15$: $J_{max} = +\ 116$ A/mm^2, $J_{min} = -\ 84$ A/mm^2

$n = 50$: $J_{max} = +\ 110$ A/mm^2, $J_{min} = -\ 99$ A/mm^2

Figure 4-31 Current density distribution at $\omega t = 2\pi$ for $I_p = 0.4 \times I_c$ and $B_a = 0$ mT. $J_c = 108$ A/mm^2. Shown is also the positive and negative saturating current density.

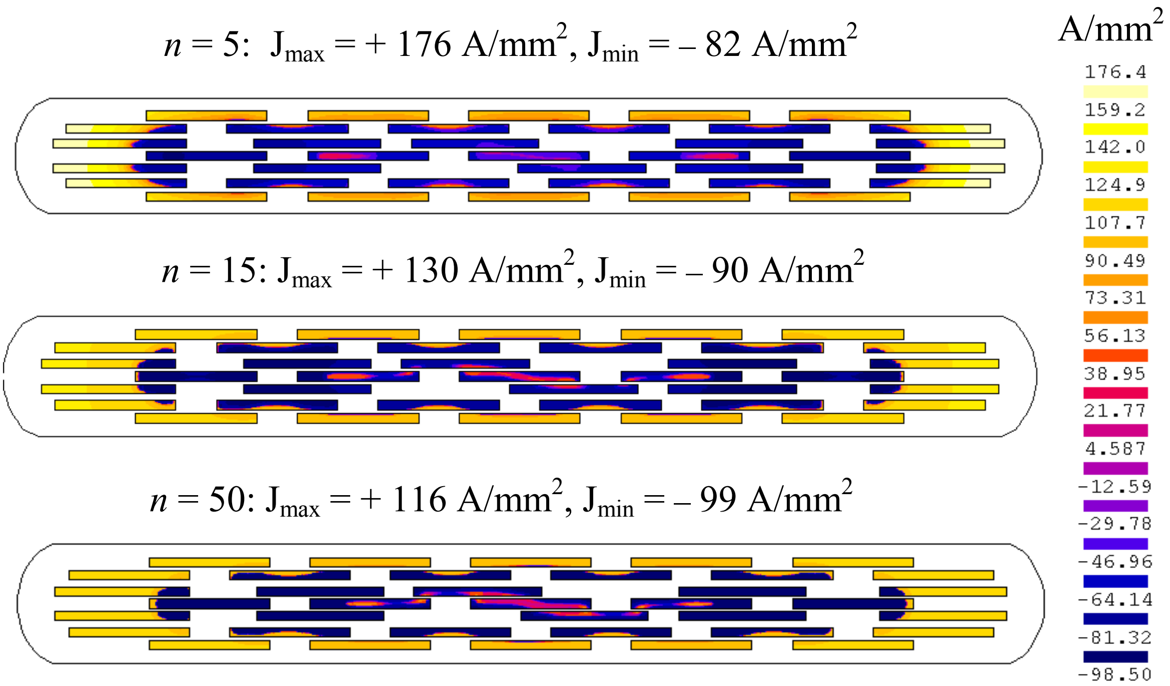
$n = 5$: $J_{max} = +\,176$ A/mm^2, $J_{min} = -\,82$ A/mm^2

$n = 15$: $J_{max} = +\,130$ A/mm^2, $J_{min} = -\,90$ A/mm^2

$n = 50$: $J_{max} = +\,116$ A/mm^2, $J_{min} = -\,99$ A/mm^2

Figure 4-32 Current density distribution at ωt = 2π for $I_p = 0.95 \times I_c$ and $B_a = 0$ mT. $J_c = 108$ A/mm^2. Shown is also the positive and negative saturating current density.

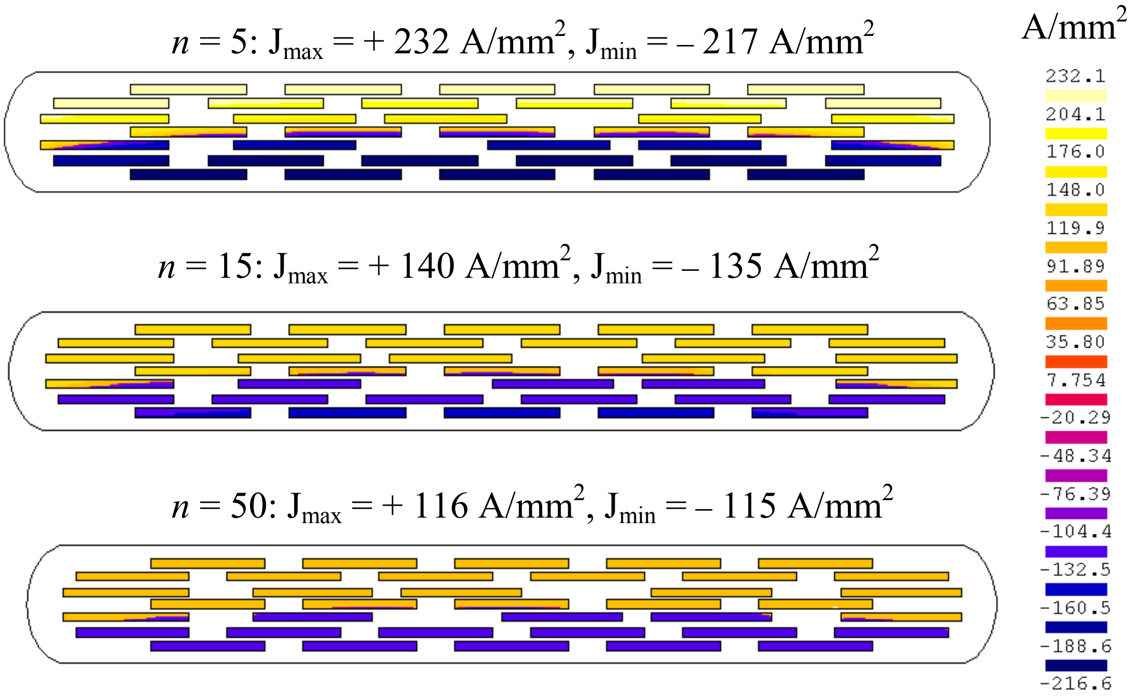
$n = 5$: $J_{max} = +\,232$ A/mm^2, $J_{min} = -\,217$ A/mm^2

$n = 15$: $J_{max} = +\,140$ A/mm^2, $J_{min} = -\,135$ A/mm^2

$n = 50$: $J_{max} = +\,116$ A/mm^2, $J_{min} = -\,115$ A/mm^2

Figure 4-33 Current density distribution at ωt = 2π for $I_p = 0.95 \times I_c$ and $B_a = 70$ mT. $J_c = 108$ A/mm^2. Shown is also the positive and negative saturating current density.

4.7.2 Influence of the *n*-value on the AC loss

We have also calculated the AC losses in self-field, and with applied current and external parallel magnetic field of 3 mT and 70 mT. The results for the three simulated cases are shown in Figs. 4-34 to 4-36.

In self-field (no external field) the AC losses for n = 15 and n = 50 are quite similar for $I_p > 0.4\ I_c$, see Fig. 4-34. The loss for n = 5 is higher than the loss for the other n-values for $I_p < 0.6\ I_c$, and lower in the range $I_p > 0.6\ I_c$. The reason for this loss behaviour is the current distribution, which varies with the n-value, as explained above. For low applied currents, the outer filaments in the tape with n = 5 are saturated well above J_c, and that is why the losses are higher than in the tape with larger n-values, in which the saturation current density is closer to J_c. At high applied currents, the current density in the outer filaments exceeds J_c for any n; the losses are higher the larger n is because the corresponding local electric field values for $J > J_c$ increase with the power of n, see Eqs. (4.20) and (4.24).

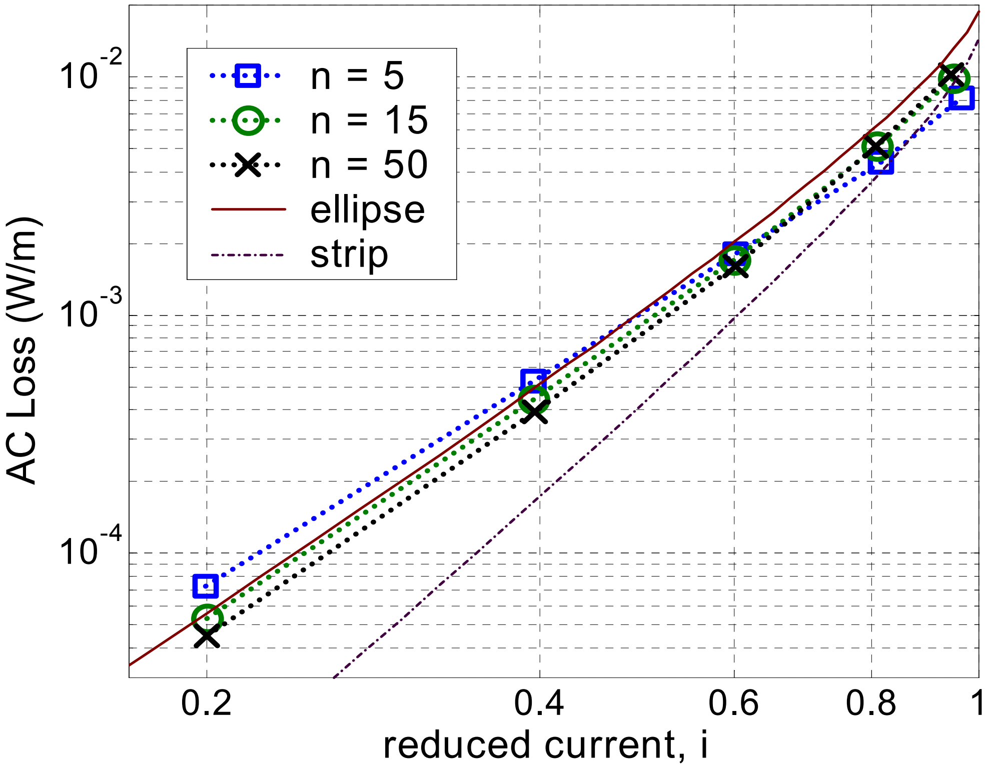

Figure 4-34 AC loss in self-field for different values of the power index *n*.

In the presence of external magnetic field, the total loss has a transport current and a magnetization loss contribution. Even at very modest applied fields, such as B_a = 3 mT, the total loss is increased considerably in the low-current region, see Fig. 4-35. At high values of I_p/I_c, the transport current loss has a stronger contribution and the total loss remains close to Norris's elliptical prediction. The loss variation for the different n-values is increased in the low-current region and decreased at high currents, compared to the self-field case.

As high values of the applied magnetic fields (B_a = 70 mT), the magnetization loss dominates completely the transport current loss regardless of the current amplitude, as shown in Fig. 4-36. The total loss is higher than Norris's elliptical prediction by order(s) of magnitude. At such applied fields, the higher the n-value of the conductor is, the lower the AC loss is – the calculated loss for n = 50 is 15% lower than the loss for n = 15, which in turn is 30% lower than the loss for n = 5 for the whole current range. The reason for that is the non-uniform current density in tapes with low n-value – the lower n, the larger the saturating current density above J_c in the outer filament layers, see also Fig. 4-33.

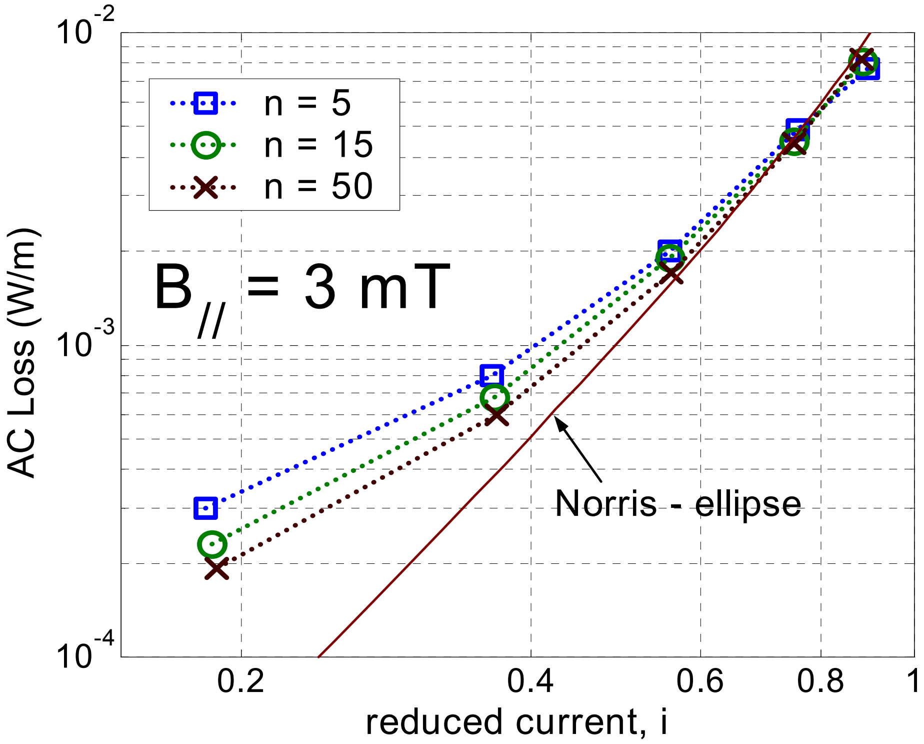

Figure 4-35 AC loss in external parallel field of 3 mT for different *n*-values.

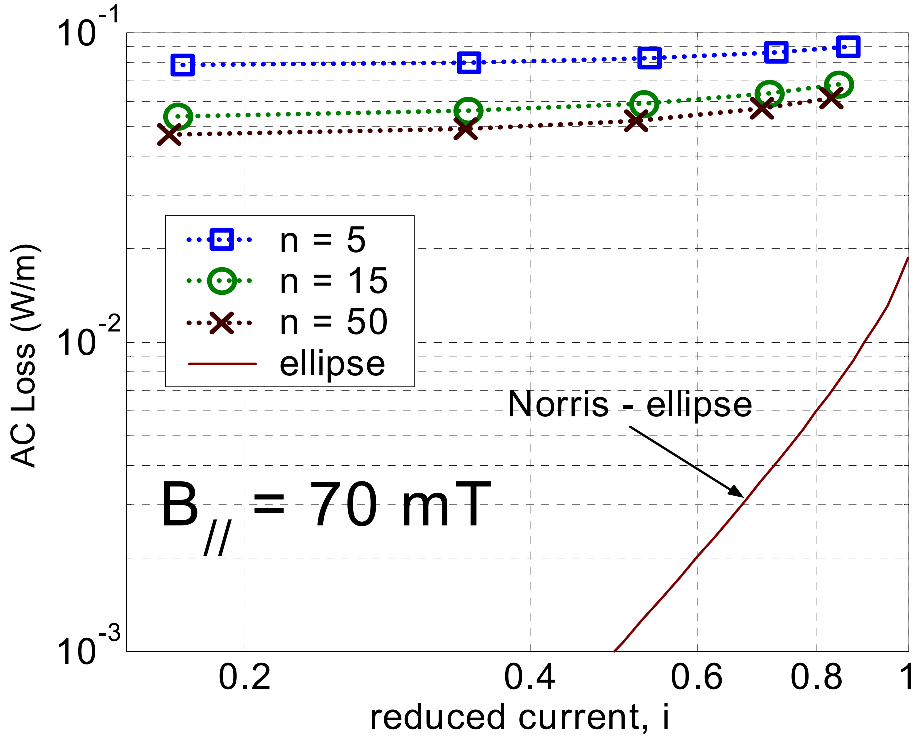

Figure 4-36 AC loss in external parallel field of 70 mT for different *n*-values.

4.8 Modelling of Bi-2223 tapes with lateral J_c variation

There is experimental evidence that the critical current density J_c is not homogeneous along the width of Bi-2223/Ag multifilamentary tapes. This is due to several factors in the manufacturing process, such as the non-uniform rolling pressure and uneven oxygen diffusion in the different filaments [Str00].

Several measurement techniques have been proposed in order to quantify the lateral J_c-distribution in Bi-2223 tapes. The strip-cutting technique [Gra95] was first applied to monofilamentary tapes. Later, non-destructive measurement methods have been developed; such as the scanning Hall probe microscopy [Vol99], magnetization hysteresis loop [Str00], as well as magnetic field gradient measurements [Hak00].

Despite some contradictory results, it has been demonstrated that in Bi-2223 tapes, manufactured by the standard oxide-powder-in-tube (OPIT) technique, the central filaments obtain better alignment and higher critical current density than the outer filaments. The reported lateral J_c variation reaches a factor of 2 to 3. Recently, it has been reported that in multifilamentary tapes, produced by a tape-in-rectangular-tube (TIRT) process [Kov01a], the middle filaments have J_c, which is lower by a factor of 2 than the J_c in the outer filaments [Kov01b].

In this section we investigate the effect of the lateral $J_c(x)$ distribution in the 7- and 37-filamentary Bi-2223 tapes, shown in Fig. 4-17 [Sta01b], [Sta01c].

4.8.1 Models of $J_c(x)$ and $n(x)$ dependence

Nordic Superconductor Technologies (NST) has employed a direct invasive measurement technique, in which a 37-filamentary tape has been incrementally cut off from one edge to the other by a high precision dimpling instrument. Before and after each cut, the DC voltage-current characteristics have been measured by a transport current set-up. The corresponding I_c and the values of the power index (n) along the width have been directly obtained from the measured V-I curves. The local critical current densities have been then calculated after electronic scanning of the remaining geometry of the tapes.

The obtained lateral J_c distribution along the width of the tape and the corresponding value of the power index, normalized by the maximum values at the centre are shown with bars in Fig. 4-37. The J_c is highest in the central filaments, and lowest in the outer filaments; its variation reaches a factor of 3.3. The variation of the n-value is much less pronounced – reaching a factor of 1.5.

In order to introduce $J_c(x)$ and $n(x)$ in our FEM implementation, we have selected a continuous Gaussian model for their normalized lateral distribution, since it fits fairly well to the measurement data and has a quite simple form:

$$\begin{aligned} J_c(x)/J_{c\max} &= a_1 + b_1 e^{-(x/c_1)^2} \\ n(x)/n_{\max} &= a_2 + b_2 e^{-(x/c_2)^2} \end{aligned} \tag{4.31}$$

where the values of x (distance from the centre of the tape) are in mm and $J_{c\max}$ and $n_{\max}$ are the maximum values of J_c and n at the centre (x = 0). The parameters a, b and c define respectively the offset, the height and the width of the Gaussian bell. The values of these parameters for the fits to the measured J_c and n are shown in Table 4.4. The corresponding models are plotted in Fig. 4-37.

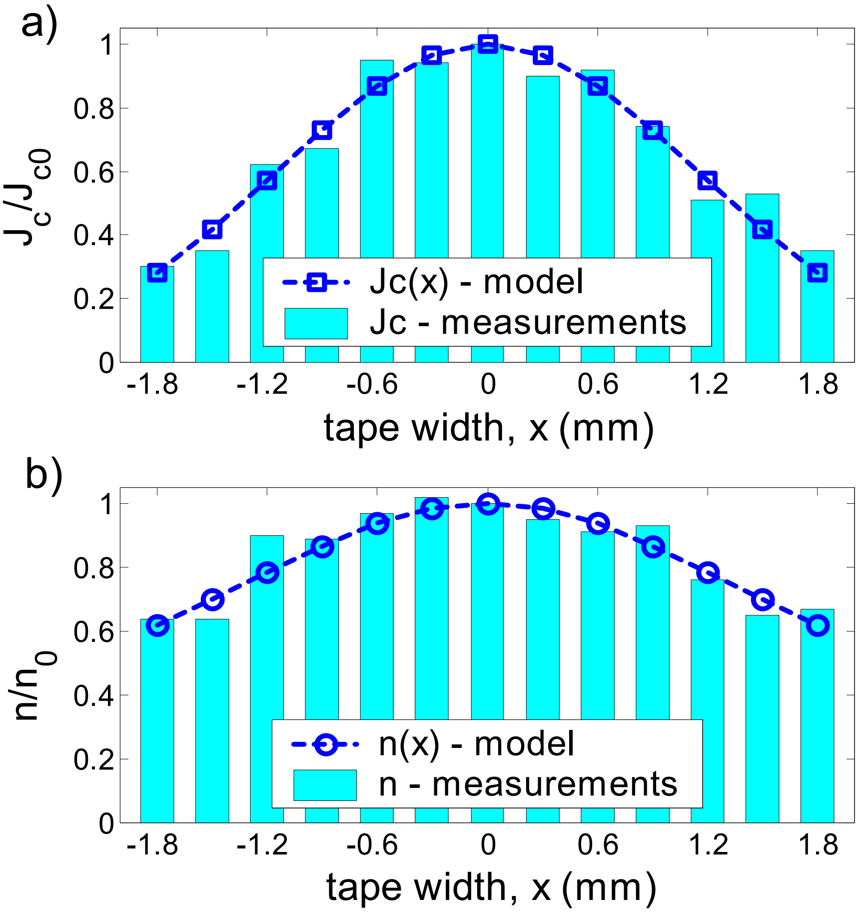

Figure 4-37 Normalized lateral distributions of J_c (a) and n (b) – obtained from cut-off measurements and the Gaussian-type models from Eq. (4-31). The maximum values of J_c and n are at the center of the tape (x = 0).

Table 4.4 Parameters for the Gaussian fits of Eq. (4.31)

	a	***b***	***c***
$J_c(x)$ - model	0.0	1.0	1.6
$n(x)$-model	0.4	0.6	1.8

We have made simulations with three models of $J_c(x)$ – a model with smoothly decreasing J_c towards the edge, as in Fig. 4-37 (bell-like J_c), a model with constant J_c and a model with smoothly increasing J_c towards the edge (U-like). These three models are shown in Fig. 4-38. The U-like $J_c(x)$ model is described with similar equation as Eq. (4.31), where the centre of the Gaussian bell is shifted from the zero to the edge of the tape.

The FEM simulations were performed with either AC transport current or external AC magnetic field at 59 Hz. The value of the power index $n_{\max}$ is 23 for the bell-like model, and a constant $n = 20$ is used for the other two models. Both the 7- and 37-filamentary tapes have the same I_c of 36.6 A. The values of $J_{c\max}$ in the bell-like and U-like models for each tape are selected in such way that the integral of the J_c for the section of the tapes gives the same I_c:

$$I_c = \int_{-x_{\max}}^{x_{\max}} J_{c\max} F(x) t(x) dx \tag{4.32}$$

where $t(\mathrm{x})$ is the varying thickness of the superconductor along its width, obtained from the tape's cross-section and $F(\mathrm{x})$ is the lateral dependence of $J_c(x)/J_{c\max}$.

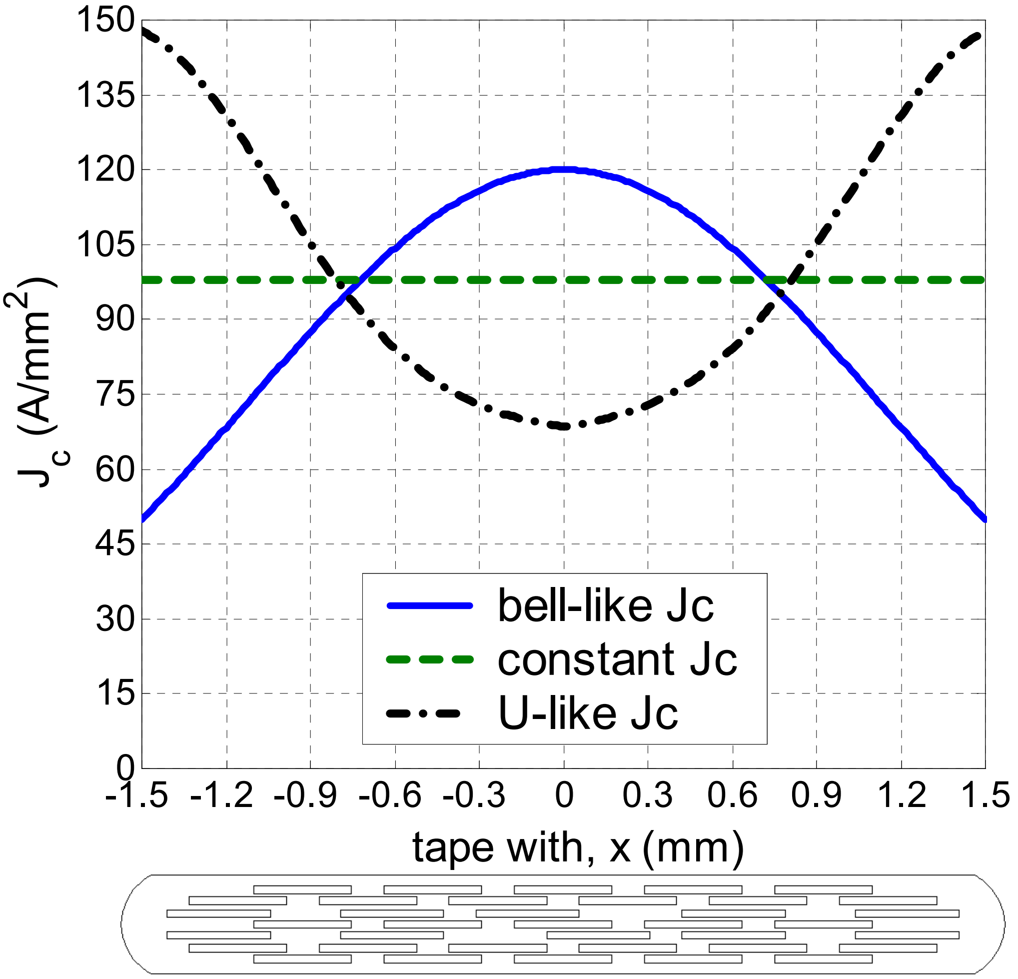

Figure 4-38 Models of the lateral $J_c(x)$ distribution for the 37-filamentary tape.

4.8.2 Current and power density distributions in multifilamentary tapes with different models of $J_c(x)$

The current density distribution in the 7-filamentary tape for applied transport current of 0.65 I_c at its peak value is shown in Fig. 4-39 with a zoom of the two right filaments. HTS materials, such as BSCCO, do not have a well-defined critical current, and therefore, unlike the critical state model, the current density may exceed locally the value of J_c. In the model with bell-like $J_c(x)$ the outer filaments are completely saturated with $J \geq J_c$ everywhere – the darkening shades in Fig. 4-39a correspond to the decreasing J_c along the width, while for the constant J_c and the U-like $J_c(x)$ model they are only partially saturated – for example, the lightest shade in Fig. 4-39b indicates the area where $J \geq J_c$. Note that for all models there is still a current free region in the middle filament(s) at 0.65 I_c even when the current is at peak value.

a) bell-like $J_c(x)$ model: $J_{c\max} = 113$ A/mm^2

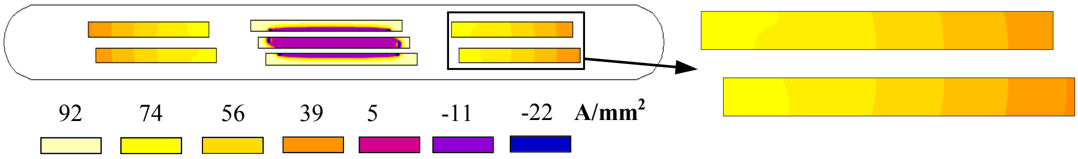

b) constant J_c model: $J_c = 84$ A/mm^2

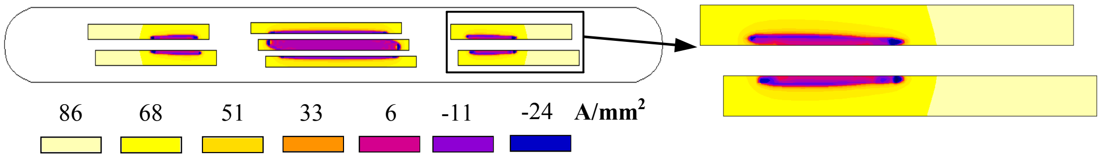

c) U-like $J_c(x)$ model: $J_{c\max} = 116$ A/mm^2

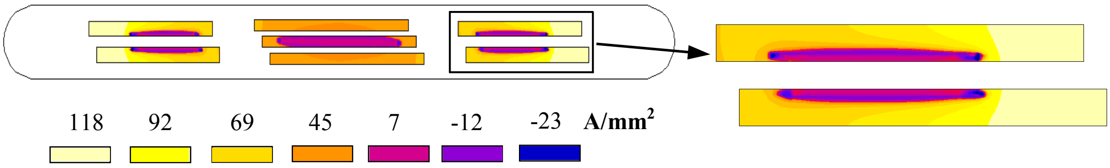

Figure 4-39 Current density distribution for $I_p = 0.65\ I_c$ at peak value ($\omega t = \pi/2$) for the models with $J_c(x)$ and constant J_c. $J_{c\max}$ in the bell-like model corresponds to the J_c value in the center, while $J_{c\max}$ in the U-like model is the J_c value at the extremities of the tape.

The instantaneous power density for $I_p = I_c$ at $\omega t = 5\pi/4$ is displayed in Fig. 4-40. This quantity is varying during the cycle. However, for all $J_c(x)$ models, the power dissipation is always concentrated in the outer filaments, which carry more current than the middle filaments and are completely saturated. In the bell-like $J_c(x)$ model, (Fig. 4-40a), the peak of the power dissipation is shifted towards the center, where the saturating current is higher since J_c is higher. In the other two models, the peak of the power dissipation is at the external edges of the outer filaments, where the current density is higher. The saturating current density in the outer filaments with the U-like $J_c(x)$ model is close to the local J_c value, and that is why the power dissipation is visibly lower than with the constant J_c and the bell-like $J_c(x)$ models, in which the saturation occurs with $J > J_c$.

a) bell-like $J_c(x)$ model

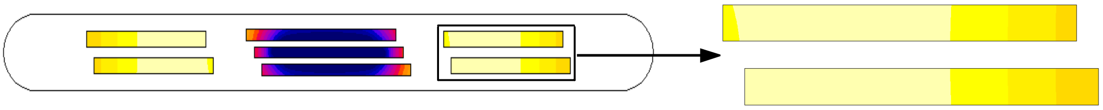

b) constant J_c model

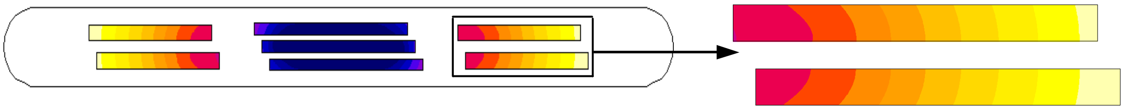

c) U-like $J_c(x)$ model

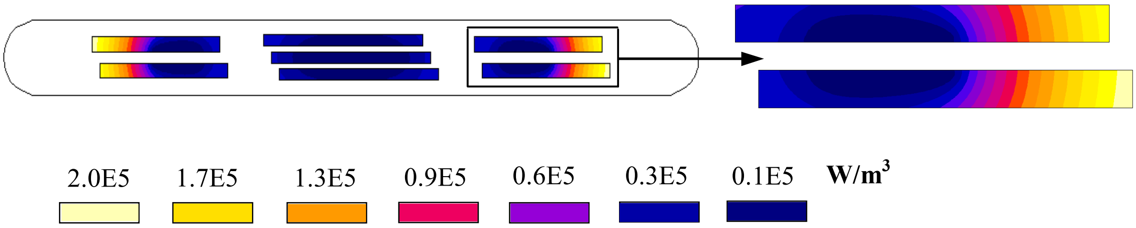

Figure 4-40 Instantaneous power density for $I_p = I_c$ at $\omega t = 5\pi/4$ for the models with $J_c(x)$ and constant J_c.

4.8.3 Current flow and AC loss in the individual filaments

The current amplitude in each filament for applied transport current of 24 A (0.65 I_c) is shown in Figs. 4-41a and 4-41c for the models with bell-like and U-like $J_c(x)$. The corresponding AC losses (the integral of the instantaneous power over a cycle) in the individual filaments are presented respectively in Figs. 4-41b and 4-41d. The bars in all 3D plots are positioned at the centre of each filament.

The 7-filamentary tape is not completely symmetric with respect to the central filament. Two of the outer filaments are slightly closer to the edge of the tape than the other two (see Fig. 4-17). Therefore, with the bell-like $J_c(x)$ model, the critical current of these filaments is a little different – 4.1 and 4.3 A, while for the three filaments in the middle the I_c is 6.6 A. As can be seen in Fig. 4-41a, all of the outer filaments are almost completely saturated (carrying above 0.95 I_c each). The middle filaments transport around half of their I_c, while the central filament is almost current free. For this reason, the AC losses in the outer filaments are higher by a factor of 15 than the losses in the other filaments (see Fig. 4-41b). Note that the two outer filaments, which are slightly closer to the edge, have 10% higher losses than the other two outer filaments.

For the model with U-like J_c, the I_c of the outer filaments is 6.0 A and 6.2 A, respectively, while the I_c in each filament in the middle group is 4.0 A. Fig. 4-41c shows that at applied transport current of 0.65 I_c there are no filaments carrying current close to their I_c. Therefore, the losses in the outer filaments are lower by some 50% than the corresponding losses in the bell-like $J_c(x)$ model – compare Fig. 4-41b and 4-41d. There is still a loss difference of one order of magnitude between the outer and middle filaments due to the partial saturation of the outer filaments; see Fig. 4-39c as well.

In both $J_c(x)$ models, as well as in the constant J_c model, at current amplitude of 0.65 I_c more than 90% of the total self-field loss in the tape is dissipated in the four outer filaments.

Bell-like $J_c(x)$ model

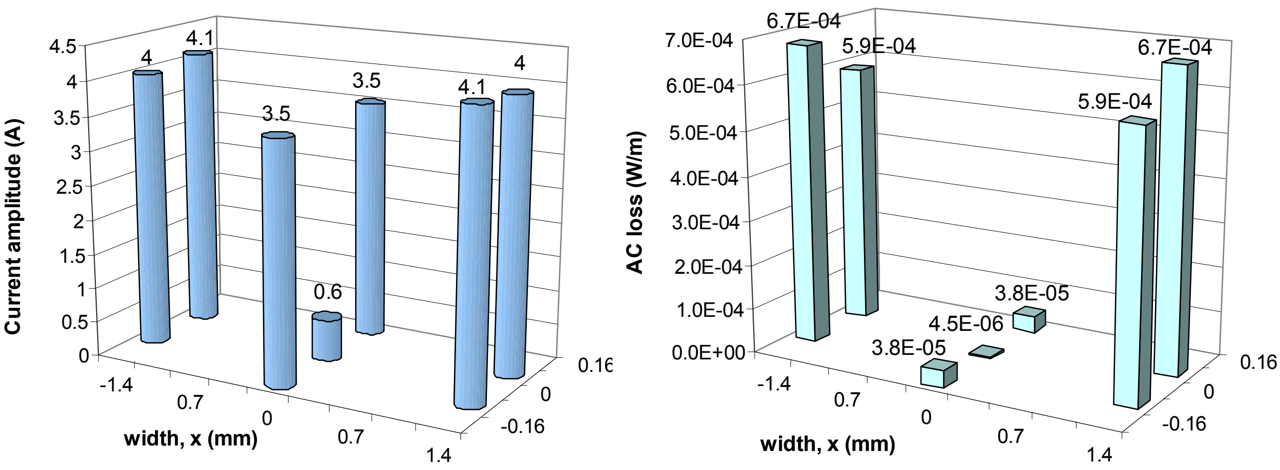

a) **b)**

U-like $J_c(x)$ model

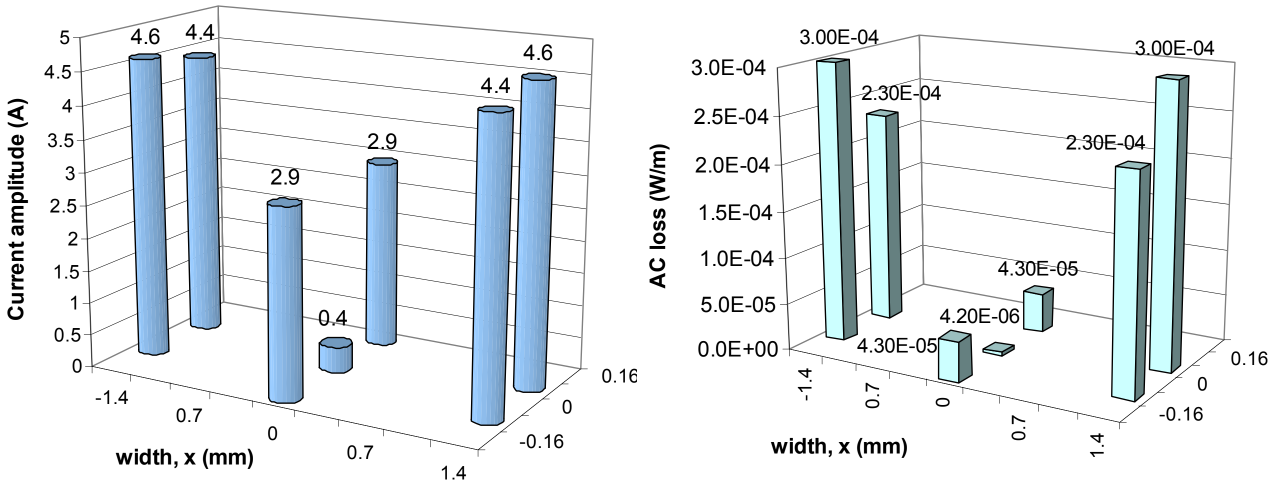

c) **d)**

Figure 4-41 Carried current (left column) and self-field AC loss at 59 Hz (right column) in each filament of the 7-filamentary tape for different models of $J_c(x)$. The applied transport current is 24 A (0.65 I_c). The bars are positioned at the center of each filament.

The simulations on the 37-filamentary tape show similar current distribution – the transport current is saturating first the 8 filaments, which are closest to the edges: with bell-like $J_c(x)$, these filaments are completely saturated even when the applied current is as low as 0.6 I_c, while with constant J_c and with U-like $J_c(x)$ none of the filaments is completely saturated at that amplitude.

As the applied transport current is increased, the middle filaments start to saturate as well. The individual filament AC losses at 0.9 I_c are shown in Fig. 4-42 for the models with bell-like and U-like $J_c(x)$. At such amplitude of the current, almost all filaments are completely saturated in both models. The saturating current density is, however, different – the closer a filament is to the edge, the higher the ratio J/J_c is. Therefore, the power dissipation is concentrated mainly in the 14 (out of 37) filaments, nearest to the edges, which account for 80 to 95% of the total self-field losses in the tape in the range 0.2 – 0.9 I_c. For the example in Fig. 4-42, with both $J_c(x)$ models cases the 7 outer filaments (out of 20) dissipate more than 90% of the total losses.

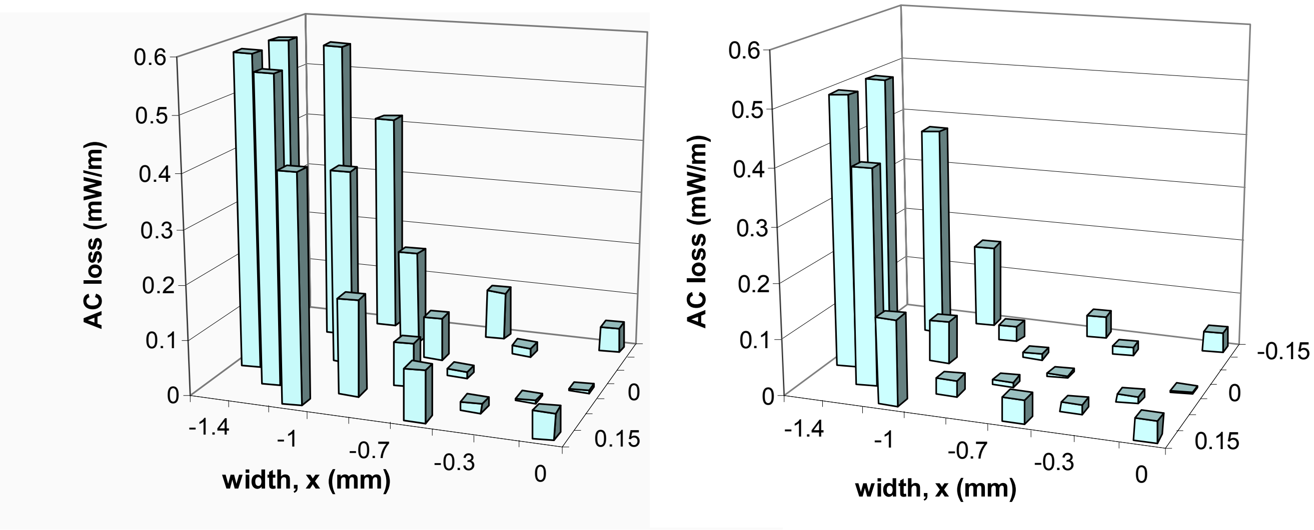

a) Bell-like $J_c(x)$ model

b) U-like $J_c(x)$ model

Figure 4-42 Self-field AC loss at 59 Hz in each filament of the left half of the 37-filamentary tape with different models of $J_c(x)$ for applied transport current of 33 A (0.9 I_c). The bars are positioned at the center of each filament.

4.8.4 AC losses in tapes with different models of $J_c(x)$ in self-field and in external magnetic field

Figures 4-43 and 4-44 show the self-field AC losses in the 7- and 37-filamentary tapes for different reduced applied transport currents. In self-field, the current density in the outer filaments is always higher than in the middle filaments. Therefore, the lower the J_c in the outer filaments, the faster they saturate and the higher their own losses and the total AC losses in the tape are. With the bell-like J_c distribution, there are more filaments near the edges, which are saturated ($J \geq J_c$) and their J/J_c ratio is higher than in a tape with U-like J_c, and consequently the self-field AC losses in the latter are considerably lower, as it was shown in Fig. 4-42.

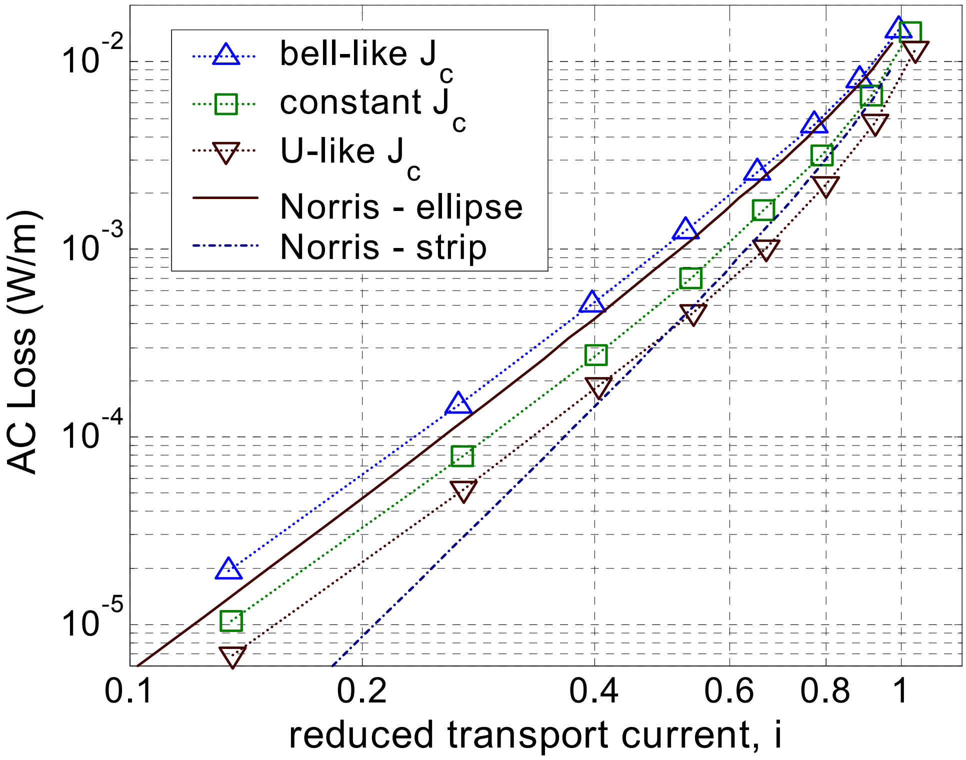

Figure 4-43 Transport current AC losses at 59 Hz for the 7-filamentary tape, using models with different lateral J_c distribution. Plotted are also Norris's analytical predictions for a strip and an ellipse.

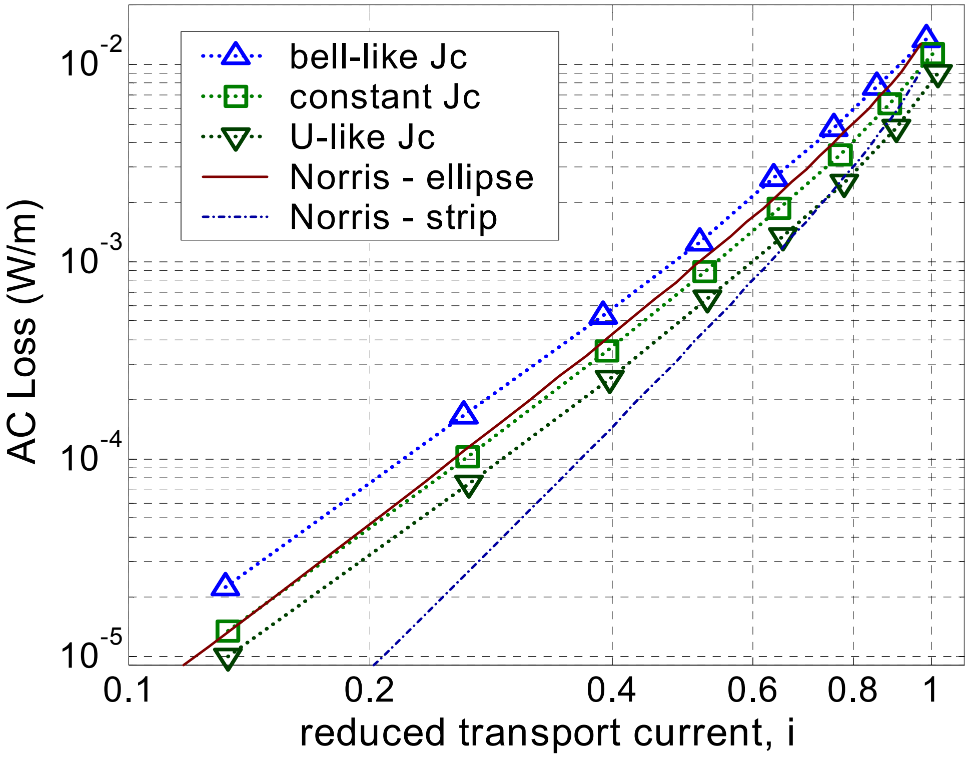

Figure 4-44 Transport current AC losses at 59 Hz for the 37-filamentary tape, using models with different lateral J_c distribution. Plotted are also Norris's analytical predictions for a strip and an ellipse.

At higher applied currents, all filaments start to saturate as $I_p \rightarrow I_c$ and the loss difference is less significant than at lower currents. The AC loss difference between the models with non-uniform J_c reaches a factor of 2.5-3 for low current (0.2-0.4 I_c), and a factor of 1.5-2 at high currents (0.8-1.0 I_c) for both tapes.

Finally, Fig. 4-45 shows a comparison between the magnetisation losses of the models with different $J_c(x)$, for applied external AC magnetic fields at 59 Hz, perpendicular and parallel to the wide side of the 37-filamentary tape without transport current.

In low perpendicular fields, which are of the order of magnitude of the self-field of the transport current, the AC loss ratios between the different models of $J_c(x)$ are qualitatively similar to the case with applied only transport current – the losses for the model with U-like J_c are lowest, and the loss difference reaches a factor of 2.5 at 0.5 mT. At higher fields, when all filaments are completely penetrated, the loss difference between the three models of $J_c(x)$ is not significant.

In parallel fields, the penetration starts from the long sides of the tapes inwards, and not from the edges towards the centre as in perpendicular field. For this reason, the lateral J_c distribution does not have any influence on the AC losses regardless of the field's amplitude.

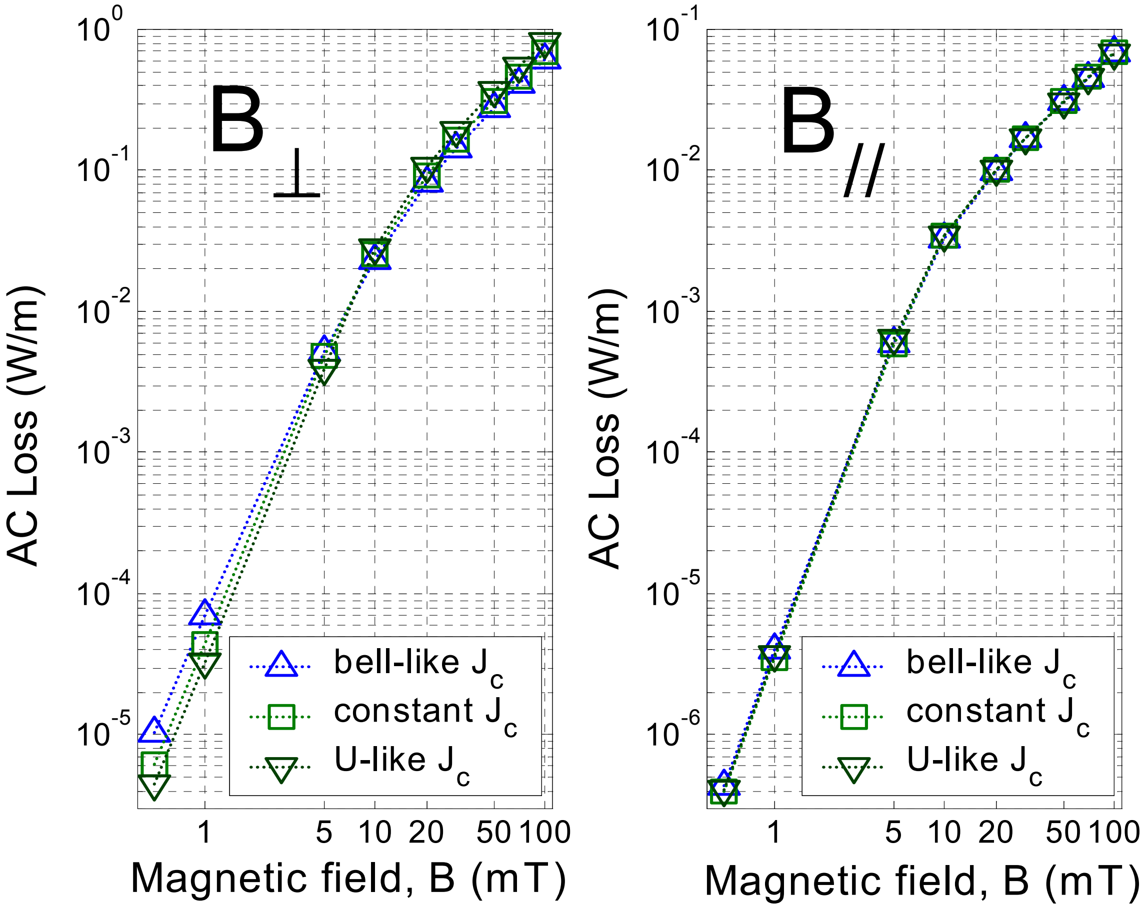

Figure 4-45 Magnetization AC losses at 59 Hz in the 37-filamentary tape with different $J_c(x)$ in perpendicular (a) and parallel (b) magnetic fields up to 100 mT.

4.9 Summary and conclusions

FEM modelling of HTS with Flux2D

A description of the implementation of the nonlinear *E-J* power law model of HTS in the finite element method package Flux2D was given. The HTS model is characterized by the nonlinear resistivity of the material and the possibility to include the dependence of J_c and n on the magnetic field. The Flux2D implementation uses the **A**-V formulation with driving voltage source. The effect of the finite residual resistivity ρ_0 was studied and described. The optimal value of ρ_0 was found to be in the range $0.001\times E_c/J_c - 0.01\times E_c/J_c$. An optimization of the FEM mesh in terms of CPU time and hard disk memory was made. A conclusion was reached that using even a rather coarse mesh leads to correct computation of the AC losses in the superconductor and saves considerable time and disk memory. However, for exact and smooth computation of the current density profiles in the superconductor, a more refined mesh is required. For modelling of multifilamentary tapes, the optimal number of finite elements in each filament was found to be between 60 and 120, depending on the filament's dimensions.

Validation of the Flux2D implementation

The validation of the FEM implementation of the nonlinear model of high-T_c superconductors in the software package Flux2D was achieved by a multi-comparison approach. The current density distribution and AC losses with applied transport current and external field of parallel and perpendicular orientation in Bi-2223 tapes were compared to results from measurements, to the theoretical solutions, based on the critical state model for strip and ellipse in self-field (Norris), strip and slab in applied field, and also to results from the analytical model, proposed by Brandt for HTS with arbitrary *E-J* characteristics.

In addition, the Flux2D implementation with voltage source was compared to other FEM models (one with a voltage source, and one with a current source), implemented in another software package, Flux3D. The results from the FEM simulations on a 37-filamentary tape were compared to a numerical implementation based on the analytical method developed by Brandt. The models were used for performing transport current simulations in self-field and applied parallel magnetic field. The different models showed very good agreement, demonstrated by similar results for current density distributions and AC loss in a number of simulations with several values of the applied transport current and magnetic field amplitude.

By plotting the AC loss vs. current in applied field, it has been shown that the voltage and current source models yield identical AC loss for the same value of the transport current. This, combined with the similarity of the current distributions in all simulated cases, sustains the conclusion that the current and voltage source models are equivalent and which one is to be used depends on the power application that has to be simulated.

The comparison between the FEM simulations and the numerical results obtained with Brandt's method, turned out to be very satisfactory. Brandt's method is analytical and gives exact solutions without the need of boundary conditions. The refined algorithm produces results with sufficient accuracy even for a comparatively low number of grid points (e.g. $N = 21 \times 21$ for the whole tape), and for such a grid it is very fast. As the grid gets finer (e.g. 41×41 points), the computation time is greatly increased since it is proportional to N^2.

The FEM models, on the other hand, require a fine mesh in the superconducting region – 20 × 3 nodes in each filament of the 37-filamentary tape, and for this reason they are not very fast. The FEM models have the advantage of easier post-processing with diverse options and what is more important – the possibility to make simulations in applied field with arbitrary angle, as well as to use more complex geometries with round or elliptical elements.

Influence of the finite *n*-value

High-T_c superconductors have a non-linear E-J relation, characterized by the critical current density J_c and the power index n. The importance of the n-value of a HTS material was demonstrated by comparing the AC loss and current distributions obtained from FEM simulations in a 37-filamentary tape with n = 5, 15 and 50 in self-field and in combined current and parallel magnetic field application. It was shown that for a superconductor with low n-value, the outer filaments may carry current density largely exceeding J_c, while for superconductors with higher n-value the current distribution is more uniform and the saturating current density is closer to J_c. As far as the AC losses in self-field and low magnetic fields (B_a = 3 mT) are concerned, the loss for n = 5 is higher than the loss for n = 15 and n = 50 below 0.6 I_c, and vice versa above 0.6 I_c; the latter is explained by the large values of the local electric field, which increases with the power of n where $J > J_c$. At high magnetic fields (B_a = 70 mT), the lower the power index, the higher the AC loss regardless of the applied current, which is due to the inferior contribution of the transport current loss with respect to the magnetization loss, and the non-uniform current density distribution in conductors with low n-value, in which the current density in the outer filaments exceeds considerably J_c.

Modelling with different lateral $J_c(x)$ dependence

FEM simulations were used to calculate the current distribution and AC losses in each filament of one 7- and one 37-filamentary Bi-2223 tape. Models with constant J_c and with non-uniform lateral J_c(x) dependence were employed and compared. In all models, the transport current tends to flow in the outer filaments, and for this reason they saturate before the middle filaments. Therefore, the closer a filament is to the edge of the tape, the more power it is dissipating. The lower the J_c in the outer filaments, the faster they saturate and the higher their AC losses are. Even when all filaments are saturated (e.g. when $I_p = I_c$), most of the power dissipation is still concentrated in the outer ones, which account for 80 to 95% of the total losses in the tape in the range 0.2 – 0.9 I_c. This is valid for all models – with constant J_c and with J_c(x).

The simulations with applied transport current have demonstrated that the AC losses of a multifilamentary tape with higher J_c in the outer filaments are considerably lower – up to a factor of 3 in the low-current range and up to a factor of 2 in the high-current range – than in a tape where J_c decreases towards the edges. In applied perpendicular fields, the lateral J_c distribution is important below the full penetration field, while in parallel fields it has no influence on the AC losses.

For reduction of the transport current AC losses in Bi-2223/Ag tapes, further improvements are required in the manufacturing process in order to insure as high J_c as possible in the outer filaments. With a U-like lateral J_c(x) distribution, the self-field AC losses obtained from the simulations are close to the lower-loss strip prediction of Norris in the power range of interest 0.6 – 0.9 I_c.

Chapter 5. FEM Modelling of Bi-2223/Ag conductors with $J_c(B)$ and $n(B)$

Abstract

This chapter contains results obtained by finite element method simulations with the Flux2D software package, in which the $J_c(B)$ and $n(B)$ dependence of Bi-2223/Ag conductors with different geometry has been implemented. Firstly, two of the most common $J_c(B)$ and $n(B)$ models in perpendicular field have been used – Kim's law and polynomial approximations, which are compared to a model with constant J_c and n-value in terms of magnetic field, current density profiles and AC losses.

In order to simulate conductors with different shape in applied field with various angles, new anisotropic and isotropic models of $J_c(B)$ and n(B) have been proposed, which take into consideration both the parallel and perpendicular components of the local magnetic field. These models have been used for simulations of monofilamentary conductors with different geometry in various operating conditions, whereby a comparison is provided between the AC losses, current and magnetic field distributions in the different conductors. The concept of effective $I_c(B)$ is introduced and its implications from a modelling point of view are discussed. The geometry considerations for use of Bi-2223/Ag conductors are drawn in a systematic way, which is in conformance with their theoretical shape factors.

For the simulation of round and square wires with different filament arrangement, the $J_c(B)$ and $n(B)$ models have been adapted using geometric transformations, which allow to model the local filament anisotropy in a wire with any filament configuration. Several round and square wires with various filament arrangements have been simulated and compared to 7- and 37-filamentary tapes. The influence of the filament arrangement on the current distribution and AC losses in the different conductors has been investigated. The reduction of the anisotropic effects in the wires with symmetric filament arrangement has been demonstrated by comparing the AC loss performance of tapes and wires in various applications. The optimal geometry and filament configuration has been defined for each application.

Original contributions of this thesis

- the detailed comparison between models with $J_c(B)$ and constant J_c
- the anisotropic models of $J_c(B_x,B_y)$ and $n(B_x,B_y)$ that can be applied for mono and multifilamentary Bi-2223 conductors with various geometry
- introducing the notion of effective $I_c(B)$ in conductors with B-dependent J_c
- the study on the optimization of the geometry and filament arrangement for AC loss minimization of Bi-2223 conductors, complemented by magnetic field and current density profiles in different applications

5.1 Introduction

The assumption for constant J_c has been widely used in theoretical derivations of AC losses in type-II superconductors and in certain numerical models. However, it has been known ever since the time when Bean devised his famous model that the critical current density decreases in the presence of magnetic field. In HTS the decrease of J_c with B is significant even for moderate values of the magnetic field, and is a very important feature of materials such as BSCCO. Moreover, HTS tapes have an intrinsic anisotropy, which results in different degradation of J_c in parallel and perpendicular fields. Hence comes the need of models that describe the observed experimental dependence of J_c on magnetic fields of varying angle. Such models are especially useful in numerical modelling of HTS, since the $J_c(B)$ dependence renders the analytical solutions of current and field equations more difficult to obtain since the field gradient dB/dx is not constant anymore.

In most large-scale applications of Bi-2223/Ag materials, such as transformers, cables and motors, the conductors carry AC current in the presence of external magnetic field. The AC losses for combined current and field applications have been well studied for Bi-2223/Ag tapes and both experimental and numerical results are available [Rab99a], [Rab99b], [Ame98b]. It has been demonstrated that due to the geometry and the anisotropic properties of Bi-2223 tapes, the magnetization losses in applied perpendicular fields are far above the desired applications levels and exceed by an order of magnitude the losses in parallel magnetic fields.

Presently, considerable research efforts are directed towards development of novel Bi-2223/Ag wires with round or square configuration [Fri01], [Su01]. One of the advantages of these new conductors, which are more convenient to use for fabrication of long-length coils and cables, is minimizing the effect of the geometry and intrinsic anisotropy of HTS tapes that results in excessive AC losses in perpendicular magnetic fields. The AC loss behaviour of Bi-2223/Ag round and square wires has not been fully explored before, and some numerical results have been reported only for monofilamentary conductors in certain applications – [Nib01b], [Ame01].

The chapter is structured as follows. Section 5.2 explains how the J_c values of Bi-2223 tapes used in numerical simulations are usually obtained; Section 5.3 gives a comparison for modelling of HTS tapes with different models of $J_c(B)$ in perpendicular fields; Section 5.4 introduces new anisotropic and isotropic models for $J_c(B)$ and $n(B)$ and gives results for monofilamentary conductors in different applications; Section 5.5 presents results from modelling of multifilamentary conductors with various filament arrangement, and Section 5.6 gives the conclusions from this chapter.

5.2 Defining the J_c values for numerical simulations of HTS

It has been confirmed by experiments that the critical current of Bi-2223/Ag tapes is carried through two paths – one is via weakly linked grain boundaries (Josephson junctions); another is through well-connected grains. The $J_c(B)$ dependence of HTS tapes reflects the combination of the dissipative mechanisms that occur in these two current-carrying paths [Hua98b].

It is a standard practice to calculate the critical current density J_c of Bi-2223 tapes by dividing the critical current I_c, obtained by DC transport current measurements with the 1 µV/cm voltage criterion, by the cross-section S of the superconductor [Gra95], [She99]. For precise calculation of S, scanning electron microscopy is usually employed. Measurements of the critical current in applied DC field have shown that I_c, therefore J_c, decrease considerably even for magnetic fields well below 200 mT [Dut99].

In the last years, different implementations using finite-difference methods, finite-element methods, as well as hybrid FEM-boundary-element methods have been proposed for numerical modelling of HTS with B-dependent J_c. These numerical methods allow simulations of HTS in various operating conditions, among which the application of AC current or magnetic field is of main practical interest. The use of $J_c(B)$ models based on measurements in DC applied field for simulations with AC current or magnetic field at power frequencies requires the assumption that the critical current density is varying during the cycle with the amplitude of the local AC field [Ame01]. There are no particular theoretical or experimental indications for opposing this assumption, at least for low frequencies, and we will use it as a basis for the modelling of $J_c(B)$ and $n(B)$ in AC operating conditions at 59 Hz.

5.3 Modelling of HTS tapes with $J_c(B)$ and $n(B)$ in perpendicular magnetic fields

5.3.1 Models for $J_c(B)$ dependence in perpendicular magnetic field

One of the first models used to describe the $J_c(B)$ dependence in perpendicular DC applied field was introduced by Kim [Kim62]:

$$J_c(B,T) = \frac{J_{c0}(T)}{1 + \frac{|B|}{B_0}} \tag{5.1}$$

where B is the magnitude of the flux density, B_0 is a constant and $J_{c0}(T)$ is the critical current density at zero field, which is a temperature dependent characteristic of the material.

Kim's model was based on experimental data for low temperature superconductors. At the same time, Anderson gave a theoretical interpretation of the $J_c(B,T)$ dependence in relation to the thermally activated flux creep [And62].

The effect of the temperature on the J_c and n-values of Bi-2223 tapes has been reported in [Wan00]. Since Bi-2223 tapes are most often operated in a liquid nitrogen bath at 77 K, we will assume that the temperature variation in the BSCCO core is insignificant at power frequencies (see also Section 3.6.3) and the J_c and n-values will be considered in the numerical simulations as temperature independent.

An experimental determination of the $J_c(B)$ and $n(B)$ dependence of Bi-2223/Ag tapes has been done in our laboratory [Dut99]. The J_c is calculated as I_c/S, where S is the cross-section of the superconductor. The I_c and n are measured with a transport current set-up by making a power-law fit to the experimental data – $V = V_c(I/I_c)^n$, where V_c is the voltage corresponding to the 1 μV/cm criterion. The data acquisition is performed with a triangular waveform AC current at very low frequency (quasi-DC) in applied DC magnetic field with varying orientation.

Assuming a constant operation temperature of the Bi-2223/Ag tapes, Kim's model will be written as:

$$J_c(B) = \frac{J_c(0)}{1 + \frac{|B|}{B_0}} \tag{5.2}$$

where $J_c(0)$ is the critical current density at zero applied field and |B| is the magnitude of the perpendicular magnetic field. The constant B_0 = 0.021 T is defined from the experimental data and corresponds to the field, at which J_c drops to half the value of $J_c(0)$.

Figure 5-1 shows the experimental $J_c(B)$ and $n(B)$ dependence in a field perpendicular to the tape's wide side. Kim's law does not fit very well the measurement data, especially for the $n(B)$ dependence. Therefore, we have made the following polynomial fits to the measurement data:

$$J_c(B) = J_c(0) + \sum_{k=1}^{m} a_k \left(\frac{|B|}{B_0}\right)^k \tag{5.3}$$

$$n(B) = n(0) + \sum_{k=1}^{m} c_k \left(\frac{|B|}{B_0}\right)^k \tag{5.4}$$

where B_0 is a normalizing constant of 1 T, formally needed to obtain dimensionless value of the polynomial term, and |B| is the absolute value of the perpendicular field in Tesla. The polynomials in Eq. (5.3) and (5.4) are of 5th and 4th degree, respectively, and the coefficients a_k and c_k are real.

The polynomial models in Eq. (5.3) and (5.4) give an excellent fit to the experimental data, as can be seen in Fig. 5-1. Other models of $J_c(B)$ in HTS tapes can also be used – a power law of the type $J_c(B) \sim B^{-\alpha}$, or an exponential dependence $J_c(B) \sim \exp(-B/B_0)$, see for example [Hua98b] and [The94].

We have made FEM simulations on a monofilamentary Bi-2223 tape of rectangular cross-section, whose technical parameters are given below in Table 5-1.

TABLE 5-1 Technical parameters of the simulated Bi-2223 tape

Tape dimensions	*BSCCO dimensions*	*BSCCO mesh nodes*	*I_c (A)*	*$J_c(0)$ (A/mm^2)*	*n(0)*
2.75 × 0.36 mm	2.20 × 0.16 mm	60 × 20	19.1	54	17

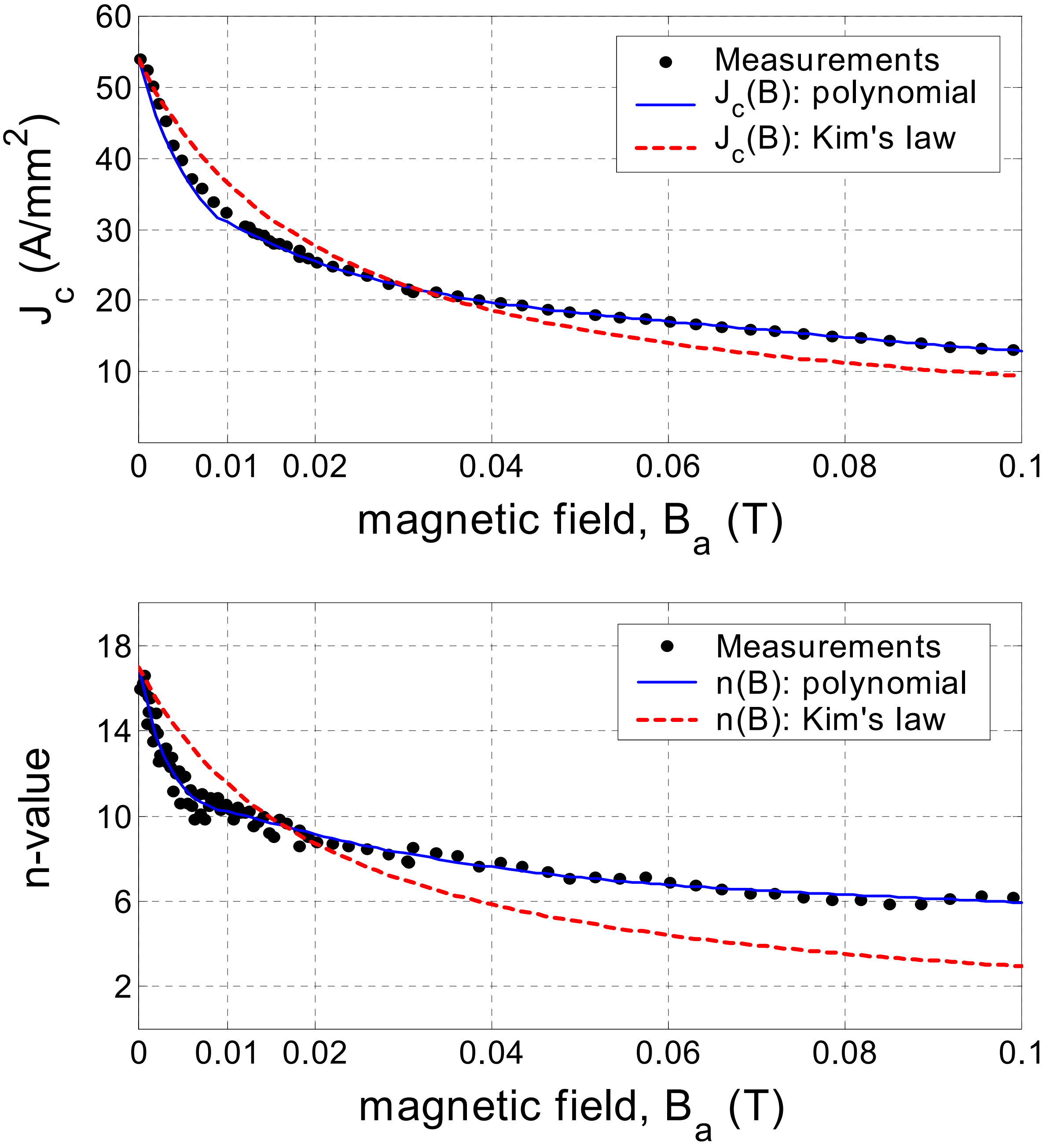

Figure 5-1 J_c(B) and n(B) dependence in applied perpendicular field. Shown are the experimental data, the polynomial fits from Eq. (5.3) and (5.4), as well as Kim's models.

5.3.2 Comparison between modelling with constant J_c and $J_c(B)$ in perpendicular magnetic field

Field of complete penetration

A very important characteristic in the critical state model is the field of full penetration H_p, at which the magnetic flux has penetrated to the center and the current density in entire specimen has reached its saturation value J_c, see Fig. 4-1. H_p has a direct bearing on the levels of magnetization losses in the superconductor since below the full penetration the losses are proportional to H_a^3 and above the full penetration the losses gradually decrease until linear dependence with the applied field H_a is reached, see Eq. (4.29) in Section 4.6.2.

For slabs and strips of rectangular cross-section $2a\times 2b$ the field of complete penetration (in Tesla) is given respectively by

$$\begin{aligned} B_p &\approx \mu_0 J_c a, && b >> a \\ B_p &\approx \mu_0 J_c (2b/\pi)\ln(2a/b), && b << a \end{aligned} \tag{5.5}$$

where b is the half-thickness and a is the half-width of the cross-section [Bra96b].

For the simulated Bi-2223/Ag tape (see Table 5-1) in perpendicular field a = 1.1 mm, b = 0.08 mm, and using Eq. (5.5) for $b << a$ we obtain B_p = 11.4 mT.

With FEM simulation the value of B_p can be obtained by plotting the current density and field profiles in the superconductor along the x-axis of the tape for different field amplitudes. This is shown in Fig. 5-2 and 5-3 for simulations with constant J_c and $J_c(B)$ for applied field of 5 and 10 mT, respectively.

The $J_c(B)$ dependence leads to faster penetration of the field and, consequently, smaller current-free region in the center, compared to the constant-J_c model, see Fig. 5-2. The current density profiles are flat in the constant-J_c model, while the current profiles are oblique with the $J_c(B)$ model due to the fact that J_c is lower where the field is higher.

When the amplitude of the external perpendicular field is 10 mT (Fig. 5-3), the magnetic flux density has completely penetrated the specimen in the case with $J_c(B)$. The full penetration field is around 8-9 mT. In the constant-J_c model, the flux is just reaching the center of the tape and, therefore, the full penetration field is around 10-11 mT, which corresponds very well to the calculated B_p value above from Eq. (5.5). Because of the $J_c(B)$ dependence, the saturating current density at the three time instants is rather different, while in the constant-J_c model it is almost unchanged during the cycle.

An important feature of HTS tapes with aspect ratio $a/b >> 1$ is the large demagnetizing effect in perpendicular field, which results in higher field amplitudes near the edges compared to the one of the applied external field. This can be observed in Fig. 5-3, where the amplitude of the flux density at the edges of the superconductor exceeds 10 mT. Also, the field profiles are not straight lines as in the CSM even for the model with constant J_c, which is in accord with the analytical solutions for a strip, given by Brandt, see Section 4.2.1 and Fig. 4.2 as well.

For applied fields above B_p, the superconductor is fully saturated. An example of the saturation profiles in the models with constant J_c and $J_c(B)$ is shown in Fig. 5-4 for external field of 30 mT. At $\omega t = k\pi$ the amplitude of the external field is passing through zero; still, the induced currents trying to oppose the change of the field are fully saturating the whole superconductor cross-section. The main difference in the models with constant J_c and $J_c(B)$ in this case is that the saturating current density in the latter is varying with the local field amplitude – the higher the local field, the lower the current density is.

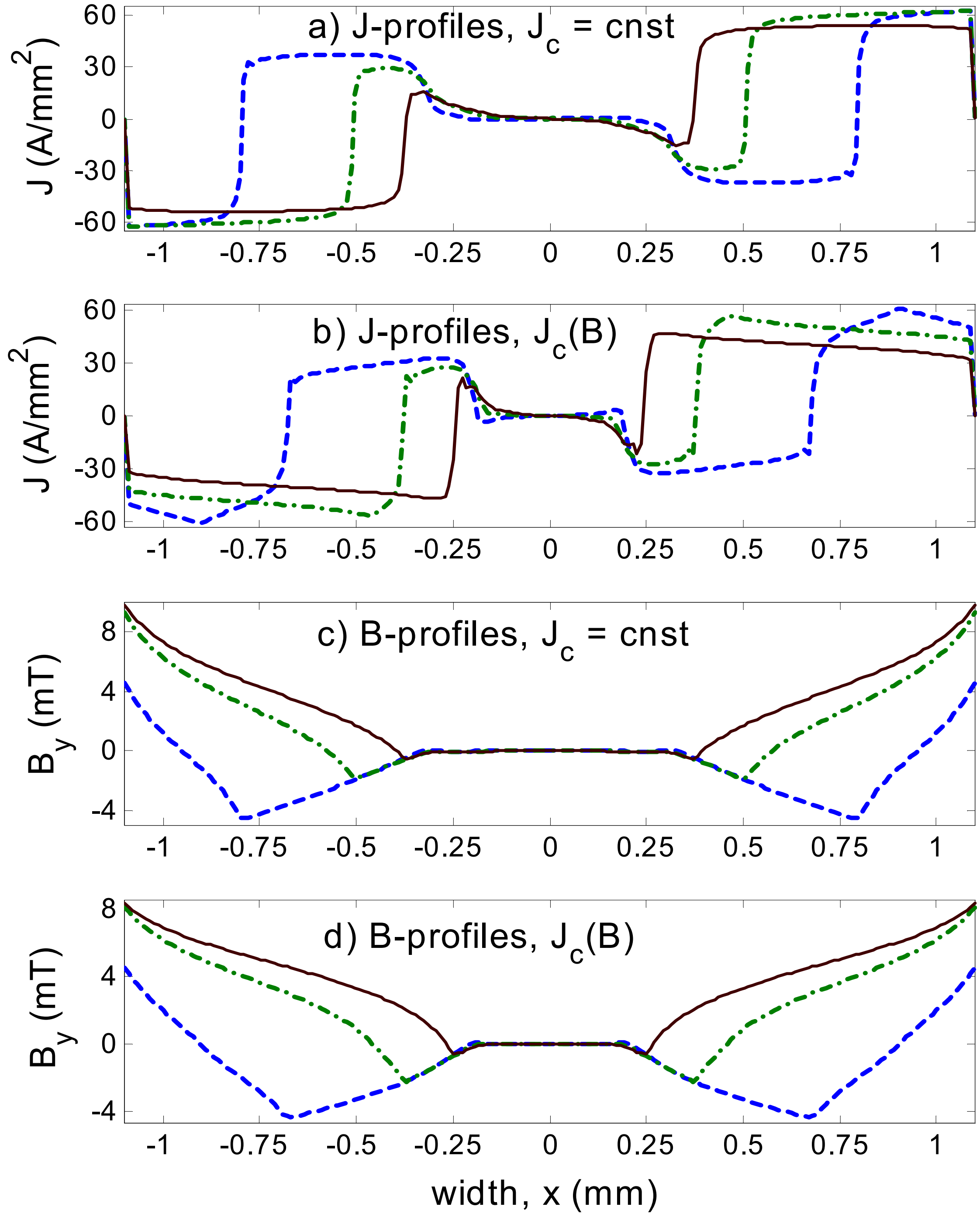

Figure 5-2 Current density and magnetic field profiles along the *x*-axis for applied perpendicular field with B_a = 5 mT. The dashed, dash-dot, and solid lines correspond respectively to $\omega t = \pi$, $5\pi/4$ and $3\pi/2$. $J_c(B)$ is the polynomial fit of Eq. (5.3).

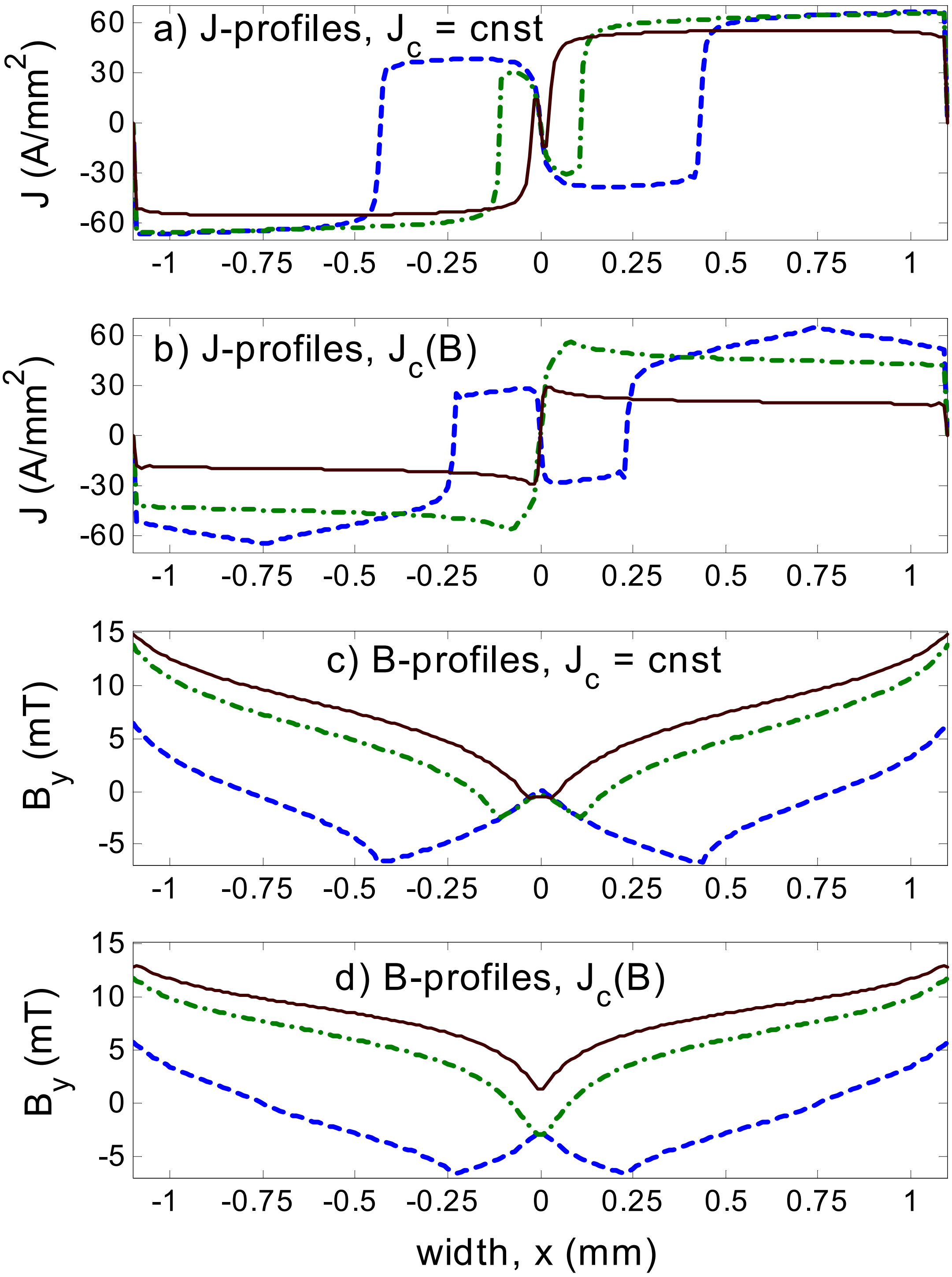

Figure 5-3 Current density and magnetic field profiles along the *x*-axis for applied perpendicular field with B_a = 10 mT. The dashed, dash-dot, and solid lines correspond respectively to $\omega t = \pi$, $5\pi/4$ and $3\pi/2$. J_c(B) is the polynomial fit of Eq. (5.3).

a) J_c = constant

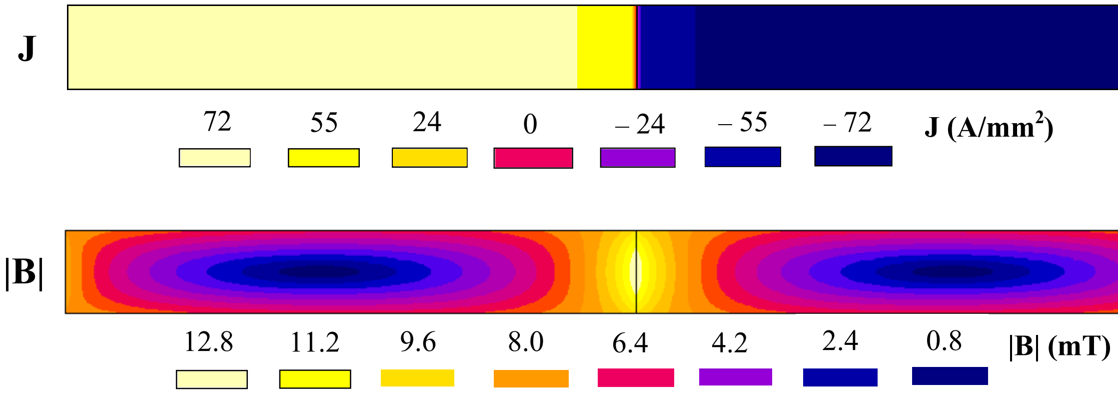

b) $J_c(B)$ – Kim's law

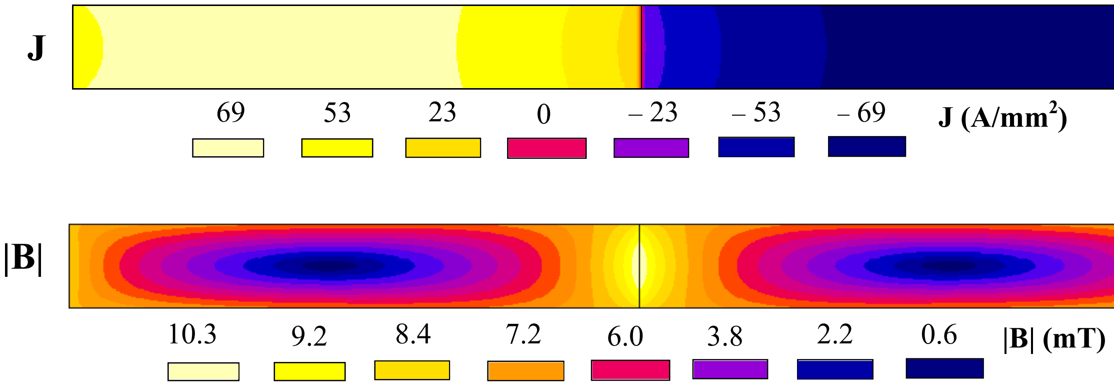

c) $J_c(B)$ – polynomial fit

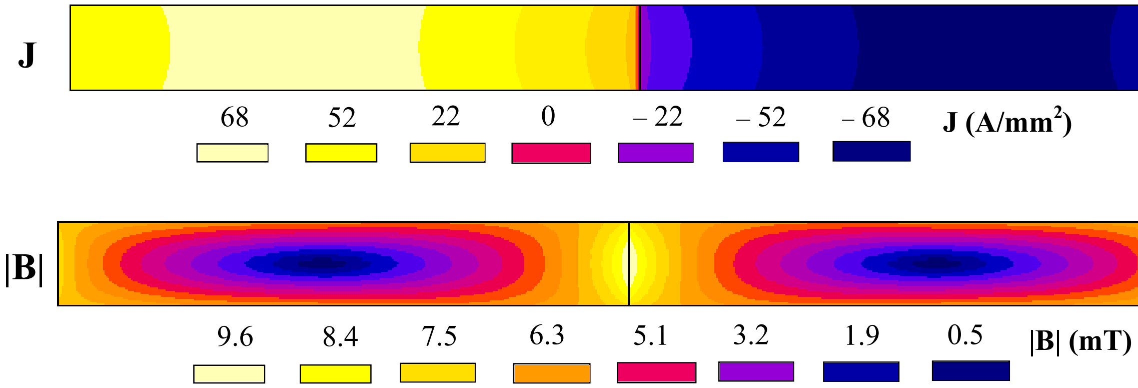

Figure 5-4 Current and flux density distribution at $\omega t = 2\pi$ in perpendicular field with B_a = 30 mT for the models with constant J_c and $J_c(B)$.

Magnetization loss in perpendicular field

The magnetization loss in the Bi-2223 tape is shown in Fig. 5-5 for increasing amplitudes of the external AC magnetic field. For values of B_a around 10 mT (the penetration field) a cross-over occurs between the AC loss curves of the model with constant J_c and the $J_c(B)$ models. Below B_p (e.g. $B_a = 5$ mT) there is a weaker penetration of the field in the case J_c is constant, as it was shown in Fig. 5-2, and therefore the AC loss is lower than with the $J_c(B)$ models. If larger $J_c(0)$ values are used, the B_p will be higher, and the AC loss difference for low fields will be easier to observe in the log-log plot. Above B_p, on the other hand, the current density in the entire specimen is equal to or exceeding the local J_c, the conductor is fully saturated and a transition from the superconducting state occurs. In this case, the $J_c(B)$ leads to reduction of the conductivity of the material, which means less induced currents, and correspondingly lower loss as well.

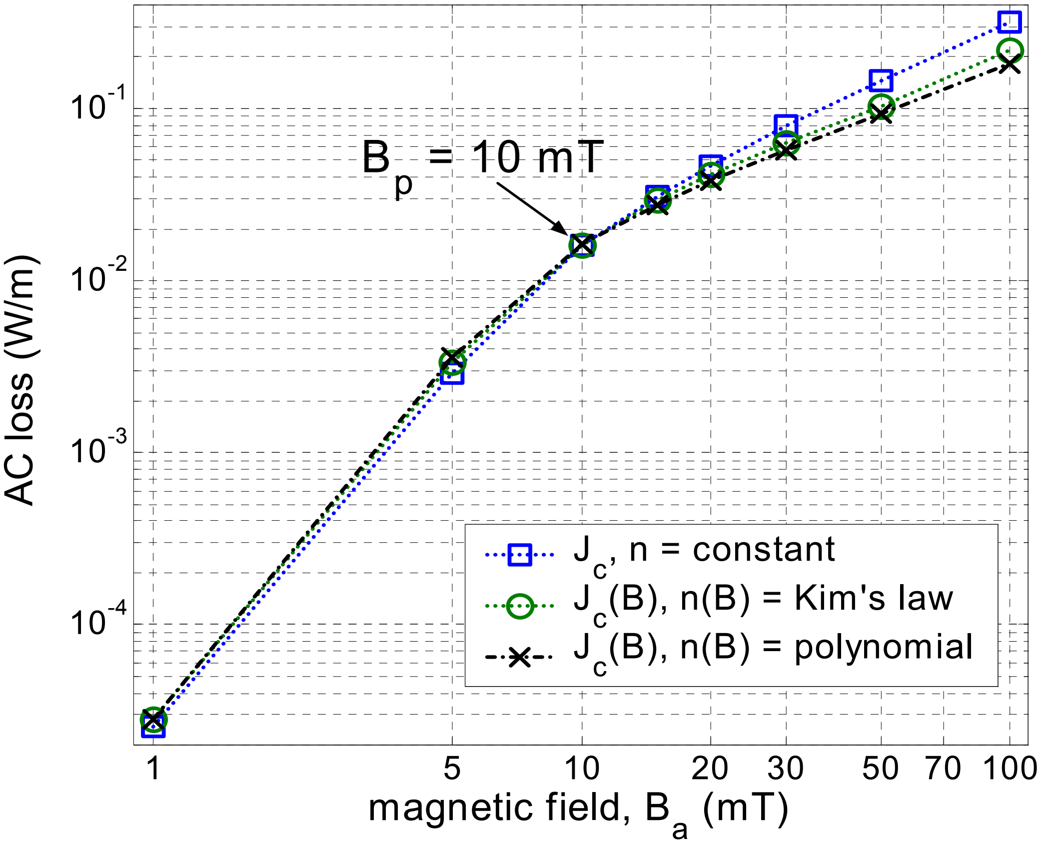

Figure 5-5 Magnetization loss at 59 Hz in perpendicular AC magnetic field for models with constant J_c and J_c(B).

In order to better understand the particular AC loss behaviour of HTS below and above B_p, we have integrated the screening current density over half of the tape's cross-section for each time step and the amplitude of the first harmonic of the induced current is plotted vs. the applied field in Fig. 5-6. Unlike the critical state model, the current density in HTS tapes may exceed J_c, and therefore the screening currents are not limited by J_c. With the constant-J_c model, the induced currents increase gradually with the magnetic field above B_p, while the $J_c(B)$ dependence results in a decrease of the induced current for fields above B_p. This explains the difference between the AC loss of the models with $J_c(B)$ and constant J_c.

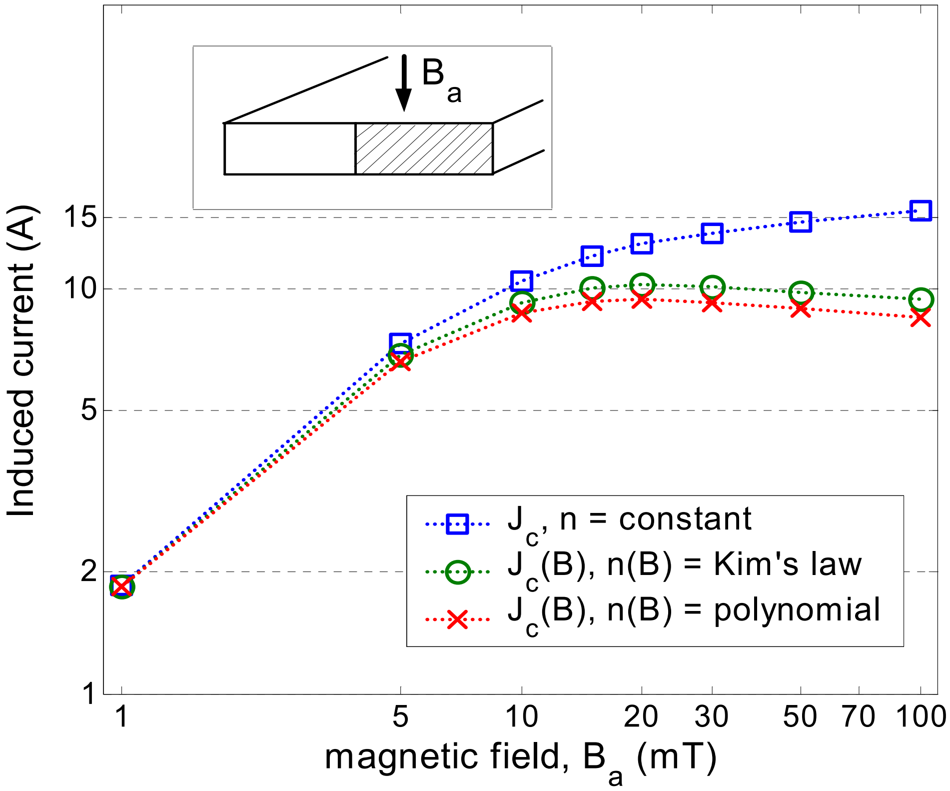

Figure 5-6 First harmonic of the induced currents in applied perpendicular field at 59 Hz.

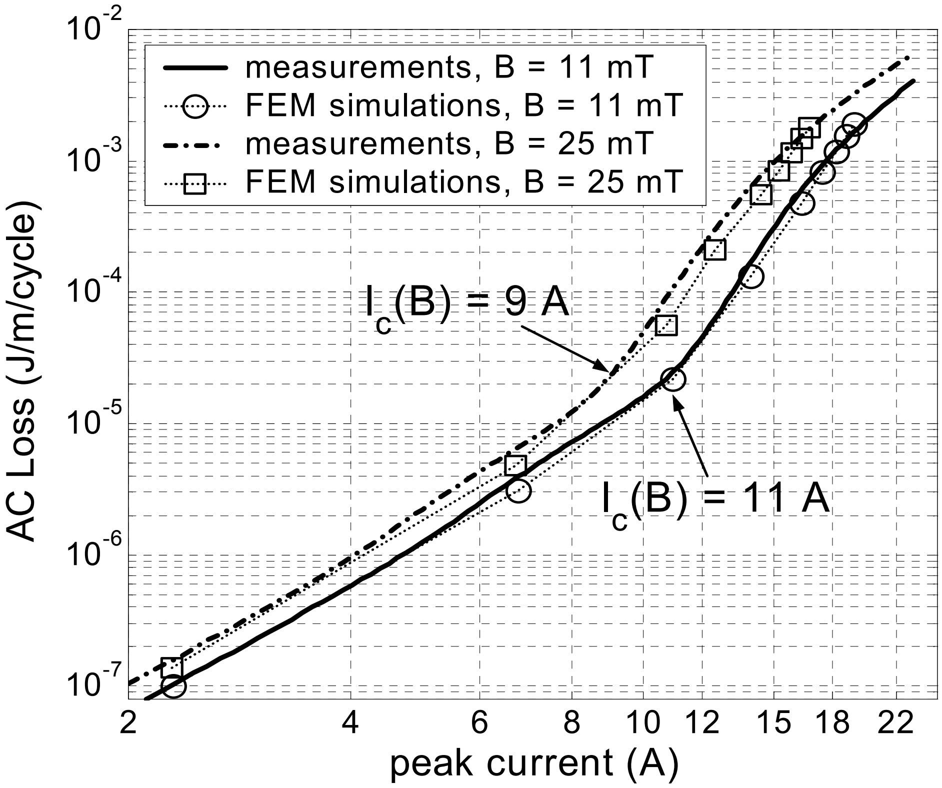

Figure 5-7 Comparison of transport current AC loss in DC external field between experimental and simulated results. The simulated $J_c(B)$ is the polynomial fit from Eq. (5.3).

5.3.3 AC losses in transport current applications in perpendicular magnetic field

Transport current in DC field

Figure 5-7 presents a comparison between measured and simulated losses when AC transport current is applied in DC perpendicular magnetic field with B_{DC} = 11 mT and 25 mT. As can be seen in the figure, there is a very close correspondence between measured and simulated results.

The points, at which a change of slope occurs on the loss curves (11 A at B_{DC} = 11 mT and 9 A at B_{DC} = 25 mT), define the effective I_c in applied DC field. The critical current density obtained by dividing 11 A and 9 A by the cross-sectional area of the superconductor is respectively 31 A/mm^2 and 25 A/mm^2, which corresponds well to the measured $J_c(B)$ values in Fig. 5-1.

Transport current in AC field

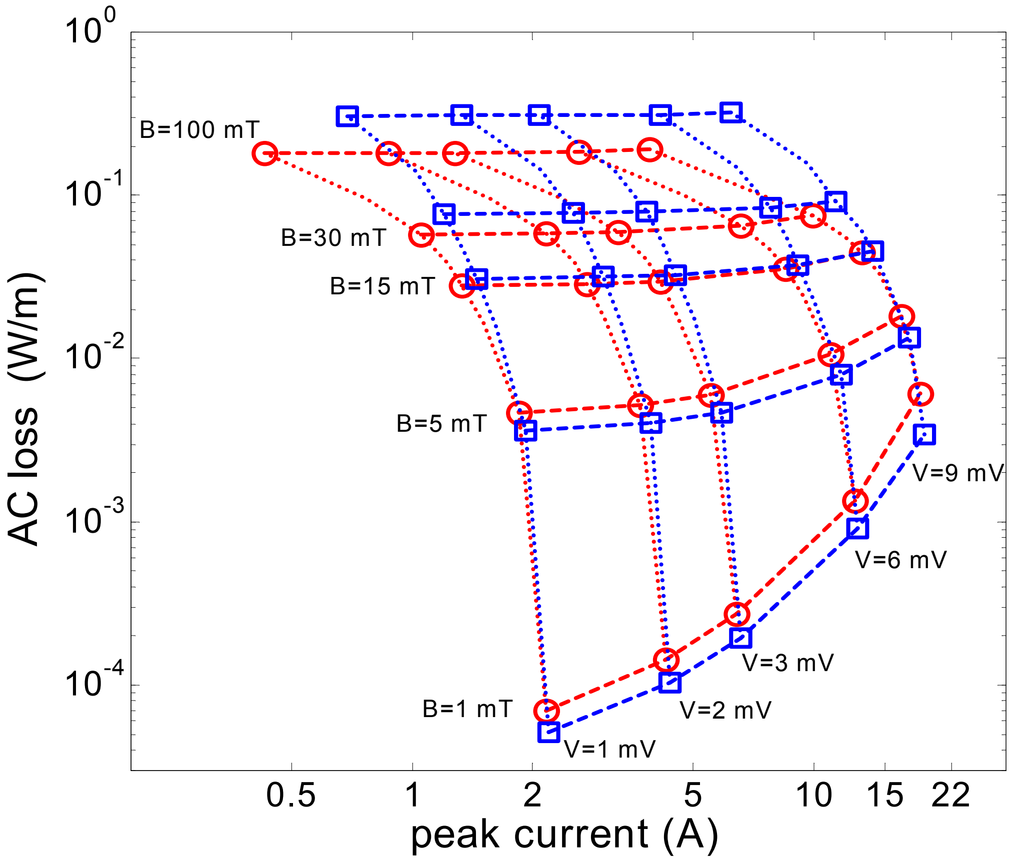

Figure 5-8 AC loss evolution when AC voltage source and AC magnetic field are applied in-phase at 59 Hz. Circle symbols are used for B-dependent J_c & n, square symbols are used for constant J_c & n. Dotted lines connect points with equal driving voltage; dashed lines connect points with equal applied field.

Figure 5-8 shows the overall evolution of the power loss in the Bi-2223 tape when in-phase AC transport current (driven by a voltage source) and magnetic field at 59 Hz are simultaneously applied. The total current (integral of the transport + induced current density through the tape's cross-section) diminishes with B since the increasing induced currents decrease the transport current capacity of the tape in simulations with voltage source. Just a reminder, the integral of the induced current density through the cross-section is always zero, since it has opposite signs in the two halves of the tape.

The total loss has a transport current and a magnetization loss contribution. The external perpendicular field causes enormous increase in the magnetization loss, which completely dominates the transport current contribution above 15 mT, where the loss is almost independent of the peak current.

As in the simulations with applied magnetic field only, the total AC loss for the constant-J_c model is lower than for the $J_c(B)$ model below the penetration field, and vice-versa above the penetration field ($B_p \sim 10$ mT).

5.4 Modelling of monofilamentary conductors in different applications

5.4.1 Isotropic and anisotropic models of $J_c(B)$ and $n(B)$ for mono-filamentary wires and tapes

Different $J_c(B)$ models have been utilized for describing the B-dependence of the critical current density and power index of HTS. Kim's model can be used for their $J_c(B)$ and $n(B)$ dependence in parallel or perpendicular fields [Ame01], [Mas98]. However, as it was shown in the previous section, Kim's model does not always fit well the experimental results for $J_c(B)$ and $n(B)$ in Bi-2223 materials, and different polynomial fits to data from measurements in DC parallel or perpendicular fields have been preferred [Ame98], [Nib01a].

The disadvantage of the above-mentioned models is that they do not take into consideration the angle of orientation of the field. The structure of raw Bi-2223 materials (non-processed oxide powder) is composed of randomly orientated and misaligned grains. After the rolling during the OPIT (oxide-powder-in-tube) process, the Bi-2223 grains are aligned and a strong anisotropy between the *a*,*b*- and *c*-planes of the tapes appears, which results in different degradation of J_c in applied parallel and perpendicular fields. Experimental investigations into the current density in Bi-2223 tapes in fields with different orientation have been reported in [Tan01] and the anisotropy has been attributed also to the different pinning forces in parallel and perpendicular fields.

Since the $I_c(B)$ and $n(B)$ relations in Bi-2223 tapes possess strong anisotropy, more precise models are required for modelling their B-dependence in fields with varying orientation. This is necessary also in the cases of self-field and combined current + field applications, where the local magnetic field has different orientation, as shown in Fig. 5-9.

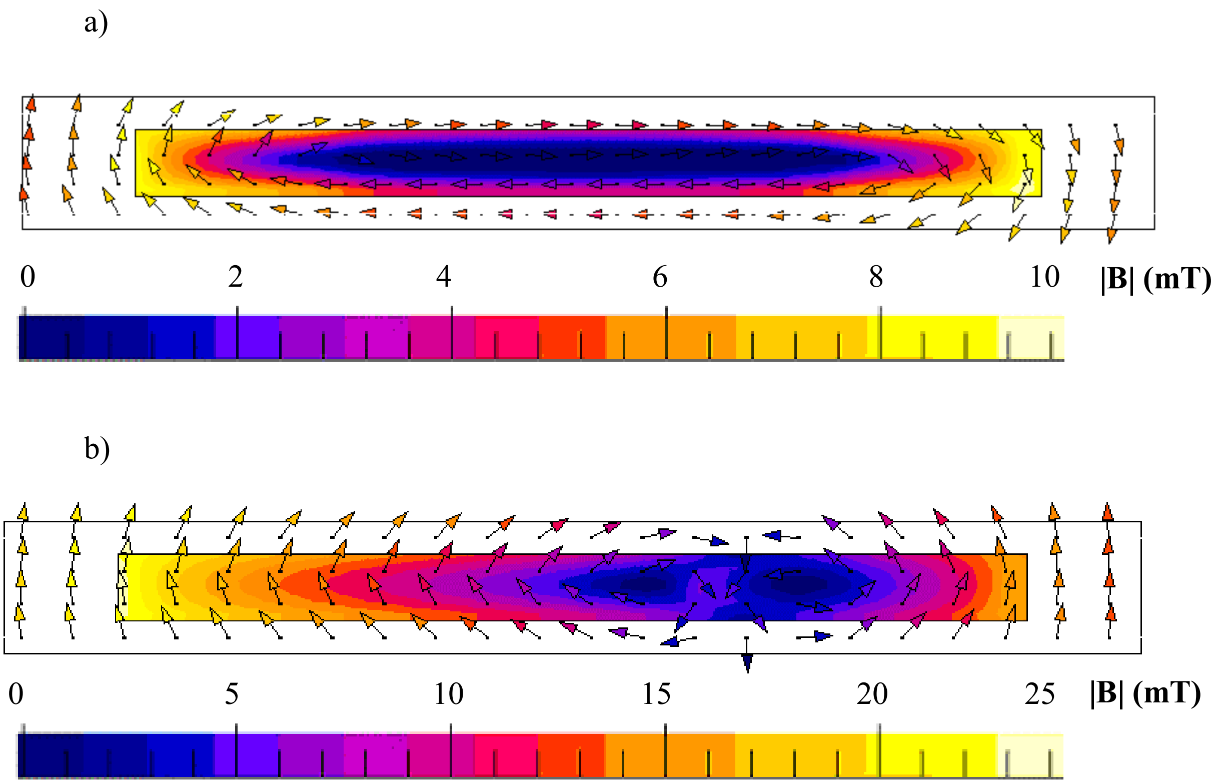

Figure 5-9 Magnitude and direction of the magnetic flux density in a rectangular tape with applied transport current of 17 A at $\omega t = \pi/2$ in self-field (a) and in external perpendicular field of 15 mT at $\omega t = \pi/4$ (b). $J_c = 80\ \mathrm{A/mm^2}$ and $I_c = 28.2$ A

Experimental results for the dependence of I_c on the angle of orientation of the field α can be found, for example, in [Kov99] but no compact mathematical expression to describe this dependence has been given. A model for $I_c(B)$ and $n(B)$ in magnetic fields at different angle, using a field-correction factor, has been already used in numerical analysis [She98], [She99], [Yaz98]. The functional dependence $I_c(\alpha,B)$, however, has not been explicitly given. Recently, a model for describing the angular dependence of I_c, based on a Gaussian distribution of the misalignment angles of the grains has been proposed in [Mee01].

The following model for the $I_c(\alpha,B)$ dependence has been derived in [Dut99]:

$$\frac{I_c(B)}{I_{c(0)}} = \frac{1+\left(\dfrac{B}{B_1}\right)^{p1}+\left(\dfrac{B}{B_3}\right)^{p3} F(\alpha,z_1)}{1+\left(\dfrac{B}{B_2}\right)^{p2}+\left[\left(\dfrac{B}{B_4}\right)^{p4}+\left(\dfrac{B}{B_5}\right)^{p5}\right]F(\alpha,z_1)} \tag{5.6}$$

This model, despite its very good fit to the experimental data, is very complicated. The necessity to identify the 10 parameters and the additional function F makes it difficult to employ for modelling or characterization purposes.

We have proposed a new model for anisotropic $J_c(B)$ and $n(B)$ dependence [Sta02a], [Sta02b], which is based on measurements of I_c and n, made on a Bi-2223/Ag tape in DC magnetic field up to 300 mT with varying angle [Dut99], described briefly in Section 5.3.1.

The measured sample is a monofilamentary tape with elliptical geometry comparable to the one specified in Table 5-3.

The $J_c(B)$ relation is modelled as

$$J_c(B) = J_{c0} F_J(B) \tag{5.7}$$

where J_{c0} is the critical current density of the material in the absence of any magnetic field (self-field or external field), and $F_J(B)$ describes the decrease of J_c in the presence of magnetic field. The $n(B)$ relation is similar. For describing the anisotropic functions $F_J(B)$ and $F_n(B)$, we have used the experimental dependence of $I_c(B)$ and $n(B)$, so that $J_c(B)$ and $n(B)$ are modelled as follows [Sta02b]:

$$J_c(B) = J_{c0} F_J(B) = J_{c0} \frac{I_c(B)}{I_c(0)} = J_{c0} \frac{1}{\alpha_1 + \alpha_2 e^{-B_{ab}/B_o} + \alpha_3 e^{-B_c/B_o}} \tag{5.8}$$

$$n(B) = n_0 F_n(B) = n_0 \frac{n(B)}{n(0)} = n_0 \frac{1}{\beta_1 + \beta_2 e^{-B_{ab}/B_o} + \beta_3 e^{-B_c/B_o}} \tag{5.9}$$

where $I_c(0)$ and $n(0)$ are the measured values at zero applied field, B_{ab} and B_c are respectively the absolute values of the magnetic field components (in Tesla), parallel to the *a,b*-axis and the *c*-axis, B_o is a normalizing constant of 1 T, formally needed to obtain dimensionless exponent, and $\{\alpha_i, \beta_i\}$ are model coefficients. J_{c0} is a characteristic of the material and is not a fitted parameter. The exponential model in Eq. (5.8) and (5.9) is based on the experimental data for the normalized $I_c(B)$ and $n(B)$ dependence, therefore different values of J_{c0} can be used.

With the transport current technique, the measured $I_c(0)$ and $I_c(B)$ values include the effect of the self-field, which cannot be avoided. However, for low applied current, the self-field is negligible compared to the applied external field. Since the $I_c(0)$ of the sample used in the $I_c(B)$ measurements is 19 A, which produces a local self-field with maximum of 6.8 mT near the edges at peak current and much lower field inside the tape (obtained with FEM simulations), we assume that the local field in the experiments is due to the applied field only and the error in the fit of $\{\alpha_i, \beta_i\}$ due to the presence of self-field in this case is negligible.

In order to select the functional dependence of $I_c(B)/I_c(0)$ and $n(B)/n(0)$ on the B_{ab} and B_c components, and to identify the model parameters $\{\alpha_i, \beta_i\}$, we have made an exhaustive search for the best least-squares fits to the measurement data using a very large data-bank with equations of 2-argument functions of various classes and complexity (more than 3800 basic equation sets). The exponential model given in Eqs. (5.8) and (5.9) has been selected for its smoothness and simplicity; it gives a fairly good fit to the experimental data and is by far the simplest model that could be found, even if some high-order Chebyshev and logarithmic polynomials produce a slightly better fit. The root mean square error of the models is 0.05 in Eq. (5.8) and 0.07 in Eq. (5.9); the largest deviation from the measurement data in both models is for fields below 20 mT with dominating perpendicular component, where the measured values are by some 10% lower than the fit.

The models described with Eq. (5.8) and (5.9) are to be used for anisotropic HTS tapes with elliptical or rectangular shape. In round or square monofilamentary conductors, which can be manufactured by extrusion without rolling, there is no anisotropy of J_c, and the following isotropic models can be used:

$$J_c(B) = J_{c0}\frac{1}{\alpha_4 + \alpha_5 e^{-|B|/B_o}} \tag{5.10}$$

$$n(B) = n_0\frac{1}{\beta_4 + \beta_5 e^{-|B|/B_o}} \tag{5.11}$$

where $|B| = \sqrt{B_{ab}^2 + B_c^2}$ is the magnitude of the local magnetic field (in Tesla) and B_o = 1 T.

Figure 5-10 shows the anisotropic and isotropic models used for the $I_c(B)$ and $J_c(B)$ dependence. Plotted are also the normalized measurement data for the Bi-2223 tape (a). In anisotropic conductors, the decrease of I_c in perpendicular field (a factor of 8.3 at 200 mT) is much more significant than in parallel field (a factor of 2.2 at 200 mT). For the isotropic model, the parameters have been selected in such a way that the decrease of I_c is intermediate – reaching a factor of 4 at 200 mT, which is based on some recent experimental results for $I_c(B)$ in novel wires with round and square geometry [Su01].

a) anisotropic model

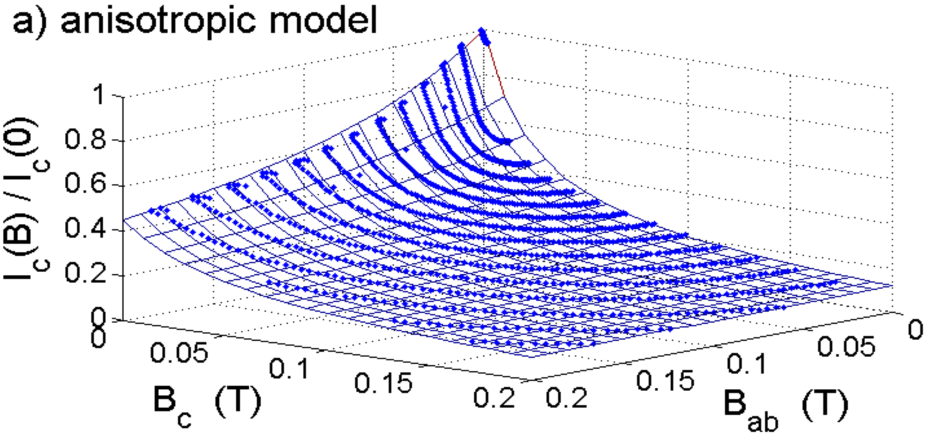

b) isotropic model

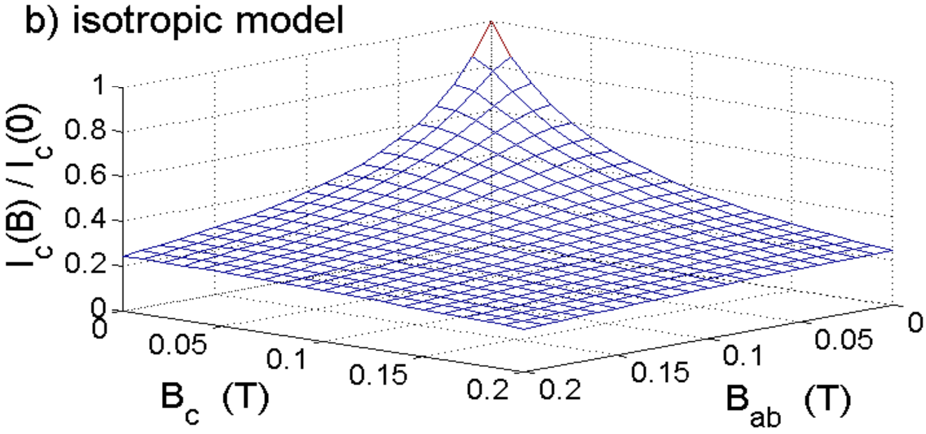

Figure 5-10 Normalized anisotropic model (a) and isotropic model (b) used for describing the decrease of J_c with B in tapes and wires. The dots in the upper plot represent the measured values of I_c in a Bi-2223/Ag tape, and the meshed surfaces in both plots are the exponential models, given in Eq. (5.8) and (5.10).

The plots for the anisotropic and isotropic *n(B)* are displayed in Fig. 5-11.

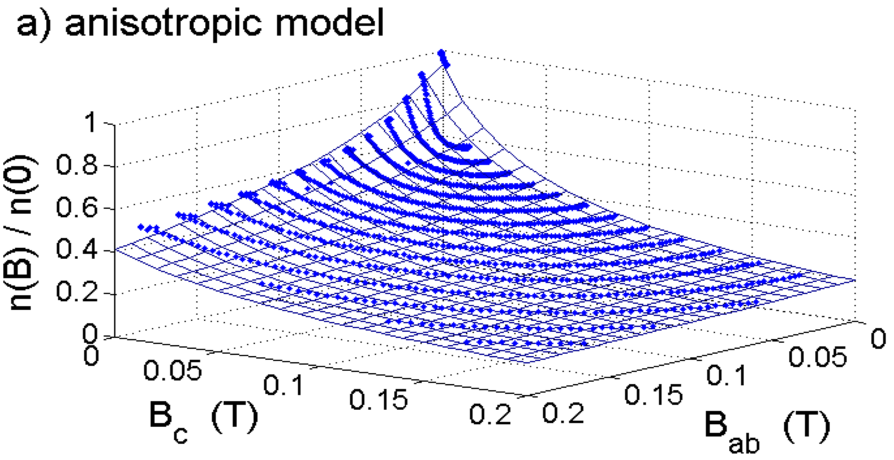
a) anisotropic model

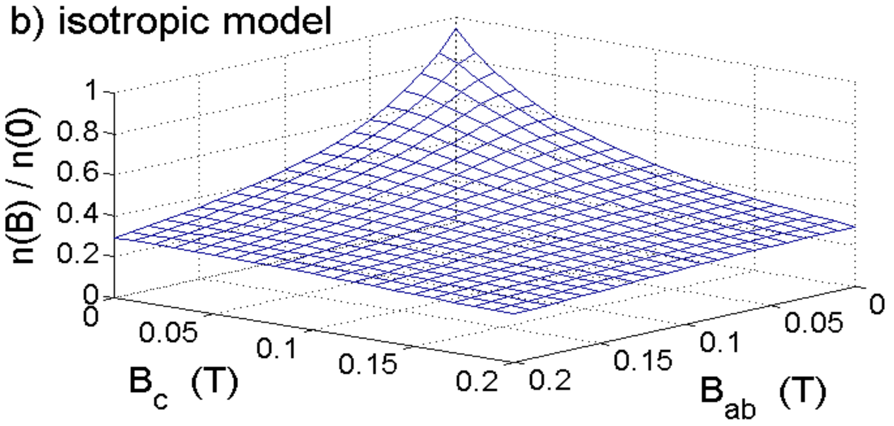
b) isotropic model

Figure 5-11 Normalized anisotropic model (a) and isotropic model (b) used for describing the decrease of the *n*-value with B in tapes and wires. The dots in the upper plot represent the measured values of *n* in a Bi-2223/Ag tape, and the meshed surfaces in both plots are the exponential models, given in Eq. (5.9) and (5.11).

TABLE 5-2 Parameters for the $J_c(B)$ and *n(B)* models

Model	*Equation*			
		α_1	α_2	α_3
***$J_c(B)$* - anisotropic**	(5.8)	48.0	-6.8	-40.2
		β_1	β_2	β_3
***n(B)* - anisotropic**	(5.9)	30.8	-7.5	-22.3
		α_4	α_5	-
***$J_c(B)$* - isotropic**	(5.10)	18.0	-17.0	-
		β_4	β_5	-
***n(B)* - isotropic**	(5.11)	14.0	-13.0	-

The values of the parameters are for magnetic field components in Tesla.

The corresponding coefficients of the anisotropic and isotropic models for $J_c(B)$ and $n(B)$ are shown in Table 5-2. The sum of the coefficients of each model must be equal to 1, so that $J_c(B) = J_{c0}$ and $n(B) = n_0$ at zero magnetic field ($B_{ab} = B_c = 0$).

The $J_c(B)$ and $n(B)$ models, presented above, can be used for modelling or characterization purposes in the presence of magnetic fields with magnitude up to 300 mT. The AC loss levels, as well as the degradation of J_c and n for applied fields above 200 mT are so high, that the use of Bi-2223 conductors in larger fields at 77 K is of no real practical interest. As a matter of fact, in almost all literature sources we have found, experimental and numerical results at 77 K have been reported for fields up to 100 mT only.

5.4.2 Specifications of the simulated monofilamentary conductors

The 2D geometry of a monofilamentary conductor in a Cartesian coordinate system is shown in Fig. 5-12. For such orientation of the conductor, $B_x \equiv B_{ab}$ and $B_y \equiv B_c$, where B_x and B_y are the magnetic field components, calculated by the FEM software. The value of $J_c(B)$ is computed at every point in the superconductor using the B_x and B_y components of the local magnetic field, which results from the interaction of the self-field and the applied external field.

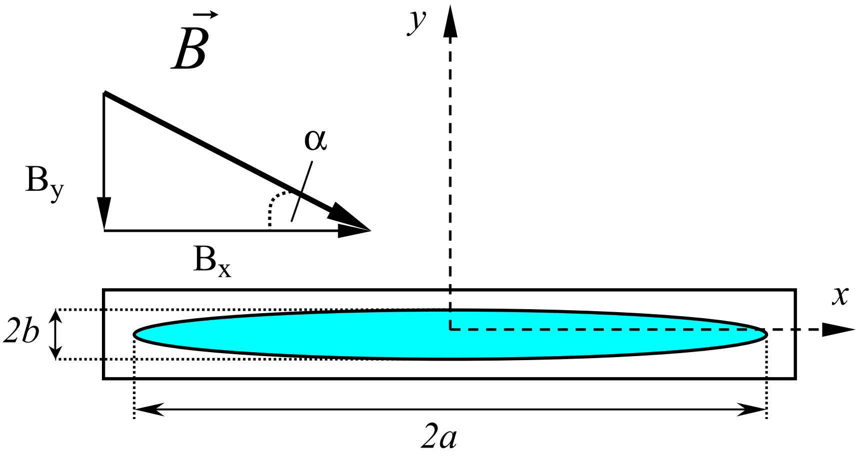

Figure 5-12 2D geometry of a Bi-2223 conductor. The external field is parallel to the *x*-*y* plane, while the current (transport or induced) is perpendicular to the *x*-*y* plane. For such orientation of the conductor, $B_x \equiv B_{ab}$ and $B_y \equiv B_c$.

We have performed FEM simulations with AC transport current at 59 Hz and/or applied AC magnetic field up to 100 mT in phase with the current on four monofilamentary conductors with different shape and aspect ratio, see Table 5-3 below: a rectangular and an elliptical tape, as well as a round and a square wire. The anisotropic models of $J_c(B)$ and $n(B)$ were employed for the simulations with the rectangular and elliptical tape, while the isotropic models were used for the round and square conductors, in self-field and/or applied magnetic fields of different orientation.

The four conductors have the same cross-sectional area of the BSCCO core and the same J_{c0} of 160 A/mm^2. The value of the power index n_0 is 20. The J_{c0} and n_0 selected for the simulations are considered as given. Other values could have been used as well.

TABLE 5-3 Geometry of the Bi-2223 core

Geometric cross-section	*BSCCO dimensions*	*Aspect ratio*
Rectangular	2.20 × 0.16 mm	13.7
Elliptical	2.36 × 0.19 mm	12.4
Square	0.59 × 0.59 mm	1.0
Round	∅ 0.67 mm	1.0

The filling factor of all conductors is 0.35. The aspect ratio is defined as the ratio of the width by the thickness (*a*/*b*) of the BSCCO core (for the ellipse this is the axes ratio).

The geometries of the four Bi-2223/Ag conductors with the FEM mesh are displayed in Fig. 5-13.

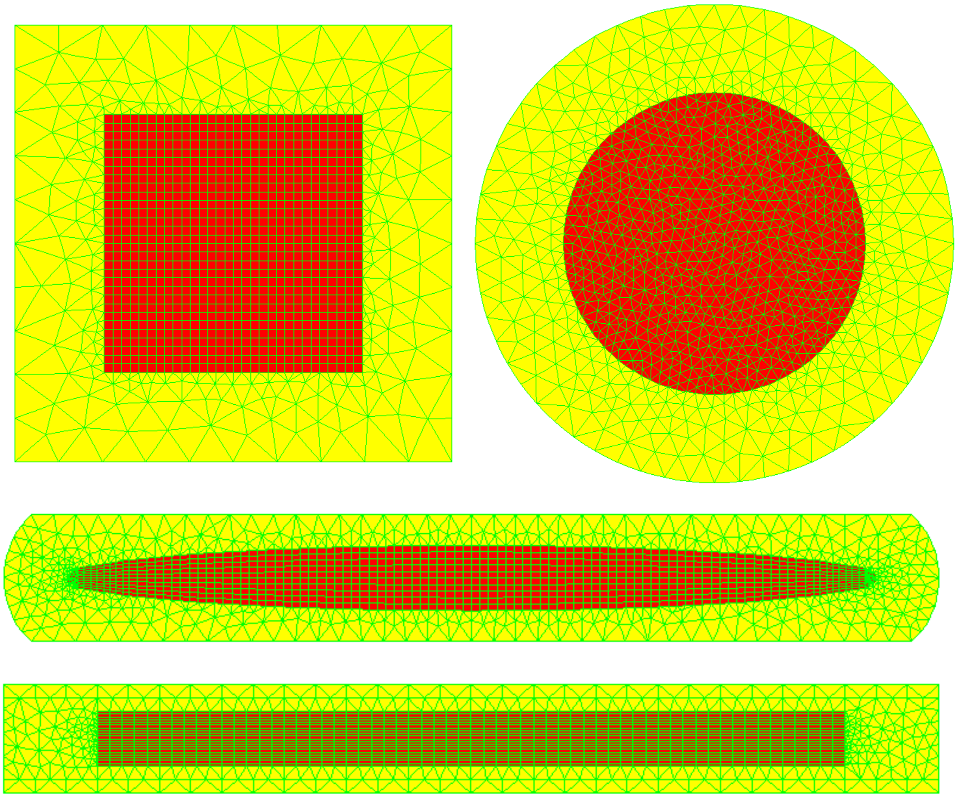

Figure 5-13 Geometry and FEM mesh of the monofilamentary Bi-2223/Ag conductors. The dark region is the superconducting core and the light region is the silver sheath.

5.4.3 Revisiting the definition of I_c in conductors with $J_c(B)$

For a given constant J_c, the critical current I_c is equal to the product J_cS, where S is the BSCCO cross-sectional area. In conductors with $J_c(B)$ and given J_{c0}, due to the decrease of J_c in the presence of magnetic field, the effective critical current is lower than the value of $J_{c0}S = I_{c0}$, which is 56.3 A for the four monofilamentary conductors.

Since the magnetic field is not uniformly distributed within the conductor's cross-section, the quantity $I_c(B)$ is calculated with the FEM software as follows:

$$I_c(B) = \iint_S J_c(B)dxdy \qquad (5.12)$$

where the integration of $J_c(B)$ is performed over the superconductor's cross-section. The integral in Eq. (5.12) changes during the cycle with the variation of the amplitude of the local magnetic field. We have selected to evaluate the $I_c(B)$ at the peak value of the self-field or the external magnetic field ($\omega t = \pi/2$ or $3\pi/2$). In applied magnetic field, $I_c(B)$ is diminished with the increase of the field's amplitude. In applied AC transport current, $I_c(B)$ depends on the self-field, which is not negligible, especially at high currents; it varies according to the geometry and may reach a magnitude of 20-25 mT at peak current of 45 A.

Figure 5-14 shows the values of $I_c(B)$ from Eq. (5.12), obtained for different applied transport current for the monofilamentary conductors. For effective I_c in AC applications, we consider the value of the transport current, at which the calculated $I_c(B)$ is equal to the amplitude of the applied current. This value is obtained from interpolation of the $I_c(B)$ vs. I_{peak} curves and corresponds to the point with equal abscissa and ordinate values.

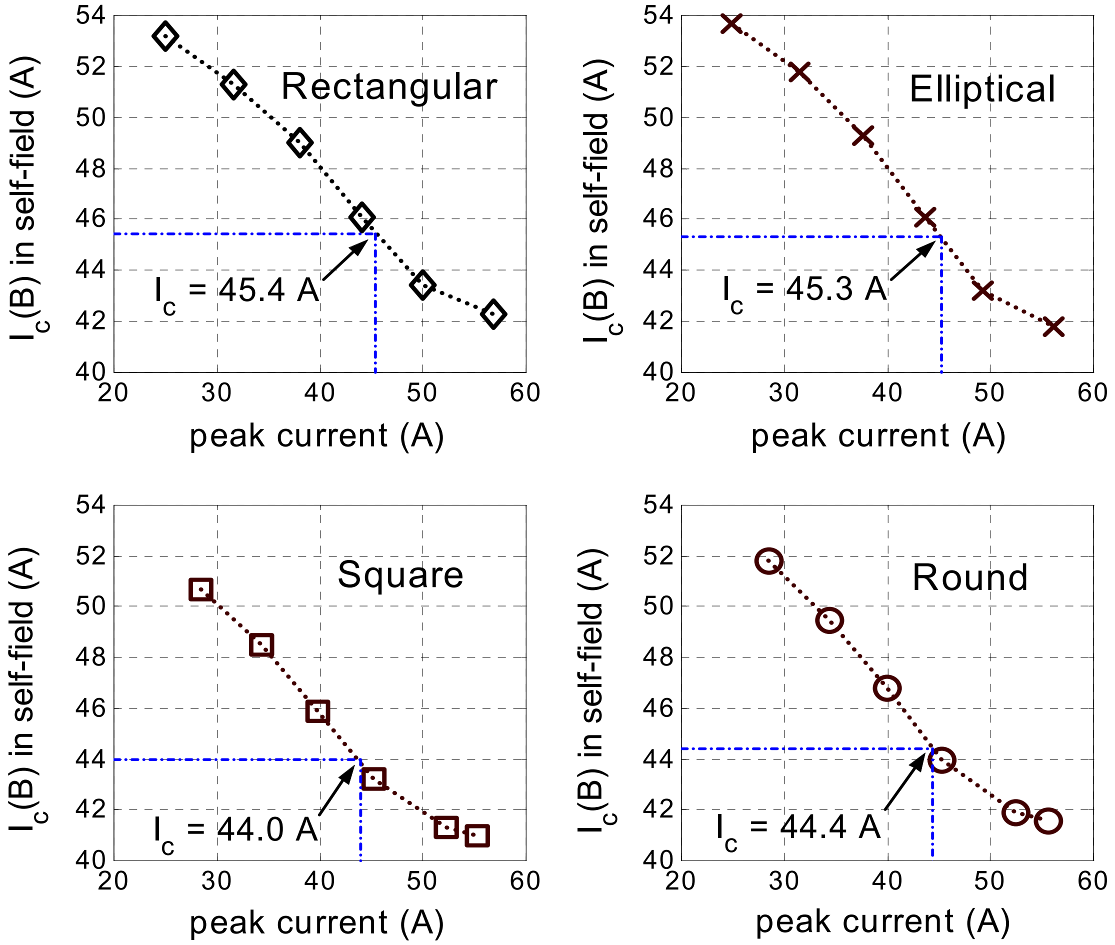

Figure 5-14 I_c(B) calculated from Eq. (5.12) for different applied currents for each conductor. The value of $I_{c0} = J_{c0}S$ is 56.3 A.

The calculated AC I_c values for the different conductors are given in Table 5-4. Since the integral in Eq. (5.12) is taken at the peak of the self-field during the cycle, the calculated effective I_c represents a minimized value. Shown is also the ratio between the effective I_c and I_{c0} (56.3 A). As can be seen from the Table 5-4, the monofilamentary conductors with different shape have similar values of their effective I_c, which is around 20 % lower than the value of I_{c0}.

TABLE 5-4 Effective I_c in AC transport current application

Geometric cross-section	*AC I_c*	*I_c/I_{c0}*
Rectangular	45.4 A	0.81
Elliptical	45.3 A	0.80
Square	44.0 A	0.78
Round	44.4 A	0.79

The AC I_c in self-field, calculated from the $I_c(B)$ vs. I_{peak} dependence for monofilamentary Bi-2223 conductors with given J_{c0}. $I_{c0} = J_{c0}S$ is 56.3 A.

The determination of the effective I_c can be verified in a simple way. The slope of the AC losses in self-field below I_c on a log-log scale is 3.5-4 (losses are proportional to $I_p^{3.5-4}$ between Norris's elliptical and strip predictions), and starts to increase as I_p exceeds I_c. Therefore, the effective I_c can be considered as the peak current, above which the self-field AC losses have steeper slope. This is shown in Fig. 5-15, in which are plotted the self-field AC losses at 59 Hz for the rectangular tape. The straight solid lines indicate the different slopes of the AC loss curves – around 3.5 below I_c and around 9 above I_c. These lines with different slope form an angle, and the interception point of its bisector with the loss curve gives the effective I_c. This simple method yields an effective I_c of 46 A, which is very close to values in Table 5-4.

The effective I_c in the monofilamentary conductors is by 20 % lower than the I_{c0}, which indicates that the influence of the self-field cannot be neglected for the determination of the AC critical current in Bi-2223 conductors with given J_{c0} and $J_c(B)$. Vice-versa, the characteristic J_{c0} value of the material is higher than the one obtained by dividing the self-field $I_c(0)$ by the superconducting cross-section. For example, let us suppose that the measured DC $I_c(0)$ is 56.3 A. In order to obtain an effective AC I_c of 56.3 A in the rectangular tape, we had to use a J_{c0} of 200 A/mm^2 in additional simulations, which is by 25% higher than $I_c(0)/S$. This is because of the non-negligible effects of the self-field on J_c for large currents.

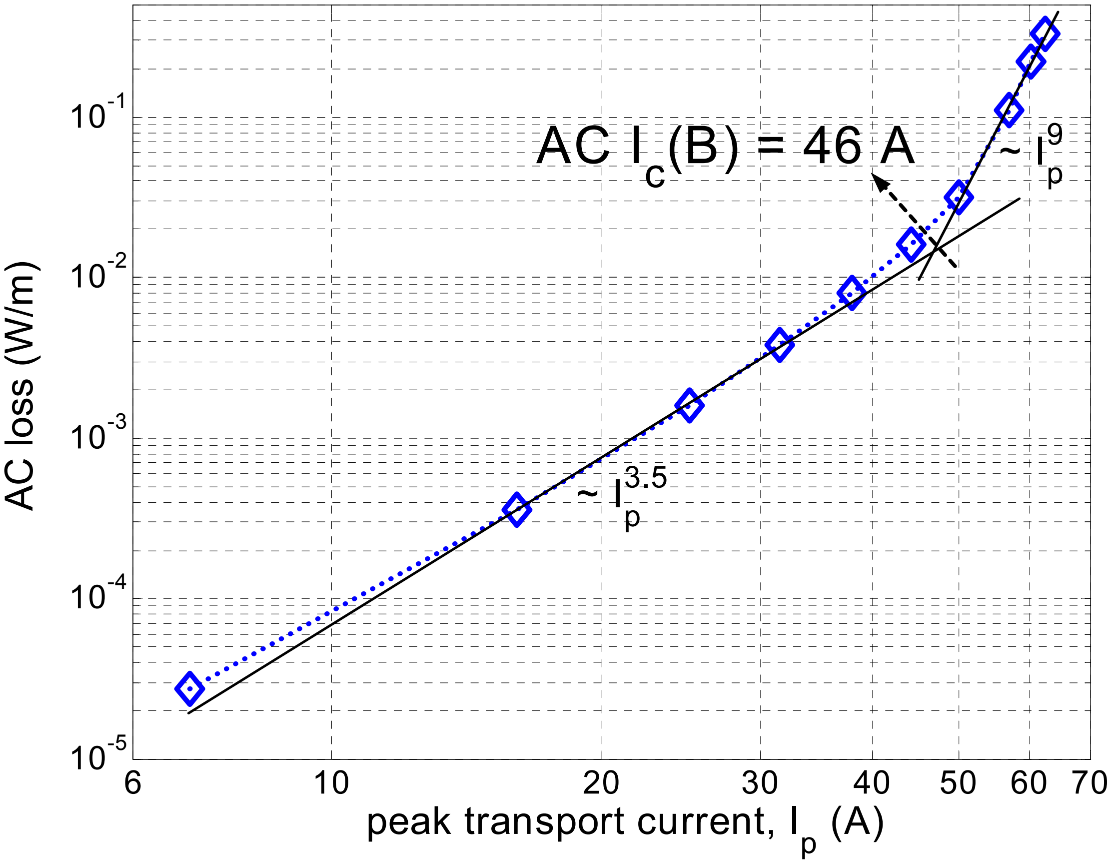

Figure 5-15 $I_c(B)$ evaluation from the self-field AC losses at 59 Hz for the rectangular tape. The solid lines indicate the different slope of the self-field AC losses below and above the effective I_c.

5.4.4 Monofilamentary conductors with transport current

The transport current AC losses (no external field) at 59 Hz are shown in Fig. 5-16 as function of the applied peak current. The simulated strip (very thin rectangle with aspect ratio of 220) has lowest losses, close to the result of Norris. For the conductors of practical interest, the lowest losses are exhibited by the rectangular tape, followed by the losses of the elliptical tape. This follows qualitatively the trend of Norris strip and elliptical predictions. The square, round and elliptical conductors have similar AC losses, higher than the losses in the rectangular tape. The difference of the AC losses is most significant at low currents, where it reaches almost a factor 2 between the rectangular and square geometry. Similar results for rectangular conductors with different aspect ratio have been obtained in [Däu98] and [Yaz98]. As the transport current is increased, the AC loss variation decreases and disappears as $I \rightarrow I_c$ due to the complete saturation of all conductors, which have similar values of the effective $I_c(B)$.

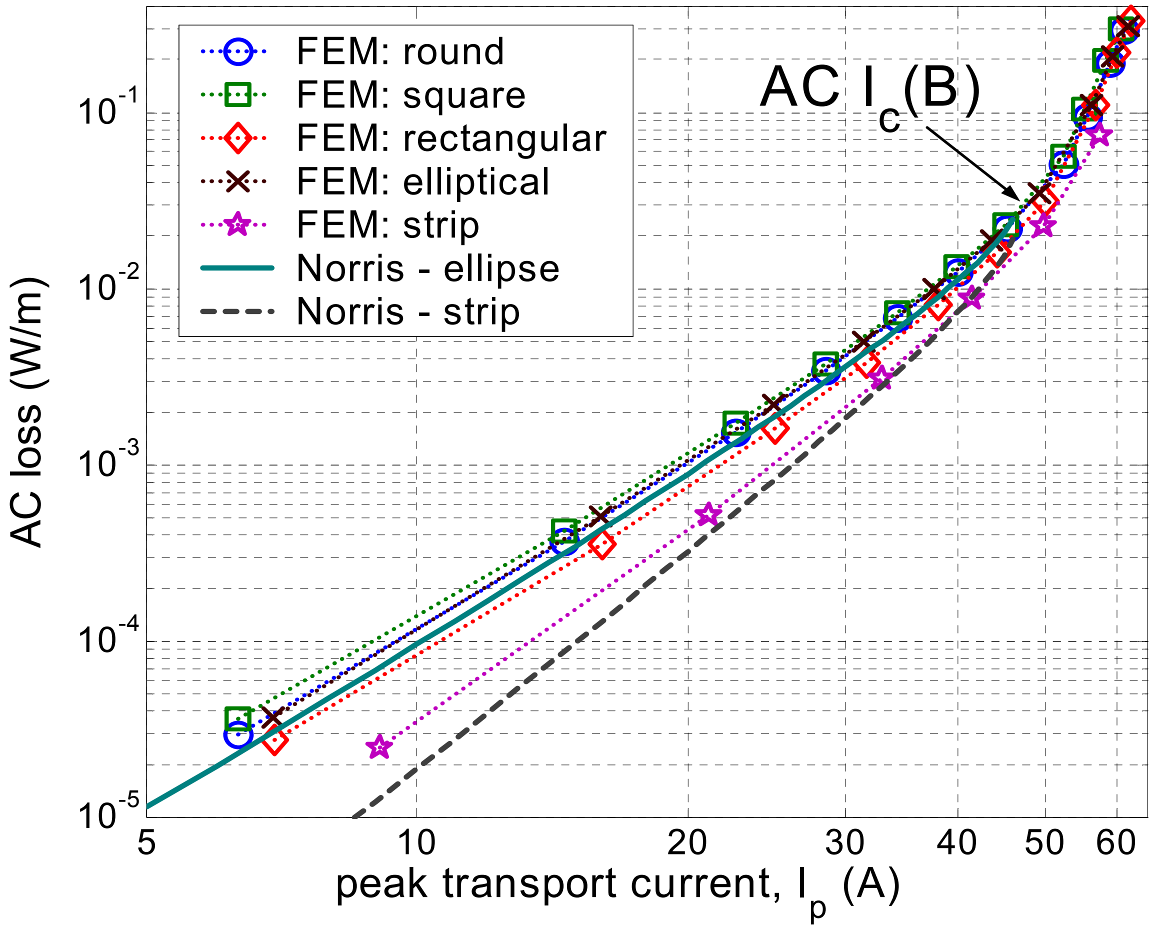

Figure 5-16 AC losses at 59 Hz in self-field obtained from FEM simulations for conductors with different geometry. Plotted are also Norris analytical predictions for I_c = 46 A. The arrow indicates the AC $I_c(B)$, above which the loss curve has steeper slope. The I_{c0} is 56.3 A.

The calculated current and magnetic flux densities in the different conductors for applied current of 44 A (close to the effective I_c) are shown in Fig. 5-17 for $\omega t = \pi/2$ (peak value). The current density profiles are quite similar – at $\omega t = \pi/2$ all conductors carry positive current and are almost completely saturated, except for a small region in the center. The magnetic flux density is highest near the edges of the tapes and towards the periphery of the wires, with shielded low-flux regions in the center of each conductor. Even if the plots in Fig. 5-17 are instantaneous pictures, it is possible to observe that the magnetic flux density penetration is stronger for the elliptical tape compared to the rectangular one (larger flux-free region in the latter), which explains why the losses in conductors with thin elliptical shape are higher than for rectangular cross-section of similar aspect ratio.

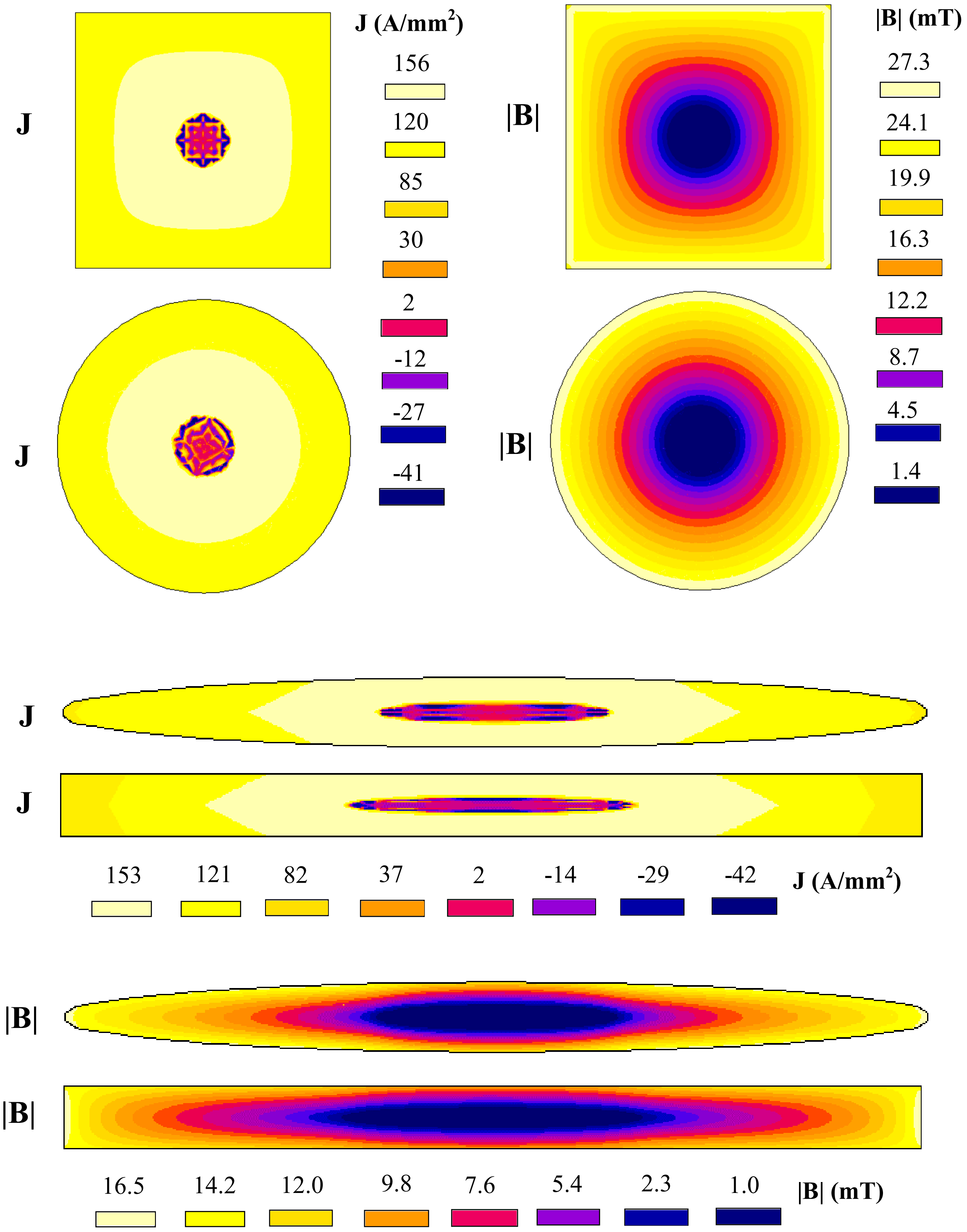

Figure 5-17 Current and flux density distribution in the different conductors at $\omega t = \pi/2$ (peak value) of applied transport current of 44 A. Shown is the superconducting cross-section.

5.4.5 Monofilamentary conductors in applied external magnetic field

Magnetization losses in applied perpendicular field

A general treatment of the losses in superconductors with different geometry in applied magnetic field is given in [Cam82]. The analysis is made for the critical state model on the basis of the magnetization loss Q_m (J/cycle/m^3) of a slab ($a << b$) in a field parallel to its long side:

$$\begin{aligned} Q_m &= \frac{2B_a^2}{\mu_0}\left[\frac{\beta}{3}\right] && \text{for} \quad \beta \le 1 \\ Q_m &= \frac{2B_a^2}{\mu_0}\left[\frac{1}{\beta} - \frac{2}{3\beta^2}\right] && \text{for} \quad \beta \ge 1 \end{aligned} \tag{5.13}$$

where β is the ratio of the applied field B_a to the full penetration field B_p. For $\beta \le 1$ the magnetization loss increases with B_a^3, while for $\beta >> 1$ it increases with B_a^1. Above B_p, the magnetization loss of a conductor with arbitrary geometry is proportional to its shape factor multiplied by the loss of the slab, provided that the time constant of the conductors is the same. The shape factor is equal to $(1-\eta)^{-1}$, where η is the demagnetizing factor of the conductor. They are given in Table 5-5 for several geometries.

TABLE 5-5 Demagnetizing and shape factors for different geometries

Geometric cross-section	*Aspect ratio*	*Demagnetizing factor*	*Shape factor*
Rectangular (slab)	a/b ($a << b$)	≈ 0	≈ 1
Square	$a/b = 1$	≈ 1/2	≈ 2
Round	$a/b = 1$	1/2	2
Rectangular (strip)	a/b ($a >> b$)	$1 - b/a$	a/b

The numerically calculated magnetization losses for conductors with $J_c(B)$ of different cross-section in applied AC perpendicular magnetic field at 59 Hz are shown in Fig. 5-18 as function of the field's amplitude B_a. The $J_c(B)$ dependence does not change the slope of the loss curves from Eq. (5-13) below and above B_p; it influences, however, the full penetration field in the conductors with different $J_c(B)$, as it was shown in Section 5.3.2. As can be seen from Fig. 5-18, conductors with similar aspect ratio and shape factor (the elliptical and rectangular tapes or the round and square wires) have practically the same AC loss in applied field. On the other hand, the tapes have considerably higher AC loss magnitudes than the wires in fields of such orientation.

In perpendicular magnetic field, tapes have much higher losses than round or square wires because of the strong demagnetizing effect of a conductor with large aspect ratio (thin ellipse or rectangle) in perpendicular field. The loss difference reaches a factor of 10 at fields below 20 mT, and decreases to a factor of 3-4 at fields higher than 50 mT. For example, at field of 100 mT the ratio between the loss of the elliptical tape and the round wire is reduced from the expected theoretical value of 6.2 (the ratio of their shape factors) to 3.1 due to the stronger decrease of the $J_c(B)$ in the ellipse in perpendicular field. The $I_c(B)$ of the elliptical tape at B_a = 100 mT is 12 A, while the $I_c(B)$ of the round wire in the same field is 22.8 A. If the magnetization loss is now normalized by the corresponding $I_c(B)$, the loss ratio turns out to be 5.9, which is very close to the critical state value of 6.2, expected for conductors with constant J_c and equal I_c.

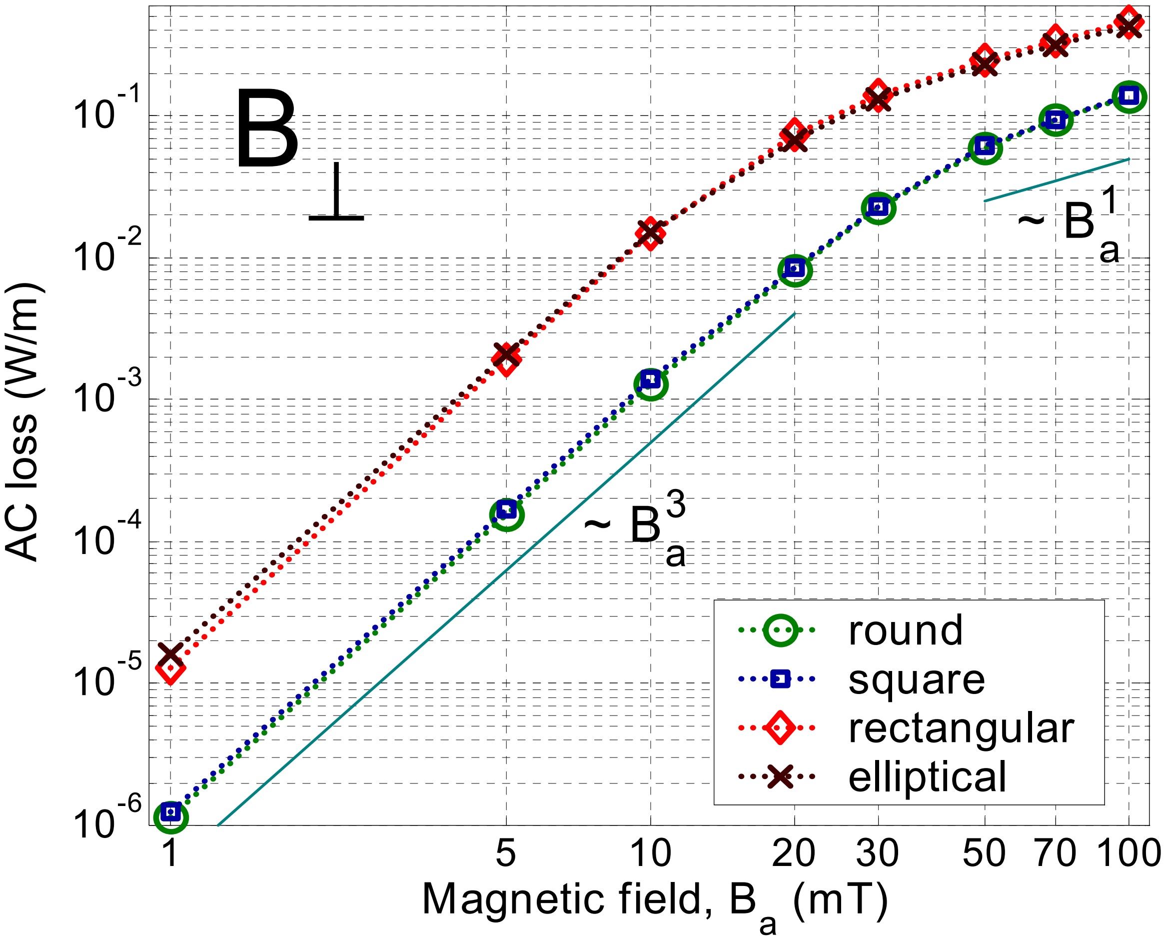

Figure 5-18 Magnetization losses at 59 Hz in conductors with $J_c(B)$ in perpendicular AC magnetic field up to 100 mT.

Magnetization losses in applied parallel field

The numerically calculated magnetization losses for conductors with $J_c(B)$ of different cross-section in applied AC parallel magnetic field at 59 Hz are shown in Fig. 5-19.

In low parallel magnetic fields, there is similar loss magnitude in all conductors until the tapes are fully penetrated. At high parallel fields, the round and square conductors have larger losses for two reasons – they have higher shape factor but also higher B_p than the flat tapes.

The penetration field can be qualitatively determined from the magnetization loss curve due to the different slope of the losses below and above B_p. Quantitatively, the value of B_p, at which the magnetic field has reached the center of the sample and the conductor is fully saturated, can be determined more precisely by examining the magnetic field and current density profiles in the different conductors – it is around 15 mT for the tapes and around 40 mT for the wires. Fig. 5-20 and 5-21 show the magnetic field profiles along the *y*-axis for AC parallel field with different B_a for the rectangular tape and the round wire. For the values of B_a in plot (a) in both figures, the penetration of the magnetic field has not reached the center of the conductors yet, while in plots (b) the full penetration has occurred.

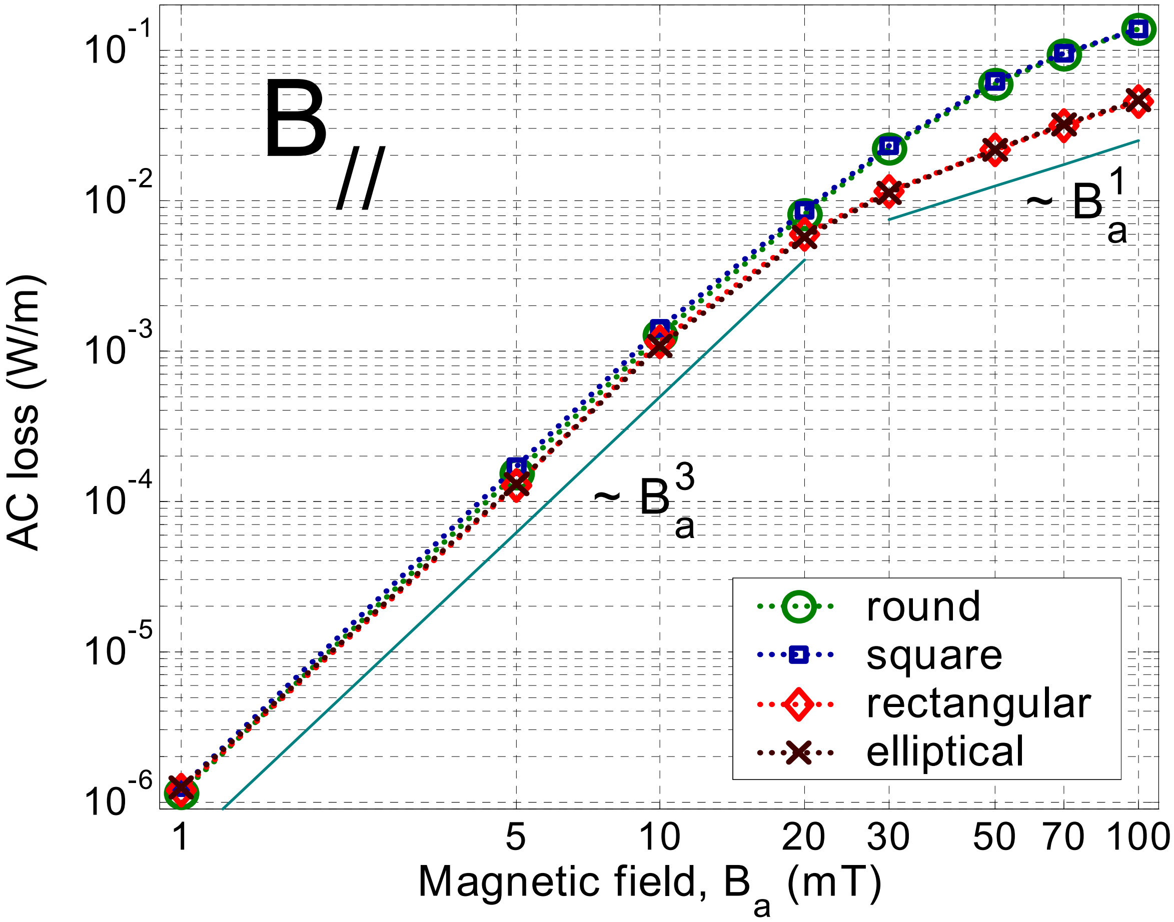

Figure 5-19 Magnetization losses at 59 Hz in conductors with $J_c(B)$ in parallel AC magnetic field up to 100 mT.

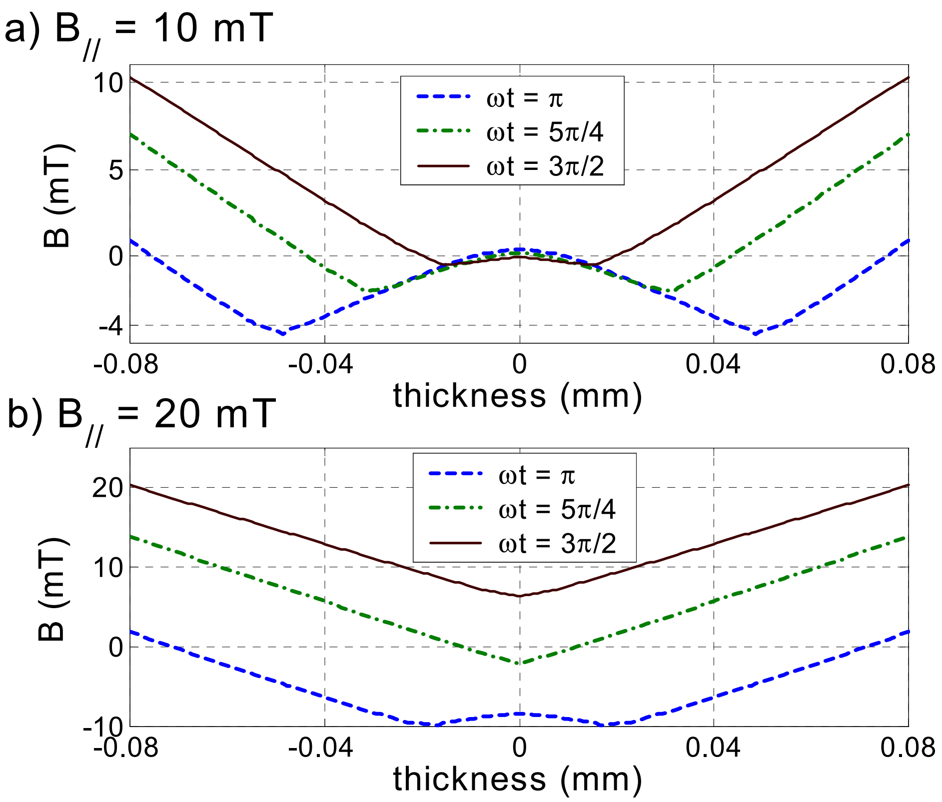

Figure 5-20 Magnetic field penetration profile along the *y*-axis of the rectangular tape for parallel AC magnetic field with B_a = 10 and 20 mT. The penetration field is around 15 mT.

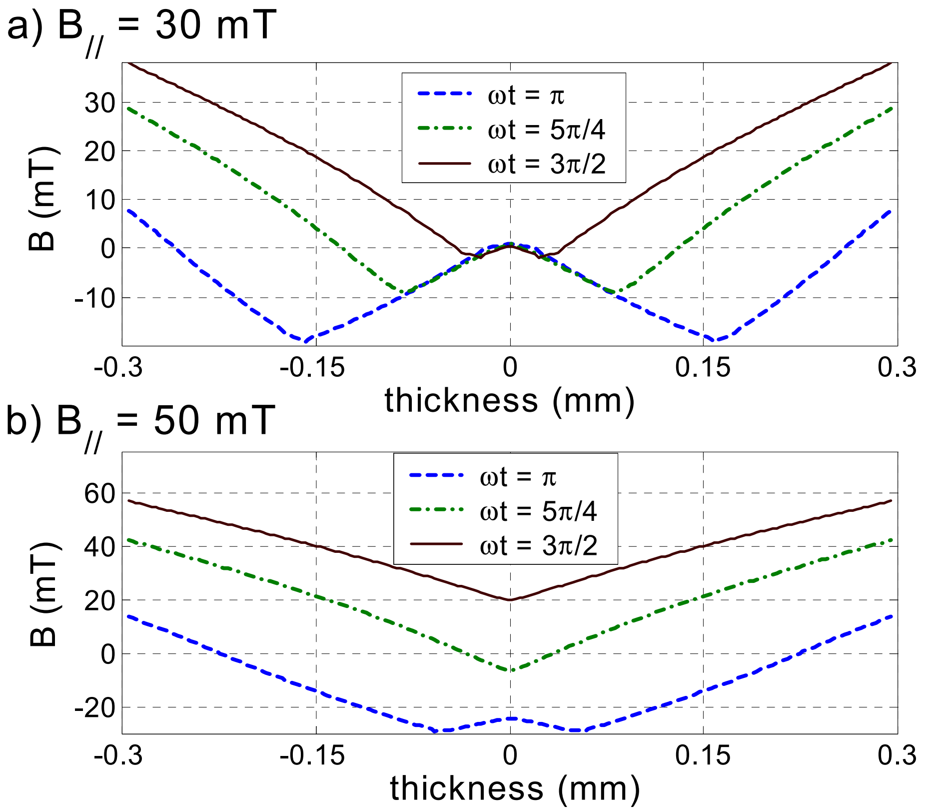

Figure 5-21 Magnetic field penetration profile along the *y*-axis of the square wire for parallel AC magnetic field with B_a = 30 and 50 mT. The penetration field is around 40 mT.

Magnetization losses in applied field of varying orientation

Because of the different $J_c(B)$ dependence in wires (isotropic) and tapes (anisotropic), the $I_c(B)$ varies both with the field's amplitude and orientation. Figure 5-22 shows the AC losses in the different conductors for external fields of 10 and 50 mT applied with varying orientation – from parallel ($\alpha = 0°$) to perpendicular ($\alpha = 90°$). For low applied field, the tapes have higher losses than the wires for any orientation, except the parallel one. The loss difference in favour of the wires reaches a factor of 10 in perpendicular fields. For high field magnitudes, the tapes have lower losses than the wires for fields with dominating parallel component ($\alpha < 20°$). The loss difference in favour of the wires increases with α and reaches a factor of 6 in perpendicular field (the ratio of the corresponding shape factors).

The angular dependence of the normalized losses for the elliptical and rectangular tapes, shown in Fig. 5-22, represents a good approximation of the way their shape factor varies as function of the field's orientation.

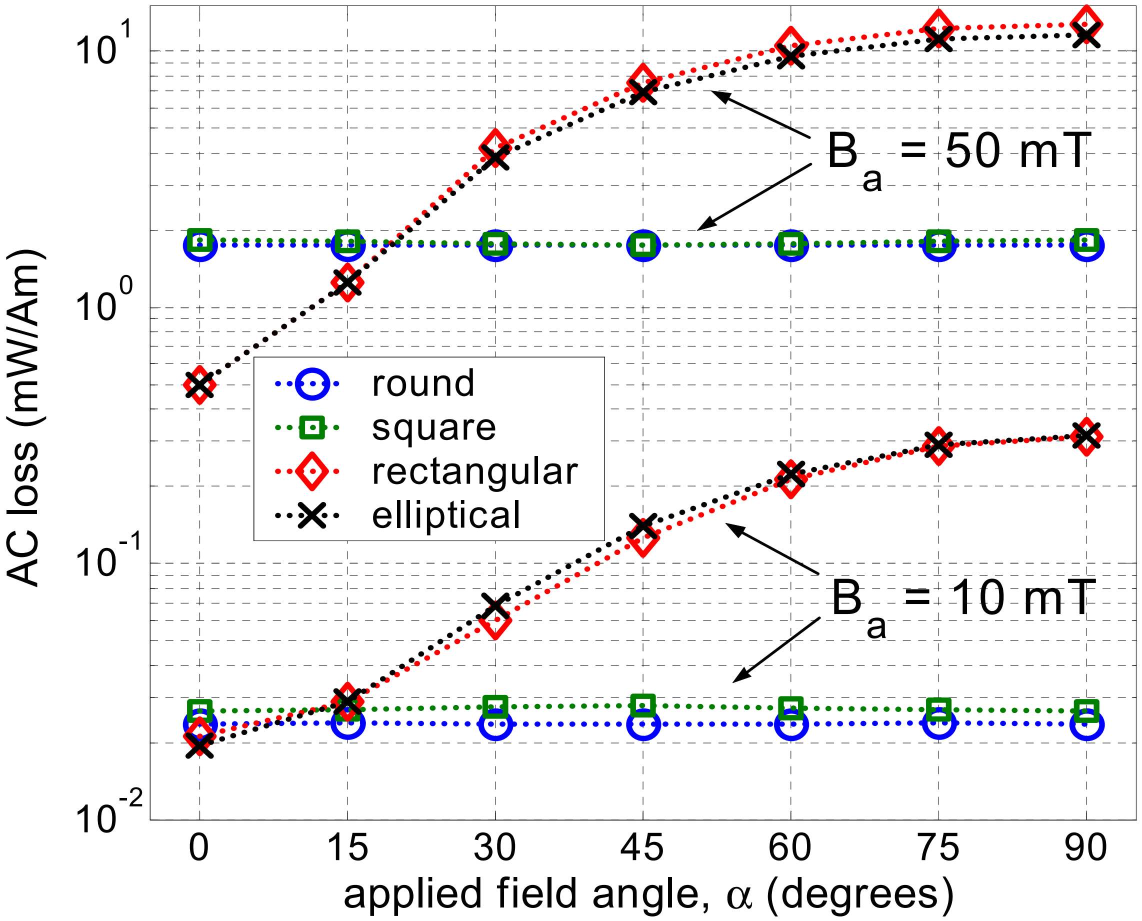

Figure 5-22 Magnetization losses at 59 Hz in conductors with $J_c(B)$ in AC magnetic field with amplitude B_a of 10 and 50 mT and varying orientation. The loss is normalized to the corresponding $I_c(B)$ for each conductor.

An example of the current and flux density distribution for applied field of 10 mT in the different conductors is shown in Fig. 5-23 for the two wires and in Fig. 5-24 for the elliptical tape. For the wires B_a = 10 mT is well below the penetration field (B_p ~ 40 mT) and there is a large flux and current-free zone in the center. Because of the geometry of the wires and the isotropic $J_c(B)$ dependence, the current and flux profiles are the same in fields of varying orientation, only the axe of symmetry is rotated. This is not the case in the flat tapes, see Fig. 5-24. In parallel field, B_a = 10 mT is not far from the penetration field (B_p ~ 15 mT); the induced currents circulate in the larger part the tape and the current-free zone is small. Because the field is oriented parallel to the long side of the tape, however, there are almost no demagnetizing effects and the maximum field inside is very close to the external field amplitude. As a result, the saturating current density (J_{max} = 137 A/mm^2) is below the $J_c(B)$, which is 150 A/mm^2 for parallel field of 10 mT, see Fig. 5-24a. In perpendicular field, B_a = 10 mT is still far from the penetration field (B_p ~ 25 mT); indeed the current and flux-free region in the center is quite larger than in parallel field, compare Fig. 5-24a and 5-24c. However, because of the strong demagnetizing effects when the field is oriented perpendicular to the long side, the maximum field inside the tape (near the edges) exceeds by far the external field amplitude. The screening current density (except in the current free-region) exceeds the local $J_c(B)$ – for example J = 105 A/mm^2 at the edges of the tape, while the corresponding $J_c(B)$ is 94 A/mm^2 for perpendicular field of 17.7 mT. Therewith comes the large difference between the magnetization losses of flat tapes in parallel and perpendicular magnetic fields.

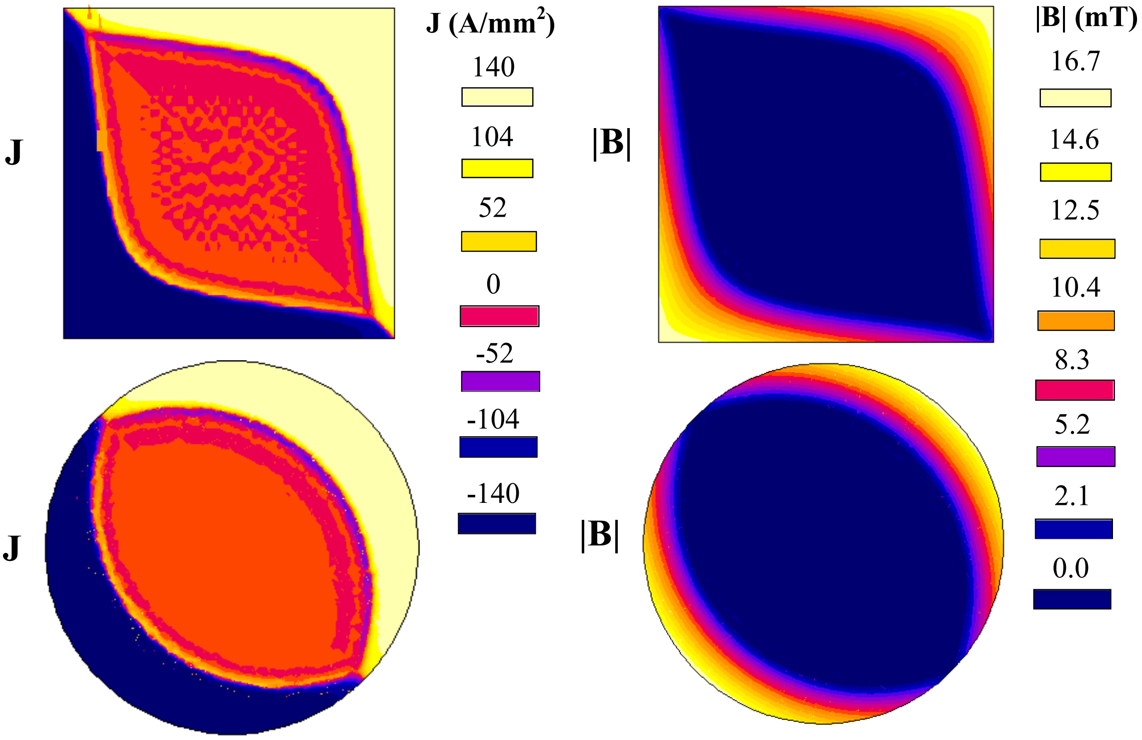

Figure 5-23 Current and flux density distribution in the superconducting core of the round and square wires at peak value (ωt = 3π/2) of external field with B_a = 10 mT applied at 45°.

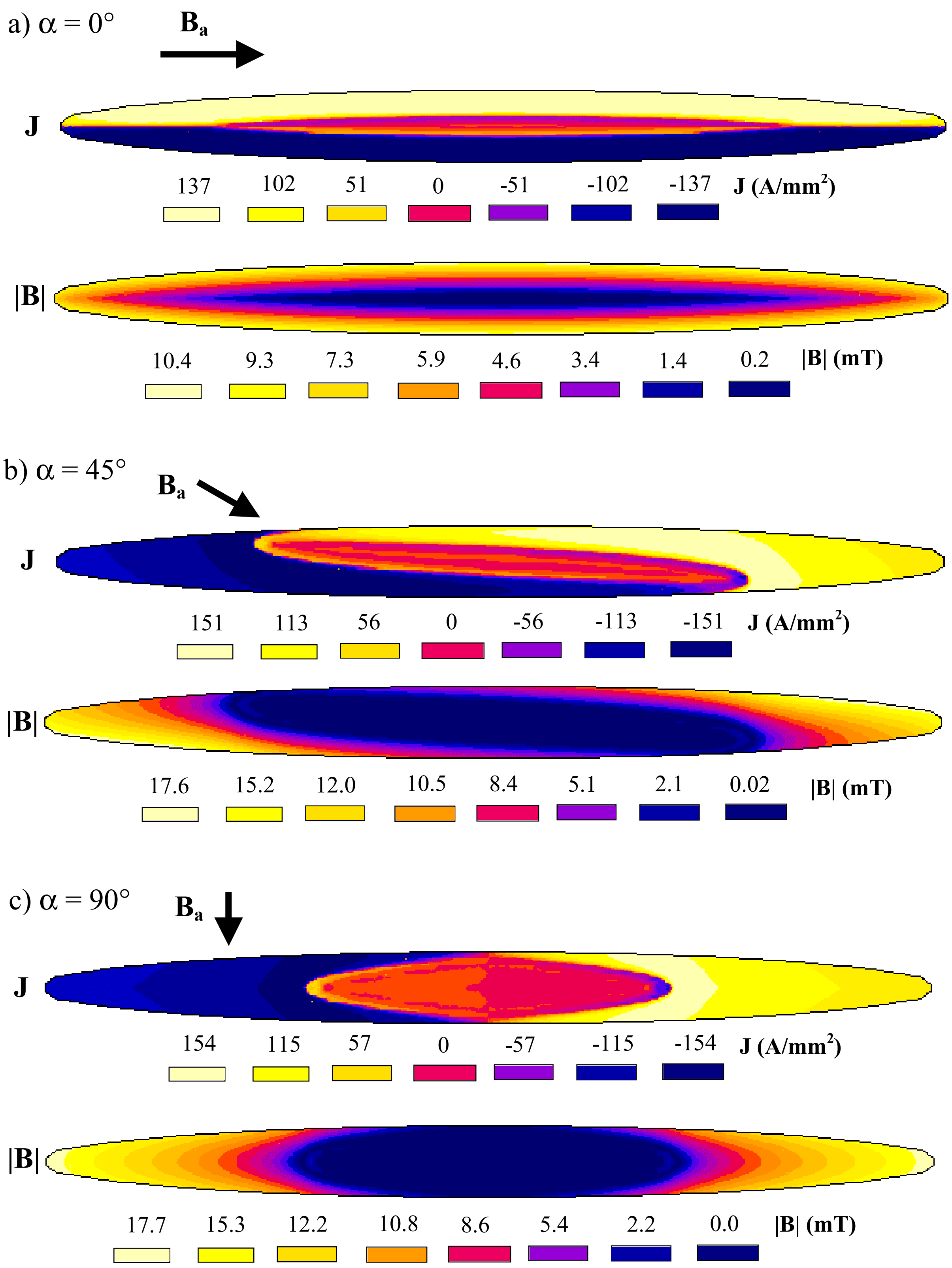

Figure 5-24 Current and flux density distribution in the superconducting core of the elliptical tape at peak value ($\omega t = 3\pi/2$) of external field with $B_a = 10$ mT, applied at different angles.

5.4.6 Monofilamentary conductors with transport current and applied magnetic field

Current density and power dissipation in combined current and field applications

The 2D analysis of the interaction between the self-field and the applied external field is rather complicated even for simple geometries in the critical state model, and for modelling of the current and magnetic field distributions in HTS superconductors with B-dependent E-J power law, the finite element method is a particularly useful and necessary tool.

HTS materials, such as Bi-2223, have smooth current-voltage characteristics. Unlike the critical state model, the value of I_c and correspondingly J_c is not well defined and depends on the employed voltage criterion (most commonly 1 μV/cm is used). The current density may locally exceed J_c, and when saturation near the edges of Bi-2223 tapes occurs, $J \geq J_c$ even though there still may be current-free zones in the center.

Figure 5-25 shows the current density (J) and power dissipation (P) in the elliptical tape for the case of applied transport current – a), applied magnetic field – b), and combined current and perpendicular field – c). The current density and the power dissipation vary along the cycle; yet these instantaneous pictures ($\omega t = \pi/4$) give a representative description of the typical current distribution in Bi-2223 tapes and where the power is dissipated. Figure 5-25a and 5-25b show that when only current or perpendicular field is applied, the current density and the power dissipation are highest near the edges of the tape. On the other hand, the current and field combination results in higher current density, and therefore larger losses in one half of the tape compared to the other half, see Fig. 5-25c.

For better insight into the behaviour of Bi-2223 conductors with $J_c(B)$, Fig. 5-26 shows the J and $J_c(B)$ profiles at $\omega t = \pi/4$ along the x-axis in the center of the tape, corresponding to Fig. 5-25. As can be seen in the upper and middle plots, the current density profiles for the cases of separately applied current and perpendicular field are quite similar (except that the currents in the left and right halves are inversed in the latter case) since both the self-field and the applied field start penetrating the sample from the edges, and the saturation proceeds from the edges towards the center of the tape. In these two cases $J > J_c$ near both edges and that is where most of the power dissipation occurs; at the same time there is a current-free zone in the center of the tape, see Fig. 5-25a and 5-25b as well. In the combined case (lower plot in Fig. 5-26), the left half of the tape is completely saturated with J considerably larger than J_c and that is where the power dissipation is concentrated, while the right half of the tape remains unsaturated ($J < J_c$ everywhere) and negligible quantity of power is dissipated in it. This specific pattern is the result of the interaction of the transport current with the induced screening current by the applied field, which circulate in the same direction in the left, and in opposite directions in the right half of the tape at that instant.

a) I_t (38 A)

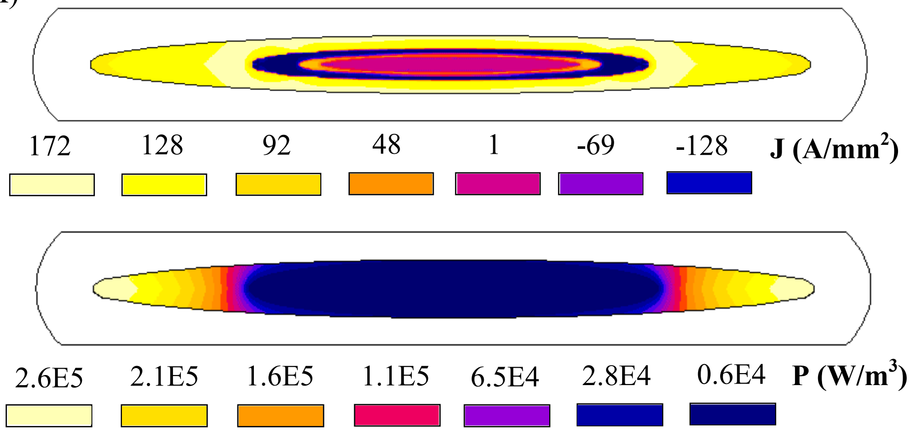

b) $B_\perp$ (10 mT)

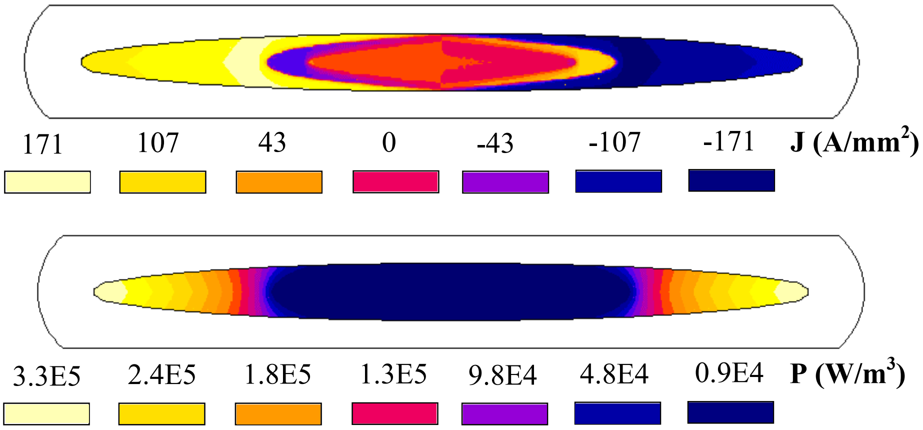

c) I_t (38 A) + $B_\perp$ (10 mT)

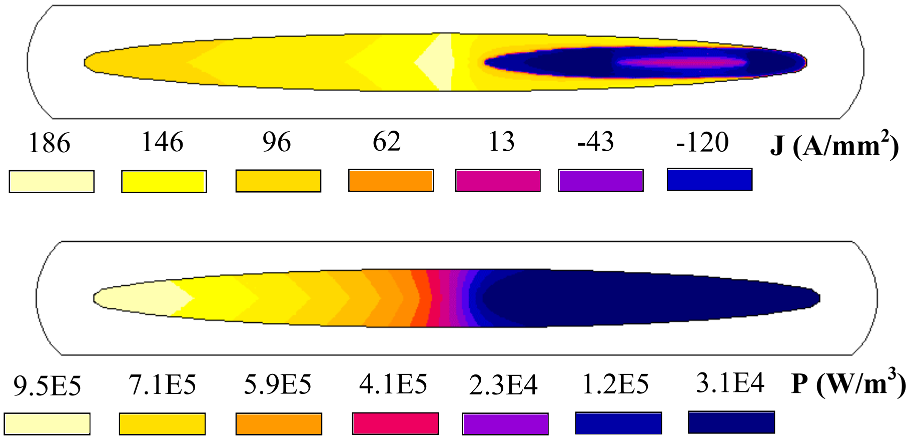

Figure 5-25 Current density (J) and power dissipation density (P) in the Bi-2223 core: for applied transport current of 38 A (a), in applied perpendicular field of 10 mT (b), and for transport current in applied perpendicular field (c). In all examples $\omega t = \pi/4$.

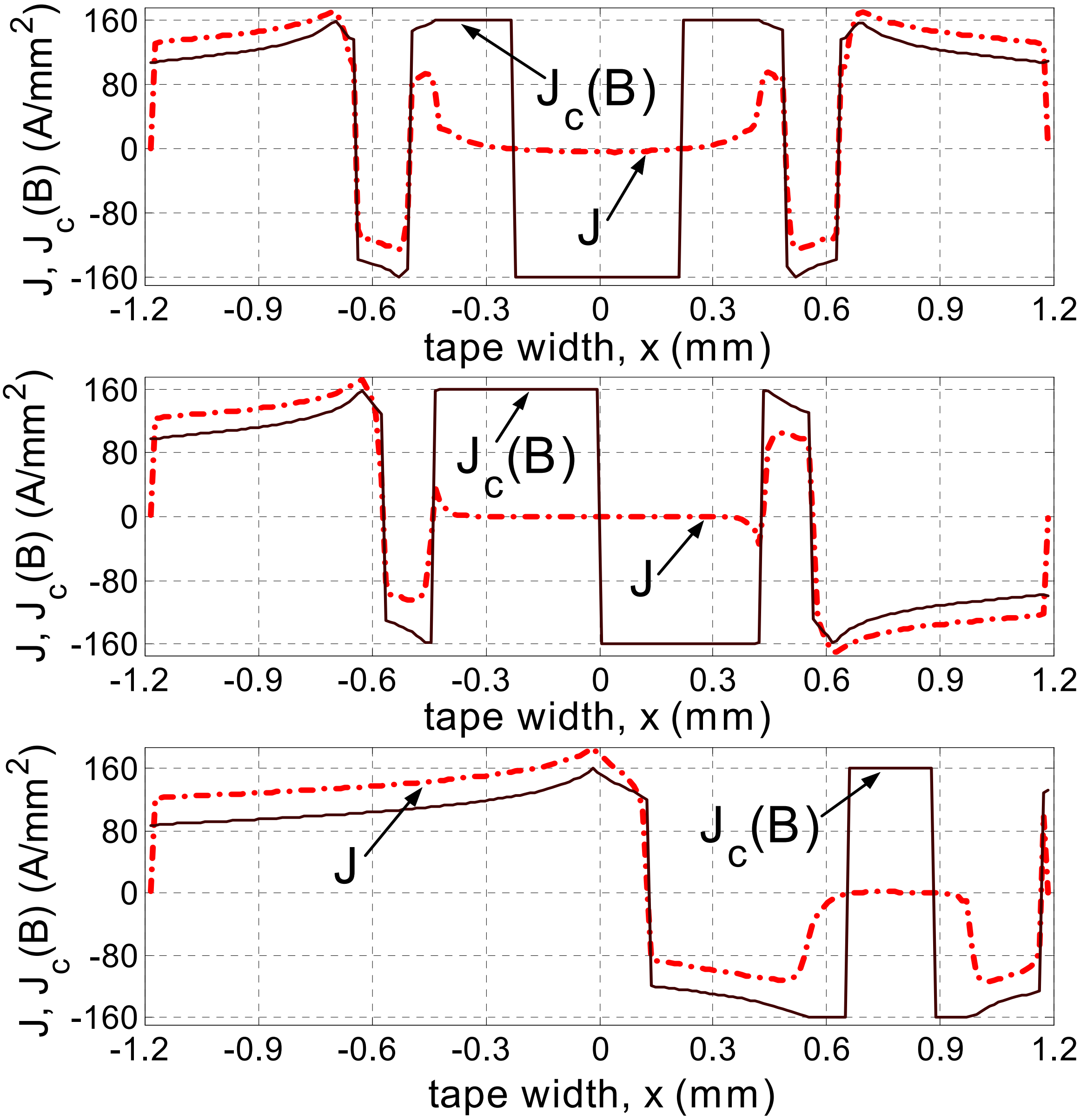

Figure 5-26 Current density J (dash-dot line) and $J_c(B)$ (solid line) profiles along the *x*-axis of the elliptical conductor. $J_c(B)$ is plotted with the same sign as J for easier comparison. The upper, middle and lower plots correspond to Fig. 5-25a, 5-25b and 5-25c, respectively.

Total AC loss with transport current and fields of parallel or perpendicular orientation

The AC losses at 59 Hz for applied perpendicular field of 10 mT are plotted vs. the applied transport current in Fig. 5-27. Even at such moderate perpendicular fields, the losses for the rectangular and elliptical tapes are considerably higher due to their shape factors than the losses in the round and square conductors – at low currents, where the magnetization loss is dominant, the loss difference reaches almost a factor of 10; at higher currents, the loss difference is reduced due to the increased contribution of the transport current loss – yet there is still a factor of 2-2.5 as $I \to I_c$.

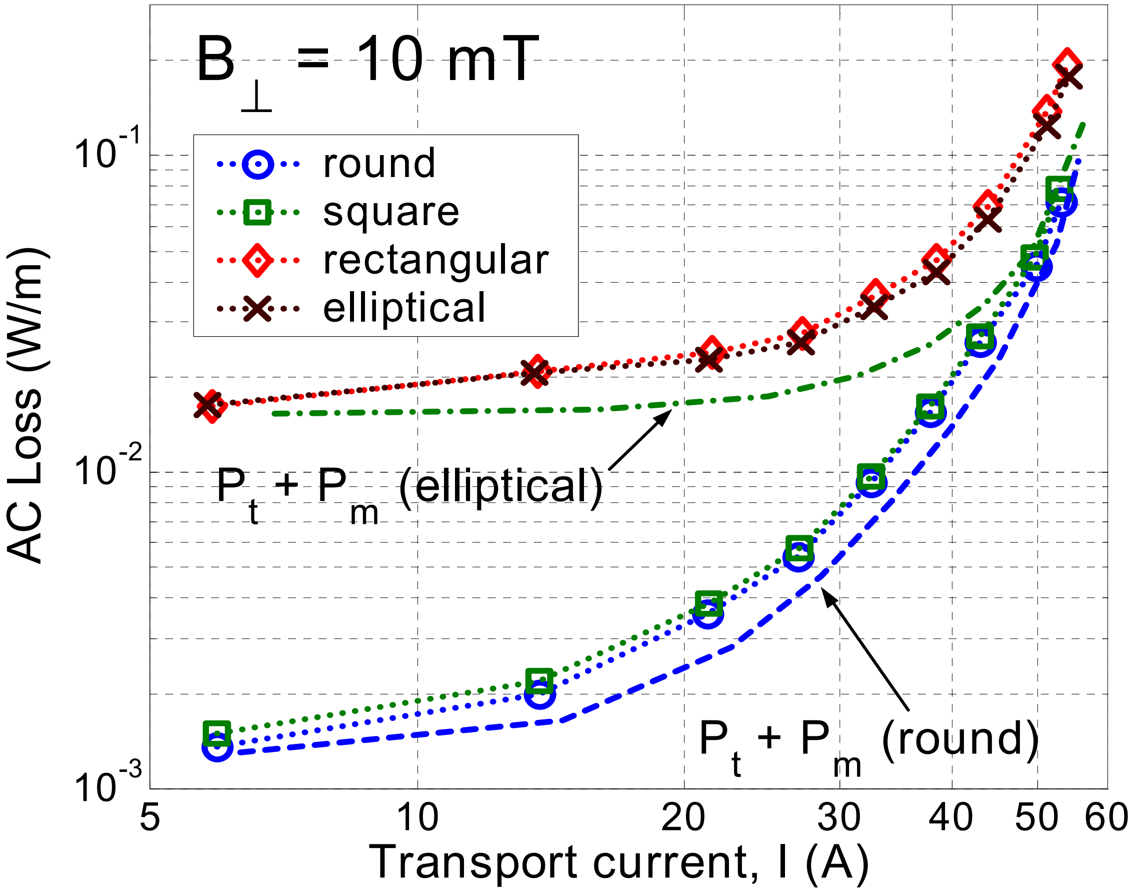

Figure 5-27 AC losses with transport current in perpendicular field of 10 mT. Plotted is also the sum of the magnetization loss at 10 mT (P_m) with the separate transport current loss (P_t) for the elliptical and round conductors.

Also plotted is the sum of the magnetization loss at $B_\perp = 10$ mT (P_m) and the separate transport current loss (P_t) for the elliptical and round conductors. The total loss in the combined current + perpendicular field case is larger than the simple sum of the separate loss contributions. The difference is 30 to 80% for the tape, and 20 to 30% for the wire. This has been observed in other numerical simulations [Ame01], and also in experiments [Rab99a], [Ash00] and has been explained by the strong interaction between the self-field and the applied perpendicular magnetic field in Bi-2223 tapes. This interaction in fields of such orientation increases with the aspect ratio of the conductors.

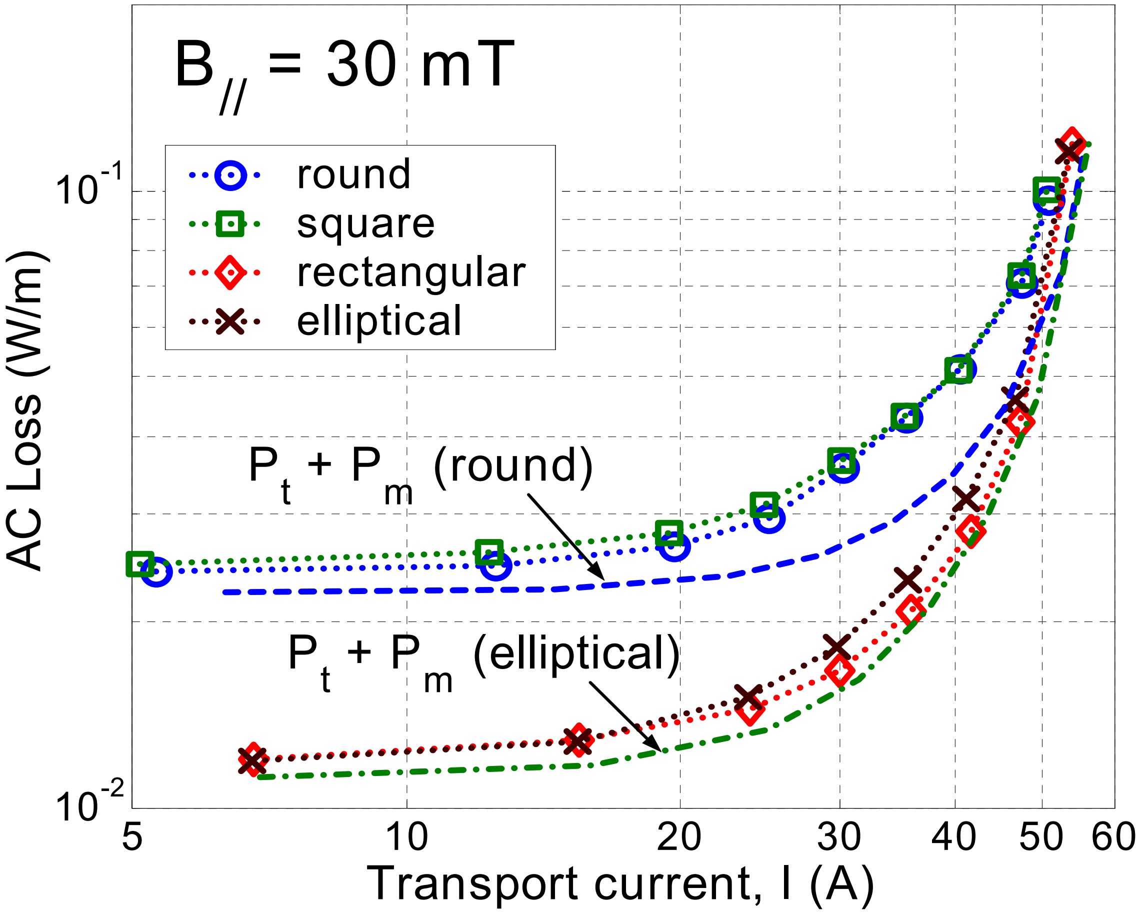

Figure 5-28 AC losses with transport current in parallel field of 30 mT. Plotted is also the sum of the magnetization loss at 30 mT (P_m) with the separate transport current loss (P_t) for the elliptical and round conductors.

Figure 5-28 shows the AC losses with applied transport current in external parallel magnetic field of 30 mT. Again, conductors with similar aspect ratio and shape factor have very close AC losses. However, in fields of such orientation, the losses in the tapes are lower than the losses in the round and square conductors. The loss difference at $B_{//}$ = 30 mT is a factor of 1.5 to 2 in favor of the tapes; it will be larger for higher parallel fields, since the increase of the magnetization losses for $B_a > 30$ mT is more significant in the wires, as shown in Fig. 5-19. The slope of the AC loss curves for the tapes in Fig. 5-28 is steeper than in Fig. 5-27, which indicates the higher relative contribution of the transport current loss in parallel field. Plotted on Fig. 5-28 is also the sum of the separate magnetization (P_m) and transport current loss (P_t) for the round and elliptical conductor; this sum is lower than the actual total loss by 20 to 40 % for the wire, and by 10 to 20 % in the tape. The little difference for thin tapes is explained by the small interaction of their self-field and the applied parallel field [Ame01], [Ash00].

Total AC loss with transport current and fields of varying orientation

Figure 5-29 shows a comparison of the AC losses in the conductors of different geometry at fixed transport current (I_p = 44 A) and magnetic field amplitude (B_a = 50 mT). The field is applied at varying angle – from parallel (α = 0°) to perpendicular (α = 90°). The losses at 59 Hz are normalized by the $I_c(B)$ calculated for each angle in the different conductors and are given in mW per Amp-meter. The AC losses for the round and square conductors remain constant as the field is rotated due to their isotropic properties and unchanging shape factor. At α = 0°, the AC losses in the tapes are lower than those in the wires by almost a factor of 2. However, the losses in the tapes increase quickly with the angle of the applied field because of the rapidly growing loss contribution due to the perpendicular magnetic field component. At α = 45°, they are higher than the losses in the wires by a factor of 3.5-4; at α = 90°, the loss difference is nearly a factor of 6.

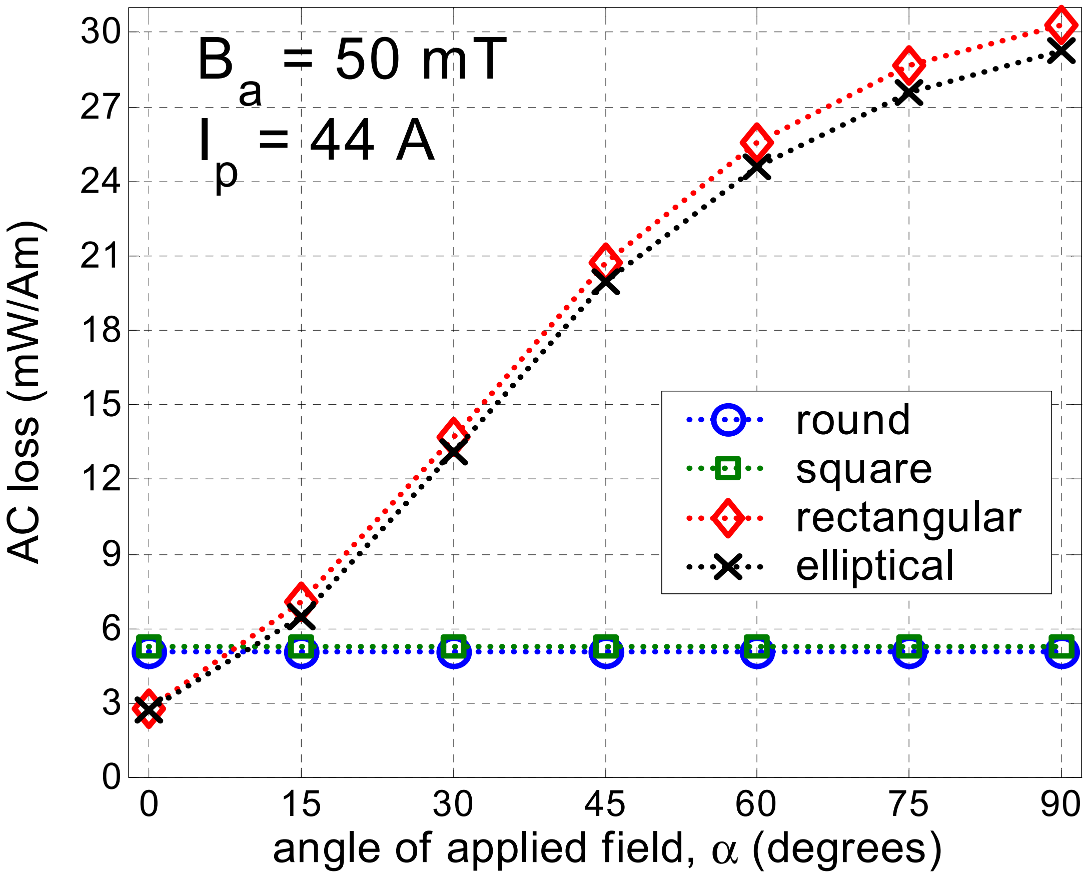

Figure 5-29 AC losses with transport current of 44 A in external magnetic field of 50 mT, applied at varying angle. The losses at 59 Hz are normalized by the corresponding I_c(B).

Finally, Fig. 5-30 displays an example of the current and magnetic flux density distributions in the four conductors of different geometry at peak values of the transport current (I_p = 35 A) and magnetic field, applied at 45° (B_a = 15 mT). Note that there is a current-free zone in the upper right corner of the round and square conductors, while the rectangular and elliptical tapes are fully penetrated – compare Fig. 5-30a and 5-30c.

At this time instant such combination of the self-field and the applied magnetic field yields highest combined field's amplitude near the lower left corners of all conductors, see Fig. 5-30b and 5-30d. Because of the $J_c(B)$ dependence, the area with highest magnetic field has lowest critical current density, and in this area $J > J_c$.

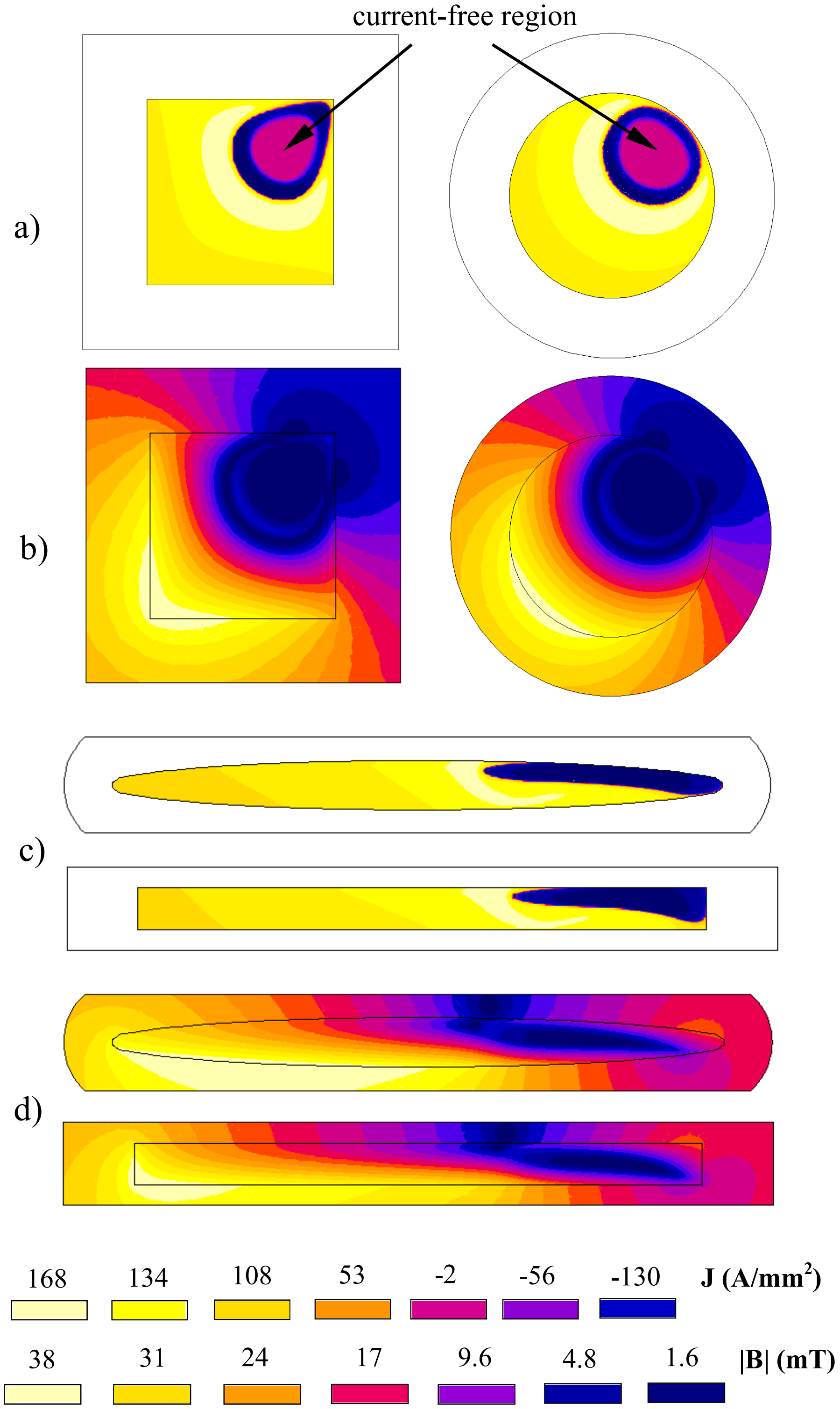

Figure 5-30 Current density in the BSCCO core – a), c) and magnetic flux density in the BSCCO core and the Ag – b), d) for I_p = 35 A in external magnetic field with B_a = 15 mT, applied at 45 degrees. $\omega t = \pi/2$ (peak values of I_p and B_a).

5.5 Modelling of multifilamentary conductors in different applications

The manufacturing of novel low-loss round and square wires with different filament arrangement has been a new research direction in the development of Bi-2223 conductors [Fri01], [Su01]. The multifilamentary wires offer better possibilities for obtaining high critical current densities than monofilamentary conductors. In addition, by twisting the wires, decoupling of the filaments in applied magnetic field can be achieved, thus reducing substantially the coupling current loss in the normal metal and the hysteresis loss in the superconductor.

The development of novel round and square Bi-2223 wires is the principle research focus of the currently undergoing European project BIG-POWA. The manufacturing of the wires is being done at the University of Geneva. The FEM modelling results presented in this section provide a feedback to the University of Geneva for the optimization of the AC loss performance of the new conductors [Sta02a].

5.5.1 Specifications of the simulated multifilamentary conductors

We have performed FEM simulations with AC transport current at 59 Hz and/or external AC magnetic field up to 150 mT in phase with the current on four multifilamentary Bi-2223/Ag wires and two tapes, whose geometry is shown in Fig. 5-31. The technical specifications of the conductors are given in Table 5-6.

TABLE 5-6 Specifications of the multifilamentary Bi-2223 conductors

Conductor	#	*Outer dimensions*	*Fill-factor*	J_{c0} *(A/mm²)*	I_{c0} *(A)*	n_0
Square, 2-stack	16	1.20 × 1.20 mm	0.30	160	69.1	20
Square, 4-stack	16	1.20 × 1.20 mm	0.30	160	69.1	20
Round, radial	24	∅ 1.4 mm	0.28	160	69.1	20
Round, peripheral	24	∅ 1.6 mm	0.21	160	69.1	20
Flat tape, 7F	7	4.0 × 0.40 mm	0.27	160	69.1	20
Flat tape, 37F	37	3.2 × 0.32 mm	0.34	186	69.1	20

is the number of filaments. The fill-factor is the ratio of the Bi-2223 to the total conductor's cross-section.
J_{c0} and n_0 are the characteristic parameters of the material in the absence of any magnetic field.
$I_{c0} = J_{c0}S$, where S is the Bi-2223 cross-sectional area.

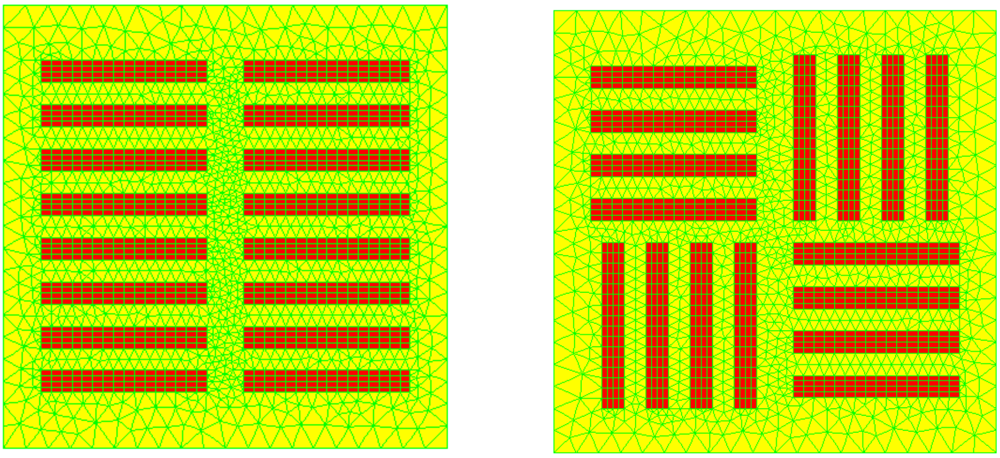

Square: 2-stack arrangement Square: 4-stack arrangement

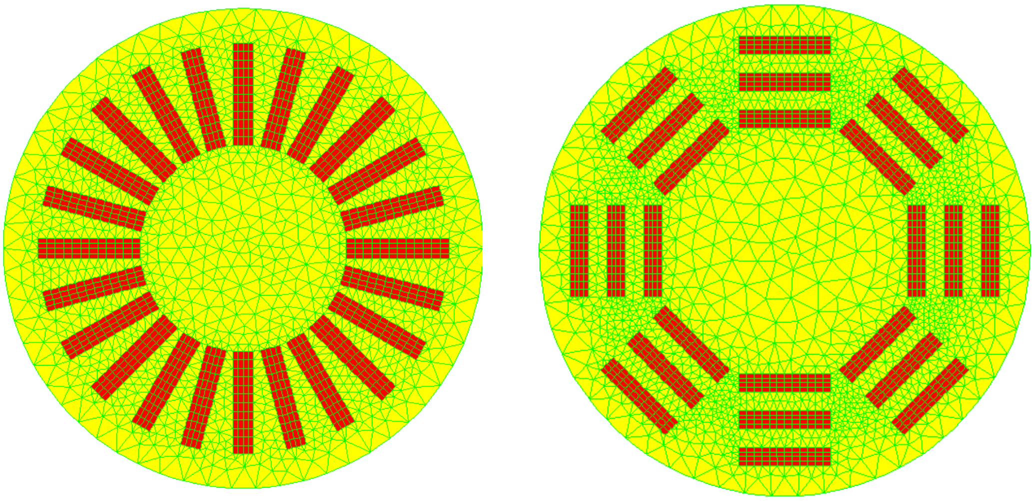

Round: radial arrangement Round: peripheral arrangement

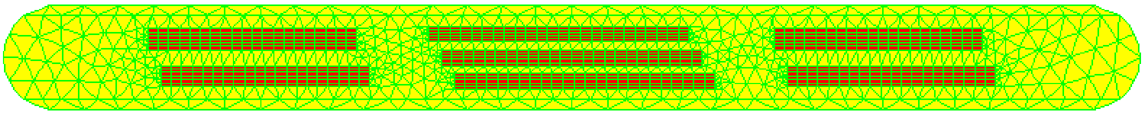

7-filamentary tape

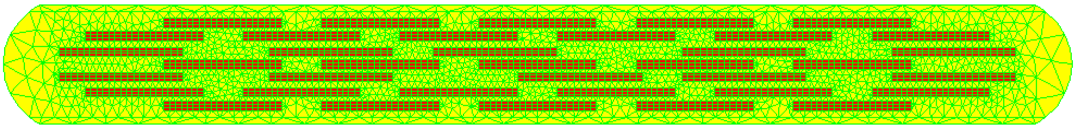

37-filamentary tape

Figure 5-31 Bi-2223 conductors with different filament arrangement and Ag matrix of square, round and tape geometry. Shown is also the FEM mesh.

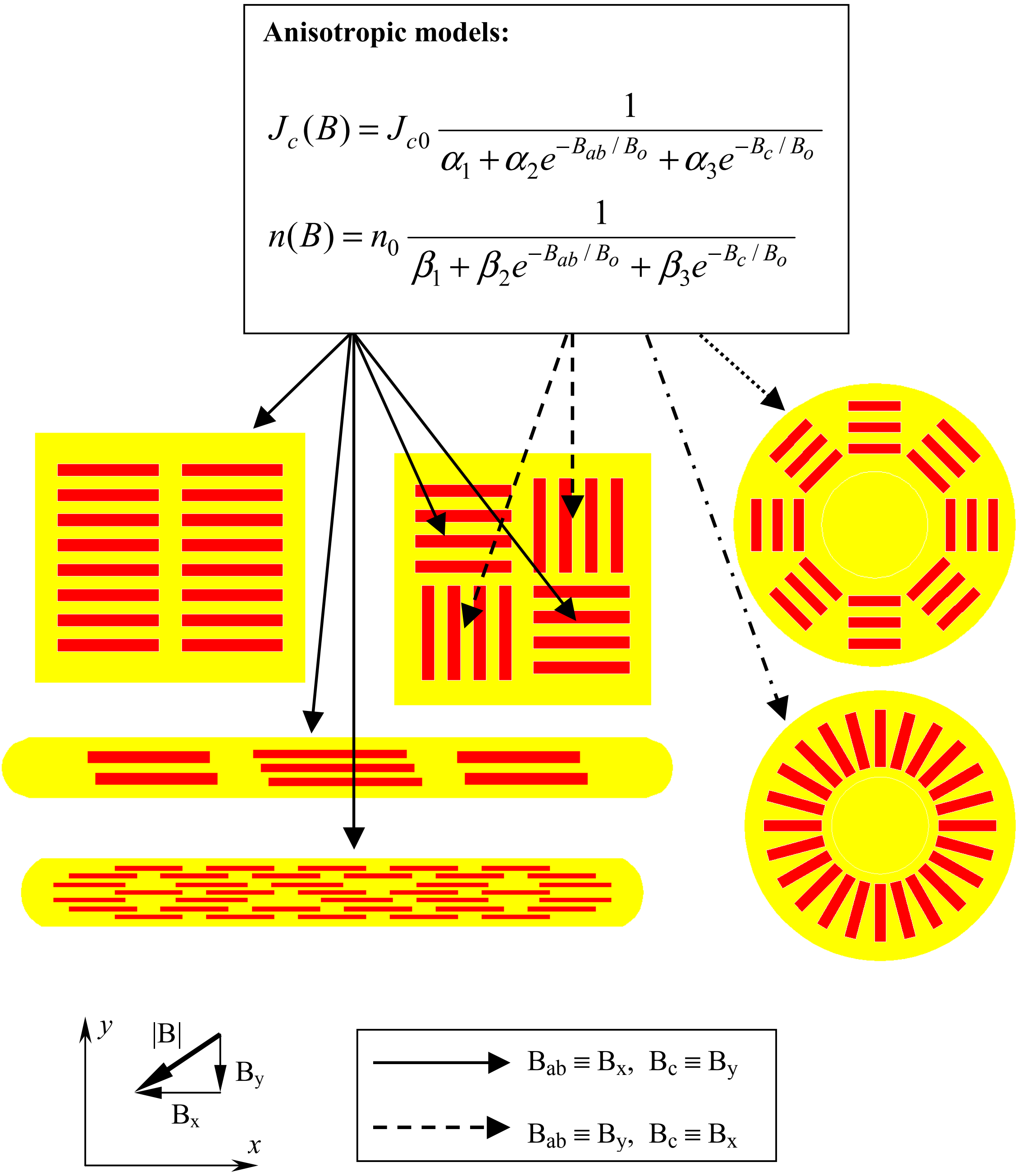

Figure 5-32 Using the anisotropic models of $J_c(B)$ and $n(B)$ for conductors with different filament arrangement. The solid and dashed arrows indicate the cases where the models can be directly applied by using the local magnetic field components B_x and B_y.

5.5.2 Modelling of $J_c(B)$ and $n(B)$ in tapes and wires with various filament arrangement

For describing the $J_c(B)$ and $n(B)$ dependence in multifilamentary conductors we have used the anisotropic models of Eq. (5.8) and (5.9) described in Section 5.4.1. The anisotropic $J_c(B)$ and $n(B)$ models have been applied locally for each filament of the conductors, as shown in Fig. 5-32. The anisotropic models of $J_c(B)$ and $n(B)$ are applied locally for each filament of the multifilamentary conductors. The FEM software calculates the local magnetic field magnitude and angle of orientation, as well as the magnetic field components, respectively parallel (B_x) and perpendicular (B_y) to the x-axis of the central coordinate system. The anisotropic models from Eq. (5.8) and (5.9) can be directly applied for filaments whose long side is parallel to the x-axis, where $B_{ab} \equiv B_x$ and $B_c \equiv B_y$; this is the case in the two multifilamentary tapes, in the square wire with 2-stack arrangement, and also in the two stacks with parallel orientation of the square wire with 4-stack arrangement (see Fig. 5-32). In the latter, the other two stacks of filaments have perpendicular orientation, so that $B_{ab} \equiv B_y$ and $B_c \equiv B_x$, and the model coefficients in front of the exponents in Eq. (5.8) and (5.9) have to be swapped.

As for both round wires, because of the rotation of their filaments with respect to the x- and y-axes, the local B_{ab} and B_c components need to be calculated in the different filaments before the computation of $J_c(B)$ and $n(B)$. This is shown in Fig. 5-33 for one point in a filament of the round radial wire, where ϕ is the angle of orientation of the local magnetic field with respect to y-axis and θ is the angle of rotation of the local coordinate system x′-y′ with respect to the y-axis. The computation of the local B_{ab} and B_c components is done for each node of the FEM mesh (there are 48 nodes in each filament of the two wires). It has been verified that the formulae shown in Fig. 5-33 are valid for the computation of B_{ab} and B_c for any values of ϕ and θ, such that $-90° \le \phi, \vartheta \le 90°$, which covers all four quadrants of the x-y coordinate system.

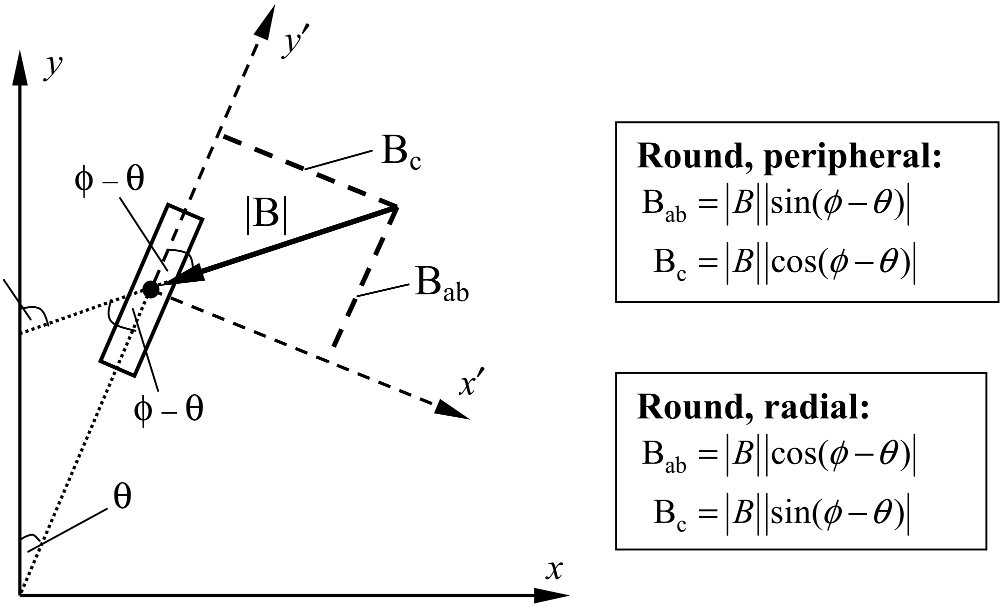

Figure 5-33 Local B_{ab} and B_c components for a point in a filament of the round wire with radial arrangement. The calculation of the local B_{ab} and B_c components for every point in the two round wires is performed by means of the equations, shown on the right.

5.5.3 Effective I_c in the multifilamentary conductors

We have used the methods for evaluating the effective $I_c(B)$ in conductors with given J_{c0} and $J_c(B)$, which were described in Section 5.4.3. Figure 5-34 shows the values of $I_c(B)$ from Eq. (5-12), obtained for different applied transport current for the round peripheral wire and for the 4-stack square wire. For effective I_c in AC applications, we consider the value of the transport current, at which the calculated $I_c(B)$ is equal to the amplitude of the applied current. This is in fact the interception point of the $I_c(B)$ vs. I_{peak} curves with the straight line $y = x$, as shown in Fig. 5-34.

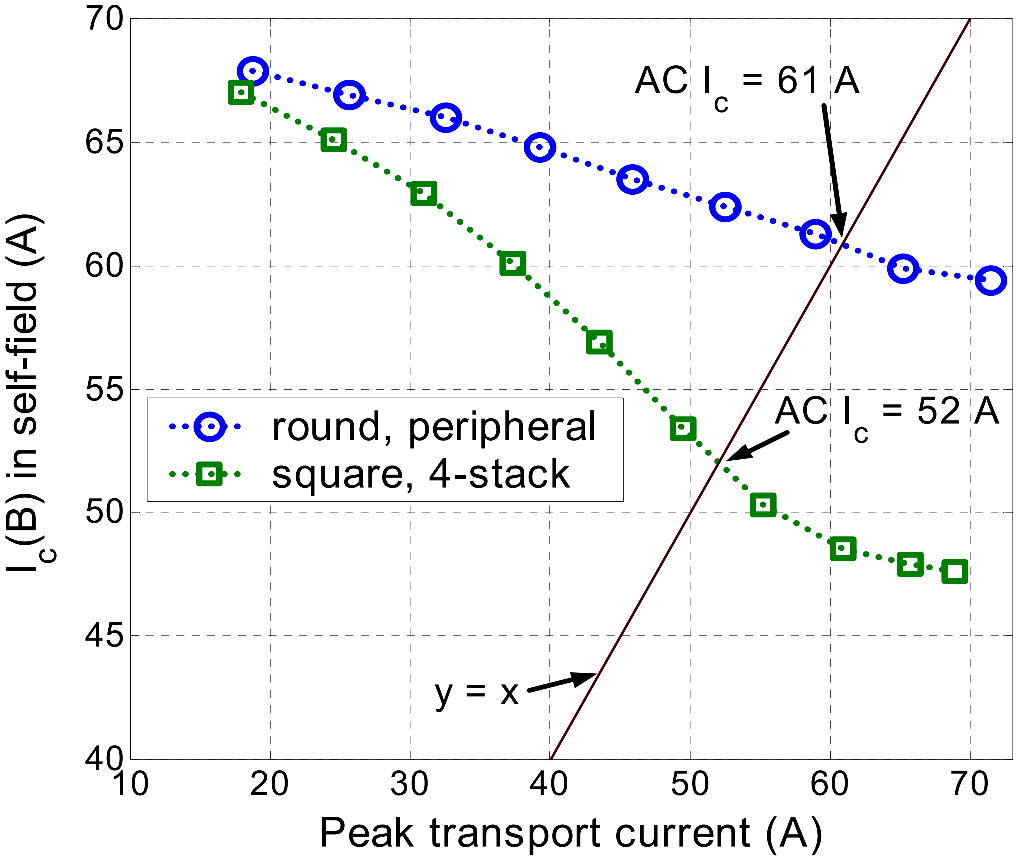

Figure 5-34 $I_c(B)$ calculated from Eq. (5-12) for different applied currents for the square wire with 4-stack arrangement, and for the round wire with peripheral arrangement. The value of $I_{c0} = J_{c0}S$ is 69.1 A.

As can be seen from Fig. 5-34, the effective AC I_c is considerably lower in the square wire. This is due to the stronger decrease of $J_c(B)$ in the latter, in which the flux lines of its self-field form an angle of 30-60 degrees with respect to the different filaments. The self-field flux lines (concentric circles) of the round wire with peripheral arrangement are almost parallel to the different filaments; therefore the decrease of J_c is lower and correspondingly the effective AC I_c in self-field is higher for this conductor.

The calculated AC I_c values for the different conductors are given in Table 5-7. Since the integral in Eq. (5-12) is taken at the peak of the current during the cycle, the corresponding self-field is at maximum and the calculated effective I_c represents a minimised value. Shown is also the ratio between the effective I_c and I_{c0}.

TABLE 5-7 Calculated effective I_c

Conductor	*AC I_c*	*I_c/I_{c0}*
Round, radial	49 A	0.71
Round, peripheral	61 A	0.88
Square, 2-stack	52 A	0.75
Square, 4-stack	52 A	0.75
Tape, 7-filamentary	57 A	0.83
Tape, 37-filamentary	56 A	0.81

The AC I_c in self-field, calculated from the $I_c(B)$ vs. I_{peak} dependence for Bi-2223 conductors with given J_{c0}. $I_{c0} = J_{c0}S$ is 69.1 A.

Table 5-7 shows that the conductors with different configuration have different values of their effective I_c, which are considerably lower than the value of I_{c0}. The lowest calculated value is for the round radial wire (29 % lower than I_{c0}), in which the concentric magnetic flux lines of the self-field are perpendicular to every filament, and consequently, the decrease of $J_c(B)$ is most significant. For the round wire with peripheral arrangement the influence of the self-field is least significant due to the specific orientation of the filaments, and as a result it has the highest effective I_c.

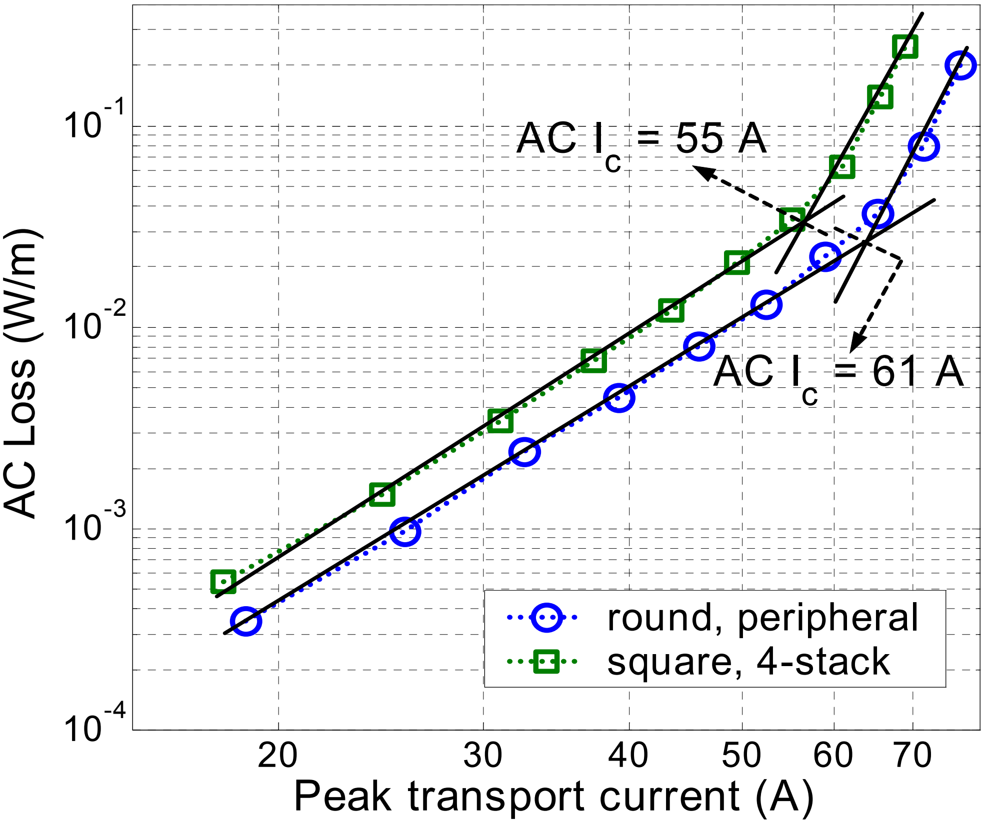

Figure 5-35 $I_c(B)$ evaluation from the self-field AC losses at 59 Hz for the square wire with 4-stack arrangement and the round wire with peripheral arrangement. The solid lines indicate the different slope of the self-field AC losses below and above the effective I_c.

The determination of the effective I_c for the different conductors has also been done by considering the point on the self-field loss vs. peak current curve, above which the losses have steeper slope. This is shown in Fig. 5-35, in which are plotted the self-field AC losses at 59 Hz for the round wire with peripheral arrangement and for the square wire with 4-stack arrangement. The straight solid lines indicate the different slopes of the AC loss curves – around 3.5 below I_c and around 9 above I_c. The values of the AC I_c evaluated in this way are given in Table 5-8; they are quite similar to the calculated effective I_c values from Table 5-7.

TABLE 5-8 Evaluated effective I_c

Conductor	*AC I_c*
Round, radial	52 A
Round, peripheral	61 A
Square, 2-stack	55 A
Square, 4-stack	55 A
Tape, 7-filamentary	56 A
Tape, 37-filamentary	58 A

The AC I_c, evaluated from the transport current loss curves of multifilamentary Bi-2223 conductors with given J_{c0}.

5.5.4 Tapes and wires with transport current

The transport current AC losses at 59 Hz (no external field) are shown in Fig. 5-36 as function of the reduced transport current *i* (I_p/I_c). In order to make comparison for conductors with different effective I_c, the losses are normalized by the square of $I_c(B)$, whose values are given in Table 5-7. The two square wires have practically the same loss in self-field, so only the loss for one of them is plotted in Fig. 5-36. The square conductors and the round radial wire have comparable AC losses in self-field, falling very close to Norris's elliptical prediction. They have AC loss behaviour similar to the monofilamentary conductors of round and square shape; see Fig. 5-16 as well. The 37-filamentary tape behaves like a monofilamentary one with elliptical cross-section and its loss is also very close to Norris's prediction. The losses for the round peripheral wire, however, are lower by 50-60 % than the ones of the mentioned conductors in the whole current range, and are similar to those of the 7-filamentary tape, whose large aspect ratio is more favourable in transport current applications in the case of monofilamentary conductors.

The low AC transport current losses in the round wire with peripheral arrangement can be explained by the higher $J_c(B)$ in that conductor compared to the $J_c(B)$ of the other wires. This is due to the configuration of its filaments, which are almost parallel to the circular flux lines of the self-field, and therefore the decrease of $J_c(B)$ in this case is least significant.

An example of the current density distribution in the different conductors for applied transport current of 44 A is shown in Fig. 5-37. At this time step ($\omega t = 2\pi$) the current amplitude is passing through zero. The current distribution pattern is typical for HTS – positive current density at the periphery of the wires and in the external filaments of the tapes; negative current density in the interior of the wires and in the tapes, and a current free-region in the center (I_p/I_c varies between 0.72 – 0.9 for the different conductors). In all wires and tapes the saturating positive current density exceeds the local value of $J_c(B)$. Note that in the round radial wire the current has penetrated to the center and there is no current-free zone as in all other conductors.

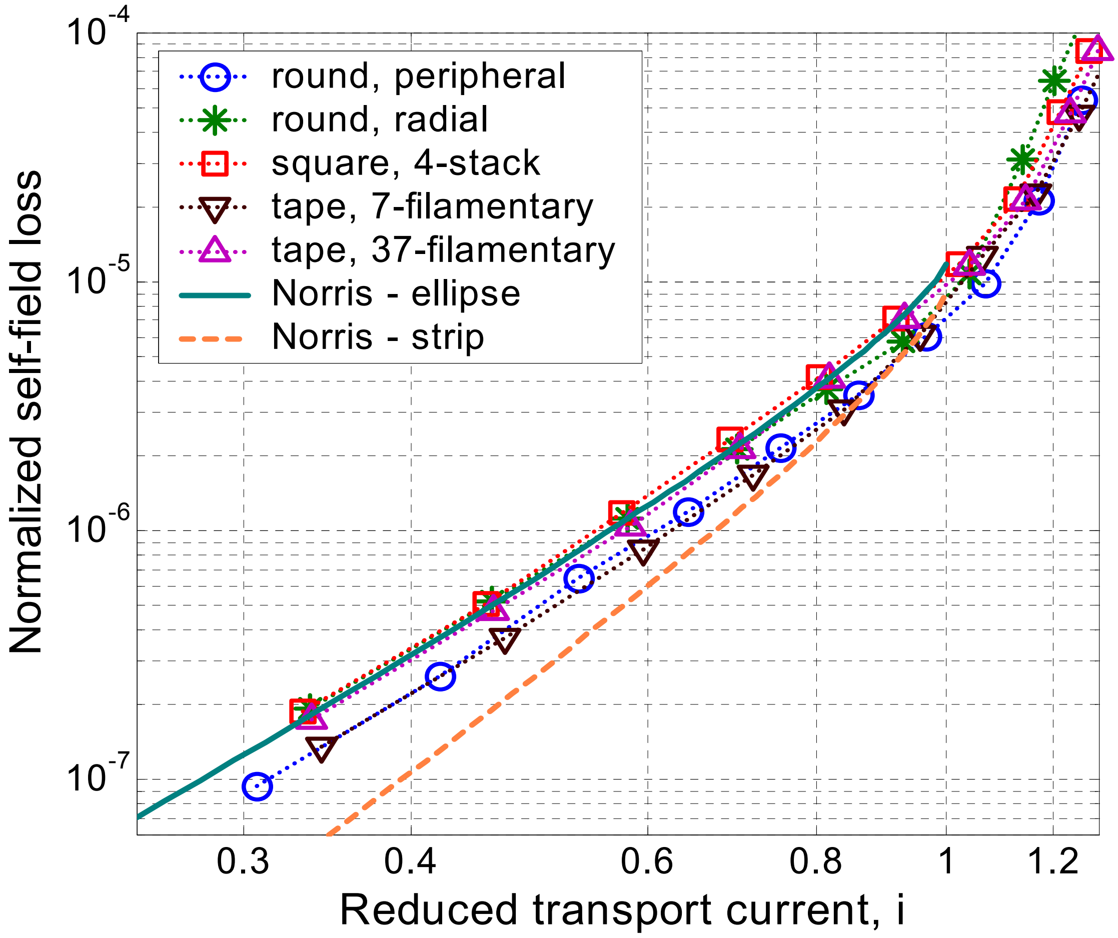

Figure 5-36 Self-field AC losses at 59 Hz for different values of the reduced transport current. The losses are normalized by I_c^2 for each conductor and compared to Norris's strip and elliptical predictions.

Figure 5-38 shows the current density distribution at peak value of applied current of 55 A in the two round wires along a line segment, parallel to the x-axis in the right half of the conductors. In the round radial wire, this line segment runs along one filament only, while in the round peripheral wire the segment goes through three parallel filaments (see Fig. 5-38c). Plotted is also the calculated $J_c(B)$ along the same segment; its decrease in the round radial wire is much stronger. As can be seen in Fig. 5-38a and Fig. 5-38b, the radial wire is completely saturated and the current density exceeds considerably the local J_c, while the peripheral wire is not saturated in the left-most filament (closest to the center), and the saturating current density in the other two filaments is just slightly above J_c. Even though the plots in Fig. 5-38 reflect an instantaneous picture only ($\omega t = \pi/2$), they give a qualitative explanation for the AC loss difference between the round wires in self-field.

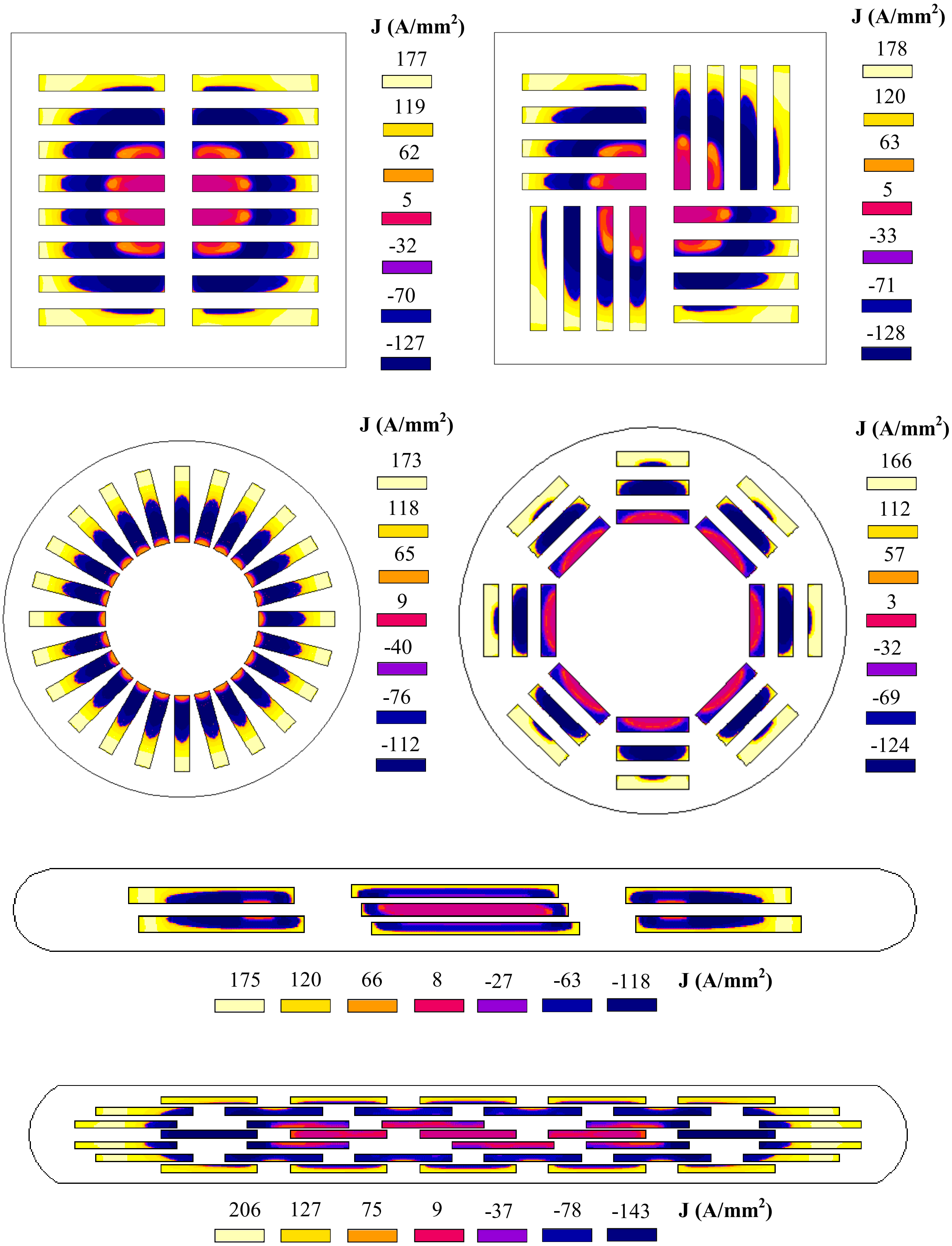

Figure 5-37 Current density at ωt = 2π for applied transport current of 44 A. The value of J_{c0} for the 37-filamentary tape is 186 A/mm^2, and for all other conductors J_{c0} = 160 A/mm^2.

a) radial

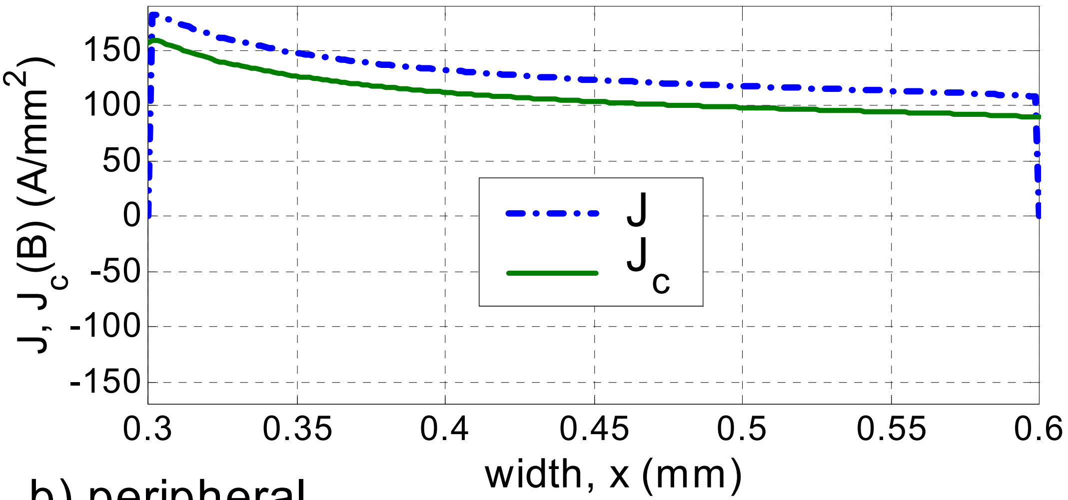

b) peripheral

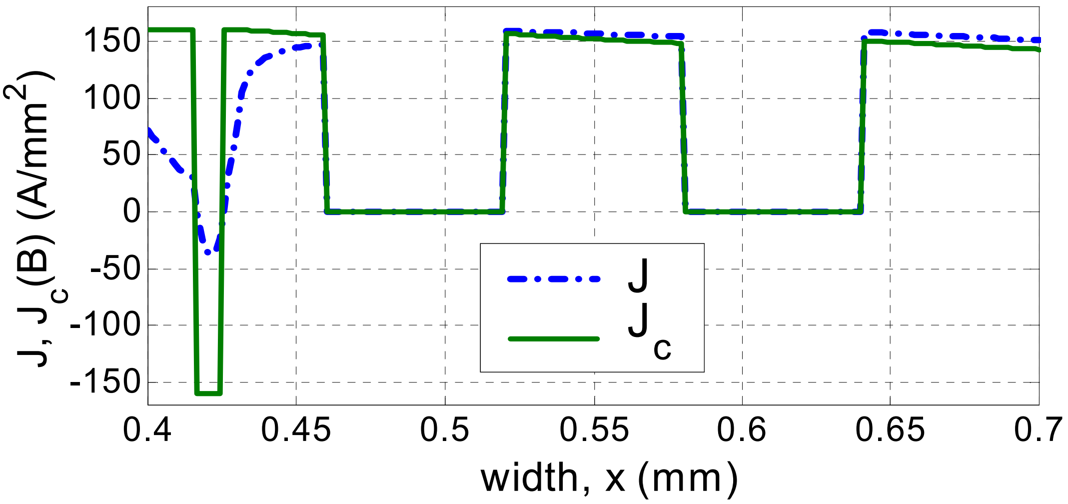

c) line-segment

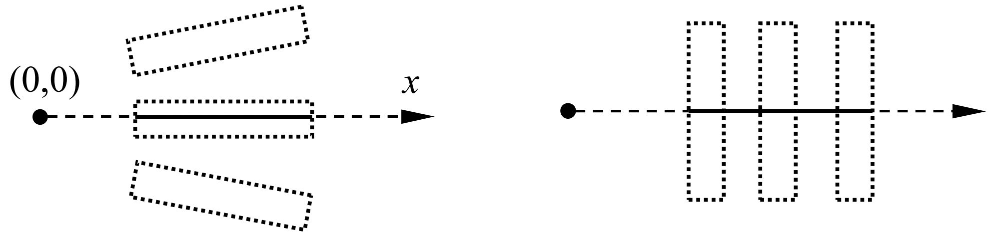

Figure 5-38 Current density J and $J_c(B)$ at peak value of applied transport current of 55 A for the round wires along a line-segment in the right half of each conductor. This segment is indicated with solid line in c). $J_c(B)$ is plotted with the sign of J.

5.5.5 Tapes and wires in applied external magnetic field of varying orientation

The numerically calculated magnetization losses at 59 Hz for multifilamentary conductors with $J_c(B)$ of different geometry and filament arrangement in applied AC perpendicular and parallel magnetic field are shown in Figs. 5-39 and 5-40 as function of the field's amplitude B_a. The 37-filamentary tape has J_{c0}, whish is higher than the one of the other conductors; its losses are within 25-30% from the losses of the 7-filamentary tape and are not shown on the figures. The $J_c(B)$ dependence and the different filament configuration do not change the slope of the magnetization loss curves below and above B_p, compared to the critical state model in Eq. (5-13); they influence, however, the penetration field B_p of the conductors.

In perpendicular magnetic field (see Fig. 5-39), multifilamentary tapes have much higher losses than multifilamentary round or square wires, which is due to the strong demagnetizing effect of a conductor with large aspect ratio in field of such orientation. The loss difference reaches a factor of 8 at field of 10 mT, and decreases to a factor of 3-3.5 at fields higher than 50 mT. Above the penetration field, the induced currents are fully occupying all filaments and the current density exceeds J_c everywhere. In this case, the stronger reduction of $J_c(B)$ for the tape in perpendicular field implies less induced currents, and correspondingly lower losses as well. This explains the decrease of the loss difference between the tapes and the wires at high perpendicular fields.

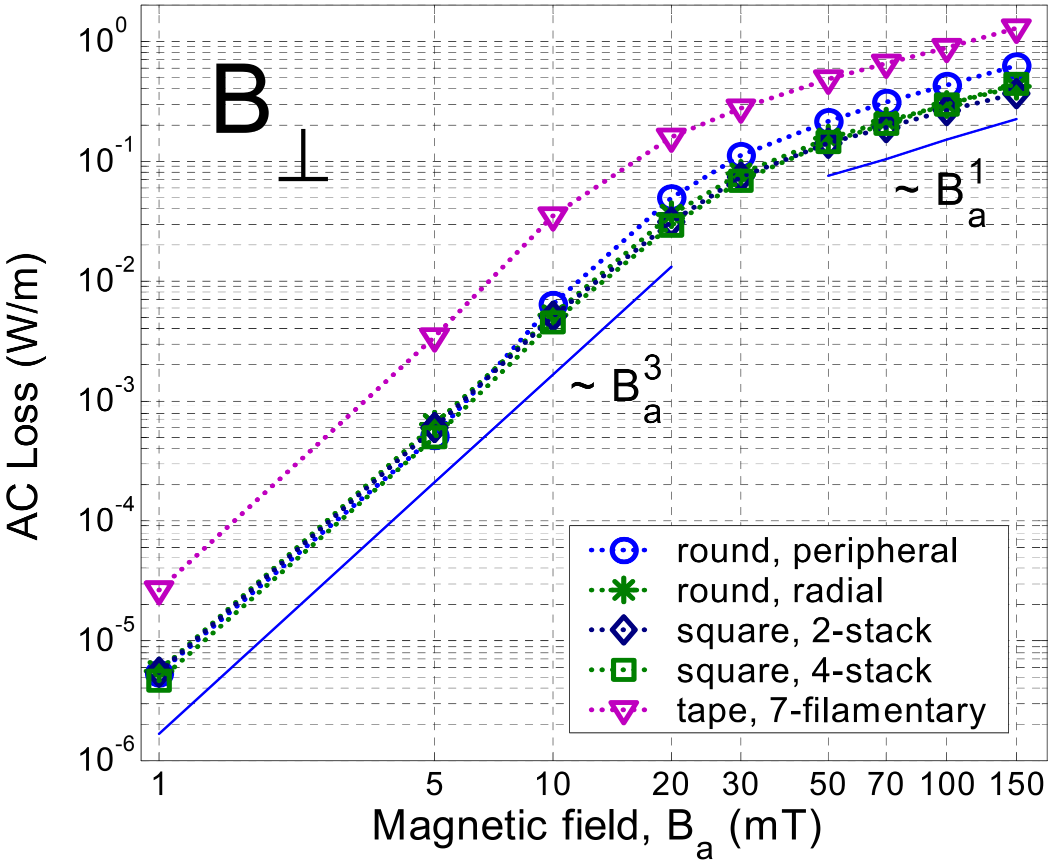

Figure 5-39 Magnetization loss at 59 Hz in multifilamentary conductors of different geometry with J_c(B) in perpendicular AC magnetic field up to 150 mT.

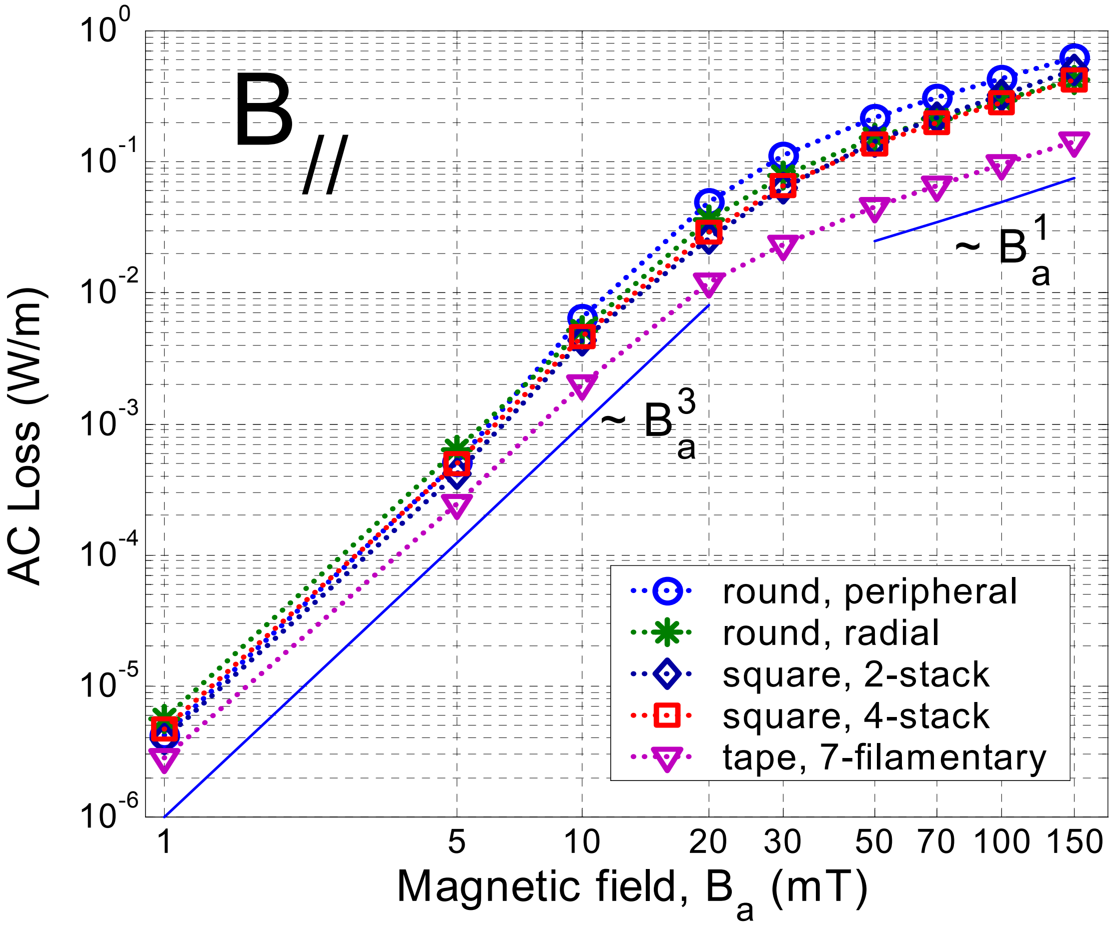

Figure 5-40 Magnetization loss at 59 Hz in multifilamentary conductors of different geometry with $J_c(B)$ in parallel AC magnetic field up to 150 mT.

In parallel magnetic fields (see Fig. 5-40), the wires have larger losses than the tape due to their higher shape factor; see Table 5-5. The loss difference is around a factor of 2 at 10 mT, and reaches a factor of 3 at fields above 50 mT.

The round wire with peripheral arrangement has magnetization losses, which are larger by 40-50 % than the ones of other wires at fields above 20 mT. A possible explanation is the configuration of its filaments, which leads to higher penetration field in this wire.

Let us recall, for convenience of the reader, the critical state model for a slab in applied external field B_a parallel to the y-axis, sketched in Fig. 5-41. The field starts to penetrate the superconductor from the edges towards the center, inducing layers of screening currents, shielding the interior of the superconductor from the external field. For $B_a < B_p$, there is only partial penetration of the field, and the center of the slab is flux-free. At $B_a = B_p$ the field penetration reaches the center of the superconductor. Then, as the field amplitude is further increased ($B_a > B_p$), the penetration profile is simply shifted upwards along the y-axis; the difference between the field at the edge and at the center remains B_p.

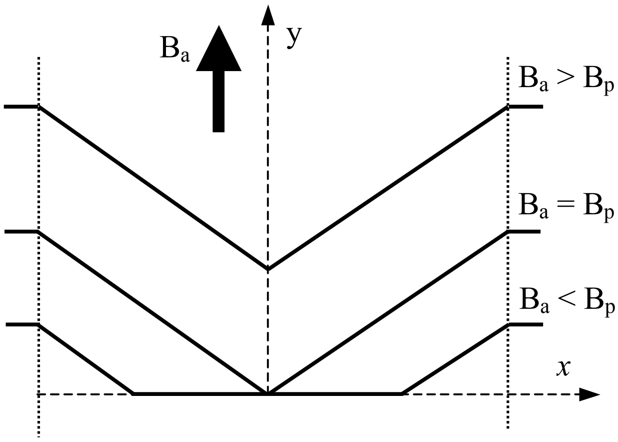

Figure 5-41 Penetration profile of magnetic field with amplitude B_a parallel to the *y*-axis for a slab in the critical state model.

In multifilamentary conductors with finite dimensions and $J_c(B)$ the field penetration pattern is more complicated than in the critical state model of a slab. Figure 5-42 shows the magnetic flux density distribution in the filaments of three different conductors, at peak value of applied perpendicular magnetic field of 30 mT. In applied field of such orientation (parallel to the *y*-axis), the penetration starts from the left and right sides towards the center of the conductors.

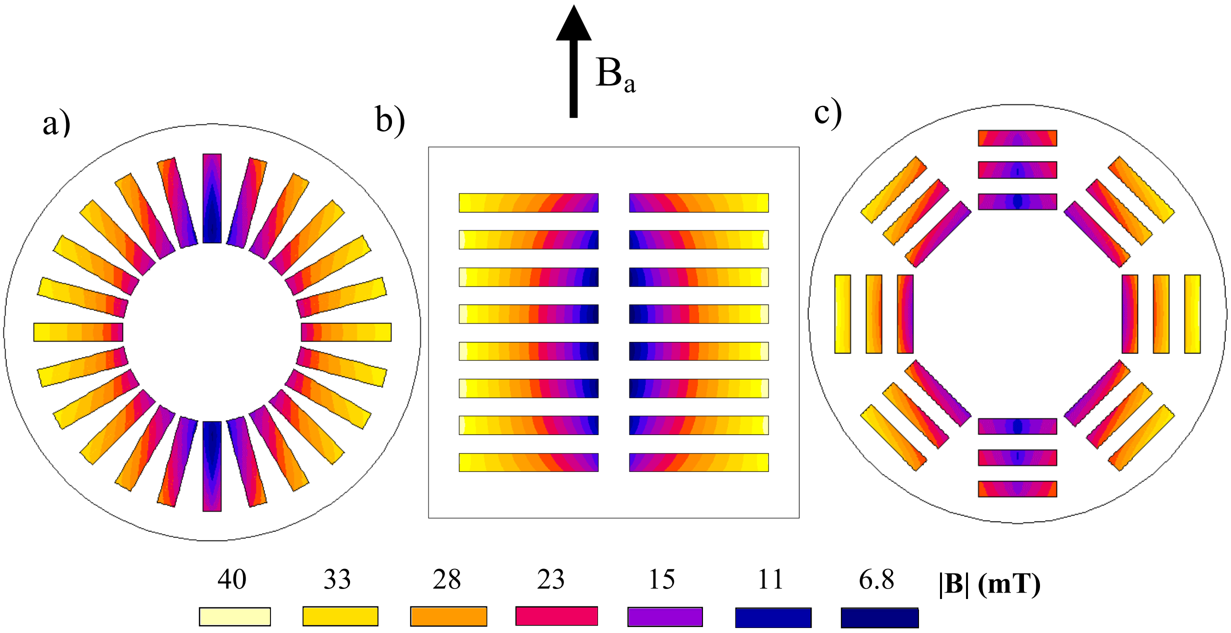

Figure 5-42 Magnetic flux density in the Bi-2223 filaments at peak value (ωt = 3π/2) of applied perpendicular field of 30 mT.

For the round radial wire, the field in the left and right-most filaments has dominating perpendicular component, the decrease of $J_c(B)$ is significant, and so the screening currents are low. Therefore, the shielding effect of the screening currents in these filaments is not sufficiently strong, and the field has penetrated almost all filaments of the conductor, as shown in Fig. 5-42a. For the square wire, the field has fully penetrated around 2/3 of the cross-section; the remaining 1/3 in the center is screened and has low magnetic field penetration, see Fig. 5-42b. As for the round peripheral wire, the filaments that are penetrated first have parallel orientation to the field. In these filaments, the decrease of $J_c(B)$ is weak, and large screening currents circulate; the screening effect is strong and the other filaments are shielded from the field, see Fig. 5-42c. As a result, the round peripheral wire has higher penetration field than the other wires. Since the loss in non-fully penetrated conductors ($B_a < B_p$) is proportional to B_a^3, and in fully penetrated conductors ($B_a > B_p$) the loss increases more slowly with B_a (see Figs. 5-39 and 5-40), the magnetization losses for fields above 10 mT in the round peripheral wire are larger than in the other wires.

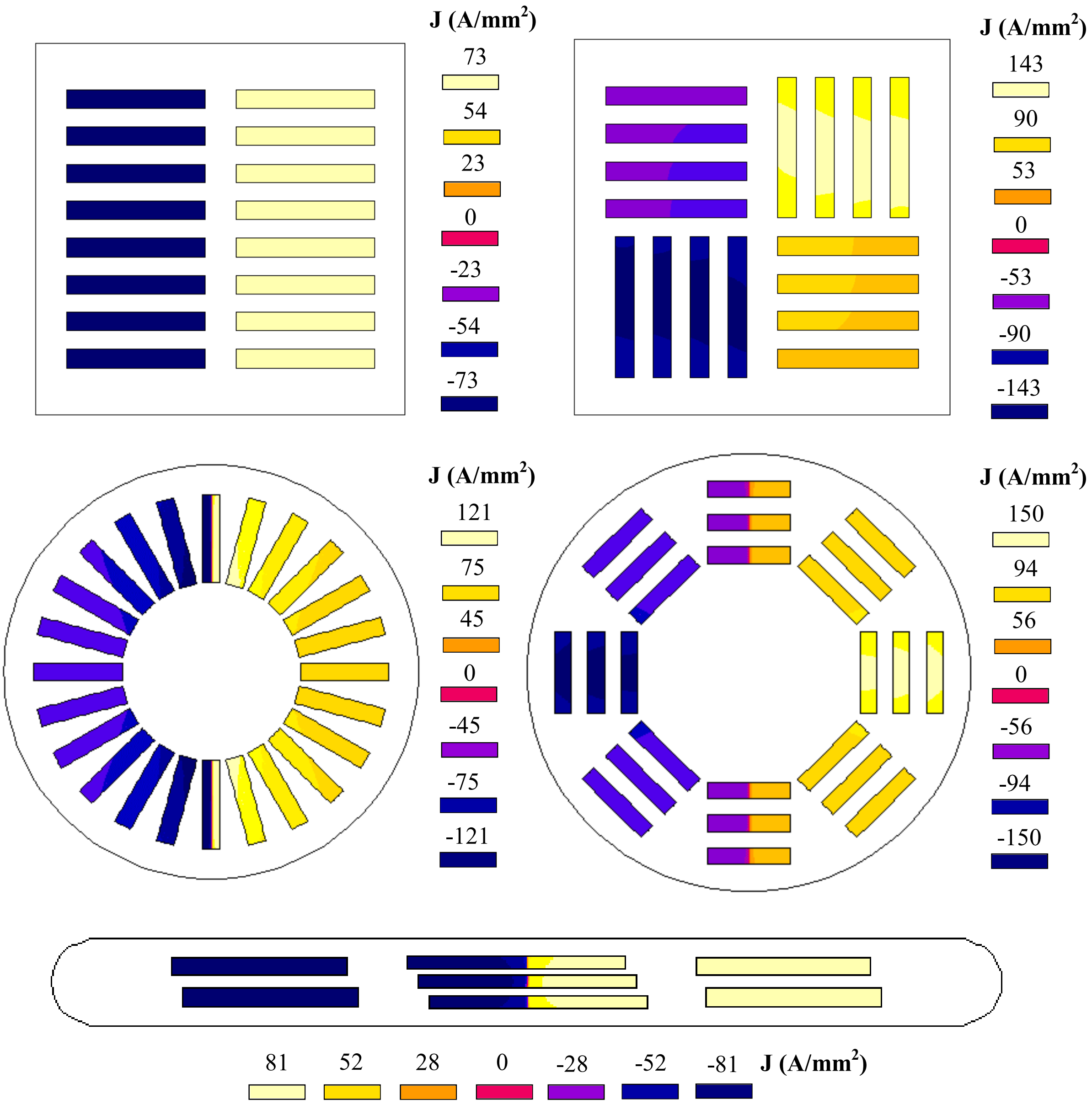

Figure 5-43 Induced current density in the Bi-2223 filaments at peak value ($\omega t = 3\pi/2$) of applied perpendicular field of 50 mT.

Next, Fig. 5-43 shows the induced current density distribution in the filaments of the multifilamentary conductors at peak value of applied perpendicular field of 50 mT. At such field amplitude, all conductors are fully penetrated. The saturating current density (J_{max}) in the filaments, however, varies considerably due to the different decrease of $J_c(B)$ in fields of varying orientation. For the 2-stack square wire and the tape, whose filaments in this case are perpendicular to the external field, J_{max} is only 73 A/mm^2 and 81 A/mm^2, respectively, while J_{c0} is 160 A/mm^2. For the other conductors, J_{max} varies between 121 A/mm^2 for the radial wire and 150 A/mm^2 for the peripheral wire in the corresponding filaments, which are parallel to the field. In the filaments, which are perpendicular to the field, the screening current density is much lower. In all cases, J_{max} is greater than the local $J_c(B)$.

It was shown in Section 5.4.6 that most of the power dissipation in self-field and in perpendicular field occurs near the edges of the monofilamentary tapes, where the local magnetic field and the ratio $J/J_c(B)$ have highest values. In table 5-9 we show the saturating current density and the corresponding local magnetic field near the edges of the filaments in the five multifilamentary conductors, as well as the corresponding $J_c(B)$ values and the ratio $J/J_c(B)$, at peak value in applied perpendicular field of 50 mT, see also Fig. 5-43. For the conductors in the last three rows, shown are the respective values in the filaments with parallel (//) and perpendicular orientation (⊥) to the field. The AC loss is proportional to the n-th power of the ratio $J/J_c(B)$. Indeed, in the 7-filamentary tape and the 2-stack square wire, all filaments are perpendicular to the field, they are completely saturated with $J/J_c(B)$ well above 1, and consequently, these two conductors have highest losses in field of such orientation, see also Fig. 5-45 below. The three other wires have filaments with different orientation with respect to the applied field – in the filaments with parallel orientation the $J/J_c(B)$ values are considerably lower than the ones in the filaments with perpendicular orientation. It is to be noted that the saturating current density in all filaments of the round peripheral wire is above the local $J_c(B)$, which may explain why the losses in this conductor are higher than in the 4-stack square wire and the round radial wire, in which the filaments with parallel orientation have $J/J_c(B)$ ratio lower than 1.

TABLE 5-9 Current density near the edges in perpendicular field with B_a = 50 mT at $\omega t=3\pi/2$

Conductor	**J (A/mm^2)**	**B, local (mT)**	**$J_c(B)$ (A/mm^2)**	**$J/J_c(B)$ -**
Tape, 7-filamentary	74-76	55-57	50-51	1.45-1.52
Square, 2-stack	66-68	51-53	52-53	1.25-1.30
Square, 4-stack	115-120 (//)	38-53 (//)	118-128 (//)	0.90-1.02 (//)
	66-68 (⊥)	51-53 (⊥)	52-53 (⊥)	1.25-1.30 (⊥)
Round, peripheral	140-142 (//)	40-42 (//)	125-126 (//)	1.12-1.14 (//)
	63-65 (⊥)	54-56 (⊥)	50-51 (⊥)	1.24-1.30 (⊥)
Round, radial	110-112 (//)	38-40 (//)	126-128 (//)	0.86-0.89 (//)
	67-69 (⊥)	52-54 (⊥)	52-53 (⊥)	1.26-1.23 (⊥)

Shown is the saturating current density near the edges of the filaments, the corresponding local magnetic field and $J_c(B)$ values, as well as the ratio $J/J_c(B)$. For the conductors in the last three rows, shown are the respective values in the filaments with parallel (//) and perpendicular orientation (⊥) to the field.

5.5.6 Tapes and wires with transport current and applied magnetic field

The 2D analysis of the interaction between the self-field and the external field in conductors with power-law current-voltage characteristic is rather complicated. As it was shown for monofilamentary conductors, due to this interaction, the total loss in the combined current and external field case is larger than the simple sum of the self-field and magnetization losses.

The total AC losses at 59 Hz for applied transport current in external perpendicular field of 30 mT are shown in Fig. 5-44. Plotted is also the total loss for the 7-filamentary tape in parallel field of 30 mT. Because of the geometry of the tape (shape factor of ~ 10 in perpendicular field and ~ 1 in parallel field), its magnetization loss in perpendicular field is much higher than in parallel field – almost a factor of 9 for the whole transport current range. As far as the wires are concerned, the AC loss in the two round conductors and the square one with 4-stack arrangement is the same in perpendicular and parallel fields because of the symmetry in the filament configuration. The total AC loss in the round and square wires is lower than the loss of the tape in perpendicular field and higher than the loss of the tape in parallel field. The loss magnitudes do not vary considerably with the transport current amplitude (a factor of 2 between the minimum and maximum applied current), which indicates that the magnetization loss is dominating the self-field loss at such and higher external fields.

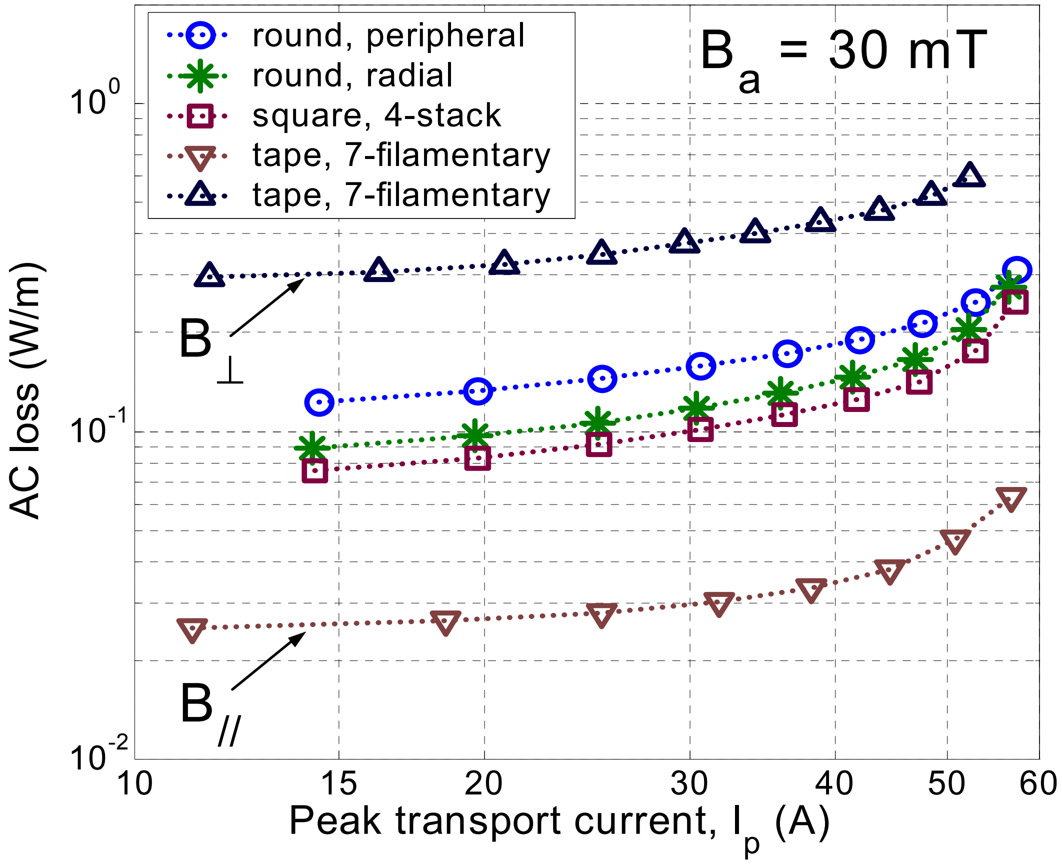

Figure 5-44 AC losses at 59 Hz in conductors of different geometry with transport current in external magnetic field of 30 mT. The losses in the 7-filamentary tape are given for both perpendicular and parallel field orientation.

Finally, Fig. 5-45 shows a comparison between the AC losses in the conductors of different geometry at fixed transport current ($I_p = 40$ A) and external magnetic field amplitude (B_a = 50 mT). The field is applied at varying orientation – from parallel (α = 0°) to perpendicular (α = 90°). The losses at 59 Hz are normalized by the $I_c(B)$ calculated for each angle in the different conductors and are given in mW per Amp-meter.

The AC losses in the tape increase quickly with the angle of the applied field because of the rapidly growing loss contribution due to the perpendicular magnetic field component. There is a difference of more than a factor of 10 between the tape's loss in perpendicular and parallel field. The loss in the square wire with 2-stack arrangement, whose filaments have the same orientation as in the tape, also increases with the applied field's angle. This increase, however, is much less pronounced – a factor of 2.5 between the perpendicular and parallel orientation, which is due to the shape factor of a square conductor. The square wire with 4-stack arrangement has lower losses in fields with dominating parallel or perpendicular component; the loss increases for intermediate fields, but the loss difference is only less than 40 % for any values of α. The loss in the round wires is independent of the magnetic field orientation due to their fully symmetric configurations. The loss in the round peripheral wire is higher than the loss in the other wires, except for the loss of the 2-stack square one at fields with α > 60°.

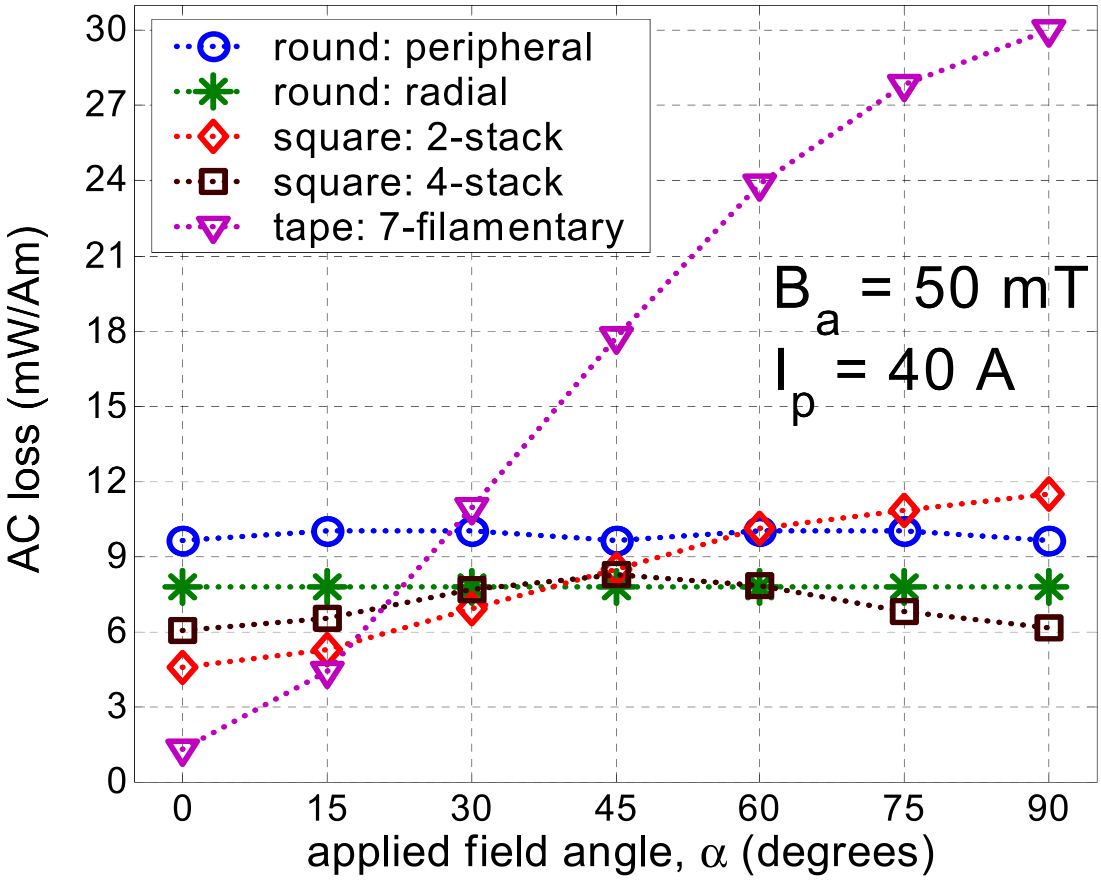

Figure 5-45 AC losses in conductors of different geometry with transport current of 40 A in external magnetic field of 50 mT, applied at varying angle. The losses at 59 Hz are normalized by the corresponding $I_c(B)$, calculated for each conductor.

All wires, however, have lower losses than the tape for fields with $\alpha > 30°$; the loss difference may reach a factor of 2.5 at $\alpha = 45°$ and a factor of 5 at $\alpha = 90°$. Among the wires, the peripheral configuration in the round one appears to be least favorable in applications with applied external magnetic field, see also Figs. 5-39, 5-40 and 5-44. The square wire with 4-stack arrangement seems to have the optimal configuration for applications with external field of changing orientation.

5.6 Summary and conclusions

This chapter presented comparative analysis of AC losses, complemented by examples of magnetic flux and current density distributions in HTS tapes with constant J_c and $J_c(B)$. It was demonstrated that different models of $J_c(B)$ and $n(B)$ can be used in perpendicular fields, for example Kim's law or polynomial fits to experimental data. The $J_c(B)$ dependence results in decrease of the penetration field in the tapes and in varying saturating current density according to the local value of the magnetic field. As far as AC losses are concerned, in tapes with $J_c(B)$ the losses are higher below the penetration field and lower above the penetration field, compared to tapes with constant J_c.

For modelling of non-twisted monofilamentary round and square wires and flat tapes, as well as multifilamentary conductors with different geometry and filament arrangement in various applications, new models of the $J_c(B)$ and $n(B)$ dependence in Bi-2223 textured materials were presented, which take into account the orientation of the local magnetic field. The models are based on experimental data and are fairly simple – isotropic for monofilamentary wires and anisotropic for flat tapes and multifilamentary conductors. In the latter, the $J_c(B)$ and $n(B)$ are calculated locally in each filament. These models allow calculation of AC losses, as well as magnetic field and current distributions in conductors of any filament configuration with transport current and/or applied external field with arbitrary orientation and magnitude up to 300 mT.

In conductors with given J_{c0} and $J_c(B)$ dependence, an effective critical current for AC applications was defined. The influence of the self-field cannot be neglected for the determination of $I_c(B)$, especially for applications with high transport current. In multifilamentary conductors, the effective I_c is not the same even if they have identical J_{c0} and $J_c(B)$ dependence because of the different orientation of the self-field to the individual filaments. The notion of effective I_c is meaningful for transport current applications, since it indicates the current amplitude, above which the losses increase much faster with the peak current. On the other hand, for applications with applied magnetic field only, the $I_c(B)$ has no special physical or engineering meaning. In such applications, it is the $J_c(B)$, which is the important quantity, because it determines the penetration field, as well as the saturating current density of the induced currents.

The relation between $J_c(B)$ and I_c can also be considered in the reverse direction. The I_c obtained from DC measurements in self-field or in external magnetic field, divided by the BSCCO cross-section, yields values of J_c, which in fact depend not only on the material, but also on the geometry of the conductors and reflect the self-field effects.

It has been demonstrated that in AC applications the loss magnitude of Bi-2223 multifilamentary conductors is determined by their shape factor and by the orientation of their filaments with respect to the local magnetic field. In transport current applications, flat tapes have in principle lower self-field losses because of their large aspect ratio. However, because of the favourable filament configuration in the round peripheral wire, its self-field AC loss turned out to be very similar to the loss of the 7-filamentary tape, and lower by nearly 50 % than the self-field loss in the other wires and the 37-filamentary tape.

In applied external magnetic field, the AC loss magnitude depends to a greater extent on the shape factor of the conductor. Tapes have lower shape factor and consequently lower magnetization loss than round or square wires in parallel field. The shape factor and the losses in flat tapes, however, increase quickly in fields with present perpendicular component. Wires with symmetrical filament arrangement, on the other hand, have magnetization losses with small variation in fields of changing orientation. This is an advantage for the AC loss calculus and design of devices (e.g. coils and cables) made of wires instead of tapes. In addition, in any real application of Bi-2223/Ag conductors, for example in a transposed and/or stranded cable, the field orientation will vary considerably with respect to the different components, and therefore the use of wires will be more favourable in most configurations. Further AC loss optimisation for use of Bi-2223 conductors can be achieved if the orientation of the external field is approximately known – for example, the 2-stack square wire is most appropriate to use in fields with dominating parallel component, while the 4-stack square wire has the optimal filament configuration for fields of varying orientation.

Chapter 6. Conclusion

6.1 General conclusions and achievements of this thesis

The contents of this thesis have been placed in the context of modelling of high-T_c superconductors for AC power applications. The reduction of AC losses is a major requirement for the large-scale utilization of HTS materials, among which Bi-2223 has for the moment an advanced manufacturing technology and will be used in most of the first industrial applications. Different approaches were used in the thesis with the primary goal of developing new models for evaluating and analysing the AC losses in Bi-2223 conductors and proposing ways for their reduction.

The total self-field AC loss of HTS tapes has hysteresis, flux-creep and eddy-current contribution. A model for AC loss-dissociation was proposed in this thesis, using results from sufficiently broad frequency range measurements obtained with the electrical characterization technique. The model is based on the different frequency dependence of the hysteresis, flux-creep and eddy-current loss components, and allows the dissociation of each loss contribution, which are not possible to be measured separately with the transport current loss set-up. Using the frequency model for AC loss dissociation, the relative contribution of the hysteresis, flux-creep and eddy-current loss to the total self-field loss has been quantitatively assessed in the range 59 Hz – 2.5 kHz. The main contribution to the self-field AC loss in Bi-2223 tapes for any applied current in the low frequency range is the hysteresis loss, while resistive flux-creep loss appears for currents above 0.8 I_c. The flux-creep loss may reach up to 30-40% of the total loss for currents close to I_c at low frequency ($f \leq 100$ Hz). For the intended current ratio in AC power applications ($i > 0.4$), the eddy-current type loss does not have any significant contribution below 200 Hz, and starts dominating the total self-field loss for frequencies well above 1 kHz. The eddy current loss in Bi-2223 tapes was also evaluated by means of FEM simulations and the possibilities for reducing this loss component by increasing the matrix resistivity and changing the sheath geometry were thoroughly investigated.

The thesis presented different approaches for evaluating the performance of Bi-2223 tapes in experiments with over-critical current excursions of various waveform, frequency and amplitude up to $20 \times I_c$, which in general showed no degradation of the superconducting properties. The temperature rise in the tapes was estimated in two different ways and the results confirmed the overall stability of Bi-2223 tapes in typical over-I_c power grid perturbations.

The major part of this thesis dealt with numerical modelling of high-T_c superconductors since the analytical solution of current and field equations in HTS with smooth current-voltage characteristics is possible only for simple geometries. The finite element method has been selected in the thesis for the electromagnetic analysis and AC loss calculation in high-T_c superconductors. Compared to other modelling approaches, the finite element method requires comparatively extensive use of CPU time and considerable memory resources. However, it is the only method, which has the capability to compute precisely the current density and magnetic field profiles in the entire cross-section, as well as the AC losses of HTS with geometry of any shape and complexity, and with J_c and n that may depend on the position or the local magnetic field. The validation of the implementation of the power-law model of HTS materials in the FEM software package Flux2D was achieved by means of comparison of the calculated current density distributions and AC losses in self-field and applied field to results from electrical measurements, theoretical predictions, and from other numerical implementations.

HTS materials are characterized by means of a nonlinear E-J relation with J_c and the power index n as parameters. Both the J_c and n depend on the voltage criterion E_c, for which most often 1 μV/cm is used. The influence of the n-value was studied in numerical simulations. It was demonstrated that in superconductors with low n-value ($n = 5$) the current distribution is not uniform, and the external filaments have saturating current density largely exceeding J_c, while for higher n-values ($n = 50$), the current distribution is similar to the critical state model – uniform in the whole cross-section with saturation close to J_c in all filaments.

The influence of the lateral variation of J_c in multifilamentary tapes was investigated. Models with constant J_c and non-uniform $J_c(x)$ were employed and compared. Since the current penetration in HTS always starts from the exterior to the interior of the superconductor, the higher the J_c in the outer filaments, the lower the transport current losses are, which is true regardless of the shape of the conductors. It was verified that the transport current loss in HTS tapes with increasing J_c towards the edges can be reduced approximately to the low-loss strip prediction of Norris in the power range of interest 0.6 – 0.9 I_c. Thus by modelling with $J_c(x)$ dependence the optimal current density distribution for a given I_c, which leads to minimized transport current loss, was obtained.

New models of the $J_c(B)$ and $n(B)$ dependence in Bi-2223 textured materials for magnetic fields up to 300 mT were presented. The models are anisotropic and take into account the orientation of the local magnetic field. They are based on experimental data and have fairly simple exponential dependence on the parallel and perpendicular field components. With certain geometric considerations, the anisotropic models of $J_c(B)$ and $n(B)$ can be applied locally to each filament of superconductors with various shape and filament configuration.

FEM simulations of Bi-2223/Ag mono and multifilamentary conductors with different geometry and filament arrangement were performed using the anisotropic models of $J_c(B)$ and $n(B)$. For conductors with given J_{c0} and $J_c(B)$, an effective AC critical current was defined. The notion of effective I_c is meaningful for transport current applications, where it denotes the current above which the AC losses start to sharply increase, while in applications with magnetic field only, the important quantity is $J_c(B)$, because it determines the penetration field and the saturating density of the screening currents.

The FEM simulations demonstrated that the AC loss magnitude of Bi-2223 multifilamentary conductors is determined by their shape factor and by the orientation of their filaments with respect to the local magnetic field. In transport current applications, conductors with high aspect ratio are preferred, since the strip geometry has lowest loss in monofilamentary conductors. However, a round wire with peripheral filament arrangement was found to have low transport current loss due to the specific filament orientation parallel to the self-field flux lines. In applications with external field, the AC loss magnitudes depend to a greater extent on the shape factor of the conductors. In nearly parallel fields flat tapes have lower losses, which, however, increase quickly in fields with larger perpendicular component. Round or square wires with symmetric filament arrangement have magnetization losses with almost no variation in fields with changing orientation. They have lower losses than flat tapes for fields with angle of orientation above 30° and the loss difference in their favour may reach a factor of 4-5 in perpendicular fields.

The AC loss analysis was supported and complemented by computation of the magnetic field and current density distributions in the different conductors. The current and field profiles calculated in the thesis were used for quantitative explanation of the AC loss difference between different geometries, e.g. ellipse and strip; for demonstrating the strong demagnetizing effect in conductors with large aspect ratio, and for defining the regions in the conductors where the ratio $J/J_c(B)$ and, correspondingly, the power dissipation are highest.

The novel $J_c(B)$ and $n(B)$ models presented in this thesis allow numerical computation of AC losses, current and magnetic field profiles in HTS tapes and wires with any geometry and filament arrangement and under various operating conditions.

Last but not least, Flux2D is not homemade software with restricted use to its creators. On the contrary, Flux2D is a software package, which is commonly used in the electromagnetic modelling community, and the developed advanced models of superconductors contribute to the progress in material modelling and give the possibility of different Flux2D users – researchers and engineers – to profit from it, since a Superconductivity module is already attached to the newest version of this software package.

6.2 Future considerations

The research attraction for 2D modelling of high-T_c superconductors has not been completely exhausted. An interesting possibility is to expand the models presented in this thesis by adding a temperature-dependence of the critical current density J_c, which appears to be indispensable for modelling of fault-current limiters, for example.

The transition to 3D is the natural extension of the FEM models presented in the thesis. Moreover, modelling of HTS devices, such as cables, coils, transformers, fault-current limiters etc., cannot be accomplished in 2D only.

Some preliminary attempts for 3D simulation of high-T_c superconductors in external magnetic field and with applied transport current have been already successfully performed with the FEM software package Flux3D. However, the transition to 3D is not simply the addition of another dimension. Considerable difficulties are encountered in building a complex 3D geometry with twisted, stranded or transposed elements accompanied by untrivial problems of meshing such a structure. In addition, there are certain convergence problems in the Newton-Raphson algorithm dealing with highly non-linear materials in 3D. An enormous increase of the CPU time is necessary for fine-mesh 3D simulations even for simple geometries. Therefore, in the 3D modelling of HTS there is a trade-off to be made between the structural complexity of the geometry and the required precision of results. Anyway, the question where the limit is for 3D modelling of HTS is left open to future research.

Appendix A. Calculation of Hysteresis Loss in Self-field

The method for calculation of the hysteresis loss in a superconductor with rectangular cross-section, presented here, has been described in [Mül97b].

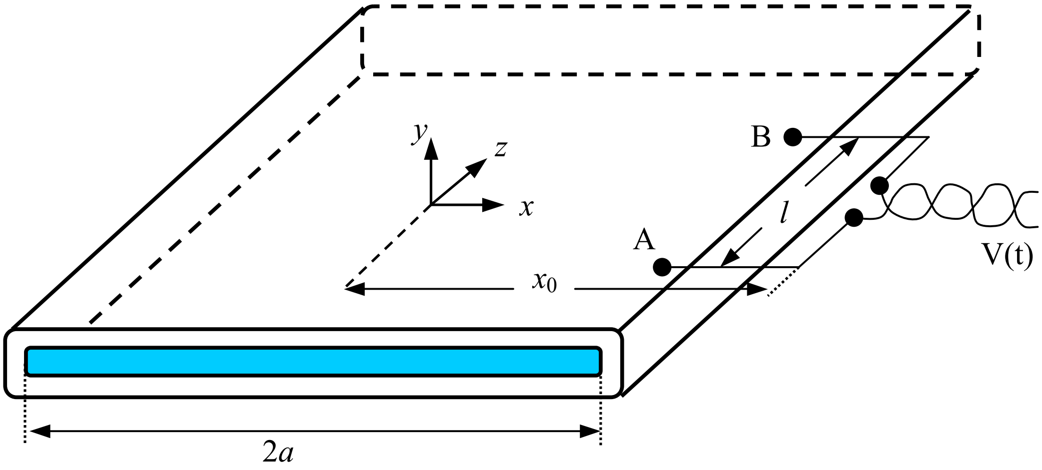

Figure A-1 Schematic representation of a Bi-2223/Ag tape. The voltage V(t) is measured between the points A and B.

Figure A-1 shows the schematic representation of an Ag-sheathed Bi-2223 tape with applied transport current $I(t) = I_m \cos \omega t$ of amplitude I_m and frequency $f = \omega/2\pi$ for electrical measurement of the voltage $V(t)$ between the points A and B. The lock-in amplifiers measure the phase-shift φ between the current $I(t)$ and the reference output signal of the sine generator, as well as the first in-phase harmonic V_1 of the voltage $V(t)$:

$$V_1 = \frac{2\omega}{\pi} \int_0^{\pi/\omega} V(t) \cos(\omega t + \delta) dt \tag{A.1}$$

where δ is the phase-angle error of φ, see also Section 3.2.

The measured power loss P_{meas} per unit length is then calculated as follows:

$$P_{meas} = \frac{I_m V_1}{2l} \tag{A.2}$$

where l is the distance between the voltage taps.

The voltage $V(t)$ between the contact points A and B (see Fig. A-1) is:

$$V(t, x_0) = -\frac{\partial \Phi(x_0)}{\partial t} \tag{A.3}$$

where the time derivative of the flux is given by:

$$\frac{\partial\Phi(x_0)}{\partial t} = \mu_0 l \frac{\partial}{\partial t}\int_0^{x_0} H_{z\downarrow}(x)dx \tag{A.4}$$

and x_0 is the width of the lead extension, as indicated in the figure. $H_{z\downarrow}(x)$ is the *z*-component of the magnetic field inside and outside the superconductor. The downside arrow (↓) indicates that $H_{z\downarrow}(x)$ is the field distribution when the transport current *I(t)* is decreasing from I_p to $-I_p$ in the first half of the AC cycle, corresponding to the interval 0 to π/ω in Eq. (A.1). It has been shown by Brandt *et al.* [Bra93] that

$$H_{z\downarrow}(x,I,I_c) = H_z(x,I_m,I_c) - H_z(x,I_m - I, 2I_c) \tag{A.5}$$

where

$$H_z(x) = H_d \ln\left(\frac{\sqrt{a^2-x^2}}{\sqrt{a^2-c^2}-\sqrt{x^2-c^2}}\right) \quad \text{for } c < x < a \tag{A.6}$$

and

$$H_z(x) = H_d \ln\left(\frac{\sqrt{x^2-a^2}}{\sqrt{x^2-c^2}-\sqrt{a^2-c^2}}\right) \quad \text{for } x > a \tag{A.7}$$

with $c = a\sqrt{1 - I^2(t)/I_c^2}$ and $H_d = I_c/(2\pi a)$.

Combining Eq. (A.1) to Eq. (A.7) gives the measured power loss per unit length as:

$$P_{meas}(\omega, I_c, I_m, \delta, x_0) = -\frac{\mu_0}{\pi}\frac{aH_d\omega^2 I_m^2}{I_c}\int_0^{\pi/\omega}\cos(\omega t+\delta)\sin\omega t \ln\left(\frac{x_0+\sqrt{x_0^2-\beta^2(t)}}{\beta(t)}\right)dt \tag{A.8}$$

where $\beta(t) = a\sqrt{1-(I_m - I(t))^2/4I_c^2}$.

The real loss P_{real} is defined as:

$$P_{real} = P_{meas}(\delta \to 0, x_0 \to \infty) \tag{A.9}$$

For $\delta \to 0$ and $x_0 \to \infty$ the integral in Eq. (A.8) can be calculated analytically and one obtains the formula derived originally by Norris for the self-field hysteresis loss for the CSM in flat superconductors of thin rectangular (strip) cross-section:

$$P_{hyst} = \frac{\mu_0}{2\pi^2}\omega I_c^2\left[(1-i)\ln(1-i) + (1+i)\ln(1+i) - i^2\right] \tag{A.10}$$

where $i = I_m / I_c$. For low applied transport current ($I_m / I_c << 1$), P_{hyst} varies as i^4.

Appendix B. Introduction to the Galerkin Finite Element Method

The finite element method (FEM) is a numerical technique with increasing popularity, used for solving complex electromagnetic problems. It has a series of advantages over other numerical algorithms, such as the finite difference method (FD), which has been extensively used in electromagnetic field analysis and still has a mathematical importance. A major difficulty with the FD method is that the discretization schemes (mesh, grid etc.) have a fixed order and arrangement, although the actual geometric distribution of mesh lines can be irregular. A further limitation of the FD arises when it is required to use higher-order terms for the basic Taylor's series to improve the accuracy of approximation [Bin92].

These difficulties are successfully surmounted by the FEM approach. One of the most effective techniques of deriving the FEM equations is the Galerkin method, which is a special case of the method of weighted residuals (MWR), which can be applied as described below [Sal95].

Consider the problem of simulating a superconductor, as shown in Fig. B-1. The problem domain (Ω) has a spatial boundary Γ, on the nodes of which the boundary conditions are defined. The domain Ω is divided into different regions – air, silver and superconducting core. Each of these regions is subdivided in turn into a number of small elements of certain shape (triangular, rectangular etc.), which are the finite elements, as shown in Fig. B-2.

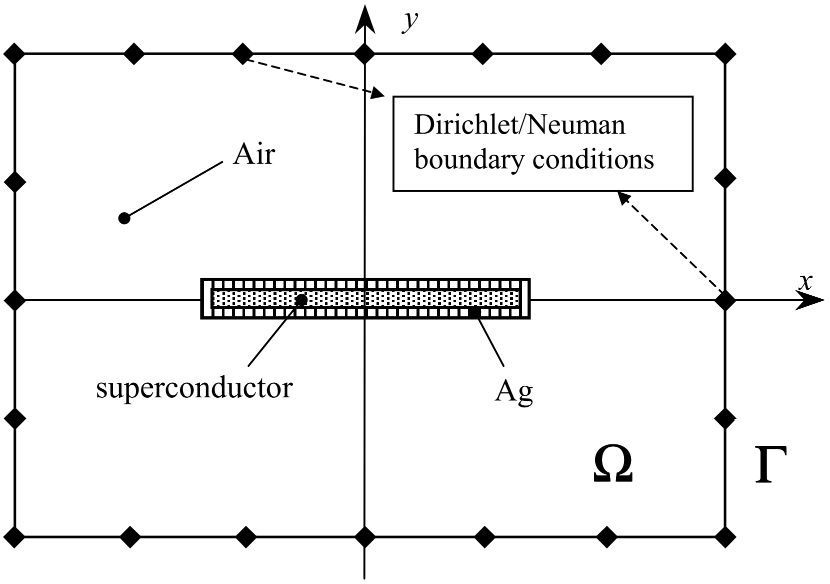

Figure B-1 Domain definition for FEM simulation of a superconducting tape. The boundary conditions are set for the nodes on the domain boundary as part of the problem definition.

To begin with, we take an operator equation:

$$\Im(x) = 0 \tag{B.1}$$

on the domain Ω. We substitute an approximate solution $\hat{x}$ into Eq. (B.1). Since $x \neq \hat{x}$, we obtain R, a *residual*.

$$\Im(\hat{x}) = R \tag{B.2}$$

The MWR now requires that the integral of the projection of the residual on a specified weighting function is zero over the problem domain. The choice of the weighting function determines the type of MWR. In the Galerkin method the weighting function is chosen to have the same form as the finite element shape function, see Eq. (B.13) below.

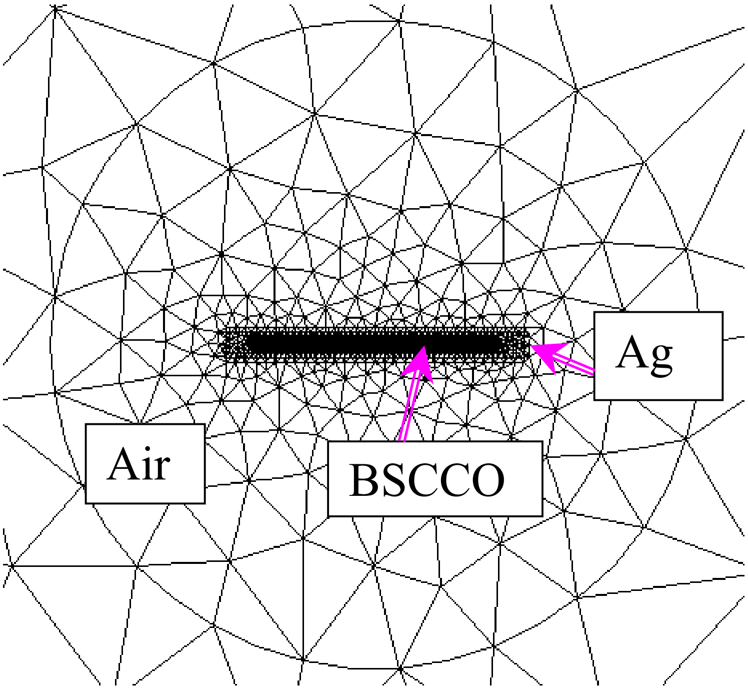

Figure B-2 Finite elements. The mesh in the BSCCO and Ag is much finer than in the air.

As an example we consider the time harmonic form of the diffusion equation with A, the z-component of the magnetic vector potential, as the unknown. In a 2D Cartesian problem,

$$\frac{1}{\mu}\frac{\partial^2 A}{\partial x^2} + \frac{1}{\mu}\frac{\partial^2 A}{\partial y^2} = -J_0 + j\omega\sigma A \tag{B.3}$$

where ω is the angular frequency, σ is the electrical conductivity, and J_0 is the applied current density.

Substituting an approximation $\hat{A}$ for A gives a residual R:

$$R = \frac{1}{\mu}\frac{\partial^2 \hat{A}}{\partial x^2} + \frac{1}{\mu}\frac{\partial^2 \hat{A}}{\partial y^2} - j\omega\sigma A + J_0 \tag{B.4}$$

Multiplying by a weighting function and setting the integral to zero,

$$\int_\Omega RW dxdy = 0 \tag{B.5}$$

Substituting for R,

$$-\iint_{\Omega} W\left(\frac{1}{\mu}\frac{\partial^2 \hat{A}}{\partial x^2}+\frac{1}{\mu}\frac{\partial^2 \hat{A}}{\partial y^2}\right)dxdy + j\omega\sigma\iint_{\Omega} W\hat{A}dxdy = \iint_{\Omega} WJ_0 dxdy \tag{B.6}$$

The first term of Eq. (B.6) is then integrated by parts and the surface integrals broken into summations over small areas. In this case the mesh consists of triangular elements, and the integral over the entire domain is replaced with the summation of the integral over the individual triangles.

Consider a triangular element (*i-j-k*) depicted in Fig. B-3. The vertices are nodes, at which the unknown vector potentials have to be eventually calculated. If we assume that the potential varies linearly in the element, we obtain what is known as a linear or first order element. With this approximation we may express the vector potential at any point in the triangle as:

$$\hat{A} = C_1 + C_2 x + C_3 y \tag{B.7}$$

where C_1, C_2 and C_3 are constants to be determined. Note that since the vector potential varies linearly, the flux density, which is the derivative of the potential ($\mathbf{B} = \nabla \times \mathbf{A}$), is constant in the triangle.

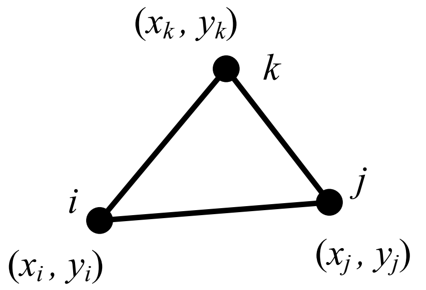

Figure B-3 First order triangular element with known coordinates (x, y) of each node.

At vertex i, we have $x = x_i$ and $y = y_i$. At this point $\hat{A}$ must be equal to $\hat{A}_i$, so that similarly for the nodes j and k, we obtain:

$$\begin{aligned} C_1 + C_2 x_i + C_3 y_i &= \hat{A}_i \\ C_1 + C_2 x_j + C_3 y_j &= \hat{A}_j \\ C_1 + C_2 x_k + C_3 y_k &= \hat{A}_k \end{aligned} \tag{B.8}$$

The linear system in (B.8) has three equations and three unknowns and can be solved for C_1, C_2 and C_3 in terms of the potentials and the geometry of the triangle. Using the results, we may express $\hat{A}$ as:

$$\hat{A} = \frac{\left(a_i + b_i x + c_i y\right)\hat{A}_i + \left(a_j + b_j x + c_j y\right)\hat{A}_j + \left(a_k + b_k x + c_k y\right)\hat{A}_k}{2\Delta} \tag{B.9}$$

where Δ is the area of the triangle and

$$\begin{aligned} a_i &= x_j y_k - x_k y_j \\ b_i &= y_j - y_k \\ c_i &= x_k - x_j \end{aligned} \qquad \text{(B.10)}$$

The coefficients of the nodal potentials in Eq. (B.9) are called shape functions. The potential can be expressed as the sum of the shape functions times the nodal potential:

$$\hat{A} = \sum_{i=1}^{m} N_i(x, y)\hat{A}_i \qquad \text{(B.11)}$$

where there are m nodes in the element and N_i are the shape functions. These functions have the following properties:

1. $N_i = 1$ at node i and is 0 at all other nodes;
2. The sum of all the shape functions at any point in the triangle is 1.

Writing the nodal potential in the element in matrix form,

$$\hat{A}^e = \left(N_i^e, N_j^e, N_k^e\right)\begin{pmatrix} \hat{A}_i^e \\ \hat{A}_k^e \\ \hat{A}_k^e \end{pmatrix} \qquad \text{(B.12)}$$

where $N_i^e = \left(a_i^e + b_i^e x + c_i^e y\right)/2\Delta$, etc.

In the Galerkin method we choose the weighting function to be the same as the shape function:

$$W^e = \begin{pmatrix} N_i^e \\ N_j^e \\ N_k^e \end{pmatrix} \qquad \text{(B.13)}$$

Taking the derivatives of $\hat{A}$ and W^e with respect to x and y, and recognizing that $\iint dxdy = \Delta$, the general equation (B.6) is then written as a linear matrix equation that can be solved.

List of symbols and acronyms

Main symbols used

Throughout the text, the vector form of a physical quantity is given in **bold style** characters, while its norm is given in standard font style.

a	[m], [mm]	Half-width of the conductor (dimension along the x-axis)
A, $\mathbf{A}$	[Vs/m]	Magnetic vector potential
b	[m], [mm]	Half-thickness of the conductor (dimension along the y-axis)
B, $\mathbf{B}$	[T], [mT]	Magnetic flux density
$\mathbf{B}_{//}$	[T], [mT]	Magnetic field parallel to x-axis
$\mathbf{B}_{\perp}$	[T], [mT]	Magnetic field perpendicular to the x-axis
B_a	[T], [mT]	Amplitude of the applied external magnetic field
$\mathbf{B_{ab}}$	[T], [mT]	Magnetic field parallel to the a,b-plane of a HTS tape
$\mathbf{B_c}$	[T], [mT]	Magnetic field parallel to the c-plane of a HTS tape
B_o	[T]	Normalizing constant of 1 T, used in the $J_c(B)$ and $n(B)$ models
B_p	[T], [mT]	Field of full penetration
d	[m], [mm]	Thickness of the Ag (Ag alloy) sheath
E, $\mathbf{E}$	[V/m]	Electric field
E_c	[V/m]	Electric field at which the critical current is defined (10^{-4} V/m)
f	[Hz]	Frequency of the applied AC current or external field
$F(B)$		Functional dependence on B
$F(x)$		Functional dependence on x
H, $\mathbf{H}$	[A/m]	Magnetic field strength
H_c	[A/m]	Thermodynamical critical field in type-I superconductors
H_{c1}	[A/m]	Lower critical field in type-II superconductors
H_{c2}	[A/m]	Upper critical field in type-II superconductors
H_{irr}	[A/m]	Irreversibility field in type-II superconductors
I_c	[A]	DC critical current obtained with transport set-up in self-field
I_m, I_p	[A]	Amplitude (peak value) of the transport current
i	[-]	Reduced (normalized) transport current (I_m/I_c)
J, $\mathbf{J}$	[A/mm^2]	Current density
J_c	[A/mm^2]	Critical current density
J_{c0}	[A/mm^2]	Critical current density without any magnetic field present
J_{max}, J_{min}	[A/mm^2]	Saturating current density
$\mathbf{M}$	[A/m]	Magnetization
n	[-]	Power index value in the E-J relation $E \sim J^n$
P	[W/m^3]	Power dissipation density
P_{eddy}	[W/m]	Eddy current loss
P_{hyst}	[W/m]	Hysteresis loss
P_{meas}	[W/m]	Measured AC loss
Q_e, Q_{ed}	[Wm^{-1}Hz^{-2}]	Eddy current loss factor
Q_h, Q_{hyst}	[J/m]	Hysteresis loss per cycle
Q_m	[J/m]	Magnetization loss in the superconductor per cycle

Q_r, Q_{res}	[W/m]	Resistive flux-creep loss
R	[Ω]	Electric resistance
S	[m^2]	Cross-sectional area of the superconductor
T_c	[K]	Critical temperature
t	[s]	Time
v	[m^3]	Volume
V	[V]	Voltage
w	[m], [mm]	Width of the Ag (Ag alloy) sheath
x	[m]	x-coordinate (in subscript means component parallel to the x-axis)
y	[m]	y-coordinate (in subscript means component parallel to the y-axis)
z	[m]	z-coordinate (in subscript means component parallel to the z-axis)
α	[degrees]	Angle between B and the x-axis
α_i	[-]	Coefficients in the $J_c(B)$ models
β	[-]	Normalized magnetic field (ratio B_a/B_p)
β_i	[-]	Coefficients in the $n(B)$ models
δ	[m]	Penetration depth of eddy currents
λ	[-]	Filling factor (ratio of superconductor to total volume)
Φ	[Wb]	Magnetic flux
η	[-]	Demagnetizing factor of the geometry
μ_0	[H/m]	Permeability of vacuum (equal to $4\pi 10^{-7}$)
ρ	[Ωm]	Electric resistivity
ρ_n	[Ωm]	Electric resistivity of a superconductor in normal state
ρ_f	[Ωm]	Flux-flow resistivity of a superconductor above J_c
σ	[S/m]	Electric conductivity
ω	[Rad/s]	Angular frequency = $2\pi f$

Acronyms used

For clarity and brevity of the text, the following acronyms have been used:

AC	Alternating current
Bi-2212	$Bi_2Sr_2CaCu_2O_x$ oxide compound
Bi-2223	$Bi_2Sr_2Ca_2Cu_3O_x$ oxide compound
Bi-2223/Ag	$Bi_2Sr_2Ca_2Cu_3O_x$ conductor with silver sheath (matrix)
BSCCO	Bismuth-strontium-copper-calcium oxide
CSM	Critical state model
DC	Direct current
FEM	Finite element method
HTS	High-temperature superconductor(s)
LTS	Low-temperature superconductor(s)
YBCO	Yttrium-barium-copper oxide

References

[Abr57] A.A. Abrikosov, J. Experim. Theoret. Phys. (USSR) 32, p.1442, 1957 (translation: Soviet Phys. – JETP 5, p. 1174, 1957)

[Ame97] N. Amemiya, K. Miyamoto, N. Banno and O. Tsukamoto, "*Numerical analysis of AC losses in high-T_c superconductors based on E-J characteristics represented wit n-value*", IEEE Trans. Appl. Supercon. 7 (2), p. 2110, 1997

[Ame98a] N. Amemiya, S. Murasawa, N. Banno, K. Miyamoto, "*Numerical modelings of superconducting wires for AC loss calculation*", Physica C 310, p. 16, 1998

[Ame98b] N. Amemiya *et al.*, "*Finite element analysis of AC loss in non-twisted Bi-2223 tape carrying AC transport current and/or exposed to DC or AC external magnetic field*", Physica C 310, p.30, 1998

[Ame01] N. Amemiya and Yoshiyuki Ohta, "*Mode of magnetic flux penetration into high T_c superconductors with various cross-sectional shape and their AC loss characteristics*", Physica C 357-360, p. 1134, 2001

[And62] P.W. Anderson, "*Theory of flux creep in hard superconductors*", Phys. Rev. Lett. 9 (7), p. 309, 1962

[Ash94] S. Ashworth, "*Measurements of AC losses due to transport currents in bismuth superconductors*", Physica C 229, p.355, 1994

[Ash00] S. Ashworth and M. Suenaga, "*Experimental determination of the losses produced by the interaction of AC magnetic fields and transport currents in HTS tapes*", Physica C 329, p.149, 2000

[Bea62] C.P. Bean, "*Magnetization of hard superconductors*", Phys. Rev. Lett., p. 250, 1962

[Bea64] C.P. Bean, "*Magnetization of high-field superconductors*", Rev. Mod. Phys., p. 31, 1964

[Bed86] J.C. Bednorz and K.A. Müller, "*Possible high-T_c superconductivity in the Ba-La-Cu-O System* ", Zeitschrift für Physik B. 64 (2), p. 189, 1986

[Bin92] K. J. Binns, P. Lawrenson and C. Trowbridge, "*The Analytical and Numerical Solution of Electric and Magnetic Fields* ", Chichester, UK: John Wiley & Sons, 1992

[Bra93] E. H. Brandt and M. Indenbohm "*Type-II-superconductor strip with current in a perpendicular magnetic field*", Phys. Rev. B 48 (17), p.12893, 1993

[Bra96a] E. H. Brandt and A. Gurevich, "*Linear Ac response of thin superconductors during flux creep*", Phys. Rev. Lett. 76 (10), p.12893, 1996

[Bra96b] E. H. Brandt, "*Superconductors of finite thickness in a perpendicular magnetic field: strips and slabs*", Phys. Rev. B 54 (6), p.4246, 1996

[Bus74] J. Bussière, M . Garber and M .Suenaga, "*The effect of cladding material on ac losses of commercial Nb_3Sn tapes*", J. Appl. Phys. 45 (10), p.4611, 1974

[Cam82] A.M. Campbell, "*A general treatment of AC losses in multifilamentary superconductors*", Cryogenics, pp. 3-16, 1982

[Car83] W. J. Carr, Jr., "*AC Loss and Macroscopic Theory of Superconductors*", New York: Gordon & Breach, 1983

[Che01] M. Chen *et al.*, "*Resistive type superconducting fault current limiter based on Bi-2212 conductor*", paper no. G4-01, EUCAS-2001, Copenhagen

[Cis95] M. Ciszek, B.A. Glowacki, S.P. Ashworth, A.M. Campbell and J.E. Evetts, "*AC losses of Ag-(BiPb)SrCaCuO-2223 tapes in combination of transverse external magnetic field and transport current*", IEEE Trans. Appl. Supercon. 5 (2), p. 709 1995

[Con01] Consortium of European Companies Determined to use Superconductivity, market survey, Dec. 2001, www.conectus.org

[Cri01] A. Cristofolini *et al.*, "*Current distribution in a composite superconducting system by means of an equivalent circuit model based on a smooth E-J equivalent material characteristic*", paper no. M4.1-10, EUCAS-2001, Copenhagen

[Däu98] M. Däumling, "*AC power loss for superconducting strips of arbitrary thickness carrying a transport current*", Physica C 310, p. 12, 1998

[Del01] V. Delafosse and J.-C. Vérité, "*An industrial simulation tool for determining AC losses in superconductors*", paper no. M2.2-06, EUCAS-2001, Copenhagen

[DoE98] U.S. Department of Energy report "*At the Frontiers of Science: Superconductivity and its Electric Power Applications*", DOE/GO-10098-434, July 1998

[Dol96] P. Dolez, M Aubin, D Willén, R Nadi and J Cave., "*Calorimetric ac loss measurements of silver sheathed Bi-2223 superconducting tapes*", Supercon. Sci. Tech. 9, p. 374, 1996

[Dre96a] L. Dresner "*Hysteresis losses in power-law cryoconductors. Part I*", Appl. Supercon. 4 (2), p. 167, 1996

[Dre96b] L. Dresner "*Hysteresis losses in power-law cryoconductors. Part II*", Appl. Supercon. 4 (7), p. 337, 1996

[Dut99] B. Dutoit, M. Sjöström and S. Stavrev, "*Bi(2223) Ag sheathed tape I_c and exponent n characterization and modelling under DC magnetic field*", IEEE Trans. Appl. Supercond. 9 (2), p. 809, 1999

[Flux2D] Flux2D software package, CEDRAT S.A., 38246 Meylan, France, www.cedrat.com

[Fri97] C. Friend *et al,*. "*Explaining the self-field AC loss behaviour of silver-clad (BiPb)-2223 tapes for power engineering applications*", Physica C 279, p.145, 1997

[Fri99] C. Friend, "*BIG-POWA*", European RTD project proposal, 1999

[Fri01] C. Friend, D. Spiller, Y. Huang and E. Martinez, "*Low loss conductors for power applications*", IEEE Trans. Appl. Supercond. 11 (1), p. 2196, 2001

[Fuk94] T. Fukunaga, S. Maruyama, T. Abe and A. Oota, "*AC losses of Ag/Bi-2223* *superconducting wires*", Physica C, p.3231, 1994

[Fuk95] T. Fukunaga and A. Oota, " *Hysteresis and eddy-current losses of Ag/Bi-2223 rod-form wires under AC transport currents*", Physica C, p.325, 1995

[Fuk99] T. Fukunaga, R. Inada and A. Oota, "*Current distributions and AC losses in self-fields for superconducting tapes and cables"*, IEEE Trans. Appl. Supercon. 9 (2), p.1057, 1999

[Fuk01] S. Fukui *et al.*, "*Analysis and measurements of AC transport current loss in BSCCO tape in external magnetic field*", IEEE Trans. Appl. Supercon. 11 (1), p. 2212, 2001

[Fum95] Y. Fukumoto *et al.*., "*Alternating current losses in mono- and multicore silver sheathed Bi-2223 tapes at 27 K in DC magnetic fields*", J. Appl. Phys.78 (7), p. 4584, 1995

[Gin50] V.L. Ginzburg and L.D. Landau, "*On the theory of superconductivity*", Zhurnal Experimentalnoi i Teoreticheskoi Fisiki 20, p. 1064, 1950 (in Russian)

[Glo97] B.A. Glowacki *et al.*, "*The influence of the Ag/Bi2223 conductor architecture on the transport AC losses*", Inst. Phys. Conf. Ser. 158, p. 1437, 1997

[Göm01] F. Gömöry *et al.*, "*Partitioning of transport AC loss in a superconducting tape into magnetic and resistive components*", IEEE Trans. Appl. Supercon. 11 (1), p.2967, 2001

[Gra95] G. Grasso, B. Hensel, A. Jeremie and R. Flükiger, "*Distribution of the transport critical current density in Ag sheathed* $(BiPb)_2Sr_2Ca_2Cu_3O_x$ *tapes produced by rolling"*, Physica C 221, p. 45, 1995

[Gra01] P. Grant, "*Advances in power applications of superconductivity in the United States"*, special plenary lecture no. SPL-2, ISS-2001, Kobe

[Hak00] B. ten Haken, H.J.N. van Eck and H.H.J. ten Kate, "*A new experimental method to determine the local critical current density in high-temperature superconducting tapes"*, Physica C 334, p. 163, 2000

[Has98] H. Hashizime and S. Toda, "*Electromagnetic thermal analysis of low/high-Tc superconducting wire*", IEEE Trans. Magnetics. 34 (5), p. 3016, 1998

[Hua98a] Y.B. Huang and R. Flükiger, "*Reducing ac losses of Bi(2223) multi-filamentary tapes by oxide barriers*", Physica C 294, p. 71, 1998

[Hua98b] Y. K. Huang, B. ten Haken, and H.H.J. ten Kate, "*Critical current of high* T_c *superconducting Bi2223/Ag tapes"*, Physica C 309, p. 197, 1998

[Hug94] T. Hughes *et al.*, "*Measurements of self-field AC losses in PbB-2223 Ag-sheathed tapes*", Physica C 235-240, p.3423, 1994

[Hug97] T. Hughes, "*Self-field AC loss in Ag-sheathed PbBi2223 tapes*", Ph.D. Thesis, University of Southampton, 1997

[Hug99] T. Hughes, Y. Yang, C. Beduz and A. Power, "*Self-field AC loss of assemblies of Ag-sheathed PbBi2223 tapes*", IEEE Trans. Appl. Supercon. 9 (2), p.774, 1999

[Ich01] T. Ichikawa *et al.*, "*Analysis of a Bi-2223/Ag multi-layered bulk sample with an R–L equivalent circuit*", Physica C 357-360, p. 248, 2001

[Ina99] R. Inada *et al.*, ”*Understanding of AC transport losses for Ag-sheathed Bi2223 multifilamentary tapes*”, Advances in Superconductivity XII, p.748, 1999

[Inn78] A.C. Rose-Innes and E.H. Rhoderick, “*Introduction to Superconductivity*”, Oxford: Pergamon Press, 1978

[Ish96] H. Ishii *et al.*, ”*The AC losses in* $(Bi,Pb)_2Sr_2Ca_2Cu_3O_x$ *silver-sheathed superconducting wires*”, Cyogenics 36, p.697, 1996

[Iwa95] Y. Iwasa and V. Adzovie, “*Index number (n) below critical current in Nb-Ti superconductors*”, IEEE Trans. Appl. Supercon. 5 (3), p. 3437, 1995

[Jil94] D.C. Jiles, “*Modelling the effects of eddy current losses on frequency dependent hysteresis in electrically conducting media*”, IEEE Trans. Magn. 30 (6), p.4326, 1994

[Kaj01] K. Kajikawa *et al.*, “*Numerical simulation for AC losses of HTS tapes in combined alternating transport current and external AC magnetic field with phase shift* ”, IEEE Trans. Appl. Supercon. 11 (1), p. 2240, 2001

[Kim62] Y. B. Kim, C. F. Hempstead and A. R. Strnad, “*Critical persistent currents in hard superconductors*”, Phys. Rev. Lett. 9 (7), p. 306, 1962

[Kim63] Y.B. Kim, C.F. Hempstead and A.R. Strnad, “*Flux creep in hard superconductors*”, Phys. Rev. 131 (6), p. 2486, 1963

[Kov99] P. Kováč, I. Husek, A. Rosova and W. Pachla, “*Thermomechanical treatment, structure and transport currents in multicore Bi(2223)/Ag tapes”*, Physica C 312, p. 179, 1999

[Kov01a] P. Kovác *et al.*, “*BSCCO/Ag tapes made by a tape-in-rectangular tube process* ”, Supercond. Sci. Technol. 14 (3), p. 139, 2001

[Kov01b] P. Kovác *et al.*, “*Transversal and longitudinal current distribution in Bi-2223/Ag tapes with high filament aspect ratio*”, paper no. E3.2-10, EUCAS-2001, Copenhagen

[Kum89] G. R. Kumar and P. Ghaddah, “*Extension of Bean's model for high-*T_c *superconductors*”, Phys. Rev. B 39 (7), p. 4704, 1989

[Kwa97] K. Kwasnitza, St. Clerk, R. Flükiger, Y. B. Huang and G. Grasso, “*AC losses of twisted high-*T_c *superconducting multifilament Bi2223 tapes with a mixed matrix of Ag and* $BaZrO_3$”, Inst. Phys. Conf. Ser. 158, p. 1389, 1997

[Kwa01] K. Kwasnitza, St. Clerk, R. Flükiger, G. Witz and Y. B. Huang, “*Geometry dependence of 50 Hz alternating magnetic field in superconducting multifilamentary Bi(2223)/Ag tapes* ”, Physica C 355, p. 325, 2001

[Lar00] D. Larbalestier, “*HTS Power Applications: Fundamentals to Wires*”, Short Course, Applied Superconductivity Conference, Virginia Beach, 2000

[Lay99] L.L. Lay, D. Spiller and O.Belmont, “*Over-critical current behaviour of Bi-2223 tapes*”, IEEE Trans. Appl. Supercon. 9 (2), p. 1324, 1999

[Law01] L.R. Lawrence, “*Foundations for Superconductivity Analysis*”, Bob Lawrence & Associates report, Aug. 2001

[Leg01] M. Leghissa *et al.*, "*Development and application of superconducting transformers*", paper no. B4-01, EUCAS-2001, Copenhagen

[Mag98] N. Magnusson and S. Hörnfeldt, "*Calorimetric apparatus for alternating current loss measurements on high-temperature superconductors*", Rev. Sci. Instrum. 69, p. 3320, 1998

[Mag01] N. Magnusson, "*Semi-empirical model of the losses in HTS tapes carrying Ac currents in AC magnetic field applied parallel to the tape surface*", Physica C 349, p. 225, 2001

[Mah99] A. E. Mahdi, A. Tami and R. Stoll, "*Modeling of magnetic properties and alternate current losses in high-T_c superconductors using a power law voltage-current characteristic*", J. Appl. Phys. 85 (8), p. 5359, 1999

[Mas97] M. Maslouh, F. Booillault, A. Bossavit and J.-C. Vérité, "*From Bean's model to the H-M charatcteristics of a superconductor: some numerical experiments*", IEEE Trans. Appl. Supercon. 7 (3), p. 3797, 1997

[Mas98] M. Maslouh *et al.*, "*Numerical modelling of superconductor materials using anisotropic Kim law*", IEEE Trans. Magnetics 34 (5), p. 3064, 1998

[Mas01] T. Masuda *et al.*, "*Verification tests of a 66 kV HTSC cable system for practical use*", paper no. WS-34, ISS-2001, Kobe

[Mee01] O. van der Meer, B. ten Haken and H.H.J ten Kate, "*A model to describe the angular dependence of the critical current in a Bi-2223/Ag superconducting tape*", Physica C, p. 1174, 2001

[Meh97] S. Mehta, N. Aversa and M. Walker, "*Transforming transformers*", IEEE SPECTRUM, p. 43, July 1997

[Mei33] W. Meissner and R. Ochsenfeld, "*Ein neuer Effekt bei Entritt der Supraleitfähigkeit*", Die Naturwissenschaften 21, p. 787, 1933

[Mul01] J. Mulholland, T. Sheahen and B. McConnel, "*Analysis of Future Prices and Markets for High Temperature Superconductors",* US Department of Energy report, Sept. 2001

[Mül95] K.-H. Müller, C. Andrikidis, H.K. Liu and S.X. Dou, "*AC hysteresis losses in monofilamentary Pb-Bi-Sr-Cu-O/Ag tapes",* Physica C 247, p. 74, 1995

[Mül97a] K.-H. Müller, "*AC Power losses in flexible thick-film superconducting tapes*", Physica C 281, p.1, 1997

[Mül97b] K.-H. Müller and K.E. Leslie, "*Self-field ac loss of Bi-2223 superconducting tapes*", IEEE Trans. Appl. Supercon. 7 (2), p. 306, 1997

[Mur77] J.H. Murphy, "*Skin effect alternating current losses in multifilamentary superconductors*", IEEE Trans. Mag. 1 (13), p. 564, 1977

[Nib97] N. Nibbio, S. Stavrev and B. Dutoit, "*Magnetic and electric simulation of eddy currents in Ag sheathed Bi2223 tapes*, Advances in Superconductivity X, p. 1369, 1997

[Nib98] N. Nibbio, S. Stavrev and B. Dutoit, "*Effect of the sheath resistivity and tape geometry* *on eddy current loss in Bi(2223) tapes*, Physica C 310, p. 208, 1998

[Nib99] N. Nibbio, "*Nonlinear electromagnetic modelling of high temperature superconducting tapes*", Ph. D. Thesis No. 2031, Swiss Federal Institute of Technology – Lausanne, 1999

[Nib00] N. Nibbio, P. Lombard and D. Taghezout, "*FEM simulation of high temperature superconducting tapes using power law E-J dependence*", proceedings of the IXth IEEE Conference on Electromagnetic Field Computation, Milwaukee, WI, June 4-7, 2000

[Nib01a] N. Nibbio, S. Stavrev and B. Dutoit, "*Finite element method simulation of AC loss in HTS tapes with B-dependent E-J power law"*, IEEE Trans. Appl. Supercond. 11 (1), p. 2631, 2001

[Nib01b] N. Nibbio and S. Stavrev, "*Effect of the geometry of HTS on AC loss by using finite element method simulation with B-dependent E-J power law*", IEEE Trans. Appl. Supercond. 11 (1), p. 2627, 2001

[Nor70] W.T. Norris, "*Calculation of hysteresis loss in hard superconductors carrying ac loss: isolated conductors and edges of thin sheets*", J. Phys. D (3), p.489, 1970

[Nou97] J.Noudem *et al.*, "*Study of the superconducting transition at high pulsed current of bulk Bi-2223 sintered and textured by hot forging*", Physica C 281, p.339, 1997

[Onn11] H. Kamerlingh Onnes, "*Further experiments with liquid helium. On the change of the electrical resistance of pure metal at very low temperature*", Leiden Comm. 122b, pp. 3-5, pp. 13-15, pp. 21-25, 1911

[Oom97] M.P. Oomen J. Rieger, M. Leghissa and H.H.J. ten Kate, "*Magnetic ac loss in multi-filamentary Bi-2223/Ag tapes*", Physica C 290, p.281, 1997

[Ore92] J. Orehotsky *et al.*, "*AC losses in powder-in-tube Bi-2223 tapes at power frequencies*", Appl. Phys. Lett., 60 (2), p.252, 1992

[Paa95] J. Paasi *et al.*, "*Electric field and losses in BSCCO-2223/Ag tapes carrying AC transport current*", IEEE Trans. Appl. Supercon. 5 (2), p. 713, 1995

[Paa96] J. Paasi *et al.*, "*AC losses in multifilamentary Bi-2223/Ag superconducting tapes*", IEEE Trans. Magn, 32 (4), p. 2792, 1996

[Paa97] J. Paasi and M. Lahtinen, "*Computational comparison of AC losses in different kinds of HTS composite conductors*", IEEE Trans. Appl. Supercon. 7 (2), p. 322, 1997

[Paa98] J. Paasi and M. Lahtinen, "*AC losses in high-temperature superconductor: revisiting the fundamentals of the loss modelling*", Physica C 310, p. 57, 1998

[Par97] M. Parizh, A. K. Kalafala and R. Wilcox, "*Superconducting magnetic energy storage for substation applications*", IEEE Trans. Appl. Supercon. 7 (2), p. 849, 1997

[Pau01] W. Paul *et al.*, "*Fault current limiter based on high temperature superconductors – different concepts, test results, simulations, applications*", Physica C 354, p. 27, 2001

[Pri97] L. Prigozhin, "*Analysis of critical state problems in type-II superconductivity*", IEEE Trans. Appl. Supercon. 7 (4), p. 3866, 1997

[Pro94] P-A Probst and A. Jaquier, "*Multiple-channel digital lock-in amplifier with ppm resolution*", Rev. Sci. Instrum. 65, p. 747, 1994

[Rab99a] J.J. Rabbers, D.C. van der Laan, B. ten Haken and H.H.H. ten Kate, "*Magnetization and transport current loss of a BSCCO/Ag tape in an external AC magnetic field carrying AC transport current*", IEEE Trans. Appl. Supercond. 9 (2), p. 1185, 1999

[Rab99b] J.J. Rabbers, B. ten Haken and H.H.H. ten Kate, "*Transport current loss of BSCCO/Ag tape in different orientations of the external magnetic field*", IEEE Trans. Appl. Supercond. 9 (2), p. 801, 1999

[Rab01a] J.J. Rabbers, "*AC Loss in Superconducting Tapes and Coils*", Ph.D. Thesis, University of Twente, 2001

[Rab01b] J.J. Rabbers, B. ten Haken, O. Schevchenko and H.H.J. ten Kate, "*An engineering formula to describe the AC loss of BSCOO/Ag tape*", IEEE Trans. Appl. Supercond. 11 (1), p. 2623, 2001

[Ros78] AC Rose-Innes and E.H. Rhoderik, "*Introduction to Superconductivity*", Oxford: Pergamon Press, 1978

[Rhy93] J. Rhyner, "*Magnetic properties and AC losses of superconductors with power law current-voltage characteristics*", Physica C 212, p. 292, 1993

[Rhy02] J. Rhyner, "*Vector potential theory of ac loss in superconductors*", Physica C, in press

[Sal95] S. J. Salon, "*Finite Element Analysis of Electrical Machines*", Norwell, USA: Kluwer Academic Publishers, 1995

[Sch01] N. Schönborg and S. Hörnfeldt, "*Losses in a high-temperature superconductor exposed to AC and DC transport currents and magnetic fields*", IEEE Trans. Appl. Supercond. 11 (3), p. 4086, 2001

[She94] T.P. Sheahan, "*Introduction to High-Temperature Superconductivity*", New York: Plenum Press, 1994

[She97] O. Shevchenko, H. Knoopers and H. ten Kate, "*Characterisation of super-conducting components using PSPICE*", IEEE Trans. Appl. Supercon. 7 (2), p. 404, 1997

[She98] O.A. Shevchenko, J.J. Rabbers, A. Godeke, B. ten Haken and H.H.J. ten Kate*, "AC loss in a high-temperature superconducting coil",* Physica 310, p.106, 1998

[She99] O.A. Shevchenko, J.J. Rabbers, B. ten Haken and H.H.J. ten Kate*, "Angle dependency of AC losses in a BSCCO-2223 tape – simulation and experiment",* Inst. Phys. Conf. Ser. No. 167, p. 879, 1999

[Sig91] T. Sigiura, H. Hashizime and K. Miya, "*Numerical electromagnetic field analysis of type II superconductors*", Int. J. Appl. Electromag. Mat. 2 , p. 183, 1991

[Sjö01] M. Sjöström, "*Hysteresis Modelling of High Temperature Superconductors*", Ph.D. Thesis No. 2372, Swiss Federal Institute of Technology – Lausanne, 2001

[Sok98] V. Sokolovsky, V. Meerovich, S. Goren and G. Juang, "*Analytical approach to AC loss* *calculation in high-T_c superconductors*", Physica C 306, p. 154, 1998

[Sta98a] S. Stavrev and B. Dutoit, "*Frequency dependence of AC losses in Bi(2223)Ag-sheathed tapes*", Physica C 310, p. 86, 1998

[Sta98b] S. Stavrev, B. Dutoit, N. Nibbio and L. Le Lay, "*Eddy current self-field loss in Bi-2223 tapes with AC transport current*", Physica C 307, p. 105, 1998

[Sta00] S. Stavrev, B. Dutoit and C. Friend, "*Response of Bi-2223 tapes to over-critical current excursions*", Physica C 339, p.69, 2000

[Sta01a] S. Stavrev *et al.*, "*Comparison of numerical methods for modelling of superconductors*", paper no. 128, COMPUMAG-2001, Evian, to be published in IEEE Trans. Magnetics

[Sta01b] S. Stavrev *et al.*, "*Numerical modelling of Bi-2223 multifilamentary tapes with position dependent J_c*", paper no. N4.1-06, EUCAS-2001, Copenhagen, to be published in Physica C

[Sta01c] S. Stavrev, Y. Yang and B. Dutoit, "*Modelling and AC losses of BSCCO conductors with anisotropic and position dependent J_c*", paper no. WSP-10, ISS-2001, Kobe, to be published in Physica C

[Sta02a] S. Stavrev, B. Dutoit and P. Lombard, "*Numerical modelling and AC losses in multifilamentary Bi-2223/Ag conductors with various geometry and filament arrangement*", accepted for publication in Physica C

[Sta02b] S. Stavrev, B. Dutoit and N. Nibbio, "*Geometry considerations for use of Bi-2223/Ag tapes and wires with different models of $J_c(B)$*", accepted for publication in IEEE Trans. Appl. Supercond.

[Ste01] N. Steve *et al.*, "*High temperature superconducting cable field demonstration at Detroit Edison*", Physica C 354, p. 49, 2001

[Str00] G. Strano, A.S. Siri and G. Grasso, "*Current distribution and microstructure studies of isolated filaments extracted from Ag-sheathed Bi(2223) tapes*", Supercond. Sci. Technol. 13, p. 1470, 2000

[Su01] X. Su, G. Witz, R. Passerini and R. Flükiger, "*New configurations for square and round Bi(2223) wires*", paper no. E3.2-18, EUCAS-2001, Copenhagen

[Syk97] J. K. Sykulski, R. L. Stoll and A. E. Mahdi, "*Modelling HTc superconductors for AC power loss estimation* ", IEEE Trans. Magnetics 33 (2), p. 1568, 1997

[Tan01] Y. L. Tang *et al.*, "*Investigation on the anisotropy of the current density characteristics and flux pinning in Ag-sheathed Bi-2223 tape* ", Physica C 351, p. 139, 2001

[Tam99] A. Tami, A. E. Mahdi and D. Mapps, "*2-D numerical model for estimation of AC losses in High-T_c superconducting tapes*", IEEE Trans. Magnetics 35 (5), p. 4088, 1999

[Tin75] M. Tinkham, "*Introduction to Superconductivity*", New-York: McGraw-Hill, 1975

[Tix95] P. Tixador, "*Les Supraconducteurs*", Paris: Hermès, 1995

[The94] H. Theuss, T. Becker and H. Kronmüller, "*Influence of geometry on angle-dependent* *critical current density measurements in thin-film superconductors*", Physica C 223, p. 179, 1994

[Vin91] V.M. Vinokur, M.V. Feigel'man and V.B. Geshkenbein, "*Exact solution for flux creep with logarithmic U(j) dependence: self-organized critical state in high-*T_c *superconductors*", Phys. Rev. Lett. 67 (7), p. 915, 1991

[Vin00a] E. Vinot, "*Modelling of HTS superconductors. Applications of AC loss calculation*", Ph. D. Thesis, Institut National Polytechnique de Grenoble, 2000

[Vin00b] E. Vinot, G. Meunier and P. Tixador, "*Different formulations to model superconductors*", IEEE Trans. Magnetics 36 (4), p. 1226, 2000

[Vin00c] E. Vinot, V. Leconte, G. Meunier and P. Tixador, "*Superconducting model with circuit coupling in 2D or axisymetrical cases*", proceedings of the IXth IEEE Conference on Electromagnetic Field Computation, Milwaukee, WI, June 4-7, 2000

[Vol99] A. Volkozub *et al.*, "*The analysis of current distribution in filamentary conductors: the influence of intergrowths*", IEEE Trans. Appl. Supercond. 9 (2), p. 2147, 1999

[Wan00] Z. Wang, Z. Chen, Y. Zhou, Z. Duan and W. Wang, "*The effect of temperature on* J_c *and n-value of Bi(2223) tapes*", Cryogenics 40, p. 681, 2000

[Wil83] M.N. Wilson, "*Superconducting Magnets*", Oxford: Clarendon Press, 1983

[Wil01] D. Willén, "*Installation and operation of a 2 kA (rms) HTS power cable in a public utility grid*", paper no. F4-01, EUCAS-2001, Copenhagen

[Yam97] K. Yamafuji, T. Wakuda and T. Kiss, "*Generalized critical state model in high-*T_c *superconductors*", Cryogenics 37 (8), p. 421, 1997

[Yan94] Y. Yang *et al.*, "*Studies of self-field AC losses in PiBi-2223 Ag-sheathed tapes",* ICEC Supplement, Cryogenics, vol.34, p.789, 1994

[Yan95] Y. Yang *et al.*, "*AC V-I characteristics of Ag sheathed PbBi2223 tapes up to 10KHz : phenomena and interpretations*" , IEEE Trans. Appl. Supercon. 5 (2), p.701, 1995

[Yan96] Y. Yang et *al.*, "*The influence of the geometry on self-field AC losses of Ag sheathed PbBi2223 tapes",* Physica C 256, p.378, 1996

[Yan99] Y. Yang, E. Martinez and C. Beduz, "*Numerical modelling of the critical state and calculation of AC losses and current profiles in multifilamentary tape* ", Inst. Phys. Conf. Ser. No. 167, p. 855, 1999

[Yaz98] T. Yazawa, J.J. Rabbers, B. ten Haken, H.H.J. ten Kate and H. Maeda, "*AC loss analysis on high-temperature superconductors with finite thickness and arbitrary magnetic field dependent voltage-current relation*", J. Appl. Phys. 84 (10), p. 5652, 1998

[Yaz99] T. Yazawa *et al.*, "*Modeling the current distribution in HTS tapes with transport current and applied magnetic field* ", IEEE Trans. Appl. Supercon. 9 (2), p. 797, 1999

[Zha99] P.X. Zhang *et al.*, "*Transport AC losses of (BiPb)-2223 multifilamentary tapes with different filament distribution*", Advances in Superconductivity XII, p. 727, 1999

Curriculum Vitae

Svetlomir
STAVREV

born on 19.08.1970
married
Bulgarian citizen

EPFL-EL-LANOS
1015 Lausanne
Switzerland

e-mail: svet70@hotmail.com

Educational Background

Postgraduate degrees, certificates	▪ Ph.D. in Electrical Engineering: June 2002	Swiss Fed. Inst. of Technology – Lausanne, Switzerland
	▪ Postgraduate Program in Communication Systems: 1996-97	Swiss Fed. Inst. of Technology – Lausanne, Switzerland
	▪ Postgraduate Course in Biomedical Engineering: 1994-95	University of Patras, Greece
Higher education	▪ Diploma Engineer in Electrical Engineering: Sept. 1995	Technical University – Varna, Bulgaria
Secondary education	▪ Diploma of Completed Secondary Education: 06.1989	English Teaching Language School – Varna, Bulgaria

Work Experience

▪ Teaching and Research Assistant	Swiss Federal Institute of Technology – Lausanne, Switzerland	08.1997- 06.2002
▪ Electrical and Electronic Engineer	Center of Ocean Engineering Ltd. – Varna, Bulgaria	06.1992 - 09.1993 & 09.1995 - 05.1996

International Experience

▪ European Project on Applied Superconductivity (BIG-POWA) – 9 European industrial and university partners	Researcher, report manager	03.2000 - 06.2002
▪ 2000 International Symposium on Circuits and Systems, Geneva, Switzerland: 1300 participants, 34 industrial exhibits	Exhibit Chair	28-31 May 2000
▪ European Project on Applied Superconductivity (SACPA) – 6 European industrial and university partners	Researcher, report manager	08.1997 – 12.1998
▪ Biomedical Technology Research Center, Trieste, Italy	Practical placement	06.1996 – 08.1996

Publications

Conference papers in proceedings

- N. Nibbio, S. Stavrev, B. Dutoit: "*Magnetic and electric simulation of eddy currents in Ag sheathed Bi2223 tapes*", Advances in Superconductivity X, vol. 2, p. 1369, 1998.

- B. Dutoit, M. Sjöström and S. Stavrev: "*Bi(2223) Ag sheathed tape characterisation under DC applied magnetic field*", ICEC17, Superconductivity, Section 10, p. 419, 1998

Conference papers in reviewed journal issues

- S. Stavrev, Y. Yang, B. Dutoit: "*Modelling and AC losses of BSCCO conductors with anisotropic and position-dependent* J_c ", ISS'2001, 25-27 Sept. 2001, Kobe, Japan, to be published in Physica C

- S. Stavrev *et al.*: "*Numerical modelling of Bi-2223 multifilamentary tapes with position-dependent* J_c ", EUCAS'2001, 26-30 August 2001, Copenhagen, Denmark, to be published in Physica C

- S. Stavrev *et al.*: "*Comparison of Numerical Methods for Modelling of Superconductors*", to be published in IEEE Trans. Magnetics, vol. 38 (2), March 2002.

- N. Nibbio, S. Stavrev: "*Effect of the geometry of HTS on AC loss by using finite element method simulation with B-dependent E-J power law*", IEEE Trans. Applied Superconductivity, vol. 11 (1), p. 2627, 2001

- N. Nibbio, S. Stavrev, B. Dutoit: "*Finite element method simulation of ac loss in HTS tapes with B-dependent E-J power law*", IEEE Trans. Applied Superconductivity, vol. 11 (1), p. 2631, 2001

- B. Dutoit, M. Sjöström, S. Stavrev: "*Bi(2223) Ag sheathed tape* I_c *and exponent n characterisation and modelling under DC applied magnetic field*", IEEE Trans. Applied Superconductivity, vol. 9, (2) , p. 809, 1999

- S. Stavrev, B. Dutoit: "*Frequency dependence of AC loss in Bi(2223)Ag sheathed tapes*", Physica C 310, p. 86, 1998

- N. Nibbio, S. Stavrev, B. Dutoit: "*Effect of the sheath resistivity and tape geometry on eddy current loss in Bi(2223) tapes",* Physica C 310, p. 208, 1998

Journal articles

- S. Stavrev, B. Dutoit, N. Nibbio: "*Geometry considerations for use of Bi-2223/Ag tapes and wires with different models of* $J_c(B)$", IEEE Trans. Applied Superconductivity, in press

- S.Stavrev, B. Dutoit, P. Lombard: "*Numerical modelling and AC losses of multifilamentary Bi-2223/Ag conductors with various geometry and filament arrangement*", Physica C, in press

- S. Stavrev, B. Dutoit, C. Friend: "*Response of Bi-2223 tapes to over-critical current excursions*", Physica C 339, p. 69, 2000

- S. Stavrev, B. Dutoit, N. Nibbio, L. Le Lay: "*Eddy current self-field loss in Bi-2223 tapes with ac transport current*", Physica C 307, p. 105, 1998